

**Diamond-like Carbon Coatings for Improved Mechanical
Performance of Polymer Materials**

Sean Michael Carley

Submitted in accordance with the requirements for the degree of
Doctor of Philosophy

The University of Leeds

School of Mechanical Engineering

May 2017

The candidate confirms that the work submitted is his own, except where work which has formed part of jointly-authored publications has been included. The contribution of the candidate and the other authors to this work has been explicitly indicated below.

The candidate confirms that the appropriate credit has been given where reference has been made to the work of others.

In the papers listed below, the primary author completed all experimental studies, evaluation of data and preparation of publications. All authors contributed to proof reading of the articles prior to publication and discussion of the results presented.

Papers contributing to this thesis:

'Diamond-like Carbon coatings for improved tribological performance of polymers.' S. Carley, T. Liskiewisz, H. Zhao, A. Neville. *POLYTRIB 2016 – 2nd International Conference on Polymer Tribology Conference Proceedings*.

'Diamond-like Carbon coatings for improved tribological and mechanical performance of coatings' S. Carley, H. Zhao, C. Wang, T. Liskiewisz, A. Neville. *43rd Leeds-Lyon Symposium on Tribology Conference Proceedings*.

'Nanoindentation of DLC coated polymers to determine mechanical properties as performance indicators.' S. Carley, C. Wang, H. Zhao, A. Neville. (*Pending Submission*)

'Diamond like Carbon coatings deposited using Microwave Plasma Enhanced Chemical Vapour Deposition on polymer substrates.' S. Carley, H. Zhao, A. Neville. (*Pending Submission*)

This copy has been supplied on the understanding that it is copyright material and that no quotation from the thesis may be published without proper acknowledgement.

The right of Sean Michael Carley to be identified as Author of this work has been asserted by him in accordance with the Copyright, Designs and Patents Act 1988.

Acknowledgements

First and foremost, I would like to thank my supervisor, Prof. Anne Neville, not only for giving me the opportunity to work on this project, but for being an outstanding mentor throughout and an inspiration in everything she has achieved. Thanks to Dr Hongyuan Zhao for the countless discussions no matter the time, and for the help in the coatings lab. Other academics who have helped in both assisting in the lab and project discussions are Dr Chun Wang and Dr Tomasz Liskiewicz. I extend my thanks to Matthias & Neville for their guidance and difficult questions throughout the project.

I'd like to thank the technical staff of iFS for their help and support whenever needed; and a special mention to Tony who always had time to help out in the coatings lab.

To all the friends I've made at Leeds over my years here, who made the difficult days more bearable, and to Dr Ivan Kolev for the enlightening discussions on all things PVD.

And finally, to my Mum, Dad, Grandparents and Ruth. Without your continued emotional, financial, and moral support over the years I wouldn't have been able to get to where I am today. I dedicate this to you.

Abstract

The use of polymers has become more widespread over recent decades as an important material for light-weighting components across many industries. As the most efficient use of oil, they allow complex geometries to be manufactured, with lower weight than metallic or alloy counterparts, whilst remaining low cost. As the use of polymers continues to increase, so does the drive towards lightweight components required for increased efficiency in many industries. Therefore, the need for engineering polymers to be useful in a wider range of applications has become a necessity.

In this study, the use of Microwave assisted Plasma Enhanced Chemical Vapour Deposition (MW-PECVD) has been investigated as a way to deposit Diamond-Like Carbon (DLC) coatings directly onto polymer substrates. A Design of Experiments (DOE) approach was used to characterise the process with respect to how deposition parameters changed the mechanical properties of the coatings.

A Hauzer Flexicoat 850 deposition system, at the University of Leeds, was used to deposit 10 unique DLC coatings onto ABS and PEI polymers using a novel MW-PECVD technique. These coatings were then characterised to quantify their hardness, Young's modulus, thickness, chemical and structural composition. Further coatings were produced to explore the limitations of characterisation techniques for hard-on-soft coating systems. Scratch testing, cross hatch tests, and contact angle goniometry were used to assess coating adhesion, and reciprocating pin-on-plate tests were used to assess tribological properties.

This study has shown that the MW-PECVD technique is able to deposit strongly adhered hydrogenated amorphous carbon (a-C:H) coatings onto polymer substrates at high deposition rates, without damaging the thermally sensitive material. The coatings demonstrated the ability to increase the hardness and Young's modulus of the surface, however substrate effects are still present at ultra-low depth indentations of <5% of coating thickness. These substrate effects show the limitation of the system to withstand

practical loads, and the measurements of P/S^2 (a measure of resistance to plastic deformation) allowed visualisation of coating strain to failure and was the only measurement that could reliably distinguish between substrates with differing mechanical properties.

Table of Contents

Acknowledgements	ii
Abstract	iii
Table of Contents	v
List of Tables	ix
List of Figures	xi
Abbreviations	xix
Chapter 1. Introduction	1
1.1 Research Motivation	1
1.2 Aims & Objectives.....	4
1.2.1 Aim	4
1.2.2 Objectives.....	4
1.3 Thesis Outline.....	5
Chapter 2. Literature Review	6
2.1 Introduction	6
2.2 Deposition Processes	6
2.2.1 Plasma Characterisation	7
2.2.2 Sputtering	12
2.2.2.1 The Balanced and Unbalanced Magnetron	18
2.2.2.2 DC Sputtering	20
2.2.2.3 High Power Impulse Magnetron Sputtering (HiPIMS)	21
2.2.3 Thermal Arc Evaporation.....	22
2.2.4 Plasma Enhanced Chemical Vapour Deposition (PECVD)	26
2.3 Polymers	27
2.4 Coatings on Polymers.....	29
2.4.1 Limitations	29
2.4.1.1 Temperature	29
2.4.1.2 Adhesion.....	32

2.4.1.3	Mechanical properties and stress.....	34
2.4.2	Measurement Methods.....	37
2.4.2.1	Scratch test.....	37
2.4.2.2	Nanoindentation.....	39
2.5	DLC Coatings	43
2.5.1	Structure and Properties	43
2.5.2	Deposition Techniques, Conditions and Performance.....	48
2.6	Summary.....	53
Chapter 3.	Experimental Methodology	55
3.1	Introduction	55
3.2	Methods of Coating Deposition.....	55
3.2.1	Substrate Materials and Preparation.....	56
3.2.1.1	Sample Preparation	58
3.2.2	PECVD	58
3.2.3	MW-PECVD.....	59
3.3	Chemical & Structural Analysis	66
3.3.1	Deposition Rate & Surface Roughness.....	66
3.3.2	Structural Characterisation.....	67
3.3.3	Chemical Composition and Bonding Characterisation.....	68
3.3.3.1	Nuclear Magnetic Resonance (NMR) Spectroscopy.....	68
3.3.3.2	Ion Beam Analysis (IBA).....	69
3.3.3.3	Raman spectroscopy.....	70
3.4	Mechanical Properties	70
3.4.1	Hardness, Young's Modulus, & P/S ²	70
3.4.2	Coating Adhesion	72
3.4.3	Tribology.....	74
Chapter 4.	Film Deposition & Adhesion	75
4.1	Introduction	75
4.2	Process characterisation	75
4.2.1	Substrate Heating.....	76

4.2.1.1	Design of Experiments Model – Substrate Heating.....	78
4.2.2	Deposition Rate	80
4.2.2.1	Design of Experiments Model – Deposition Rate.....	82
4.2.3	Coating Roughness.....	84
4.2.4	Coating Adhesion	87
4.2.4.1	Pre-deposition Argon Plasma Immersion.....	87
4.2.4.2	Crosshatch Test.....	88
4.2.4.3	Scratch Test.....	90
4.3	Conclusion	94
Chapter 5. Coating Structure & Composition		96
5.1	Introduction	96
5.2	Structure	96
5.3	Composition.....	103
5.3.1	Raman Spectroscopy	103
5.3.2	Solid state NMR spectroscopy (SSNMR).....	105
5.3.3	Elastic Recoil Detection (ERD).....	106
5.4	Conclusion	109
Chapter 6. Mechanical Properties		110
6.1	Introduction	110
6.2	Hardness.....	110
6.2.1	Polymer Properties.....	110
6.2.2	Composite Properties.....	111
6.2.3	Design of Experiments model – Hardness.....	120
6.2.3.1	ABS Substrate	121
6.2.3.2	PEI Substrate.....	123
6.3	Young's modulus	124
6.3.1	Polymer Properties.....	124
6.3.2	Composite Properties.....	125
6.3.3	Design of Experiments model – Young's Modulus.....	132
6.3.3.1	ABS Substrate	132

6.3.3.2	PEI Substrate.....	133
6.4	Resistance to plastic deformation (P/S^2).....	135
6.4.1	Polymer Properties.....	135
6.4.2	Composite Properties.....	136
6.5	Hardness, Young's modulus, and P/S^2 at increased indentation depth.....	144
6.6	Tribological Performance.....	148
6.7	Conclusion.....	153
Chapter 7. Discussion.....		155
7.1	Introduction.....	155
7.2	Uniqueness of this coating system.....	155
7.3	Discussion of results.....	160
7.4	Practical applications.....	171
7.5	Summary.....	174
Chapter 8. Conclusion.....		176
8.1	Conclusions.....	176
8.1.1	MW-PECVD technique for coating deposition on polymers.....	176
8.1.2	Substrate effects.....	177
8.1.3	P/S^2 as a measurement of system performance.....	178
8.2	Further Work.....	178
References.....		180
Appendix A: Temperature evolution during deposition.....		188
Appendix B: Supplementary DOE Analysis data.....		193

List of Tables

Table 2-1 - Typical DLC film properties adapted from [84].	45
Table 3-1 - General properties of polymers in relation to suitability for vacuum plasma coating.	57
Table 3-2 - General properties of polymers (cont.). The examples of coating found in the literature are not exhaustive and are intended only to demonstrate that hard coating materials have been deposited using PVD methods.	57
Table 3-3 – Nominal properties of substrate materials as provided by supplier.	58
Table 3-4 - Proposed DOE parameters for a 10 leg model.	62
Table 3-5 - Actual Deposition parameters for 10 leg DOE design.	64
Table 3-6 - Example of Main effects plot output from DOE analysis.	66
Table 3-7 - Classification of cross hatch results as given by Elcometer. (based on ISO2409).	73
Table 4-1 - Proposed and actual parameters used to deposit the DLC coatings.	75
Table 4-2 - Effect summary of DOE model for heating rate.	79
Table 4-3 - Effect summary of DOE model for deposition rate on ABS substrate.	82
Table 4-4 - Effect summary of DOE model for deposition rate on PEI substrate.	84
Table 6-1 - Deposition conditions and observed structure from cross section images.	102
Table 6-2 - Raman D and G peak positions, with intensity ratio for each of the 10 coatings produced.	104
Table 5-1 – Effect summary for DOE model of hardness on ABS substrate.	121
Table 5-2 - Effect summary for DOE model of hardness on PEI substrate.	123
Table 5-3 - Effect summary for DOE model of Young's modulus on ABS substrate.	133

Table 5-4 – Effect summary for DOE model of Young's modulus on PEI substrate... 134

Table 7-1 - Mechanical properties of carbon coatings deposited on polymer from the literature. 158

Table 7-2 – Hardness of DLC coatings measured at 5% of coating thickness on ABS and PEI substrates. 161

Table 7-3 – Young’s modulus of DLC coatings measured at 5% of coating thickness on ABS and PEI substrates. 161

Table 7-4 - Significant deposition conditions, coating structure and resulting mechanical properties..... 164

List of Figures

Figure 2-1 - Classification of PVD processes. Those shown in red are available at the University of Leeds Advanced Coatings Laboratory.....	6
Figure 2-2 - Energy ranges of PVD processes [7].	7
Figure 2-3 - Non-linear voltage-current characteristics of a DC discharge [10]......	10
Figure 2-4 – Binary elastic collision mechanism of sputtering (adapted from [11]).	13
Figure 2-5 - Possible secondary collision target atom ejections due to normal incident projectile [9].	14
Figure 2-6 - (a) Empirical data for sputter yield of targets with different projectile masses, (b) Theoretical sputter yield of target materials with different mass projectiles and (c) the error of the simplified theoretical model compared to a more complex collision model [12].	16
Figure 2-7 - Dependence of incident angle on sputter yield of polycrystalline Cu with high energy (<20KeV) Ar ⁺ ions [13].	17
Figure 2-8 - Balanced and Unbalanced magnetron configurations [15].	19
Figure 2-9 – HiPIMS (HPPMS) plasma density in comparison to other coating processes [20].	21
Figure 2-10 - Thermal energy flux of DC, pulsed-DC and HiPIMS plasma discharges [22]	23
Figure 2-11 - Particle flux during arc evaporation [7].	23
Figure 2-12 - Degree of ionization of emitted cathode species [24].	24
Figure 2-13 - Droplet incorporation into Ti films at varying temperatures and bias voltage [26].	25

Figure 2-14 - Aksenov quarter taurus macro-particle filter used in filtered arc evaporation. Adapted from [27].	26
Figure 2-15 - Temperature development of Polymer, Glass and Metal during film deposition from an ion-assisted technique [33].	30
Figure 2-16 - Peel energy of different metal films deposited on ABS substrate [37]. ...	33
Figure 2-17 - Influence of surface roughness on adhesion. Ar plasma treated PTFE substrate with TiN PECVD interlayer and electroplated copper coating [34].	34
Figure 2-18 - Model for the formation of thermal residual stress for a ceramic coating on a metallic substrate [40].	35
Figure 2-19 - Cracking behaviour of coatings on polymers: (a) buckling of a coating as a consequence of compressive growth stress and insufficient adhesion and (b) tensile stress cracking caused by different thermal expansions of the substrate and coating [33].	36
Figure 2-20 - Pile-up and sink-in phenomena of thin films during indentation, from [64].	41
Figure 2-21 - Showing the two carbon structures; (a) tetrahedral bonds as in diamond, and (b) planar bonds as in graphite.....	44
Figure 2-22 - Ternary phase diagram for DLC coatings [83].	45
Figure 2-23 - Characteristic Raman spectra of some carbon-based materials excited by $\lambda=514.5\text{nm}$ Ar ⁺ laser (from [90]).	46
Figure 2-24 - Deposition mechanisms of PECVD deposited DLC coatings; from [75].	50
Figure 3-1 - Schematic of the deposition chamber layout in the Hauzer Flexicoat 850 PVD system.....	56
Figure 3-2 - Example of interaction profile produced from DOE analysis.	65
Figure 3-3 - Method of determining the parameters P and S from nanoindentation loading curves.....	72

Figure 4-1 - Temperature evolution during leg 1 of DOE.....	77
Figure 4-2 – Average heating rate of DLC deposition step from each DOE leg.....	77
Figure 4-3 - Interaction profiles of full model for factor effect on heating rate.	80
Figure 4-4 - Coating thickness of ten coatings produced for DOE.....	81
Figure 4-5 - Deposition rate of ten coatings produced for DOE.....	81
Figure 4-6 - Interaction profiles for main factors and deposition rate on ABS substrate.	83
Figure 4-7 - Interaction profiles for main factors and deposition rate on PEI substrate.	84
Figure 4-8 - Average surface roughness of DOE coatings on ABS substrate.....	85
Figure 4-9 - Average surface roughness of DOE coatings on PEI substrate.	85
Figure 4-10 - Contact angle on ABS as pressure and duration of plasma exposure are varied.....	88
Figure 4-11 - Cross hatch test on untreated ABS polymer with DLC coating.....	89
Figure 4-12 - Cross hatch test on DLC coated ABS, with optimal Ar plasma pre- treatment.	90
Figure 4-13 - Coating response to constant load scratch test with and without adhesion pre-treatment.	91
Figure 4-14 - Scratch hardness as a function of sliding speed for a Cr coated polymer.	93
Figure 4-15 - Scratch track a width and coating fracture of 3.5N load at different sliding speeds on Cr sputtered coating on ABS.	93
Figure 6-1 - Cross section of DOE leg 1 coating on ABS substrate.....	97
Figure 6-2 - Cross section of DOE leg 2 coating on ABS substrate.....	97
Figure 6-3 - Cross section of DOE leg 3 coating on ABS substrate.....	98

Figure 6-4 - Cross section of DOE leg 4 coating on ABS substrate.....	98
Figure 6-5 - Cross section of DOE leg 5 coating on ABS substrate.....	99
Figure 6-6 - Cross section of DOE leg 6 coating on ABS substrate.....	99
Figure 6-7 - Cross section of DOE leg 7 coating on ABS substrate.....	100
Figure 6-8 - Cross section of DOE leg 8 coating on ABS substrate.....	100
Figure 6-9 - Cross section of DOE leg 9 coating on ABS substrate.....	101
Figure 6-10 - Cross section of DOE leg 10 coating on ABS substrate.....	101
Figure 6-11 - Correlation between I_D/I_G and hardness.....	104
Figure 6-12 - SSNMR spectra for three DLC coatings.	105
Figure 6-13 - ERD spectrum for DLC coated ABS sample with gold overcoat.....	106
Figure 6-14 - Chart showing C and H atomic percentages for samples split by different samples analysed over multiple runs.	107
Figure 6-15 - Chart showing C and H atomic percentages for all analysed samples.	108
Figure 6-16 - Chart showing C/H ratios for all analysed samples.....	108
Figure 5-1 - Hardness of ABS and PEI polymer substrates at different indentation depths.	111
Figure 5-2 - Hardness of DOE leg 1 at increasing indentation depths.....	112
Figure 5-3 - Hardness of DOE leg 2 at increasing indentation depths.....	112
Figure 5-4 - Hardness of DOE leg 3 at increasing indentation depths.....	113
Figure 5-5 - Hardness of DOE leg 4 at increasing indentation depths.....	113
Figure 5-6 - Hardness of DOE leg 5 at increasing indentation depths.....	114
Figure 5-7 - Hardness of DOE leg 6 at increasing indentation depths.....	114
Figure 5-8 - Hardness of DOE leg 7 at increasing indentation depths.....	115
Figure 5-9 - Hardness of DOE leg 8 at increasing indentation depths.....	115

Figure 5-10 - Hardness of DOE leg 9 at increasing indentation depths.	116
Figure 5-11 - Hardness of DOE leg 10 at increasing indentation depths.	116
Figure 5-12 - Hardness of the coatings measured on both substrates as a function of coating thickness.	118
Figure 5-13 - Hardness vs normalised depth of two thickness variations (2.2 μm & 4 μm) of the coating from DOE leg 6 on ABS substrate.	118
Figure 5-14 – Hardness comparison of all 10 coatings measured on ABS.	119
Figure 5-15 - Hardness comparison of all 10 coatings measured on PEI.	120
Figure 5-16 - Interaction profiles for DOE model of hardness on ABS substrate.	122
Figure 5-17 - Interaction profiles for DOE model of hardness on PEI substrate.	123
Figure 5-18 - Young's modulus of ABS and PEI polymers measured at different depths.	124
Figure 5-19 - Young's modulus as a function of depth on two coating produced at different thicknesses on ABS substrates.	125
Figure 5-20 - Young's modulus as a function of depth for DOE leg 1.	126
Figure 5-21 - Young's modulus as a function of depth for DOE leg 2.	126
Figure 5-22 - Young's modulus as a function of depth for DOE leg 3.	127
Figure 5-23 - Young's modulus as a function of depth for DOE leg 4.	127
Figure 5-24 - Young's modulus as a function of depth for DOE leg 5.	128
Figure 5-25 - Young's modulus as a function of depth for DOE leg 6.	128
Figure 5-26 - Young's modulus as a function of depth for DOE leg 7.	129
Figure 5-27 - Young's modulus as a function of depth for DOE leg 8.	129
Figure 5-28 - Young's modulus as a function of depth for DOE leg 9.	130
Figure 5-29 - Young's modulus as a function of depth for DOE leg 10.	130

Figure 5-30 - Young's modulus comparison of all 10 coatings on ABS.	131
Figure 5-31 - Young's modulus comparison of all 10 coatings on PEI.	132
Figure 5-32 - Interaction profiles for DOE model of Young's modulus on ABS substrate.	133
Figure 5-33 - Interaction profiles for DOE model of Young's modulus on PEI substrate.	134
Figure 5-34 - P/S^2 at different depths of ABS and PEI polymers.	136
Figure 5-35 - P/S^2 as a function of depth on two thicknesses of coating on ABS substrates.	137
Figure 5-36 - P/S^2 as a function of depth for DOE leg 1.	138
Figure 5-37 - P/S^2 as a function of depth for DOE leg 2.	138
Figure 5-38 - P/S^2 as a function of depth for DOE leg 3.	139
Figure 5-39 - P/S^2 as a function of depth for DOE leg 4.	139
Figure 5-40 - P/S^2 as a function of depth for DOE leg 5.	140
Figure 5-41 - P/S^2 as a function of depth for DOE leg 6.	140
Figure 5-42 - P/S^2 as a function of depth for DOE leg 7.	141
Figure 5-43 - P/S^2 as a function of depth for DOE leg 8.	141
Figure 5-44 - P/S^2 as a function of depth of DOE leg 9.	142
Figure 5-45 - P/S^2 as a function of depth for DOE leg 10.	142
Figure 5-46 - Comparison of P/S^2 as a function of depth of all coatings on ABS.	143
Figure 5-47 - Comparison of P/S^2 as a function of depth of all coatings on PEI.	144
Figure 5-48 - Hardness as a function of depth for coated ABS and PEI.	145
Figure 5-49 - Reduced Modulus as a function of depth for coated ABS and PEI.	145
Figure 5-50 - P/S^2 as a function of depth for coated ABS ad PEI.	146

Figure 5-51 - Example loading-unloading curve from nanoindentation, showing pop-in behaviour.....	147
Figure 5-52 - Loading-unloading curves for two coating thicknesses.	148
Figure 5-53 - Friction coefficient of three coated polymers in reciprocating pin-on-plate test.....	149
Figure 5-54 - Coefficient of friction of 4 DLC coated ABS samples sliding against ABS.	150
Figure 5-55 - Comparison of friction for DLC coated polymer sliding against DLC and ABS.	151
Figure 5-56 - Wear track of ABS plate from ABS-ABS contact.....	152
Figure 5-57 - Wear track of DLC coated ABS from DLC-DLC contact.....	152
Figure 5-58 - Coefficient of friction for two samples of DLC6 with different thicknesses sliding against steel.	153
Figure 7-1 - Thickness of coating achieved during same time period based on sample position within the chamber (from [117]).	156
Figure 7-2 - Correlation between Hardness and Young's modulus measured by nanoindentation.	162
Figure 7-3 - Correlation between deposition rate and coating hardness, as measured at 5% coating depth on ABS and PEI substrates, showing observed structure for extremes in deposition rates.....	165
Figure 7-4 – Proposed mechanisms of coating deformation during nanoindentation for fibrous and amorphous coating structures.	166
Figure 7-5 - Correlation between sp ² /sp ³ ratios determined by solid state NMR analysis and hardness determined by nanoindentation.	166
Figure 7-6 - Correlation between sp ² /sp ³ ratio, and C/H ratio of 3 DLC coatings.....	168

Figure 7-7 – Correlation between acetylene partial pressure and hardness ($H_{5\%}$) of the coatings deposited on ABS and PEI substrates..... 169

Abbreviations

ABS	Acrylonitrile Butadiene Styrene
a-C:H	Amorphous hydrogenated carbon
CTE	Coefficient of Thermal Expansion
CVD	Chemical Vapour Deposition
DC	Direct Current
DLC	Diamond-Like Carbon
DOE	Design of Experiments
E	Young's Modulus
ECR	Electron Cyclotron Resonance
EELS	Electron Energy Loss Spectroscopy
E_r	Reduced Modulus
ERDA	Elastic Recoil Detection Analysis
H	Hardness
HiPIMS	High Power Impulse Magnetron Sputtering
IBA	Ion Beam Analysis
L	Mean Free Path
MAS-NMR	Magic-Angle Spinning Nuclear Magnetic Resonance
MW	Microwave
MW-PECVD	Microwave assisted Plasma Enhanced Chemical Vapour Deposition
N_a	Avogadro's Number
N_D	Debye Number
NMR	Nuclear Magnetic Resonance
P	Load
PA	Polyamide (Nylon)
PC	Polycarbonate
PE	Polyethylene
PECVD	Plasma Enhanced Chemical Vapour Deposition
PEI	Polyetherimide
PET	Polyethylene Terephthalate
PET-G	Polyethylene Terephthalate (Glycol modified)
PMMA	Polymethylmethacrylate
PP	Polypropylene
PTFE	Polytetrafluoroethylene
PU	Polyurethane
PVD	Physical Vapour Deposition
RF	Radio Frequency
RF-PECVD	Radio Frequency assisted Plasma Enhanced Chemical Vapour Deposition
S	Contact Stiffness
SEM	Scanning Electron Microscopy
SSNMR	Solid State Nuclear Magnetic Resonance
ta-C:H	Tetrahedral amorphous carbon

T_g	Glass transition Temperature
T_m	Melting Temperature
U_{sb}	Surface Binding Energy
UV	Ultra-Violet
XPS	X-ray Photoelectron Spectroscopy
λ_D	Debye Length
ν	Poisson's Ratio

Chapter 1. Introduction

1.1 Research Motivation

Artificial plasma has found uses in many industrial sectors including metallurgy, metal cutting/welding, lighting and jet propulsion. Surface engineering is now one of the largest markets utilising artificial plasmas regularly and was estimated to be worth £21.3billion and affects products with a total value in excess of £143billion in 2005 [1].

There are many material processing techniques designed to alter material properties through surface modification or coating that utilise the high energy nature of plasma to carry out the process. These include plasma spraying, ion implantation, ion etching, physical vapour deposition (PVD) and plasma enhanced chemical vapour deposition (PECVD). The advantage of many of these plasma processes over their more conventional predecessors is that they can treat large surface areas, are considered as (mostly) dry processes and so do not use large amounts of harsh chemicals, are therefore almost pollution free, can be easily automated for consistent results and can be employed to produce surfaces with anti-corrosion and anti-wear properties, increased fatigue strength, biocompatibility, anti-bacterial properties, or a tuneable range of all these.

The first report of arc vaporization was in 1839 by Robert Hare and was related to electrical contact engineering. The first report from a study of sputtering was sometime later in 1852 by W.R. Grove. While holding a needle close to a silver surface he sputtered from the wire onto the silver, noticed from a deposit on the silver surface when it was the anode in a circuit [2]. The processes and mechanisms, presumably, were not understood until much later. Wright has been credited with perhaps the first use of PVD for a specific purpose, when in 1877 he published a paper on the use of “electrical deposition apparatus” to manufacture mirrors; it is still not certain whether this process was sputtering or arc deposition [2].

The technology and processes were developed during the following century allowing the deposition of many coatings for different application, including hard coatings for cutting tools (1970-1980), transparent oxide coatings for optical applications (from 1933), and one of the largest industries using PVD methods, semi-conductor manufacture (from 1947) [2]. These industrial applications are still amongst the top where demand for PVD coating is concerned.

The trend in the coating industry is to add functionality to the substrate material that will improve performance to an extent which would either be impossible or economically unviable by any other method. To this extent, it is usual for hard coatings to be deposited onto already hard substrates, optical coatings (e.g. anti-reflective, filters) to be deposited onto optical glass etc.

Whilst plastics have been coated using galvanic treatments and electroplating, the first commercial use of sputter coated plastics parts was in 1975 when Chevrolet produced chromium coated grills for automobiles. The ease of manufacture of complex parts using moulding and forming at low temperatures led to the adoption of plastic in many industries. However, plastic is often less hard than a metal counterpart and does not have the same appearance. These decorative coatings have expanded into a market of their own and it is possible to produce many different colours by changing the material and deposition parameters.

As engineering materials, polymers are very useful, due to the wide range of chemical compositions, material and mechanical properties available; they can be coloured for aesthetic reasons, are easy to mould and form, and the majority of common thermoplastics are cheap to synthesise. As such, polymer use is increasing and can be found in products as simple as drinks bottles and food packaging, all the way up to high performance automotive components such as intake manifolds.

The very same properties that make polymers useful in many situations also lead to them being unsuitable for many applications. The main barrier for use in engineering applications is the low modulus, prohibiting use in high load applications, and the low

glass transition temperature, limiting use in environments with sustained high temperature.

The decorative coating of plastic parts has expanded into markets such as household plumbing, automotive interior and exterior trim and consumer electronics. The low cost of manufacture, whilst maintaining a luxury product, has been the driving force. Traditionally, these metal coatings were deposited using wet chemical processes such as galvanising or electroplating. Typically, Acrylonitrile Butadiene Styrene (ABS) substrates were submerged in a bath of hexavalent chromium ions to produce a chrome coated part. The use of these Cr^{6+} processes was banned in Europe under the 2007 Restriction of Hazardous Substances Directive and is heavily regulated in the USA by the Environmental Protection Agency, due to evidence proving them to be carcinogens. PVD processes for coating plastics, without the use of 'wet chemical' treatments feature on commercial coating promotional material [3, 4]. Despite the claim these coating machines and systems can provide decorative finishes that mimic traditional metal components, for the most part they utilize Ultra-Violet (UV) cured lacquers to overcome some of the specific issues encountered when coating polymers and the coating is rarely deposited directly onto the polymer surface for applications in which the coating would be mechanically loaded. This lacquer is thick enough to smooth the surface, allowing a smooth conformal coating to be produced with high gloss, and provides some thermal protection to the polymer during coating. If the UV lacquer encases the polymer, it will also prevent outgassing of volatile compounds adsorbed during synthesis or forming that can have detrimental effects when present in the deposition chamber. These contaminants lead to poor adhesion if they remain on the polymer surface and film imperfections if incorporated into the plasma during deposition.

Coating of polymers for decoration and electronic applications by galvanic deposition and evaporation have been called 'state-of-the-art' [5], however, the wear protection has not been the focus of development. In both decorative and optical coatings on polymers the main function is appearance; decorative coatings must be aesthetically pleasing,

while optical coatings must allow transmission of light and are therefore transparent, at least to the required wavelengths of light. A by-product of using these metal and ceramic coatings is an increase in surface hardness which provides scratch and wear resistance. However, as these coatings have a primary function, these secondary functions are not of concern when the deposition parameters are being optimized and so do not reach a peak [6]. As such, the scientific literature does not focus reporting on the mechanical properties of these films when deposited onto polymers and concentrates solely on the primary functions of the thin film coating.

1.2 Aims & Objectives

1.2.1 Aim

To design a coating system based on Diamond-Like Carbon (DLC) coatings applied directly to the polymer substrate that can increase the robustness (defined below) of common thermoplastic and engineering polymers, with a view to understanding the limitations these substrates impose and how to best negate these effects.

1.2.2 Objectives

- Increasing robustness will mean at least one of the following:
 - o Increasing hardness at the surface or near-surface.
 - o Increasing elastic modulus at the surface or near-surface.
 - o Reducing friction against a sliding counterpart.
- The increase of robustness will be of a magnitude that extends the use of the polymer into applications where it was previously deemed unsuitable.
- The coating system will be designed around the use of physical vapour and/or plasma enhanced chemical vapour deposition processes available in the University of Leeds Advanced Coating Laboratory, using the Hauzer Flexicoat 850 coating system.
- To study the relationship between polymer mechanical properties, coating material properties and deposition parameters to give a fundamental

understanding of how the performance of coated polymer systems are affected by variation of these.

- To investigate the effects of plasma treatment on polymers for use as an adhesion modifier, prior to film deposition.

1.3 Thesis Outline

Chapter 2 contains a literature review covering basic plasma theory, and how this pertains to methods of plasma based film deposition. It covers coatings on polymer materials and the measurement methods employed in the literature to determine film properties, and finally concentrates on DLC coatings successfully deposited onto polymeric substrates.

Chapter 3 covers the experimental methods used in this work, including the methods of coating deposition and substrate preparation, chemical and structural analysis, and mechanical analysis.

Chapter 4 through to Chapter 5 present the results of this study. The results are split into the deposition of the coatings, showing effects of varying deposition parameters on coating growth, temperature evolution of the deposition chamber, coating roughness, and adhesion (Chapter 4); characterisation of the mechanical properties of the coating system (Chapter 6); and finally, the coating structure and chemical composition, based on a sample of the coatings produced (Chapter 5).

Discussion of the results can be found in Chapter 6 giving details of the uniqueness of the work contained in this thesis, as well as limitations and practical applications of the presented coating system. Concluding remarks are given in Chapter 8, with recommendations for further work based on the findings presented here.

Chapter 2. Literature Review

2.1 Introduction

In this chapter a review of the relevant literature will be presented. The review will cover an introduction to plasma deposition processes and coating growth, polymer materials, DLC coatings, methods of measuring coating properties and examples of DLC coatings deposited onto polymer substrate materials.

2.2 Deposition Processes

This section will describe the surface engineering plasma processes of PVD; specifically arc evaporation and sputtering, and PECVD. It will focus on how they are used to coat a substrate material and the benefits and disadvantages associated with each coating method. Figure 2-1 shows the classification of the aforementioned PVD processes.

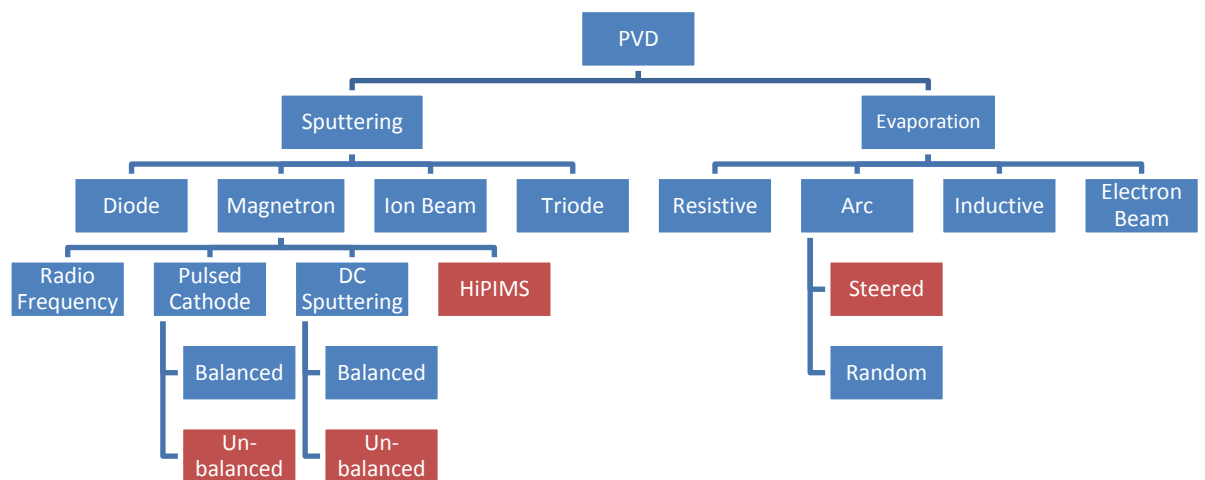


Figure 2-1 - Classification of PVD processes. Those shown in red are available at the University of Leeds Advanced Coatings Laboratory.

The energy ranges of the PVD processes differ as shown in Figure 2-2. Thermal evaporation processes rely solely on the electrical heating of a liquid or solid to evaporate a stream of vapour for deposition. As such, the deposition rates are generally much lower and produce films with lower quality than plasma processes when considering hard, wear and corrosion resistant coatings. In this figure arc evaporation can be considered as ion

plating; despite being a thermal evaporation process, the evaporation is explosive and the energy involved is much higher than crucible evaporators. There is considerable overlap between the energy of sputter deposition and arc evaporation due to the tunability of the processes.

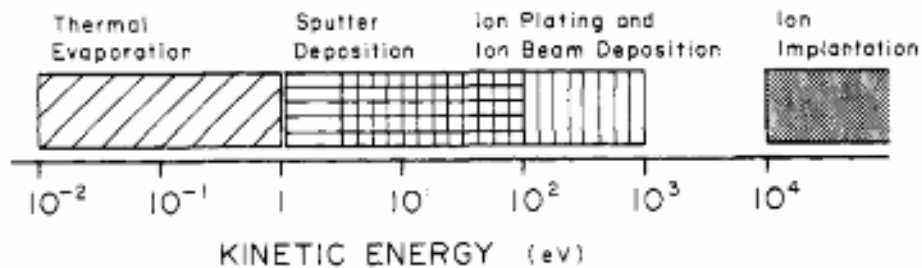


Figure 2-2 - Energy ranges of PVD processes [7].

2.2.1 Plasma Characterisation

Plasma is considered to be the fourth state of matter after solids, liquids and gases. States of matter are governed by the energy of the atoms in the volume of matter; if the average kinetic energy of an atom exceeds the binding energy, the crystal structure of a solid will break up giving a liquid (or in some cases a gas). If the average kinetic energy then increases further, the van der Waals bonds will break leading to gas formation. If the energy is increased further still, the ionization energy of the species will be reached, leading to ionisation and the creation of the plasma state.

Plasma can also be considered as a class of gases consisting of electrons, ions and atoms/molecules, instead of only atoms/molecules. Because of the charges of electrons and ions, plasma behaviour is governed by the interaction of electric currents generated when they move and therefore also electromagnetic forces acting on these species. An important property of plasma is its tendency toward electrical neutrality; that is, in any given macroscopic volume the charge of positive and negative species is equal. This is due to the large charge density of electrons giving them a significant electric field, which in turn will transport them into any area where a positive electrical charge (ions) has built up; the electrons will follow the ions due to their much smaller mass. In order to be

considered a true plasma, rather than just an ionised gas, it should contain enough free charged particles to electrostatically shield itself from an applied electric field, within a distance smaller than the Debye length [8]. In order to do this it must meet 3 criteria:

i. $L \gg \lambda_D$,

Where L is the mean free path – the distance a particle will travel, on average, before colliding with another, and λ_D is the Debye length – the measure of a charge carrier's net electrostatic effect. This means that the interactions in the bulk of the plasma are more influential than those at its edges where boundary effects such as plasma sheathing may take place.

ii. $N_D \gg 1$

Where N_D is the Debye number – the average number of charged particles expected to occupy a volume defined by a Debye sphere; a sphere with radius equal to the Debye length. This means that the particles making up the plasma show collective behaviour, as the behaviour of one particle will have an effect on more than one neighbouring particle.

iii. $\omega t > 1$

Where ω is the electron plasma frequency and t is the time between collisions. This means that electrostatic interactions will dominate over the normal kinetic interactions found in gases.

The Debye length, or Debye shielding length, is the measure of a charge carrier's net electrostatic effect. It is defined as

$$\text{Debye Length } \lambda_D = \sqrt{\frac{\epsilon_0 K_B / q_e^2}{n_e / T_e + \sum_{ij} j^2 n_{ij} / T_i}} \quad [\text{eqn. 2.1}]$$

$$\lambda_D = \sqrt{\frac{\epsilon_0 K_B T_e}{n_e q_e^2}}. \quad [\text{eqn. 2.2}]$$

ϵ_0 is the vacuum permittivity, K_B is the Boltzmann constant, q_e is the charge of an electron, T_e and T_i are the electron and ion temperature, n_e is the density of electrons and n_{ij} is the density of the atomic species i , with positive ionic charge $j q_e$. When the mobility of ions is negligible compared to the process timescale [eqn. 2.2] can be used. The ionic terms

have been dropped as the difference in mass between ions and electrons leads to the simplification that motion of ions is negligible compared to that of electrons when subjected to electromagnetic forces. This is the most commonly used form of the equation when used to describe shielding in plasma. In other words, shielding is the polarization of the plasma medium, through redistribution of charge density, thereby preventing the effects of an external electrical field entering the plasma because of the net effect of the charged particles attracted to the applied charge.

As previously mentioned, plasma is created by increasing the energy of matter above the ionization energy of the species present and this occurs naturally throughout the universe. Stars and lightning are forms of naturally occurring plasma created by the energy released during nuclear fusion and the release of electrostatic energy stored within regions inside or between clouds within the atmosphere.

Artificial plasma can be created providing enough energy is input to the system in some form. In order to sustain the plasma, the energy input must remain high enough that the three criteria introduced in the previous section are upheld i.e. enough particles remain as charge carriers. The energy required for this will depend on the pressure of the fluid and the elemental species present.

Artificial plasma discharges can be roughly categorised by the method used and conditions under which they are created:

- i. Energy source – Direct Current (DC), Radio Frequency (RF), Microwave (MW).
- ii. Pressure – Ultra High Vacuum, Vacuum, Moderate Vacuum, Atmospheric.
- iii. The degree of ionization.
- iv. The temperature – Thermal ($T_e = T_i = T_{\text{gas}}$), non-thermal or 'cold' ($T_e \gg T_i = T_{\text{gas}}$).
- v. The magnetization – Magnetized (both ions and electrons are manipulated by magnetic fields), partially magnetized (only electrons are influenced) and non-magnetized.
- vi. The electrode configuration.

The simplest configuration to create an artificial plasma would be an anode and cathode separated by a non-conducting fluid. Once a current is passed through this circuit an

electric field will be created providing the energy for ionization. Once an electron and ion are generated they will move toward the anode and cathode respectively; as the high energy electron moves through the fluid it will collide with another particle which will be ionized, giving 2 electrons and one ion. This chain reaction will continue until the fluid is ionized to an equilibrium level based on the energy input. This process is referred to as a 'Townsend avalanche' [9].

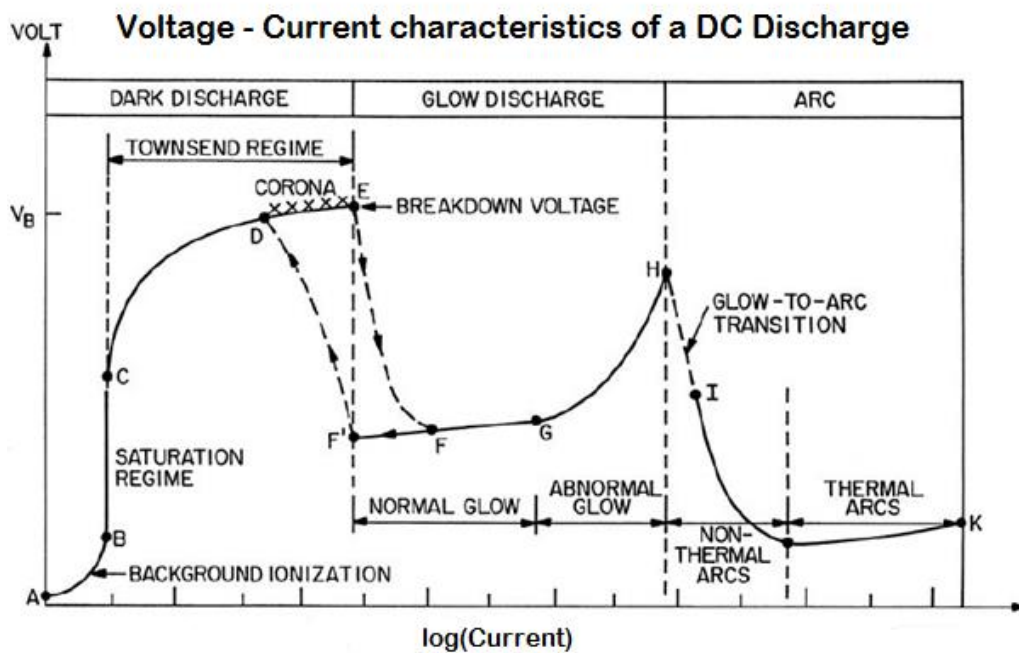


Figure 2-3 - Non-linear voltage-current characteristics of a DC discharge [10].

The characteristics of a DC plasma discharge are shown in Figure 2-3. The non-linear relationship between voltage and current requires that a balanced resistor is incorporated into the DC power supply such that only one current value will be available for selection for a given voltage; this allows the selection of the discharge regime.

In the region of A-B, the background radiation (or low energy source) will ionize atoms of the gas. The background energy level will be so low such that these electrons will be accelerated toward the cathode without ionizing further particles upon collision. As the voltage is increased past B the background energy level, caused by the electric field imposed by the voltage, will create a Townsend avalanche that results in a dark discharge; so called because it does not emit light which can be seen by the naked eye.

If the voltage is reduced at this stage the plasma will extinguish as the removal of the electric field would cause the current to reduce as the mobile electrons would not be attracted to the anode; this regime is therefore not self-sustaining.

If the voltage is increased further still, the ions created will have enough kinetic energy that when they accelerate towards and collide with the cathode they will cause the ejection of electrons from the cathode itself. These electrons will then be accelerated toward the anode causing further electron impact ionization as they do so. The majority of ions created in the discharge are now done so through this mechanism. The voltage at which this occurs is known as the breakdown voltage and is noted as V_B in Figure 2-3. As more free electrons are created the current increases, but the voltage required to maintain it is reduced as the charged particle densities within the body of the plasma have increased. The neutral body of the plasma becomes equipotential due to increased conductance, sheaths form at the electrodes and the electric field becomes concentrated in the cathode sheath [9]. This regime is a glow discharge, so called because of the light emission observed, and is classed as self-sustaining meaning that it no longer depends on an external ionizing source.

The area in Figure 2-3 from the breakdown, E, to G is the normal glow region. This region is characterised by the current being able to assume a number of values despite voltage remaining constant, in a simplified model. The charge density remains constant at the cathode but the electric field is stronger at the edges or around asperities which increases secondary electron emission, leading to a rise in current. It must be noted that the increase in current under the normal glow regime is due to the electric field being spread over a larger cathode area resulting in increased secondary electron emission. If the whole cathode area is used for secondary electron emission, an increase in voltage (energy) is required to further increase emission and therefore current. At this point (G), the abnormal glow regime is reached. The final regime is the arc. Arcing occurs when enough energy is built up on the cathode surface that thermionic electron emission occurs resulting in increased current.

For film deposition the glow discharge and arc regimes are used. The abnormal glow region is typically used in sputter coating processes and the arc region is used for arc evaporation processes. One of the main differences between the two plasma regimes is the voltage-current relationship; glow discharges are higher voltage, lower current whereas arcing is low voltage, high current.

The following sections will give an overview of coating methods that are available on the Hauzer Flexicoat 850 PVD coating system and those used throughout the work contained in this thesis.

2.2.2 Sputtering

Sputtering is the process of removing material at an atomic level by colliding high energy particles with a target material. The high energy particles come from, typically, an abnormal glow discharge and the plasma is created using argon gas. The mass of argon atoms and their characteristically inert nature gives them relatively low ionization energy and reduces the chances of the non-ionized molecules reacting with any other species.

The mechanism of sputtering can be explained through a basic model in which binary elastic collisions occur between hard spheres arranged in a grid (Figure 2-4). The target surface is held at a negative voltage (cathode) in order to accelerate positive ions towards it. Upon collision with the surface, atoms will be displaced causing a linear cascade. The mechanism shown in Figure 2-4 is known as collisional sputtering, and this example is backward sputtering, whereas if the sputtered atoms were to be ejected travelling in the same direction as after the initial collision of the argon ion, this would be forward sputtering. Backward collisional sputtering is the most commonly used method of magnetron sputtering as the target thickness is then not of concern.

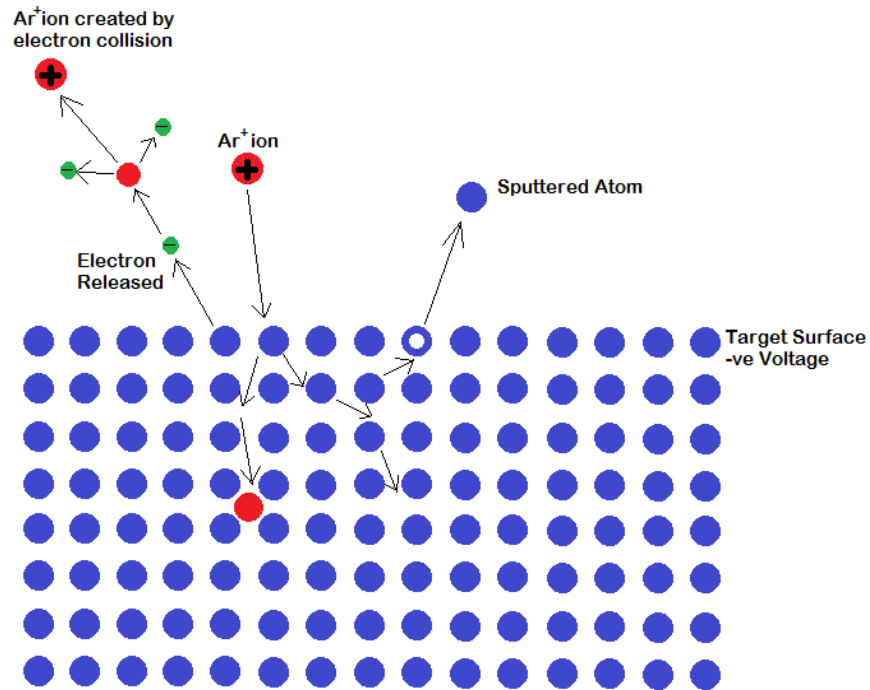


Figure 2-4 – Binary elastic collision mechanism of sputtering (adapted from [11]).

The surface binding energy can be considered, as it does not differ significantly from, the heat of sublimation [9]. The surface binding energy can be found using:

$$U_{sb} = \frac{\Delta_{fus}H + \Delta_{vap}H}{N_a} = \frac{\Delta_{sub}H}{N_a} \quad [\text{eqn. 2.3}]$$

$\Delta_{fus}H$, $\Delta_{vap}H$ and $\Delta_{sub}H$ are the heat of fusion, vaporization and sublimation, respectively, and N_a is Avogadro's number. An estimate of the surface binding energy can be found from the literature, but using a single value for a single target material ignores crystallographic structure and orientation at the surface and the number of nearest neighbours of a given surface site. It is said that the science of sputtering is not accurate enough for these small differences to matter in most cases [9].

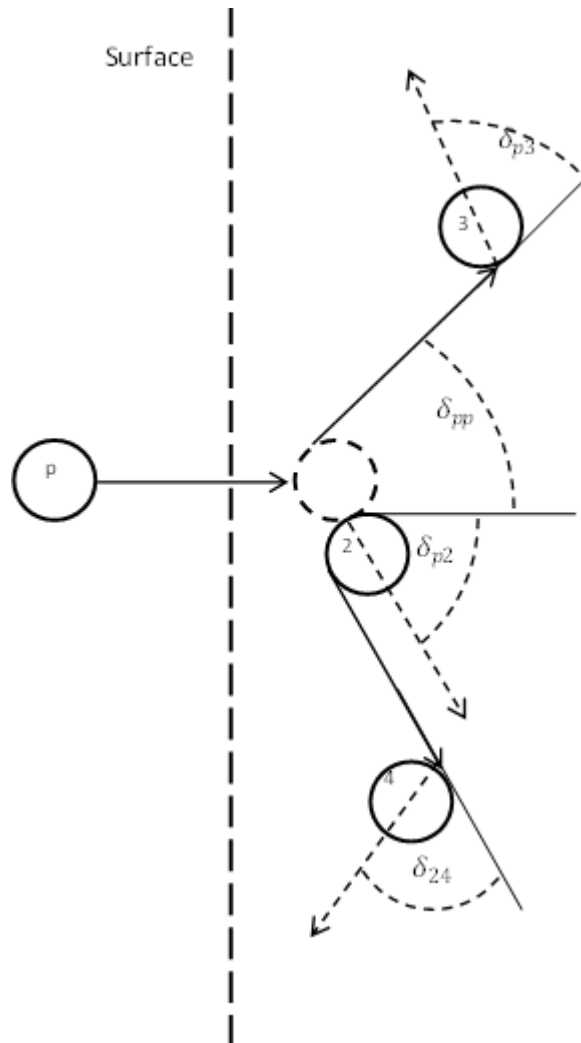


Figure 2-5 - Possible secondary collision target atom ejections due to normal incident projectile [9].

Given the surface binding energy, it is possible to calculate the threshold energy of projectiles that would sputter from a target, assuming that at the threshold the sputtered atom would have zero velocity (no energy) outside the target. If the projectile incident angle is normal to the target surface it would be impossible for the primary collision to result in the ejection of a target atom; in this case there are three possible scenarios under which a target atom will be ejected due to secondary collisions. The projectile strikes and ejects particle 3 (after colliding with particle 2), the primary recoil atom (particle 2) expels particle 4, or the primary recoil atom is ejected after collision with particle 4 (shown in Figure 2-5). The energy transfer function for elastic collisions between hard spheres is:

$$T(\delta_r) = \frac{4m_p m_r}{(m_p + m_r)^2} (\cos \delta_r)^2 \quad [\text{eqn. 2.4}]$$

$$\gamma \equiv \frac{4m_p m_r}{(m_p + m_r)^2} \quad [\text{eqn. 2.5}]$$

where m is the mass of the projectile or recoil, δ_r is the angle of recoil measured from the incident and γ is the energy mass transfer factor. It can be seen that when the masses differ, the transfer function tends to zero, giving rise to the greatest energy transfer when the masses are equal. As two collisions are necessary, any collisions involving atoms from the target will transfer more energy, and so the collision path of projectile to 2, atom 2 to atom 4, and the ejection of atom 4 or 2 will require the lowest energy from the projectile.

If atom 2 is to eject atom 4, then the kinetic energy must equal $U_{sb}/(\cos \delta_{24})^2$. If atom 2 is to have this kinetic energy then the projectile must have had kinetic energy equal to $[U_{sb}/(\cos \delta_{24})^2]/\gamma(\cos \delta_{p2})$. If atom 4 is to be ejected then it must be also be true that $\delta_{p2} + \delta_{24} \geq 90^\circ$, given that at threshold $\delta_{p2} = 90^\circ - \delta_{24}$. The threshold energy for the projectile is, therefore, $E_{th} = U_{sb}/[\gamma(\cos \delta \sin \delta)^2]$. Since the angles must complement each other and must equal 90° at threshold, the maximum scattering angle is 45° . With this relationship the threshold energy can simply be written as

$$E_{th} = \frac{4U_{sb}}{\gamma} \quad [\text{eqn. 2.6}]$$

If three collisions occur for ejection of an atom then the threshold energy would be reduced due to higher energy transfer as the incidence angle of collisions is reduced. The theoretical minimum value for the threshold energy is $E_{th} = U_{sb}/\gamma$ for a large number of collisions; however, the probability of more than two collisions occurring is lower than the minimum (two) due to the spatial distribution of atoms. Equation [eqn. 2.6] can be used to compare against experimental results with a reasonable degree of accuracy [9]. Many models for calculating the sputter yield have been proposed, but those which use a collisional model (as above) have been proven to be the most accurate representation;

whilst even simple models have been shown to offer very similar yield results as more complex models. A simple collisional model developed by Mahan & Vantomme [12] has been shown to give similar results to experimental values (shown in Figure 2-6). As sputtering is governed by a complex relationship of probability functions and energy distributions, it could be argued that the need for a truly accurate model of sputter yield is not required as in reality there are many variables which could affect the accuracy of said model due to experimental setup.

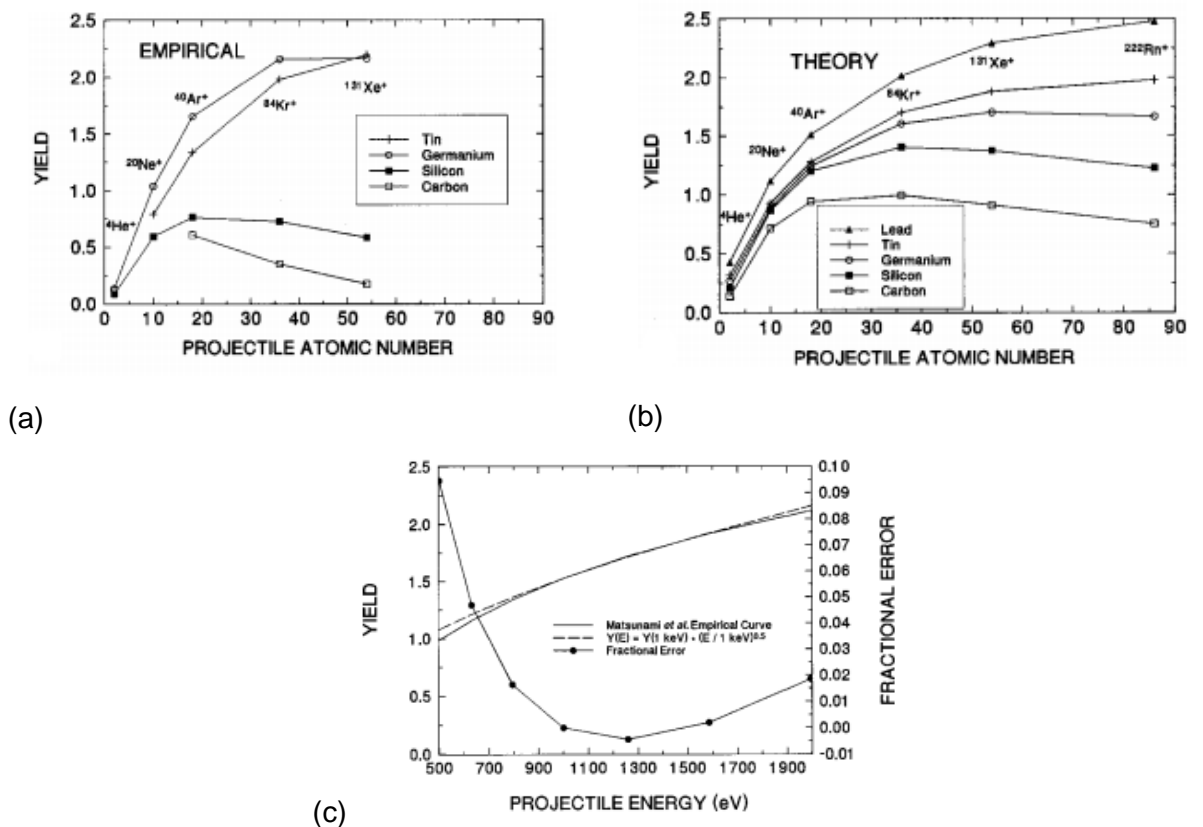


Figure 2-6 - (a) Empirical data for sputter yield of targets with different projectile masses, (b) Theoretical sputter yield of target materials with different mass projectiles and (c) the error of the simplified theoretical model compared to a more complex collision model [12].

Figure 2-7 shows the sputter yield ratio of polycrystalline copper using argon ions. It shows that in reality the sputter yield is actually at a minimum when the incidence angle is perpendicular to the surface. As the incidence angle is increased, the sputter yield also

increases, up to roughly a 75% increase at an angle of 70° when using Ar⁺ ions with energy levels of 1.05KeV (those typically used for sputter film deposition). As the angle is increased it allows atoms from the surface to be ejected from the primary collision, requiring less energy and also having higher probability of occurring. During sputtering the angle of incidence can be well controlled if an ion gun is used, however, if plasma is generated as the ion source the electric field at the target/cathode will dictate the incidence angle.

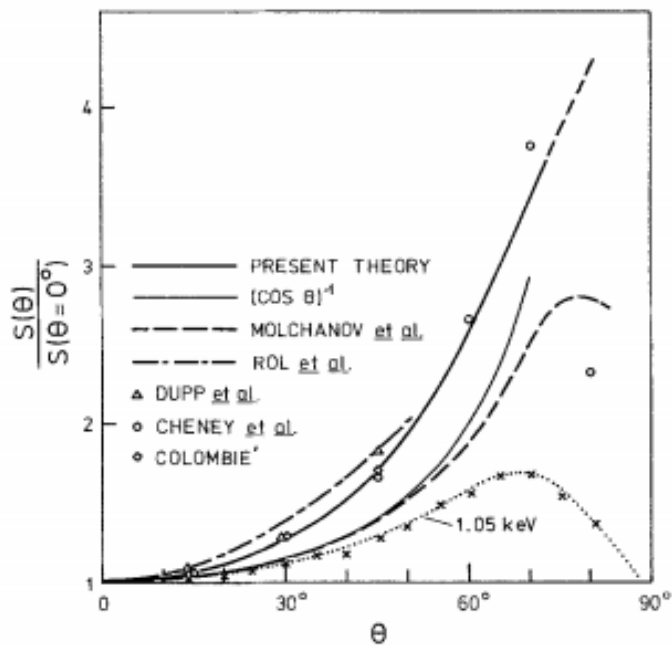


Figure 2-7 - Dependence of incident angle on sputter yield of polycrystalline Cu with high energy (<20KeV) Ar⁺ ions [13].

As material is vaporized through sputtering it is incorporated into the plasma. The mean free path now becomes an important factor as to the probability of a sputtered particle arriving at the substrate surface. As the majority of the sputtered particles are not charge carriers they are unaffected by both the magnetic and electric fields, so the only mechanism available for the majority to reach the substrate is the momentum gained when ejected from the target.

The mean free path is defined as:

$$L = \frac{K_B T}{\sqrt{2} \pi d^2 p} \quad [\text{eqn. 2.7}]$$

Where K_B is the Boltzmann constant, T is Temperature, d is the diameter of the gas particles and p is the pressure. It describes the average distance a particle can travel before energy transfer or direction changes occur through collision. If the mean free path is increased, through increasing temperature or decreasing pressure, then the likelihood of a sputtered particle reaching the substrate is increased. However, the pressure of the system must be balanced in order to maintain the plasma and obtain satisfactory sputter yield without having to increase the energy, which can cause adverse effects such as arcing.

Arcing occurs when charges build up on the surface of the target causing high current discharges (arc plasma). Arcs occurring on the target during sputtering are similar to those used to evaporate material during arc evaporation processes and so can only occur on conducting target materials and give rise to the same coating defects (such as droplets).

2.2.2.1 The Balanced and Unbalanced Magnetron

Magnetron sputtering is founded on the principles in the previous sections, but by using a series of magnets behind the target surface it is possible to control the plasma density. The magnetic field lines will act to confine the secondary emission electrons, which in turn create more ions due to electron impact ionisation, thereby increasing the plasma density in the area surrounding the target. The ions are unaffected by the magnetic field but due to strong electrostatic forces, their movement is influenced by the capture of the electron.

Figure 2-8 shows the 3 main configurations of a magnetron sputtering system; by systematically changing the configuration of a conventional magnetron it was found to have a profound effect on the characteristics of the plasma created [14]. A balanced magnetron is one in which the strength of the magnetic poles is balanced such that the

magnetic field lines are closed between the central and outer poles. This creates dense plasma in front of the target as all electrons are confined to an area in front of the target. The unbalanced magnetron is a system where either the inner or outer poles of the magnet are strengthened relative to the other. In these cases the magnetic field lines are not closed and extend further away from the target.

A type-1 unbalanced magnetron has a strengthened central pole resulting in field lines that extend away from the target and towards the chamber walls. The plasma density at the target is decreased compared to the balanced magnetron and the plasma density at the substrate is low. For this reason type-1 unbalanced magnetrons are rarely used as they result in low ion current to the substrate, hence lower quality films are deposited.

Type-2 magnetrons are those in which the outer poles are strengthened, resulting in magnetic field lines which extend away from the target and towards the substrate. This results in a lower plasma density, but the plasma extends towards the substrate leading to a higher number of ions that reach the substrate, leading to an increased ion current density without using a large (if at all) bias voltage. The increase of bombarding particles on the substrate surface can be used to either etch the substrate for cleaning, or during film deposition to increase the film density and potentially change the structure of the film obtained.

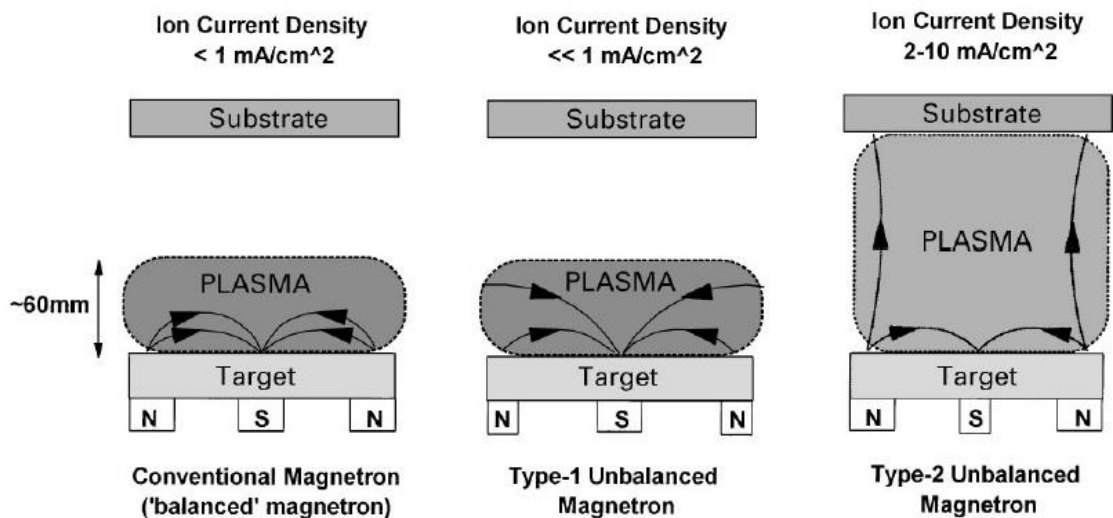


Figure 2-8 - Balanced and Unbalanced magnetron configurations [15].

2.2.2.2 DC Sputtering

DC sputtering is one of the most commonly used sputtering techniques. A glow discharge is created by increasing the power through a DC power supply. Once the glow discharge is ignited (usually using an argon gas source), sputtering will take place through the mechanisms mentioned in previous sections.

Sputtering of insulating films is difficult using DC discharges; the power densities required can cause practical issues such as excessive target heating and low deposition rates are common. In all PVD coating processes it is inevitable that the chamber walls will be coated during deposition. If the coating is an insulator and the anode is covered with this material then the plasma is likely to extinguish; the so called 'disappearing anode'. To overcome this, RF discharges can be used, however the equipment required for these systems is complex and still results in low deposition rates [15]. Reactive sputtering can be employed to overcome these issues, however new complications are introduced. The reactive gas will poison the target away from the 'racetrack'; the area eroded by the plasma, leading to random arcing events as charge builds up on the poisoned (insulating) surface [16].

Pulsing the magnetron cathode power supply has been shown to negate all of these effects with TiN and AlO being deposited onto steel substrates using unipolar and bipolar pulsed magnetron sputtering respectively [16]. By pulsing not the magnetron cathode, but the bias voltage supply, Olbrich [17] deposited a functional, hard TiN tool coating onto high speed steel. It was found that by pulsing the bias voltage supply during arc deposition the critical load for a scratch test (measuring adhesion) was greater at a given temperature than a conventional constant bias supply; this is due to the deposition temperature being lower for a higher voltage when pulsed. Superimposing a pulsed bias voltage onto a low, constant bias voltage improved adhesion further, showing an almost 50% improvement over a constant bias voltage at the same temperature.

On Polyethylene Terephthalate (PET) substrates, pulsed DC sputtering has been shown to produce up to 50% harder optical coatings of TiO_2 and Al_2O_3 , than compared to atomic

layer deposition processes. Whilst High Power Impulse Magnetron Sputtering (HiPIMS) increases the hardness above that obtained with pulsed DC sputtering [18].

2.2.2.3 High Power Impulse Magnetron Sputtering (HiPIMS)

HiPIMS is a sputtering technique by which high peak power ($>1\text{kW}/\text{cm}^2$), low duty cycle ($<10\%$), low frequency ($<10\text{kHz}$) pulses, are used to maintain the plasma discharge [19]. Varying the duty cycle, power and frequency allows the plasma density to be tuned, allowing a range of deposition conditions (shown in Figure 2-9). The pulsed nature of the discharge makes it suitable for sputtering non-conducting targets for the same reasons as pulsed DC sputtering; it avoids charge accumulation on the surface of the target which causes arcing. HiPIMS can be thought of as a sputtering technique which employs the sputtering mechanism of vapour production, but with high levels of ionisation more akin to arc evaporation. The high ionisation leads to dense, defect free coatings, and the ability to coat complex shaped substrates. The ion bombardment of the film during deposition gives rise to a breakdown of the classical film deposition structure zone models due to the energy provided through ion bombardment replacing thermal energy. This makes HiPIMS suitable for depositing functional films at lower temperatures than when using other methods.

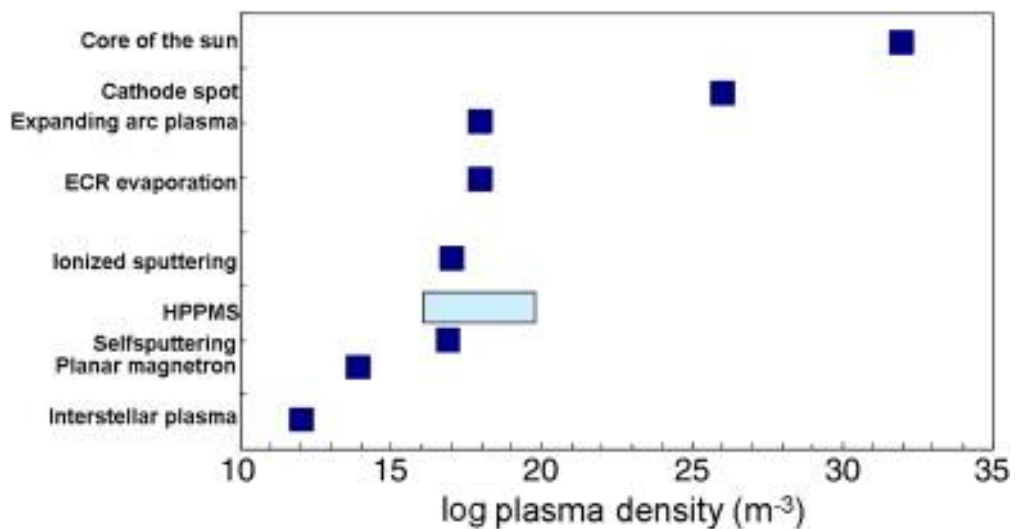


Figure 2-9 – HiPIMS (HPPMS) plasma density in comparison to other coating processes [20].

Recently, Moghal et al. [21] deposited AlO_x thin films onto polyethylene naphthalate film using radio frequency, DC and HiPIMS sputtering at low temperature ($<120^\circ\text{C}$). Each process was optimized and the adhesion, chemical composition and scratch resistance determined. The HiPIMS process resulted in a film of similar composition to radio frequency sputtering (more Al-O bonding, less O-Al-O bonding) compared to DC sputtering and also contained less chemisorbed water species compared to DC sputtering. The adhesion of the HiPIMS film was the greatest (interfacial shear strength – 186 MPa), however it also resulted in a crack density when under strain similar to that of DC sputtering (interfacial shear strength – 169 MPa).

HiPIMS is not without problems however, with the equipment required to produce such high power, pulsed, discharges requiring significant capital investment. As a process, HiPIMS is still in its infancy, particularly compared to conventional sputtering and evaporation techniques; as such it is not yet well developed enough to have a substantial following amongst industrial coaters.

Due to the thermal energy flux to the substrate being lower than conventional DC and pulsed DC sputtering discharges (shown in Figure 2-10) and a deposition rate of the same order of magnitude as pulsed-DC sputtering it has been suggested as a suitable technique for coating temperature sensitive substrates such as polymers [22].

2.2.3 Thermal Arc Evaporation

During arc evaporation a high current, low voltage arc is generated that strikes the surface of a cathode, known as the target. The high energy will create an area called a cathode spot, with very high local temperatures, from which the target material will vaporize causing the emission of ions. The high energy nature of this process results in a high percentage of the resultant vapour being ionized, with multiple-charged ions and high energy electrons present. These characteristics of the process result in dense, uniform coatings that adhere well to the substrate and are deposited at high rates.

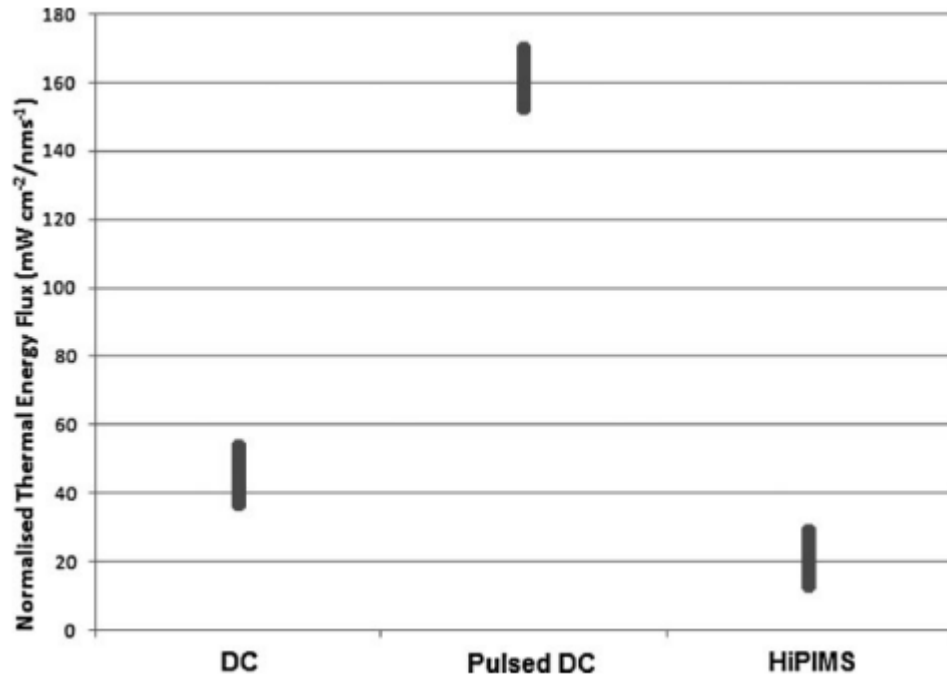


Figure 2-10 - Thermal energy flux of DC, pulsed-DC and HiPIMS plasma discharges [22]

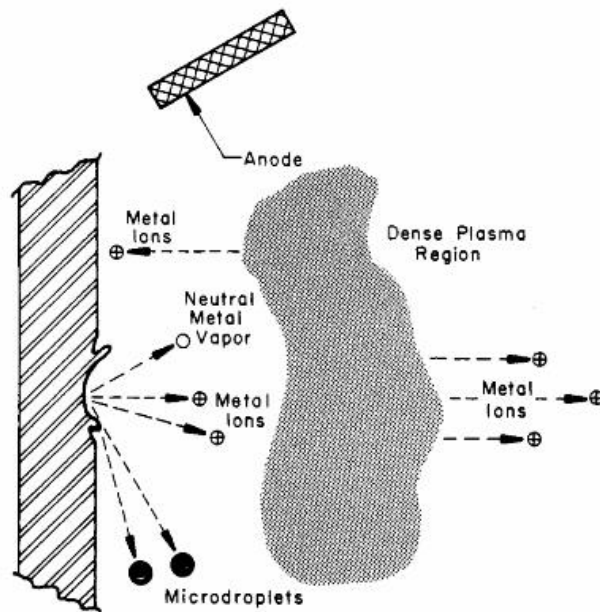


Figure 2-11 - Particle flux during arc evaporation [7].

Once the metal ions/neutrals are expelled from the target they are transported into the bulk plasma where they will either react with gases, such as nitrogen introduced to deposit nitride coatings, or will continue to be transported towards the substrate where they will condense and grow into a film. Some metals ions will be incorporated back into

the target due to negative charge accumulation on the target surface (Figure 2-11). Droplets can be produced from the cathode spot due to explosive evaporation caused by intense heating [23]. These macro-particles have extremely high mass compared to the particles making up the evaporated vapour and are generally expelled at lower angles. Despite this they are still transported to the substrate and can degrade the quality of the coating produced.

Cathode metal	Degree of ionization (%)	Ions registered on mass spectrograms	Ion Content ^b (%)		
			<i>i</i> = 1+	<i>i</i> = 2+	<i>i</i> = 3+
Mg	80–100	Mg ¹⁺ , Mg ²⁺ , Mg ²⁺ → Mg ¹⁺	50 ± 5	50 ± 5	0
Al	50–60	Al ¹⁺ , Al ²⁺ , Al ³⁺ Al ³⁺ → Al ²⁺ Al ²⁺ → Al ¹⁺ , Al ³⁺ → Al ¹⁺	60 ± 4.5	38 ± 4	2 ± 0.5
Ni	60–70	Ni ¹⁺ , Ni ²⁺ , Ni ³⁺ Ni ³⁺ → Ni ²⁺ , Ni ²⁺ → Ni ¹⁺ , Ni ²⁺ → Ni ¹⁺	6.5 ± 4.5	33 ± 4	2 ± 0.5
Cu		Cu ¹⁺ , Cu ²⁺ , Cu ³⁺ Cu ¹⁺ , Cu ⁴⁺ → Cu ³⁺ Cu ³⁺ → Cu ¹⁺ , Cu ²⁺ → Cu ¹⁺ , Cu ³⁺ → Cu ²⁺			
Ag	50–60	Ag ¹⁺ , Ag ²⁺ , Ag ³⁺ , Ag ³⁺ → Ag ²⁺ , Ag ³⁺ → Ag ¹⁺ , Ag ²⁺ → Ag ¹⁺			
Zn	15–20	Zn ¹⁺ , Zn ²⁺ , Zn ²⁺ → Zn ¹⁺			
Cd	12–15	Cd ¹⁺ , Cd ²⁺ Cd ²⁺ → Cd ¹⁺	9.7 ± 0.0	0.3 ± 0.05	0
Pb	18–25	Pb ¹⁺ , Pb ²⁺ , Pb ²⁺ → Pb ¹⁺			
LS-59	60–70	(Cu/Zn) ¹⁺ , (Cu/Zn) ²⁺ , (Cu/Zn) ³⁺ , (Cu/Zn) ³⁺ → (Cu/Zn) ²⁺ , (Cu/Zn) ²⁺ → (Cu/Zn) ¹⁺ , (Cu/Zn) ³⁺ → (Cu/Zn) ¹⁺			

Figure 2-12 - Degree of ionization of emitted cathode species [24].

The arc can occur randomly on the surface due to natural charge build-up, or can be steered by magnetic fields to control the location of the cathode spot. Steering the arc, and hence controlling the cathode spot, has been shown to reduce droplet formation by reducing the localised heating [25].

The metal ions expelled from the target will carry different charges dependant on species and energy. The electron shell arrangement of the metal species dictates the availability of electrons which will readily be lost from the atom upon increasing the energy. Figure 2-12 shows the degree of ionization of metallic cathode material and the percentage contribution of ion content. A large number of ions expelled from the target carry multiple charges and this demonstrates the high energy nature of the process.

Figure 2-13 shows how varying the deposition parameters can reduce the incorporation of macro-particles in the deposited film. Increasing the temperature with no bias voltage gives no significant reduction in droplets, however increasing the bias voltage to -200V increases ion bombardment during film growth and reduces the droplets size at all temperatures with a noticeable reduction in number and size when both increased temperature and a high bias voltage are used.

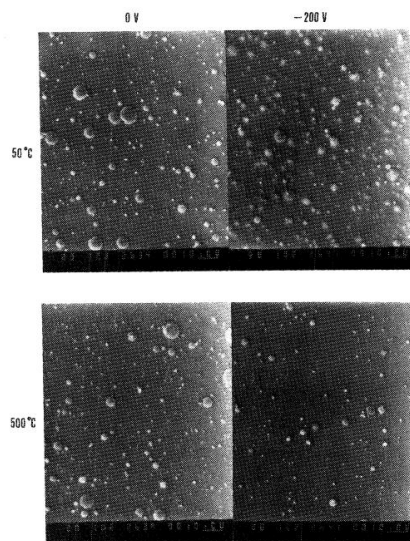


Figure 2-13 - Droplet incorporation into Ti films at varying temperatures and bias voltage [26].

Applying a negative bias voltage to the substrate will cause the positively charged cathode material and gas species present in the plasma to be accelerated to the substrate as a function of the charge density of the particle. This increases the energy of the particles further still and increases mobility of the particles once on the surface.

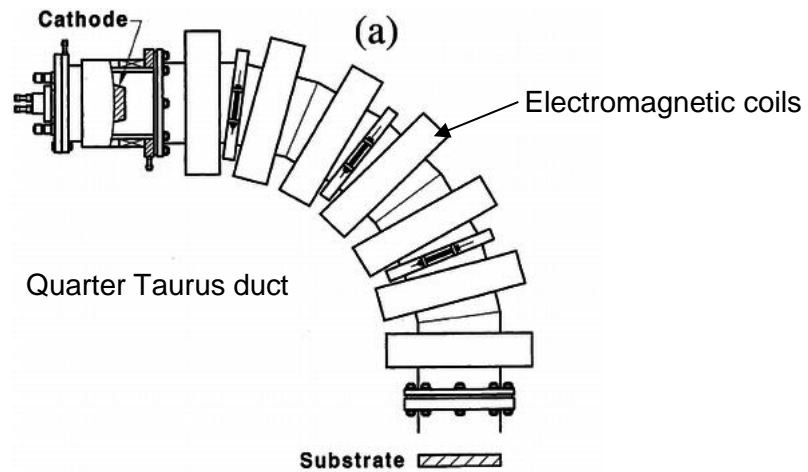


Figure 2-14 - Aksenov quarter taurus macro-particle filter used in filtered arc evaporation. Adapted from [27].

Zhitomirsky et al. [28] demonstrated the use of a filtered vacuum arc deposition technique for depositing optical SnO_2 coatings onto polymer substrates with the suggested use for protection of an otherwise vulnerable material in uses such as vehicular and aircraft canopies. The filtered arc utilises the same method of evaporation as conventional arc evaporation techniques, but the metal plasma is then streamed through a taurus based macro-particle filter using electromagnets. The heavier, uncharged macro-particles, or droplets, will be unable to turn through the Taurus removing them from the vapour available for film deposition (Figure 2-14). The deposited SnO_2 coatings of 160-1200 nm were adherent to Polycarbonate (PC) and Polymethylmethacrylate (PMMA) substrates, were relatively hard, and possessed light load scratch resistance.

2.2.4 Plasma Enhanced Chemical Vapour Deposition (PECVD)

Chemical Vapour Deposition (CVD) relies on a precursor and reactant chemically reacting to form a deposit on the surface of the substrate. Gaseous by-products are created due to the reaction and removed from the deposition chamber by gas flow. PECVD introduces energy to the chemical reaction through plasma, enabling film deposition at lower temperatures.

In the Hauzer Flexicoat 850, carbon is supplied by acetylene gas molecules which are ionised using the cathodes or using remote microwave antenna to assist the 'cracking' of the molecules. The different methods and range of plasma densities available allow different properties of film to be produced.

PECVD SiOCH films have been deposited on PC with a peak hardness of roughly 2.3 GPa; approximately 25% of the hardness of comparable SiO₂ sputtered coatings [29]. Other optical PECVD coatings (DLC) on PC deposited at low power and temperature have been shown to increase scratch resistance of the surface by almost 50% [30].

The most commonly used PECVD techniques for depositing coatings onto polymeric substrates will be covered in detail later in this chapter.

2.3 Polymers

Polymers, on an atomic level, are long chain hydrocarbons with a repeating unit that remains the same throughout the chain. The term polymer encompasses many different materials and as such they can be either semi-crystalline or amorphous in structure. The polymer naming convention is mostly dependent upon the organic molecule upon which it is based – for example a polymer made up of a repeating chain of ethylene molecules is referred to as Polyethylene (PE).

Despite the seeming simplicity of the molecular structure of polymers, especially those such as PE, there is an abundance of different grades of PE with varied mechanical and thermal properties; these depend on the complexity of the molecular structure. A low density PE (LDPE) has a short chain structure and is characterised by its low weight and high ductility. An ultra-high molecular weight PE (UHMWPE) has much longer chains with more branching and is therefore much denser, harder, and less ductile. As a general rule, as the molecular weight increases so does the melting temperature [31].

A polymer is said to be amorphous when these molecular chains are randomly oriented. Generally this means that measurable mechanical properties such as hardness and modulus are the same in all orientations. As chain orientation is introduced, polymers

exhibit orientation specific properties. When the orientation of molecular chains becomes ordered the polymer is said to be crystalline [31]. In reality, polymers are rarely fully oriented and a mixture of ordered chains and randomly oriented chains will be present; this is especially true for thicker sheets or injection moulded polymers where orientation does not occur due to manufacturing processes. These are said to be semi-crystalline polymers.

As well as the average molecular weight of the polymer there are other phenomena which directly affect the properties of the material. Crosslinking is the term used to describe how much the molecular structure deviates from linear chains of repeating units.

Crosslinking is a function of either the manufacturing process or a further process with enough energy input to break the chemical bonds present in the polymer and create dangling bonds or free-radicals. These species, if close enough to a similar neighbour on a different chain in the material, will recombine to form a chemical bond across two chains thus forming a crosslink. An increased degree of crosslinking allows less molecular movement and so manifests itself as an increase in hardness and elastic modulus.

Once crosslinks are formed the thermal properties of the material can vary dramatically; enough to cause a change in the categorisation of the material. Most common polymers, such as PE, are thermoplastics; meaning that they become pliable and/or mouldable above a certain temperature, then return to the same solid state upon cooling. This behaviour can be attributed to the chains becoming more mobile at higher temperatures and being able to move with respect to each other as only weak intermolecular bonds prevent this movement of molecules at room temperature. As the degree of crosslinking increases, more molecules are held in place by much stronger chemical bonds, and so are unable to move upon heating. Upon heating, instead of becoming pliable, these materials will simply break up and degrade and then will not reform into the same solid state upon cooling [31]. This class of polymer are called thermoset.

As well as a melting temperature (T_m), thermoplastics have a glass transition temperature (T_g). This can be described as the temperature at which the thermal properties of the material undergo changes, without the material undergoing a change of state. From a practical standpoint, thermoplastics become pliable at this temperature but are not yet liquids [31]. LDPE has a $T_g \approx 0^\circ\text{C}$ and is very ductile at room temperature. On the other hand, ABS has a $T_g \approx 105^\circ\text{C}$ and is an elastic-plastic solid at room temperature with far lower ductility than LDPE.

2.4 Coatings on Polymers

The structural, chemical and mechanical properties of polymers compared to metals create specific challenges to coating designers. As a general rule it could be summarised that common engineering metals are much more robust than common thermoplastics, especially with respect to mechanical and thermal properties. Where polymers can be beneficial compared to metals is where weight is of concern and where harsh chemical environments are encountered [32].

2.4.1 Limitations

2.4.1.1 Temperature

The generally accepted thermal window of most PVD and CVD processes is $200\text{-}600^\circ\text{C}$. This relatively high temperature is far larger than the T_g and T_m of most common and engineering thermoplastics. As such, the same process parameters used to coat metal substrates are not suitable for use when coating polymers as they will almost certainly cause melting or degradation of the substrate material.

During sputter deposition the heating of the substrate is caused by the bombardment of high energy particles. As such the rate of heating and T_{max} of the substrate are a function of the number of bombarding particles and the average energy. Figure 2-15 shows a typical heating curve for metal, glass and polymer materials during film growth in an ion-assisted deposition technique. Under the same conditions, starting from room temperature, the polymeric material heats up quicker and has a higher maximum

temperature. There are multiple methods that can be employed to control these in a metal substrate system; the bias voltage, the power of the plasma used for sputtering and the coil current in an unbalanced magnetron system.

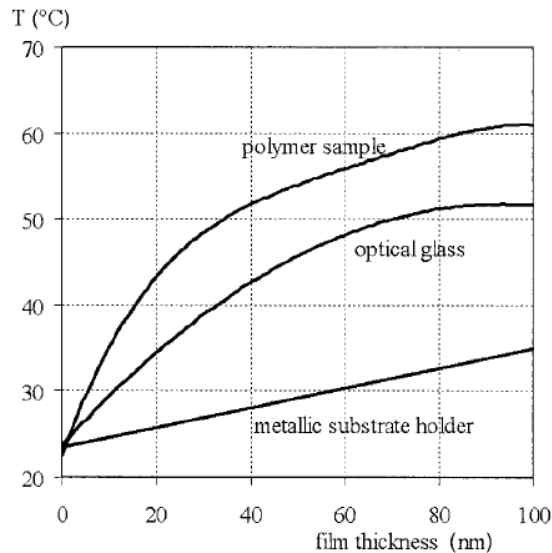


Figure 2-15 - Temperature development of Polymer, Glass and Metal during film deposition from an ion-assisted technique [33].

As many polymers are non-conductive and the majority of sputtered particles carry no charge, any introduction or change of bias voltage would be expected to have little to no effect, dependant on the load, or distribution of parts, in the deposition chamber and how the bias voltage is applied. It is possible to apply a bias to insulating substrates using radio frequency power [34].

As mentioned, plasma power can be controlled by varying voltage, current and pressure. The plasma power expresses the energy of the particles in the plasma and as the discharge is expected to be in the glow regime for sputter deposition processes, it is expected that there is a large degree of ionisation and therefore a large number of charged particles. As such, any positively charged particles (the particles used for sputtering) will be accelerated towards the cathode at a rate determined by the cathode voltage and charge density of the particle. Upon ejecting (sputtering) a particle from the target, the energy of the sputtering particle will determine how much energy is transferred to the sputtered particle and hence the energy transferred to the substrate; this manifests

as substrate heating. To lower the substrate temperature, the plasma power and cathode voltage must therefore be decreased. This would lower the average energy of the sputtered particles and also reduce the sputter yield resulting in fewer particles reaching the substrate, both resulting in less substrate heating. If certain parameters are necessary to deposit a certain film of given structure and thickness, it is possible to lower the maximum substrate temperature reached by depositing the coating in stages. For example, Sarto et al [35] kept the temperature of polycarbonate substrates below 50°C by depositing a coating during 3 runs of 12 minutes with intermediate cooling periods of 1 hour. This process could also be viewed as helping to eliminate intrinsic stresses in the film, manifesting in well adhered coatings, although the effects of ion treatment and film stress were not separated in this study.

The coil current in a magnetron determines the strength of the magnetic field and therefore, in this instance, the ability of the magnetron to control the path of electrons in the deposition chamber. As the coil current is increased in a type-2 unbalanced magnetron (the most commonly used configuration for coating), then the sputter yield is increased due to increased electron confinement at the target. Also, more electrons will be streamed towards the substrate, resulting in bombardment from electrons and positive ions. Both of these would increase substrate heating and therefore reducing coil current is advantageous for coating temperature sensitive substrates, such as polymers.

Arc deposition techniques tend to allow lower temperature deposition than sputter coating techniques for coatings with similar characteristics, despite the cathode spot being heated to ~3000K during arc evaporation as reported for a 20 ampere arc on a copper target [36]. The evaporated vapour does not transport all this energy to the substrate. Instead, substrate heating is influenced more by high kinetic energy particle bombardment. High bias voltages are therefore more likely to heat the substrate, which are required in order to produce certain crystal structures and amorphous films through increasing the surface energy.

2.4.1.2 Adhesion

In order to have a successful coating it must be well adhered to the substrate. The level of adhesion required is determined by the application of the coating system; applications involving high loads and stresses, such as tool coating, will require better adhesion than low load coatings, such as gas barrier films. The adhesion of coatings is an active area of research and the exact mechanisms that govern adhesion are likely to be dependent on the system as a whole and as such there is not likely to be an accurate model which can predict the behaviour of all coating systems.

In many coating systems an adhesion interlayer is used; this is a layer of material which is known to adhere to the substrate being coated and also to the functional material of the coating. The adhesion layer is often a thin layer of the transition metal used in hard coatings; for example a Ti interlayer would be used for a TiN hard coating.

It has been shown that both the polymer substrate and deposited material affect the level of adhesion. Figure 2-16 shows the peel energy of different metal films on ABS substrates. Al offers the best adhesion followed by Cr, Ti, then Cu. Using ABS as a reference, the adhesion of different substrate materials can be ranked: PP(0.005) < PET(0.03) < PC(0.11) < PET-G(0.30) < ABS(1) [37]. In this study, the film deposited on each polymer type was not optimised and the same conditions were used, varying only deposition time to account for variations in film growth rate on the substrates. Evidence of increased adhesion after plasma treatment was also presented and this correlated with decreased contact angles.

There are two main schools of thought on the mechanisms which govern adhesion of thin film coatings; molecular bonding and mechanical interlocking.

The molecular bonding mechanism of adhesion is caused by the strength of any chemical bonds at the interface of the substrate and coating. The adhesion strength is therefore governed by the type of bonds, the strength of the bond determined by atomic size and electron arrangement, and the bond density. The intermolecular interactions at

the interface of the substrate and coating can be very weak, such as dipole-dipole interactions or very strong, such as covalent bonding.

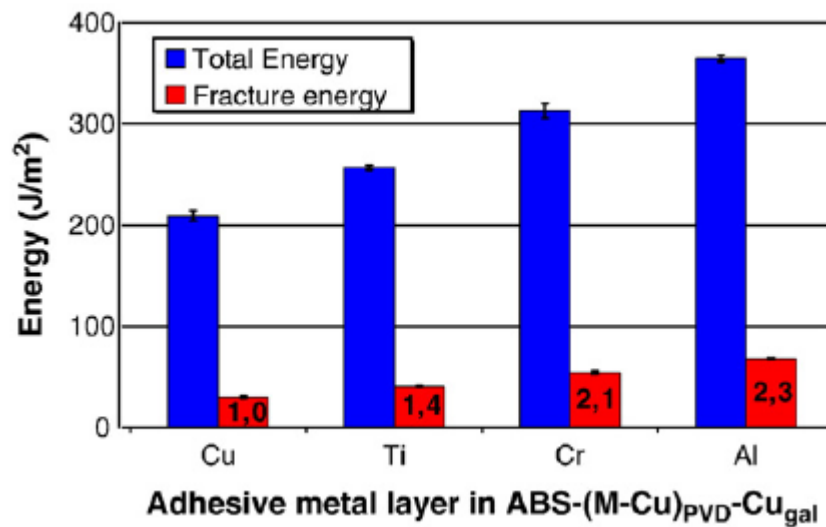


Figure 2-16 - Peel energy of different metal films deposited on ABS substrate [37].

The molecular bonding mechanism of adhesion is not fully understood. This in part is due to the sheer number of combinations of adhesive/coating and substrate, but also, in part due to the complexity of the chemical interactions at the interfaces of these systems despite the analytical techniques available. The use of data rich techniques such as X-ray photoelectron spectroscopy (XPS), along with conventional methods such as peel tests has overcome some of these issues and despite the difficulties, the molecular bonding mechanism of adhesion is the most widely accepted [38].

Mechanical interlocking is governed by the surface roughness of the substrate. Small nano and micro scale asperities on the substrate surface allow coating material to form around them. As the coating grows the asperities are engulfed by the coating material and the uneven interface creates what can be described as nano-scale hooks that mechanically grip the coating; much like Velcro, but on a small scale. The adhesion strength in this case is a function of the mechanical properties of the materials used. Figure 2-17 shows an apparent increase in adhesion of a PECVD interlayer as surface roughness of the substrate increases.

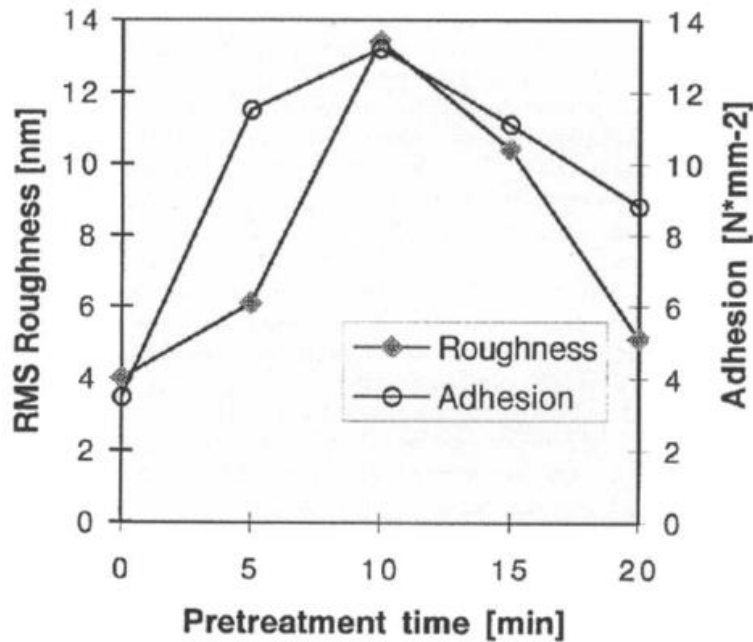


Figure 2-17 - Influence of surface roughness on adhesion. Ar plasma treated PTFE substrate with TiN PECVD interlayer and electroplated copper coating [34].

It could also be argued that the roughness of the substrate increases the 'real' surface area exposed to the coating material, and so offers the potential of having a greater number of chemical bonds for the same perceived surface area. Also, the correlation between roughness and adhesion could be due to chemical changes at the surface brought about by the increased ion bombardment time.

A phenomenon with little evidence and no further research was demonstrated by Trakhtenberg et al. [39], whereby the substrate temperature was seen to have an effect on adhesion of DLC films to polyethylene substrates. Using both an X-cut tape test and thermal cycling to test the magnitude of adhesive force between the film and substrate, showed that adhesion was improved when the substrate temperature was held at 83 – 95 °C; just below the melting point of the substrate.

2.4.1.3 Mechanical properties and stress

Where a hard coating is needed, the mechanical properties of the coating and substrate are likely to differ dramatically; by an order of magnitude in some cases. Where in more traditional hard coating systems the coating is hard, stiff and deposited to increase

hardness above what would be feasible using a bulk material, depositing the same coating on a substrate with much lower hardness or stiffness is likely to cause problems. The substrate will elastically deform more than the thin film, causing fractures which would ultimately lead to failure. Little has been reported specifically on this phenomenon.

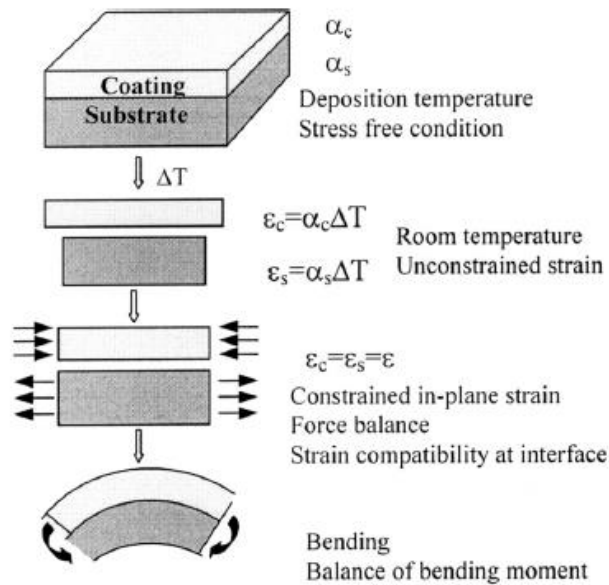


Figure 2-18 - Model for the formation of thermal residual stress for a ceramic coating on a metallic substrate [40].

A more thoroughly understood phenomenon is stress cracking in thin films due to residual internal stresses from the heating and cooling of the coating during deposition. There are three main sources of stress in coatings: thermal stresses caused by heating and cooling and differing coefficients of thermal expansion (CTE) in the substrate and coating, coating growth stresses, and external stresses from bending or applied stress [40]. Coating growth stress can be further classified as either geometrically induced; where stress concentrations build up due to competing crystal growth at geometrical features, or intrinsic stresses that are the cumulative result of chemical and structural defects in the deposited film. Whereas thermal stress is a function of the CTE of the substrate and coating materials, intrinsic stresses are process sensitive and the stress state can be compressive or tensile, with generalizations as to the anticipated state of stress unable to be made [41]. Most researchers turn to the so-called Stoney method of

determining thin film stresses, which measures substrate curvature before and after coating deposition [42]. The simplicity of the test procedure is likely the cause for widespread adoption, even allowing measurement of bi-directional stresses from a simple geometric parameter. The downside however, is that substrates must not be easily deformed from handling or thermal cycling, as this would reduce the accuracy of the calculation; an unavoidable problem when dealing with polymer materials.

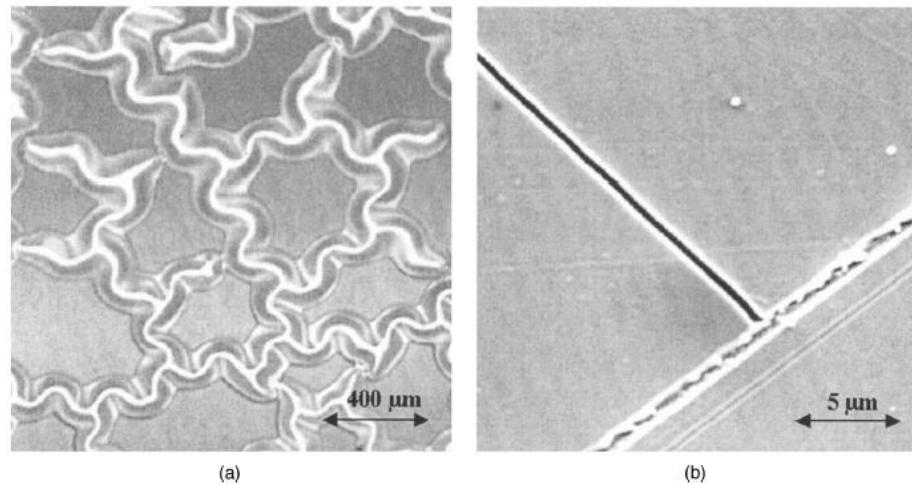


Figure 2-19 - Cracking behaviour of coatings on polymers: (a) buckling of a coating as a consequence of compressive growth stress and insufficient adhesion and (b) tensile stress cracking caused by different thermal expansions of the substrate and coating [33].

Figure 2-18 shows a model for how the residual thermal stresses are formed due to balance of the bending moments from the stress free condition at deposition temperature to cooling and subsequent material shrinkage. The model applies to a generalized ceramic on metal coating system, however due to the CTE ratio in this system ($CTE_{\text{substrate}} > CTE_{\text{coating}}$) being similar to a metal or ceramic on polymer system the same result is to be expected when coating polymers. Figure 2-19 shows the failure modes of compressive and tensile stresses in deposited thin films.

In most cases the stresses in a coated polymer system are detrimental, however Lackner et al [43] has deposited thin films with intrinsic growth stresses which lead to controlled deformation of the surface. This gives rise to a nano-wrinkled surface with improved

tribological performance under certain conditions due to the elastic smoothing of the wrinkles under load; a concept inspired by the tribology of human skin.

2.4.2 Measurement Methods

2.4.2.1 Scratch test

The scratch test is a mechanical test whereby a stylus is loaded and moved along a straight trajectory on a flat sample surface. The premise of the scratch test is that during the scratch, the coating – substrate interface will be subjected to shear stresses brought about by the frictional forces between the stylus and coating surface, and the coating will be subjected to tensile and compressive stresses as the coating deforms around the area of contact.

It has been used in the field of coating analysis to determine the adhesion of coatings to the substrate following the investigation of adhesion of Al films on glass using Cr interlayers [44]. The developments in scratch testing to evolve the use as an adhesive test [45-49] have not resulted in a successful correlation between critical loads and coating adhesion, despite their widespread use to investigate coating adhesion in the literature. In a comparative study of 6 different methods of determining the adhesion of hard coatings, none were in agreement [50]. Depending on how the analysis was carried out on the scratch test data, both a positive and negative correlation was found with pre-sputtering time used to enhance adhesion. It can be surmised that the information that can be gathered from the test, combined with the simplicity of the method (e.g. no further adhesives required and simple mechanical equipment) has led to the widespread adoption of the test.

When Hienke et al. [51] compared scratch testing of different nitride layers to Rockwell adhesion tests and impact tests, they generally showed the same qualitative results; that is CrN coatings were more brittle than TiN coatings and failed at lower loads. They demonstrated some dependence of the critical load used to quantify adhesion on the coating thickness, also shown in a review of adhesion tests by Volinsky et al. [52].

When considering coatings on polymer materials where substrate behaviour dominates the response, further complications with the scratch test become apparent; namely the inclusion of viscoelastic and plastic effects of the substrate on the contact behaviour between the material surface and the stylus. Most studies use the concept of a critical load, a load determined through observation of some phenomenon related to failure of the film, to explore the behaviour of the contact. The behaviours exhibited range from ductile sliding, where no damage is observed, through to brittle contact, where the coating fractures. Since the mechanical properties of polymers are time and temperature dependant, no single critical load can describe the possible range of mechanical behaviour possible in a polymer system.

The viscoelastic effect of polymers have been shown to have a large effect on the inaccuracy of contact geometry determination [53]; the elastic recovery of the groove can recover as much as 90% in cases where the elastic component of deformation is high. This is caused by the strain hardening of polymers whereby an increase in strain hardening will increase the elastic recovery at the trailing edge of the stylus, both decreasing the apparent friction coefficient and increasing the measured hardness of the material. Damasceno et al. [54] demonstrated this when micro-hardness and scratch hardness results did not show the same trend as a function of bias voltage for DLC-Si coatings on polyurethane. This realisation means that in order to increase scratch resistance of polymers the surface must be hard and elastic at the same time; only the resistance to plastic deformation need be increased. Developed from this, Gauthier [55] demonstrated the necessary requirements of a thin scratch resistant coating on viscoelastic materials to have to reduce the local friction coefficient between the scratch tip and surface.

The literature does not contain an in depth analysis of the response of brittle coatings on polymer substrates having undergone scratching. Ollivier and Matthews [56] deposited DLC coatings onto two polymer films using a radio frequency PECVD technique and then characterized the scratch response against predicted adhesion behaviour based on

plasma treatments. They showed that although critical loads cannot show any improvement in the adhesion following plasma treatment, calculating interfacial shear strength from assumed forces acting on the surface or scratch geometry does capture this behaviour. These methods are still only suitable as semi-quantitative measures of adhesion for ranking purposes and fail to incorporate viscoelastic and viscoplastic material effects.

The same inability of the test to determine adhesion in different coated polymer systems was also demonstrated in [57], where DLC films deposited on bare PC and PMMA substrates were removed by tape test, but remained adhered if the substrate was treated with O₂ plasma prior to deposition. The scratch test was able to show a two fold increase in adhesion to PMMA following treatment, but critical load values for treated and untreated PC remained within error.

2.4.2.2 Nanoindentation

Nanoindentation has become a widely accepted standard method of measurement for determining thin film mechanical properties; namely Young's modulus and hardness. Oliver and Pharr stated that to ensure negligible substrate effects during nanoindentation of thin films the indentation depth should be less than 10% of film thickness [58]. Most researchers have used this 'rule of thumb' to determine Young's modulus and hardness of coatings, as deposited on the substrate material. The advantages of the techniques proposed by Oliver and Pharr [59], and likely the reason they are still in wide use, are that they allow easy interpretation of the nanoindentation data without resorting to numerical solvers.

It has been recognised that using critical depths of less than 10% is feasible for coatings that are roughly a micrometre in thickness, thinner coatings present a much greater challenge to measure [60, 61]. Nanoindentation measurements on coatings less than 2 μ m thick, where Young's modulus and hardness are determined by the Oliver and Pharr method would require indentations that are so shallow that greater errors from tip

rounding, surface roughness, and indentation size effects are introduced. In such cases, more complex methods are required to remove substrate effects. Saha and Nix [62] deposited a number of soft coatings on hard substrates and showed that in such systems the depth of indentation had a greatly reduced effect on the measurements compared to when a hard film is deposited onto a softer substrate.

In recent years, numerical studies [63, 64] have shown that in certain circumstances the critical depth of indentation is less than 10% of coating thickness. The ratio of yield stress of the coating and substrate were found to be an important characteristic of how the system would respond during indentation. Hence, the ratio of yield stresses of film and substrate should be used to determine the critical depth for the coating system of interest. In reality, the yield stress of a coating is difficult to measure, and despite methods being available, they have not become widely adopted. The numerical studies also include assumptions about the coating system, that although are difficult to guarantee when performing nanoindentation, have led to greater understanding of material behaviour.

One of the biggest limitations of the Oliver and Pharr method when used to accurately determine thin film properties is that it does not take into account the true contact area of the indenter tip; pile-up and sink-in phenomena around the indenter tip serve to increase and decrease the contact area respectively. For hard film on soft substrate systems, sink-in behaviour is expected [62]. The sink-in effect occurs when the substrate is unable to support the load applied by the indenter tip onto the surface of the film, causing plastic flow of the substrate that is greater than that of the coating. This leads to a situation in which a reduction of real contact area compared to the assumed contact area used to calculate hardness is present (Figure 2-20), the result of which is an underestimation of the hardness of the surface; this can be seen in the finite element studies of Pelegri & Huang [60]. For soft films on hard substrates, the opposite is expected, where the soft film flows plastically around the indenter tip and so little of the load is transferred to the harder substrate [62, 65].

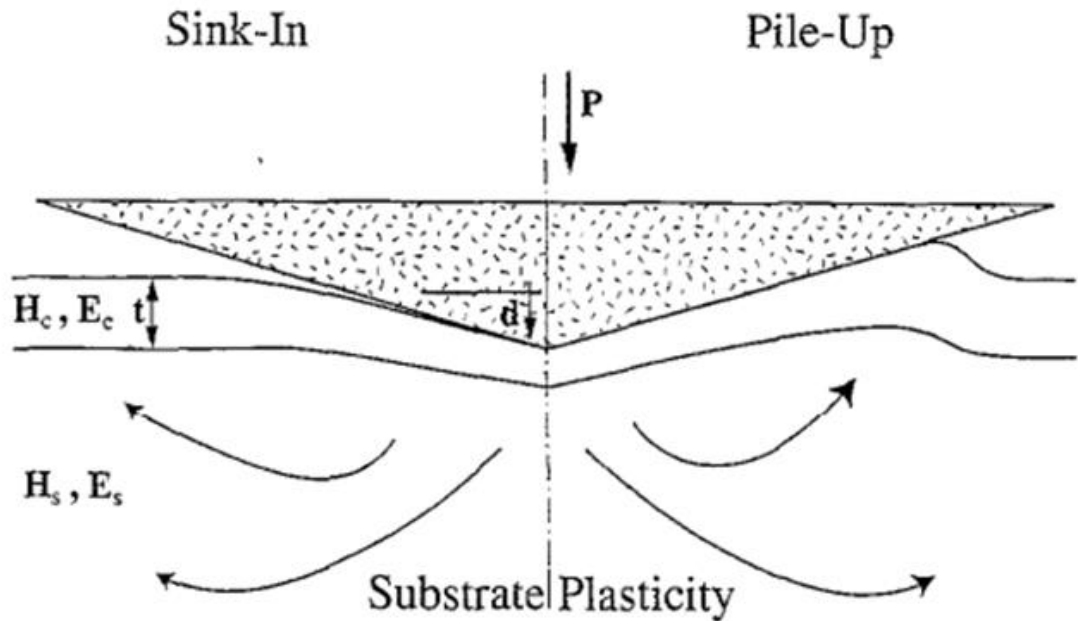


Figure 2-20 - Pile-up and sink-in phenomena of thin films during indentation, from [66].

Joslin and Oliver [67] developed a method suitable for use in systems where the film and substrate are elastically mismatched. P/S^2 (or H^3/E_r^2) is found from the maximum load of the indentation, P , and the contact stiffness during unloading, S . They proposed that P/S^2 was useful in that it defined a material's ability to resist permanent damage. For a given hardness, a lower modulus would result in more elastic deformation being possible before permanent damage occurs; for a given modulus, increased hardness of the surface will result in reduced plastic strain. The parameters P and S are derived from the maximum load reached during the loading cycle, therefore the exact geometry of the indenter tip is not required, nor is accurate depth sensing as the initial point of contact with the surface is not required. However, because of this, hardness and modulus cannot be solved for separately from P/S^2 . Joslin and Oliver also argued that due to the relationship between permanent damage indication and elastic accommodation provided by P/S^2 , it would be a better indicator of resistance to abrasive wear than either the hardness or modulus alone. This proposal has since been expanded with respect to coatings by Leyland & Matthews to include H/E , the elastic strain to failure [68].

Recently, certain studies have shown that increased H^3/E^2 (as well as H/E) of coatings correlates with reduced wear measured from pin/ball on disc sliding tests [69, 70], while other studies have shown no correlation and this has been attributed to differences in coating microstructure, architecture and residual stresses [71, 72]. The findings from [71] show that residual compressive stresses in the coatings give rise to different tribological properties and critical loads during scratch tests, suggesting that H/E or H^3/E^2 cannot be used as a substitute for toughness, and considered in isolation they are an unreliable method for predicting wear resistance. Despite differing opinions on the importance of H/E and H^3/E^2 , they have been shown to provide a performance indicator in certain tribo-couples. As no standard exists for wear testing with respect to applied initial point contact pressure and differences in coating to substrate mechanical property ratios, it could be argued that the relative contribution of the coating and substrate properties in these studies differs. Therefore, considering the mechanical properties of the coating in isolation only tells part of the story as to how the surface responds in any given contact.

Despite interest in coated polymers, there are no widely accepted test methods to determine film properties and studies involving 'hard on soft' coating systems do not investigate such drastic mismatches in material properties as exhibited by coated polymer systems, nor do the substrate materials exhibit the same properties as polymers, such as viscoelasticity. This can be attributed to only recent developments in plasma coating technology unlocking the potential to coat polymers using clean processes, with thin films that offer increases in surface hardness and modulus [73-76]. With the use of a novel PECVD coating technique, fast growth of DLC films at low temperatures with tuneable mechanical properties has become possible, allowing the study of hard films on soft polymer surfaces to determine suitable methods for understanding the behaviour of such systems.

As such there is a need to characterize these coated systems in a meaningful way such that the properties can be related to performance, instead of defining this based on

properties as measured on more traditional coating systems involving metallic substrates.

2.5 DLC Coatings

DLC coatings have become an area intensively researched due to the possibilities of creating coatings with an infinitely tuneable range of properties based on deposition technique and conditions, carbon source, and dopants used to introduce desirable qualities.

DLC was first discovered in the 1950s [77], but the phrase 'diamond-like carbon' was not used until later, when thin DLC films were deposited with biased substrates and carbon electrodes by an ion beam technique [78]. The results from this study confirmed DLC as having high hardness, scratch resistance and corrosion resistance, leading to the research area growing steadily up to the present day. Comprehensive reviews are available for the tribology [79-81], biomedical applications [82, 83] and specific deposition techniques [81, 84], however these concentrate on the coating of hard substrate materials such as metals and silicon.

2.5.1 Structure and Properties

DLC is an amorphous mixture of both diamond like tetrahedral bonded carbon and graphitic carbon with a shared double bond. Where the two constituent bond types in their diamond or graphite forms are crystalline, DLC coatings will contain a mixture of both bonding types with different molecular weights and distribution. Carbon coatings ranging from crystalline through to amorphous, and with a tetrahedral diamond structure (industrial diamond) through to polymer like are possible.

Where the carbon hybridization occurs between an s-orbital and 3 p-orbitals the resulting covalent bond (σ bond) will be short, and hence strong. Each carbon can form 4 (one for each valence electron) of these bonds giving rise to the crystalline diamond structure. In a graphitic crystalline structure the s-orbital will mix with only 2 p-orbitals giving rise to a planar structure with 3 neighbours, with the fourth electron in the p-orbital being free to

move above or below the plane. This delocalized electron has no affinity to bond with any particular carbon in the planar structure and so the resulting bond (π bond) with all three neighbours is much weaker. Figure 2-21 shows the two carbon structures.

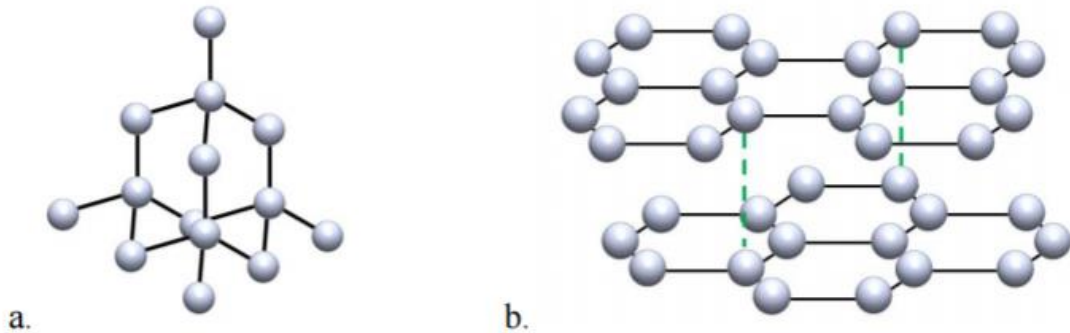


Figure 2-21 - Showing the two carbon structures; (a) tetrahedral bonds as in diamond, and (b) planar bonds as in graphite.

The distribution of bond types in a DLC material can be characterized by two compositional determinations (ignoring doping): the ratio of sp^3 bonded carbon to sp^2 bonded, and the inclusion of hydrogen. The so-called sp^2/sp^3 ratio is an important relationship which governs the mechanical properties of the resulting material. A higher degree of sp^3 bonds increases the diamond like contribution and decreases the graphitic like contribution giving rise to a harder, stiffer material, and vice-versa. Figure 2-22 shows the classification of carbon coatings based on the two aforementioned criteria. The DLC classification is based on the sp^2/sp^3 ratio that is displayed on the ternary phase diagram as location in the up-down direction. DLC types with an increased sp^3 content, and therefore expected to be harder, are towards the top of the diagram. As more hydrogen is incorporated in the coating, resulting in a softer coating in most cases, the coating is placed further to the right of the diagram. A summary of the structure and composition of different DLC coatings is given in Table 2-1.

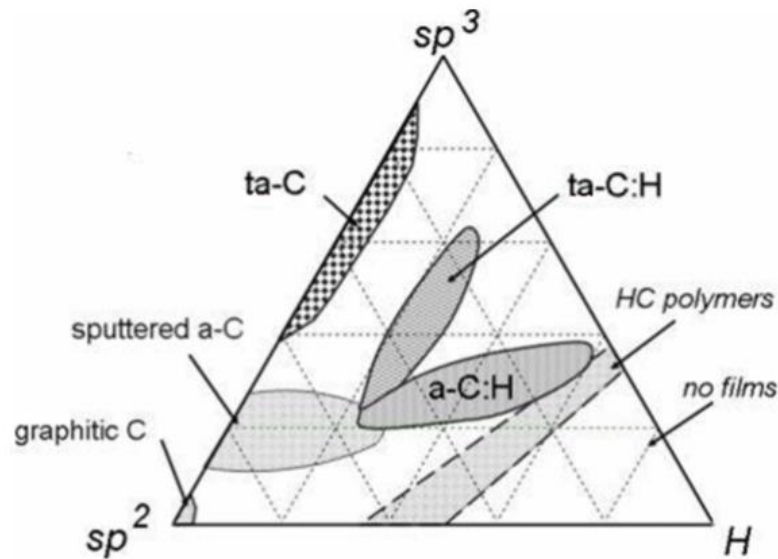


Figure 2-22 - Ternary phase diagram for DLC coatings [85].

Table 2-1 - Typical DLC film properties adapted from [86].

Type	Hydrogen (%)	Sp3 (%)	Hardness (GPa)	Elastic Modulus (GPa)
Diamond	0	100	100	1144
Graphite	0	0	0.2	9 – 15
a-C:H (hard)	30 – 40	40	10 – 20	140 – 170
a-C:H (soft)	40 – 50	60	<10	50
ta-C	0	80 – 88	40 – 90	757 ± 47.5
ta-C:H	30	70	<50	300 ± 49
W DLC	20	~50	13	100 – 150
Si DLC	15	60 – 84	14 – 25	100 - 175

Raman spectra, produced by recording inelastic scattering of monochromatic light due to molecular vibrations, can reveal how a DLC structure is composed. The study of visible and UV spectra can provide the fraction of sp^2 sites and their degree of order in amorphous carbon [87, 88]. The so-called 'G' peak, centred at roughly 1580cm^{-1} , is due to the relative motion of sp^2 hybridized atom pairs, while the 'D' peak, centred at roughly 1360cm^{-1} is due to breathing modes of ring structures [89]. A typical Raman spectra response for a DLC coating will have a broad G-peak, with a broad D-peak shoulder.

Deconvolution of these two responses based on a fitting of the two peaks using Lorentzian, Gaussian or a combination of these functions allows an intensity ratio (I_D/I_G) to be determined based on the area of the two peaks. This intensity function has been shown to correlate with sp^2/sp^3 ratios measured by other techniques [90, 91]. Figure 2-23 shows a typical Raman spectra for multiple carbon-based coatings, including DLC coatings.

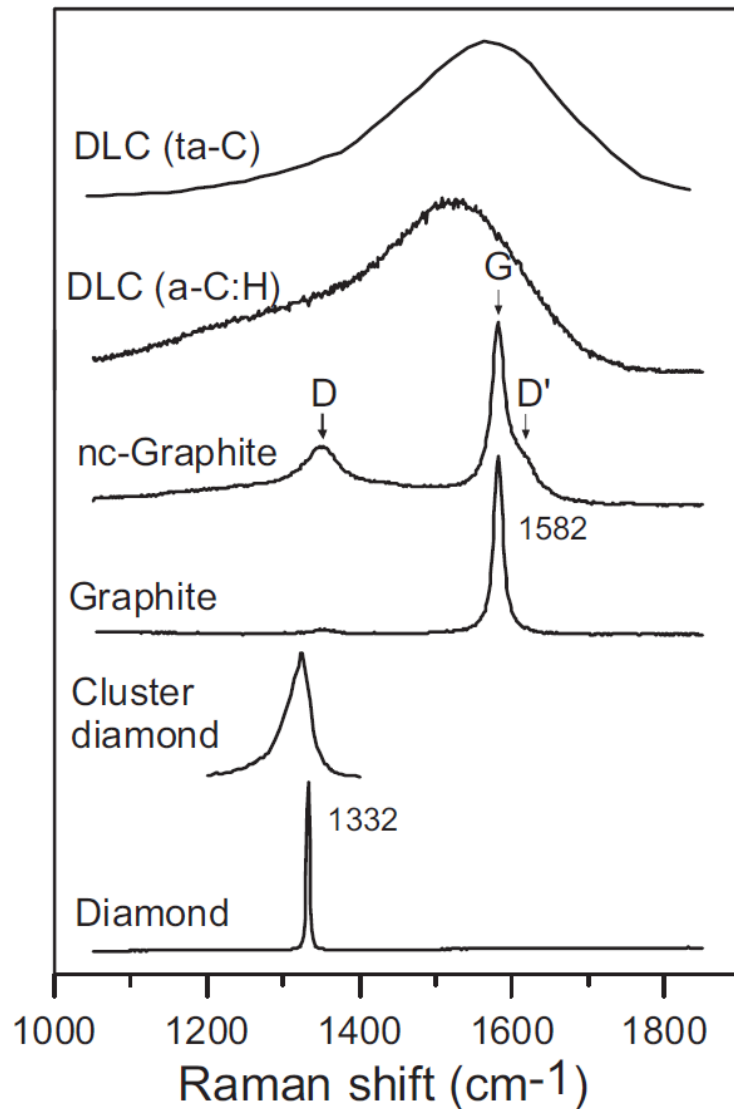


Figure 2-23 - Characteristic Raman spectra of some carbon-based materials excited by $\lambda=514.5nm$ Ar^+ laser (from [92]).

Two similar techniques exist which involve measuring electron energy to determine carbon bonding types present in a sample; x-ray photoelectron spectroscopy (XPS) and electron energy loss spectroscopy (EELS). With XPS the sample is irradiated by an x-

ray source causing the emission of electrons from the sample surface, whereas EELS bombards a thinly sliced section with high energy electrons which undergo inelastic scattering. In both cases the energy of the electrons are measured allowing determination of the species which have emitted or interacted with them.

XPS is widely used to determine sp²/sp³ ratios of carbon films. When applying this technique to polymeric materials difficulties can include sensitivity and degradation due to x-rays, temperature build-up on the sample surface, surface charging, and outgassing. The main problem faced is surface charging and methods exist to combat this, such as electron flooding [93], yet the most commonly used technique is manually shifting the spectra based on calibration of the C1s peak position. The reference value used is commonly taken to be either 284.6 eV or 285.0 eV [94] and it is noted that the C1s peak position is likely to move based on its chemical environment.

EELS sample preparation is more involved than XPS because of the requirement for electron transparency. Thin sections obtained by either focussed ion beam (FIB) milling or micro-toming are time consuming and are not possible to achieve with all materials. Despite this, EELS remains in wide use as the current method of choice for structural analysis of DLC films [85].

Nuclear Magnetic Resonance (NMR) is a physical process by which atomic nuclei absorb and emit magnetic radiation. A specific resonance frequency can be assigned to atoms based on the strength of the magnetic field and the magnetic properties of an isotope. In the case of DLC the spectroscopic techniques mentioned above have been shown to not accurately quantify the two ratios of hybridized carbon atoms, except for in the case of Raman spectroscopy, where UV sources are used [85, 88]. The use of ¹³C solid state magic-angle nuclear magnetic resonance (MAS-NMR) has been used to accurately determine sp²/sp³ ratios [95]. Despite the advantages gained in accuracy from direct excitation of both species of interest; the method itself requires bulk quantities of the coating with the substrate removed which can be difficult to achieve, especially with smaller plasma reactors. The main advantage of this technique for analysis of insulating

films and substrates is the lack of sample charging compared to those involving electron/ion emission.

In the case of hydrogenated DLC (a-C:H), the final piece of compositional information required for a complete analysis is the hydrogen content. Few techniques are able to quantify the hydrogen content with respect to other elements, however elastic recoil detection analysis (ERDA) was demonstrated to be able to meet this requirement by Doyle and Peercy [96]. ERDA makes use of MeV ion beams to irradiate a sample and then measure the energy of the scattered particles. Compared to all other spectroscopic techniques ERDA measures the target particles ejected under forward scattering, rather than backscattered primaries, and it is this mechanism that enable the identification of light elements. The importance of determining hydrogen content of DLC films has been shown in its influence on tribology whereby increased hydrogen leads to decreased friction [97], the measured hardness of coatings [98, 99] whereby decreased hydrogen increases film hardness, and also on biological response [100]. The equipment necessary for such high energy analysis techniques is expensive and not widely available, yet despite this ERDA is a primary technique for determining hydrogen content of thin films.

2.5.2 Deposition Techniques, Conditions and Performance

From Figure 2-22 it is clearly shown that the structure of a coating is influenced by bond types and composition. The variation of these is available through the deposition technique employed and the deposition conditions. Coating properties also depend on the structure of the coating and these effects have been studied in the literature.

Microwave (MW) energy can be introduced to a plasma to increase the ionisation rate of the species within a plasma without detrimentally affecting the coating. The different methods of introducing MWs to ignite and sustain a glow discharge have been described in the literature [101]. Many examples of coatings deposited with MW plasmas use electron cyclotron resonance (ECR), a process by which multiply charged ions are

confined to an area to increase the number of particle collisions that occur giving increased ionisation of the plasma [102, 103]. The adoption of this process has been seen in research but scaling up of these devices and use in industry is not yet widespread.

MW plasmas, having a frequency of 2.45 GHz, differ from other plasmas due to a higher number of electrons, and therefore ion pairs formed per unit of delivered energy. This behaviour is described by the electron energy distribution function which gives the rates of elastic collisions and inelastic properties such as ionisation and excitation [104]. A higher ion flux and dissociation rate is also achieved within MW plasmas due to ambipolar diffusion [105]. When a concentration gradient occurs within the plasma, the electrons, due to higher charge density and low mass, move at greater speed than any ions giving rise to polar regions with positive charge. A restraining electric field develops to equalise the diffusion coefficient of both the electrons and ions and hence the ambipolar diffusion dictates the mobility of all species within the plasma [106].

Coating growth of DLC during PECVD processes occurs due to the interaction of active species within the plasma and the substrate/coating surface. The interaction of both active species and neutrals with the surface is shown in Figure 2-24 and can be described as follows:

- Neutrals with closed electron shells that have low sticking coefficients do not affect the film.
- Mono-radicals, those with single free electrons, incorporate into the surface. Atomic hydrogen will cause hydrogen abstraction from the surface leaving carbon dangling bonds from which carbon radicals can join to aid growth, or provided there is enough energy will subplant and passivate dangling bonds beneath the surface.
- Di-radicals, based on carbon chains, will join the surface leading to coating growth.

- Ions (usually Ar^+) will sputter the surface, removing species, typically hydrogen, to create dangling bonds. Where these ions have increased energy, sub-surface dangling bonds can be created.

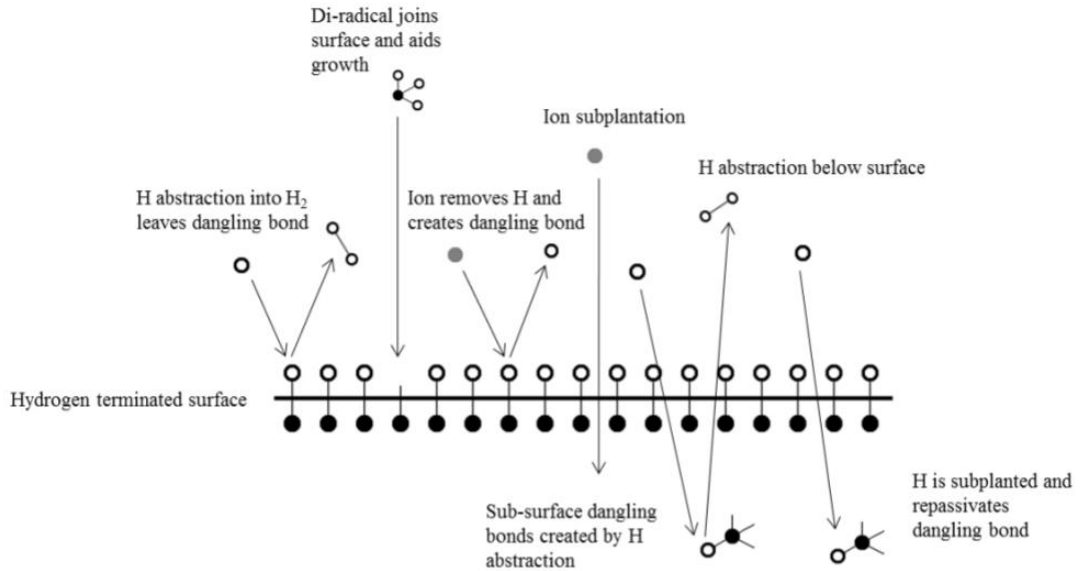


Figure 2-24 - Deposition mechanisms of PECVD deposited DLC coatings; from [77].

From these mechanisms it can be shown that increasing the energy of ionic species coming into contact with the surface will lead to greater hydrogen abstraction providing greater chance for carbon rich species to join the surface for growth, as will generating a plasma using a carbon rich gas with lower hydrogen. That is, provided the energy distribution and total energy of the impacting ions does not greatly exceed the binding energy of the surface species leading to sputtering of the growing film and decreased coating growth. The formation of carbon networks with low hydrogen incorporation will lead to increased hardness and modulus as shown in the ternary phase diagram (Figure 2-22) and Table 2-1; the difference in hard and soft a-C:H coatings being the amount of hydrogen, whereby the sp^3 content is also seen to increase. The increased sp^3 content does not contribute to better mechanical properties due to the reduced branching of the amorphous structure as the hydrogen increase leads to chain termination.

From Figure 2-24, it can also be theorized that growing DLC using PECVD techniques on polymers will lead to covalent bonding of the coating to the substrate, with adhesion being improved by the hydrogenation, or reactivity of polar groups on the polymer surface with respect to abstraction by hydrogen radicals. Fischer et al. [107] showed that the increased energies used to produce a rigid DLC film vs. a flexible DLC film grown on polyethylene formed an interlayer with different carbon centres. This work was said to confirm the nano-scale mechanical interlocking mechanism of adhesion for DLC on polymer systems as presented by Hoshida et al. [108]. However, the mixing of material to form such an interlayer could be evidence of sub-plantation of carbon species and hydrogen abstraction resulting in a gradient whereby the structure transforms from polymer to DLC with an intermediate zone; the size of which dictated by the growth conditions. The nano-fibrils observed by Hoshida et al. would then arise from removal of the interlayer due to increased stress and lower adhesion compared to the bulk of the polymer.

RF plasmas use the internationally allowed standard frequency of 13.56MHz. Using RF power sources to generate plasma circuits is useful when non-conductive materials are being processed as the alternating current used will avoid charge accumulation on insulating surfaces. The RF cycle will accelerate electrons to the surface during positively charged periods. Where RF generators become more useful in the coating of insulating materials is when used to generate a bias voltage to accelerate ions to the substrate during coating. An RF voltage will be conveyed capacitively through insulating layers where a DC voltage cannot be applied directly.

The disadvantage of these systems is the cost and complication [109]; the RF electrode behaves as a radio antennae and so non-uniform plasma densities occur, of which the shape is governed by the substrate and fixture. Added to this, if insulating substrates are used they should cover the electrode else an electrical short will occur between metals and the plasma. When using a large scale deposition chamber with rotating fixtures, such

as the Hauzer Flexicoat 850 used throughout this body of work, the application of an RF biasing system becomes impractical for the coating of insulating substrates.

The ability to bias the substrate leads to increased bombardment of the surface during deposition, giving increased mechanical performance of the coating. The use of RF biasing on a polymer whilst depositing a DLC coating has been shown to dramatically increase the measured hardness from 3.44 GPa to 17.96 GPa by increasing bias voltage from -150 V to -300 V [110]. Higher scratch resistance has also been achieved through increasing the incident power of the plasma for DLC coatings on polycarbonate [30]. Relying on the self-bias of the substrate in a parallel plate DC PECVD reactor produces much lower hardness films at similar voltages; -500 V pulse voltage, producing films with hardness in the 1.2 – 2.5 GPa range [111]. To increase the self-bias the pulse voltage was required to rise significantly to produce harder films.

Amongst the most commonly reported properties of DLC films on polymer substrates are those relating to the use as an optical coating. In many cases the optical transmittance of DLC coatings is above 80% when wavelengths above 500nm are used [6, 30, 54, 112, 113]. The difference between coatings produced under different conditions become apparent when approaching the UV spectrum (<500nm). As working pressure decreases or plasma power increases, the optical transmittance is shown to decrease [6, 30]. The effect of thickness has also been shown to be greater at near-UV and UV wavelengths [113]. Thicker films (300nm) had a transmittance of <10% and thinner films (20nm) had transmittance of roughly 60% at 300nm wavelengths despite performing similarly in the 500-900nm range. The optical band gap has been shown to increase, whilst the refractive index decreases, when incident power is increased [30, 54].

The tribological performance of DLC coatings has also been shown on multiple different polymer substrates. Results have been reported for PMMA [57, 111, 114, 115], PC [57, 116], PU [57], PTFE [57] and PA [117, 118]. The general trend shown in the literature is of DLC coatings reducing the coefficient of friction with a metallic or ceramic contact

compared to that of the uncoated polymer [115-118], except in the case of PTFE substrates [57], which already have an extraordinarily low coefficient of friction.

Of particular note is the work by Matsumoto et al. [57] where evidence was given to suggest that plasma pre-treatments (in this case O₂) would lead to different friction performance on different coated polymers; some cases performing better and others worse. In this case the coating thickness was low (0.15 μm), suggesting that either the structure of the DLC was affected by the differing surface chemistry, or a roughening of the surface occurred due to the oxygen plasma exposure. Argon etching did not show any effect on the friction coefficient of PC [116], however in an abrasive contact any surface roughness changes would quickly be negated due to asperity removal and friction properties would be expected to quickly revert back to those of the bulk material once the affected surface area has been removed. In the early stage of the test differences were observed and different morphologies of the surfaces were confirmed by SEM micrographs suggesting this to be the case.

Evidence exists in which the authors claim show a correlation between bombarding energy during film growth and coefficient of friction [114, 115]. In both cases increased bombarding energy is said to manifest in reduced coefficient of friction. However, in both cases negligible changes are shown, and no indication of sample size or error is given. A weak correlation can be seen, but this could be within error and so these claims are unsubstantiated.

2.6 Summary

The literature review has covered the subjects of PVD and PECVD deposition processes, coatings on polymers and the measurement of coating properties, and existing coatings deposited on polymer substrates; specifically DLC coatings and the structures and properties observed.

There are multiple examples of DLC coatings deposited onto polymers using an RF-PECVD method, however the novel MW-PECVD technique shown to deposit hard DLC

coatings on metallic substrates [119] has not been demonstrated on polymer substrates. The range of polymer substrates coated in the literature is also mostly limited to PC and PMMA, mainly due to their use as ophthalmic lenses and optical media. The majority of coatings produced to provide mechanical protection to these polymers have been limited in thickness by their primary function of being able to transmit visible and IR wavelengths.

The mechanical characterisation of such films with thicknesses typically less than 1 μm has been limited to indentation and scratch testing. A limited understanding of the complex interactions between polymer substrate and metal/ceramic coatings means that much of the reported data tells little as to how the coating system, that is the coating and substrate together, will behave under given conditions. A test method to show how these systems behave does not exist and quoting mechanical properties of the coating alone, determined through ultra-low load nanoindentation techniques, does not add to this understanding.

Utilising the MW-PECVD technique, a range of coatings thicker than those found in the literature will be produced. The coating system properties will then be determined using nanoindentation to investigate the usefulness of mechanical characterisation of such systems where substrate effects on the measurements will be difficult to mitigate. The coatings produced will be characterised in order to show the range of coating properties which can be produced on non-conductive polymer substrates using the novel MW-PECVD process.

Chapter 3. Experimental Methodology

3.1 Introduction

This chapter describes the methods employed to undertake the experimental work for this thesis. The techniques used to deposit coatings onto polymers are described, which include DC sputtering and PECVD, followed by analysis of the coatings. The analysis will be covered in two parts; the first relating to the chemical composition and structure, and the second relating to the mechanical properties.

3.2 Methods of Coating Deposition

All coating work undertaken for this thesis (except for SEM sample preparation) was carried out on a Hauzer Flexicoat 850 coating system situated in the Advanced Coatings Laboratory at the University of Leeds. A schematic of the system can be seen in Figure 3-1. The machine is a modular system containing power supply, electrical distribution, control, and pneumatic/hydraulic hardware cabinets. In the configuration used throughout this work the deposition chamber was equipped with two 600 x 50 mm sputtering targets, three circular arc evaporation targets, and two 1200W microwave antennae installed in parabolic reflectors. An additional remote plasma source consisting of a copper anode and tungsten cathode wire with a maximum current of 200A was also installed.

The two sputtering targets could be operated in DC, pulsed DC, and High Power Impulse Magnetron Sputtering (HiPIMS) modes. It is generally accepted that in order to produce a high quality, hard coating, biasing of the substrate is necessary. As the polymer substrates used were insulating, these sputtering methods were not investigated and further discussion is beyond the scope of the work presented in the following chapters. The two main coating techniques used to deposit coatings onto polymer substrates in this body of work are both based on PECVD.

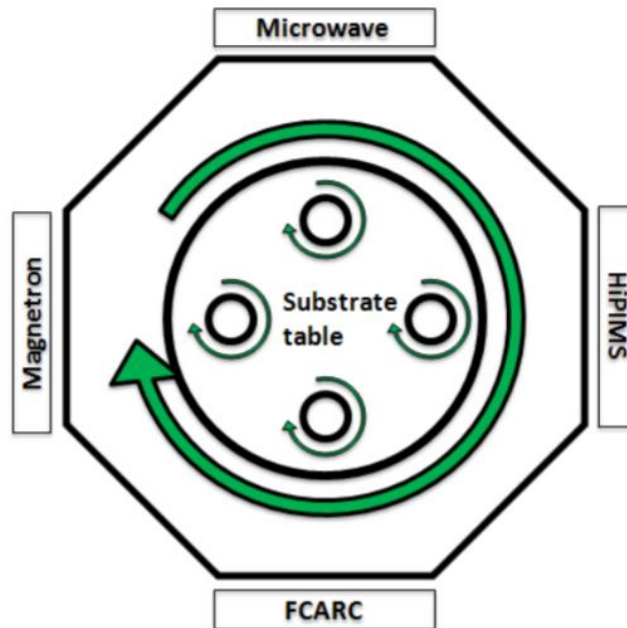


Figure 3-1 - Schematic of the deposition chamber layout in the Hauzer Flexicoat 850 PVD system.

3.2.1 Substrate Materials and Preparation

Table 3-1 and Table 3-2 give details of a range of common thermoplastic polymers in use in industrial applications ranging from semi-conductor manufacture through to automotive heat shielding. In order to determine the suitability of different polymers to the conditions inside the vacuum chamber during deposition a selection of these polymers were prepared and coated with a thin ($<1\mu\text{m}$) sputtered Cr coating and PECVD a-C:H coating. The observation of these samples was then used to reduce the number of substrate materials to a temperature resistant and thermally sensitive example.

The majority of the polymers selected have low water absorption and low outgassing. This is a recommendation for use with ultra-high vacuum pumps and equipment which relies on ultra-high vacuum. Outgassing of the samples will affect the chemical composition and pressure of the plasma during deposition and to minimize this, material selection was the simplest method. The polymers that exhibit higher levels of outgassing and water absorption will be suitable for use for this application and using our equipment.

The large volume of the deposition chamber used and small volume of sample will minimize gas contamination.

Table 3-1 - General properties of polymers in relation to suitability for vacuum plasma coating.

Abbrev.	Name	Glass Transition (°C)	Thermal Conductivity (W/mK)	Thermal Expansion (µm/mK)	Young's Modulus (GPa)	Hardness (Rockwell R)
PTFE, molded	Polytetrafluoroethylene	323	0.261	107	0.556	58.7
PI	Polyimide	309	0.243	33	5.98	126
PSU	Polysulfone	215	0.285	42.8	5.56	122
PEI	Polyetherimide	208	0.32	39	6.83	121
PP, molded	Polypropylene	159	0.254	114	1.71	95.7
PEEK, unreinforced	Polyetheretherketone	144	0.261	49.9	4.52	124
ABS, moulded	Acrylonitrile-butadiene-styrene	107	0.179	79.9	2.3	107
N66	Polyamide 6,6	50	0.25	90	3.6	155

Table 3-2 - General properties of polymers (cont.). The examples of coating found in the literature are not exhaustive and are intended only to demonstrate that hard coating materials have been deposited using PVD methods.

Abbrev.	Water Absorption (% mass)	Outgassing (<1% weight loss)	Coated in Literature	Adhesion	Coating
PTFE	0.0064	Y	Y	?	Ti, Ta, Nitrides
PI	0.454	Y	Y	2.2-3.8MPa	TiN/Cu
PSU	0.352	Y	Y	Y/N	Ti, TiN/Nb, Zr, Nitrides
PEI	0.269	N	Y	?	
PP	0.0714	Y	Y	3-6Mpa	Cu/Cr
PEEK	0.198	Y	Y	Y	Cu/Ti/TiN
ABS	0.402	Y	Y	Y	Cu/Ti/Al/Cr
N66	0.7	N	Y	?	Ti, Zr

The ABS polymer and PEI polymer thermoplastics were supplied by RS Pro and Goodfellow Cambridge respectively. The nominal properties of the supplied sheet are shown in Table 3-3.

Table 3-3 – Nominal properties of substrate materials as provided by supplier.

Polymer	ABS	PEI
Elastic Modulus	2.4 GPa	2.9 GPa
Elongation at break	20%	60%
Tensile Strength	50 MPa	85 MPa
Water Absorption (/24 hrs)	0.3%	0.25%
Thermal Conductivity	0.17 W/mK	0.22 W/mK
Thermal Expansion Coefficient	$8 \times 10^{-5} \text{ K}^{-1}$	$5.6 \times 10^{-5} \text{ K}^{-1}$
Maximum Operating Temp.	75 °C	170 – 200 °C

3.2.1.1 Sample Preparation

All samples underwent a three stage cleaning process; the first involving a chemical cleaning agent, and the final two under vacuum in the deposition chamber.

The first step is intended to remove the bulk of any organic oils or particle contamination on the substrate surface deposited by manufacturing, storing or handling procedures. A suitable solvent of high volatility, which would not degrade or damage the polymer surface and would evaporate quickly in order not to attract dust, was chosen. Isopropyl alcohol was used on lint free tissue to wipe down the sample surfaces before mounting in the deposition chamber using Kapton tape. The samples would then undergo a period of vacuum storage at high vacuum in the deposition chamber in order to outgas. Following the outgassing, the substrate surfaces would be subjected to Ar⁺ ion bombardment to atomically clean any remaining surface contaminants. The duration of the ion bombardment would depend on the deposition process to be carried out.

3.2.2 PECVD

PECVD, as explained in Chapter 2, utilises a high voltage potential across a working gas to ignite and sustain a plasma. The bias voltage in the Hauzer Flexicoat 850 deposition system is applied through the substrate holder. In the case of electrically conductive

substrate materials, this results in positive ions within the plasma accelerating towards the substrate, giving a densified coating with improved mechanical performance. In the case of electrical insulators, such as the polymers used in this study, the plasma characteristics around the cathode become more complex.

The inability of the substrate to allow a current to pass through will reduce the charge effects on the species within the plasma, as no electrostatic attraction will occur between the positive ions and the substrate. Any ions which come into contact with the substrate surface will be doing so at reduced energies, giving reduced surface mobility of species, ultimately leading to a reduction in coating properties compared to a metallic substrate under the same conditions.

For this reason, the PECVD deposition method was carried out but not fully characterised. A limited range of coating properties would be achievable due to a limited process envelope, and the growth rate of the film would be greatly reduced compared to the MW-PECVD method. DLC coatings produced using the PECVD method were included for analysis by ERDA.

3.2.3 MW-PECVD

The focus of this study was the characterisation of coatings produced using a novel MW-PECVD method. Two remote microwave antennae (2.45 GHz) mounted within stainless steel parabolic reflectors to direct the plasma into a quasi-parallel beam are used to input energy into the working gas at up to 1.2 kW each. The antennae are made from silver plated brass tube and overheating of the components is prevented by a combination of air cooling in the centre of the antennae and water cooling in the reflector. The antennae are protected by vacuum sealed quartz tubes with both a fixed and removable ceramic sheath to facilitate cleaning of the equipment.

The substrate table is used to both mount the substrates within the deposition chamber and also to move the substrate with respect to the plasma source in order to improve coating uniformity of batch to batch processing. Two-fold rotation of the substrates was

used throughout the coating work contained within this thesis to simulate the properties and deposition rates achievable within a scaled-up production. During deposition the substrate table is able to be biased using a voltage supplied through a DC power supply; the supply can be constant, pulsed, and bi-polar pulsed. As mentioned previously, biasing electrically insulating substrates has no effect and was not used during this study. Only the self-bias of the plasma was present in order to accelerate positive species towards the substrates. The self-bias was not measured due to limitations of the machine software/hardware.

A design of experiments (DOE) approach was chosen to characterise the process in order to economise on experiments required, and therefore the number of samples requiring analysis in order to determine the effects of varying deposition conditions on the properties of the resultant coating. The reduction in the number of experiments required to characterise the process is brought about by the ability to vary more than one input factor at a time compared to a conventional approach of varying one input factor at a time. DOE requires that each input is independent of the others; due to the operation of the Hauzer Flexicoat 850, the input factors were not entirely independent.

To maintain vacuum in the deposition chamber a constant pump speed is maintained; the pump speed can be controlled based on coarse adjustment of pump speed by selection of discrete fractions of full speed (33%, 66%, and 100%). These speeds are determined by the manufacturer in order to allow pressures in the chamber to be reached that allow a stable plasma to be ignited based on the power input, input of working gases and chamber geometry for a given process. To control the pressure, the flow rate of the working gas mixture must be adjusted. The working gases are introduced to the deposition chamber by a metered volumetric flow rate (SCCM), therefore the input factors of flow rate of the working gases and working pressure are interdependent. To mitigate this effect, the flow rate ratio of acetylene and argon introduced into the chamber was determined and used in further analysis. As the flow rate of the gases is controlled

volumetrically, the partial pressure of the gas species in the mixture can be assumed to be constant if the gas mixture is assumed to behave as an ideal gas.

For the design of experiments (DOE) approach used to characterize the process, the first step was to define the design space. This was achieved by running the machine without substrates, and using a trial and error approach, modifying parameters until the plasma would extinguish. The parameters changed were the gas ratio (C_2H_2 & Ar), MW power, and working pressure. The extreme limits of the combination of these settings were found, with respect to maintaining a stable discharge by monitoring light emission within the chamber, and this design space was used to populate the experiments.

Table 3-4 shows the deposition conditions that were to be used to deposit the 10 coatings for investigation in this thesis. The design point distribution used to model the process was provided by Proctor & Gamble Quantitative Sciences, Greater London Innovation Centre, UK. The aim of utilising this model was to gain the most information possible on cause and effect of coating properties, with respect to the deposition conditions used to produce the coating. This would be a more efficient approach to allow mechanical characterization of the design space, than a conventional approach where one parameter is varied at a time.

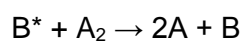
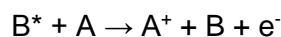
In practice the extremes of the design space were unachievable with regards to maintaining a stable plasma for film deposition. Factors affecting the long term stability of the plasma were deemed to be variability of the gas flow and chamber condition with respect to surface conductivity. As such the deposition conditions for the model were modified to account for what was achievable; the details of deposition conditions for each leg of the DOE are shown in Table 3-5.

Table 3-4 - Proposed DOE parameters for a 10 leg model.

Leg	Microwave Power (W)	Working Pressure (mbar)	Gas flow rate ratio (Ar & C₂H₂) (C₂H₂%)
1	900	0.013	100
2	1050	0.011	100
3	900	0.009	100
4	1050	0.009	10
5	1200	0.009	73.9
6	1200	0.011	10
7	1200	0.013	100
8	900	0.013	10
9	900	0.011	55
10	1050	0.013	55

The governing factors for a stable plasma are mean free path of the species and the energy of those species. The lowest MW powers could not be used to sustain a glow discharge when the pressure was at the lowest setpoint, and the working gas constituted of only acetylene. To combat this, the lowest MW power used was raised to 1050W, the working pressures remained the same, but the partial pressure of acetylene was reduced. The amount of acetylene was diluted with argon, a heavy monatomic gas with low ionisation energy, in order to reduce the ionisation energy of the gas mixture as a whole.

The reduction of the ionisation energy of the gas mixture can be partially attributed to Penning ionisation and excitation. This is the ionisation or excitation of an atom or molecule by the transfer of the excitation energy from a metastable atom. This mechanism can occur when the excitation energy of the metastable atom is greater than the excitation or ionisation energy of the target atom/molecule. When a metastable species collides with a neutral species the metastable species will transfer the excess energy to the neutral species causing ionisation or dissociation:



In the case of a gas mixture of acetylene and argon, the excited states of argon are in the range of 11.55 – 14.30 eV [120], whereas the ionisation energy of acetylene is less than this, at 11.40 eV [121]. Collision probabilities are expressed in terms of a cross section, which is a measure of the area that a species occupies. For argon, as the excitation energy increases so does the cross section [122], meaning that as the excitation energy increases, so does the probability of a collision occurring. Thus, in a gas mixture where excited states of one species are above the ionisation energy of other species, Penning interactions become an important mechanism for ionisation of the mixture, effectively increasing the number of free electrons available for electron ionisation through the increased probability of impact ionisation between the two species in the gas mixture.

Recombination and three body recombination serve to bring the ionisation of the mixture to an equilibrium state under given parameters:



Where \rightarrow denotes an increase of energy gained through the inelastic collision. In the case of a gas mixture with more than one species, dilution of the mixture with species with lower cross section will serve to decrease the probability of collisions without affecting system energy. Therefore, the addition of species with lower ionisation energy and smaller cross section will serve to create more free electrons with a reduced recombination rate, serving to increase the ionisation rate for a given energy input.

In the case of acetylene plasmas, the ionisation energy of 11.40 eV applies to the first ions created, however further energy input in the range of 17.22 – 25.60 eV [121] is required in order for other monatomic and molecular ions to appear. The increased energy demand to create further charged species and free electrons within the single

species gas leads to a low ionisation rate compared to that of a monatomic gas, such as argon.

In combination with the dilution of pure acetylene, the lowest concentration of acetylene was increased in order to ensure a visible film was grown that would allow direct measurement of the mechanical properties as deposited. As the distance of the extreme points of the design space were now reduced, intermediate design points were redistributed in order to provide a representative spread of the new design space.

Table 3-5 - Actual Deposition parameters for 10 leg DOE design.

Leg	Microwave Power Setpoint (W)	Microwave Power (Actual) (W)	Working Pressure (mbar)	Gas flow rate ratio (Ar & C₂H₂) (C₂H₂%)	C₂H₂ Partial Pressure (mbar)
1	1050	1032	0.012	94	0.0113
2	1100	1087	0.011	92	0.0101
3	1050	1032	0.011	85	0.0094
4	1100	1087	0.009	40	0.0036
5	1200	1178	0.009	74	0.0067
6	1200	1178	0.011	42	0.0046
7	1200	1178	0.011	91	0.0100
8	1050	1032	0.013	43	0.0056
9	1050	1032	0.011	66	0.0073
10	1100	1087	0.013	67	0.0087

Figure 3-2 and Table 3-6 illustrate the output of the DOE analysis. The interaction profile (Figure 3-2) shows how possible interactions will have an effect on the response of the model; in this case the heating rate. In each plot, all possible interactions are shown. The x-axis scales belong to the factor in that column (for example the first column is MW Power Setpoint (W)), and the annotated plot values belong to the factor in the same row, for example the first row, with 1050 and 1200 annotated line plots are relating to MW Power). In these interaction profiles, the most important observation is that of the gradients of the lines. Where the gradient of the two lines in a subplot are similar, there is likely to be no interaction, however, if the gradient is dissimilar then there is a likelihood

that an interaction effect is present. In the example, the lower centre subplot shows a possible interaction effect between working pressure and gas flow rate ratio on the response of heating rate. This effect is logical as the pressure and gas flow rate define the ionisation rate of the working gas mixture, which is then used as a medium to transfer energy to the substrate.

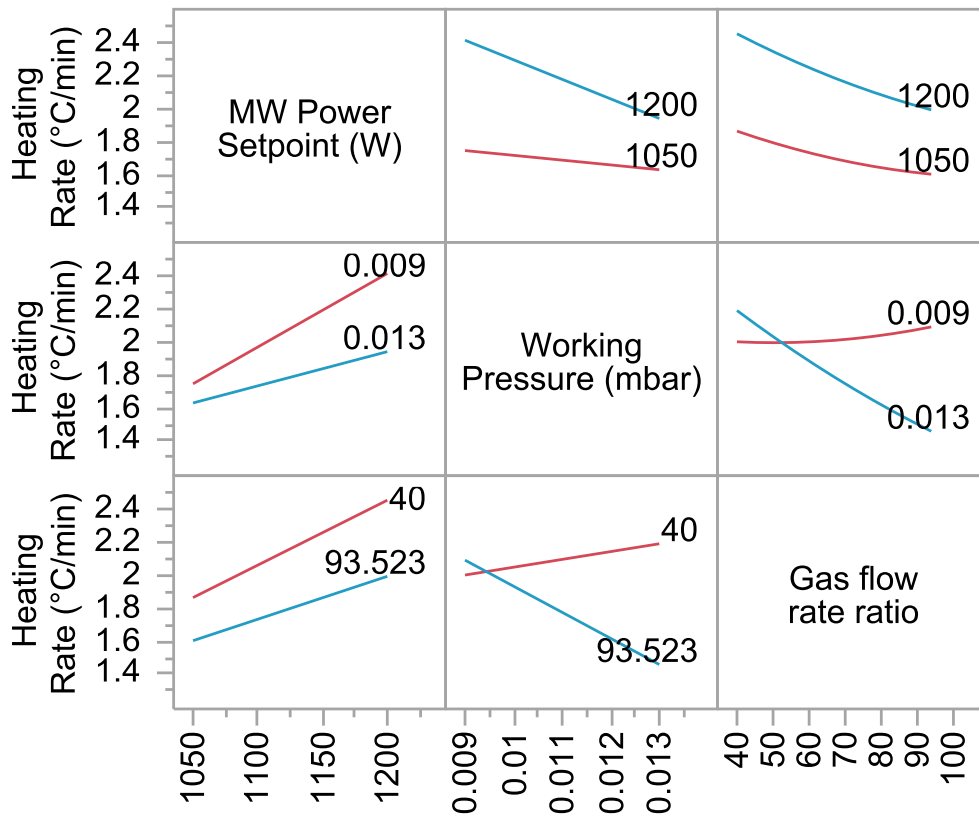


Figure 3-2 - Example of interaction profile produced from DOE analysis.

If a possible interaction exists, the main effect plot (Table 3-6) must then be used to determine the probability of this interaction existing. The main effects of the model are ranked in order of probability; the most influence on the outcome of the process will be from the first factor in the plot, in this case MW power. The bar chart included in the table gives a visual representation of the importance of each factor on the model response, using a log scale. The blue line in this plot represents a value of 2, equal to a p-value of 0.01 ($-\log_{10}(0.01)$). Therefore any bar (or log worth value) exceeding 2 can be said to have a significant effect on the model with a 99% confidence interval. If this is not the case then the p-values and log worth values must be examined more closely. A p-value

of 0.05 and log worth value of 1.3 both correspond to a confidence interval of 95%; that is, there is a 95% chance that the effect of the factor or interaction on the model response is real. The log worth ranking shown in the table can be used to rank the effects in order of significance of the effect of varying the factor on the response of the model. Further information from the statistical models presented in Chapter 4 and Chapter 6 can be found in Appendix B.

Table 3-6 - Example of Main effects plot output from DOE analysis.

Source	Log Worth	P-Value
MW Power set point (W)	1.394	0.04037
Gas flow rate ratio	1.091	0.08109
Working Pressure (mbar)*Gas flow rate ratio	0.610	0.24549
Working Pressure (mbar)	0.562	0.27447 ^
MW Power set point (W)*Gas flow rate ratio	0.307	0.49318
MW Power set point (W)*Working Pressure (mbar)	0.299	0.50272
Gas flow rate ratio*Gas flow rate ratio	0.134	0.73439

3.3 Chemical & Structural Analysis

3.3.1 Deposition Rate & Surface Roughness

White light interferometry is a non-contact profilometry technique. By combining light waves from a source and the same light source reflected from a specimen surface it is possible to deduce the surface morphology of the specimen due to constructive and destructive wavelength superposition.

A Bruker NPFLEX interferometer was used to determine the coating thickness and surface roughness of the substrates and MW-PECVD coatings. To determine coating thickness, a small area of the sample surface was masked using polyimide (Kapton) self-adhesive tape. Following deposition of the coating the tape was removed to show the bare substrate and cleaned with heptane to remove any residual adhesive without damaging either the substrate or coating. A scan of the surface using interferometry was carried out on the sample and a line profile of the sample was used to determine the

coating thickness from the step change in height of the two material surfaces. A scan of a larger area of the masked area, and the coated area of the sample was then used to determine average surface roughness.

Using Bruker vision64 software, data filtering techniques were used to improve the quality of the data before measurements were taken. Interferometry techniques are limited by shadowing effects whereby surface asperities will block light from reflecting off the surface depending on the angle of the incoming light. In these cases the surface scan would result in 'missing data', which was rectified by using the data restore interpolation function. The terms removal (F operator) filter was used on all samples to remove tilt and curvature of the sample surface. Selection of the optimum input area and algorithm (spherical, cylindrical, tilt only, etc.) was determined for each sample individually.

3.3.2 Structural Characterisation

A Hitachi SU8230 scanning electron microscope was used to examine sample surfaces and freeze fractured cross sections of the coatings produced. Typically, electrons are emitted from an electron gun by thermionic or field emission. This stream of electrons is accelerated, under vacuum, towards and through an aperture in an anode. The beam is then focussed through magnetic condenser lenses and objective lenses are used to focus the beam to a fine spot diameter which is directed over the sample surface.

Two main types of interaction occur between the electrons from the incoming beam and the sample; backscattering and secondary emission. Backscattered electrons occur due to electrostatic attraction between the negatively charged free electron and the positive nucleus of atoms within the surface of the sample. The elastic collision between the two species, known as Rutherford scattering, can cause the electron to escape the surface allowing them to be detected. Secondary electrons are emitted from the atoms of the sample under examination due to interactions between these and the incoming free electrons.

Charging effects on the sample surface will introduce unwanted noise into the signal used to image the surface and so samples must be conductive to produce the best results. The non-conductive samples consisting of polymer substrates and MW-PECVD DLC coatings were prepared for analysis in order to avoid these surface charging effects. The samples were mounted on metallic holders using self-adhesive carbon pads, with carbon gel applied to the sample edges to create a conductive path from the surface to the sample holder. A carbon coating (~3nm) was then evaporated onto the sample to allow surface charges to dissipate through the sample holder.

Conventional conductive materials can be milled using a focussed ion beam to produce images of the cross section. The nonconductive nature of the substrate, combined with poor thermal properties, meant this method would likely give poor results. A mechanical method was instead employed utilising the embrittlement of polymers at low temperatures to allow the samples to be fractured when exposed to liquid nitrogen. A slit was first cut into the sample using a small saw to create a weak point from which the crack would propagate. The samples were then dipped into liquid nitrogen before being secured in a vice with a protective wrapping and snapped to produce two exposed faces. These samples were then prepared for loading into the SEM chamber as described above.

3.3.3 Chemical Composition and Bonding Characterisation

3.3.3.1 Nuclear Magnetic Resonance (NMR) Spectroscopy

NMR techniques utilise the phenomenon in which atomic nuclei absorb and re-emit electromagnetic radiation when exposed to a magnetic field. Solid-state NMR uses this to characterize solid materials based on anisotropic interactions of isotopes with an odd number of protons (e.g. ^{13}C & ^1H). The analysis of ^{13}C isotopes can be used to quantitatively determine the bonding state of the carbon within the sample; in other words, determine the sp^2/sp^3 ratio of the DLC coating. The advantage of using solid state NMR techniques compared to others, such as RAMAN and EELS (Electron Energy

Loss Spectroscopy) is the analysis of a bulk sample (>100 mg) compared to drastically smaller areas of thin cross sections (vs. EELS), and direct excitation of the carbon species under investigation (vs. RAMAN).

Solid state NMR spectroscopy was carried out using a Bruker Avance III HD spectrometer at the EPSRC UK National Solid-state NMR Service at Durham University, UK. Analysis was carried out as in [95], at 100.63 MHz for ^{13}C with a double-tuning probehead and using the magic-angle spinning technique with sample rotation frequency of 10 kHz. The chemical shifts were determined relative to carbon and tetramethylsilane.

In order to analyse the coating using this technique, it was necessary to remove the coating from the substrate to not include substrate material analysis in the results. Coatings were produced on aluminium foil, instead of on a polymeric substrate, using the same deposition conditions as for deposition on the ABS/PEI substrates. This foil was then dissolved in HCl solution over 2hrs to leave flakes of the coating. The flake like products were filtered from the solution, washed in deionised water and left to dry at room temperature for 48hrs. The destructive nature of this sample preparation technique is negated as the solid-state NMR technique provides information on the 2-3 atoms from the irradiated nuclei and only the top surface of the films (~3-5nm) is affected by the process [95]. In this specific case, the films may differ due to deposition on a non-conductive and conductive substrate. It is assumed that the self-bias of the plasma will remain at similar levels between the substrates and the NMR results will be indicative of the composition when deposited onto polymeric, non-conductive, substrate materials.

3.3.3.2 Ion Beam Analysis (IBA)

In order to determine the ratio of carbon to hydrogen contained within the films IBA was utilised to directly measure these species. IBA is a collective term for multiple, complementary techniques, all based on exposing the sample to a beam of accelerated, focussed ion bombardment.

The work in this thesis was carried out at the Ion Beam Centre, University of Surrey, UK, using a $^4\text{He}^+$ beam at 1.5 MeV from a 2 MV Tandatron accelerator (High Voltage Engineering Europe). Rutherford Backscattering Spectrometry (RBS) and elastic recoil detection (ERD) were used together to allow hydrogen content to be determined. The ERD signal from one detector is interpreted relative to the RBS detector. Samples were gold coated ($\sim 3\text{nm}$) prior to analysis to avoid surface charging effects.

3.3.3.3 Raman spectroscopy

The coatings produced using the MW-PECVD technique were analysed using Raman spectroscopy in order to estimate the sp^2/sp^3 ratio of the carbon structure. The samples were exposed to a 488 cm^{-1} laser mounted in a Renishaw InVia Raman microscope. The high energy of the laser source could easily damage the sample, resulting in erroneous data, therefore the exposure of each sample was controlled. The laser power was fixed at 1% of maximum output, and spectrum data accumulated over 5 exposures of 5 seconds. The laser source used had a power output of 16mW, however maximum power at the sample is reduced to 10mW due to optical packages used to focus the beam. The actual power of the beam will be less than the quoted (percentage of) maximum due to natural degradation of the source over time.

3.4 Mechanical Properties

3.4.1 Hardness, Young's Modulus, & P/S²

Nanoindentation tests were performed using a Micromaterials Nanotest platform equipped with a Berkovich tip. Indentations were made at depths in the range of 1% to 200% of the film thickness to determine how the depth of indentation of the coated polymers influenced the measurement due to substrate effects.

Hardness (H) and reduced modulus (E_r) were determined using the Oliver and Pharr method [59]. Hardness was calculated using the classical definition

$$H = P/A', \quad [\text{eqn. 3.1}]$$

where P is the load, and A' is the projected contact area of the indenter tip calculated from the measured depth. Reduced Modulus was determined using a power law fitting method from the unloading curve. The Young's modulus of the material being measured can then be determined using

$$\frac{1}{E_r} = \frac{(1 - \nu^2)}{E} + \frac{(1 - \nu_i^2)}{E_i} \quad [\text{eqn 3.2}]$$

Where E_r is the reduced modulus, ν_i and E_i are the Poisson's ratio and modulus of the indenter tip respectively, and ν and E are the Poisson's ratio and modulus of the sample. The diamond Berkovich indenter tip was assumed to have $E_i=1141$ GPa and $\nu_i=0.07$.

In cases where indentations are made on materials with Young's modulus orders of magnitude less than that of the diamond indenter, the indenter can be assumed to be rigid. On more ductile materials, the indented material terms become larger, whereas the indenter terms remain the same, giving rise to a reduced effect. This allows removal of the indenter terms from eqn 3.2, leaving:

$$\frac{1}{E_r} = \frac{(1 - \nu^2)}{E} \quad [\text{eqn 3.3}]$$

For all calculations in this thesis, the Poisson's ratio of the surface was assumed to be 0.35.

Loads were applied using a constant loading rate of 0.1mN/min and unloading rate of 0.01mN/min. Loading rates were chosen to reduce any viscoelastic effects of the polymer substrate, with a dwell time of 20s to allow elastic relaxation of the coated sample before unloading.

P/S^2 was calculated from the maximum load measured during each indentation (P), and the contact stiffness (S), which was determined from the gradient of the unloading curve between 50% and 80% of total indentation depth. An example of this is shown in Figure 3-3.

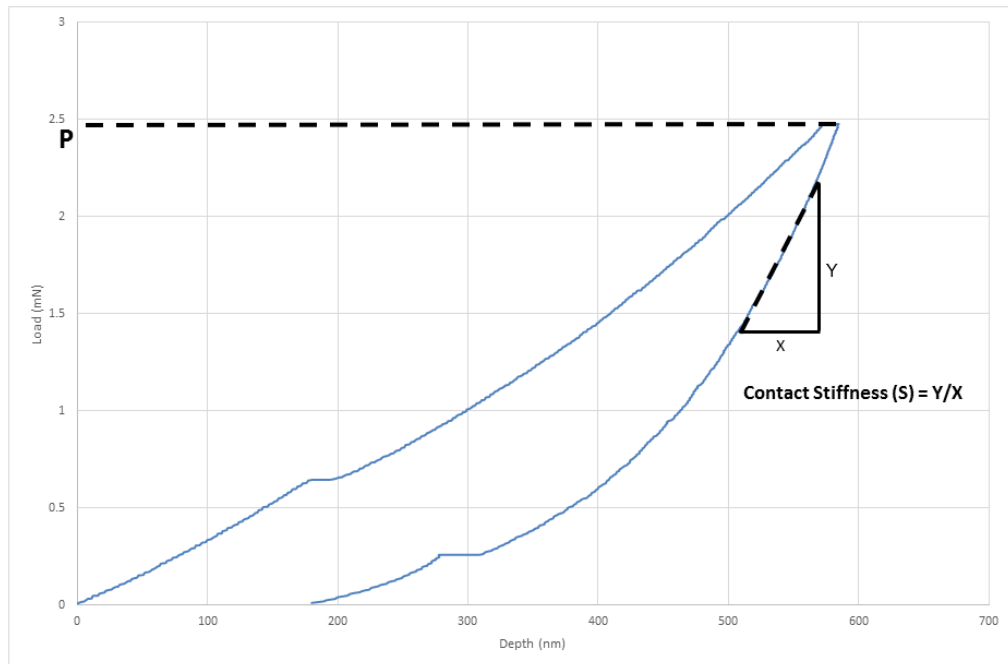


Figure 3-3 - Method of determining the parameters P and S from nanoindentation loading curves.

3.4.2 Coating Adhesion

Coating adhesion measurements were attempted by loading the coating sample directly and by indirect methods of testing the substrate without depositing the coating.

The scratch test was performed to determine the adhesion of the coating based on the appearance of cracks in the contact area with the scratch tip. Tests were performed using a Tribotechnic Macro Scratch Tester (Millennium 200) and a Rockwell C diamond tip with a 500 μm tip radius. Scratches were performed using a linear load in the range of 6 – 10 N. The scratch tracks were then examined to determine at which load the coating had failed. Tests were performed with a single load, varying the sliding speed in order to determine the effect of the viscoelastic response of the polymer on the scratch resistance of the coated surface. Sliding speeds of 0.5 – 15 mm/min were investigated.

The cross-hatch test, whereby a grid of squares are cut into the sample surface using a multi-bladed knife, and subsequently attempted to be pulled from the substrate using tape, was performed to qualitatively rank adhesion.

Contact angle goniometry was performed to quantify the wettability of plasma treated polymer surfaces as a proxy for the availability of dangling bonds to form strong chemical bonds with radicals in the plasma during coating nucleation. Ar⁺ species in a bombarding plasma would sputter surface contaminants, and potentially cleave hydrogen atoms from the molecular chains of the polymer. The yield of these so-called 'dangling bonds' would be a function of plasma power and duration of the exposure. Upon opening of the chamber and exposing the dangling bonds to moisture in the air, the formation of OH groups would occur giving increased polarity of the surface. The increased polarity would lead to an increase of surface energy that would be detectable by a reduction in the contact angle with water.

Table 3-7 - Classification of cross hatch results as given by Elcometer (based on ISO2409).

Description of Result	ISO Classification
The edges of the cuts are completely smooth, none of the squares of the lattice are detached.	0
Detachment of small flakes of the coating at the intersections of the cuts. A cross cut area no significantly greater than 5%, is affected.	1
The coating has flaked along the edges and/or at the intersections of the cuts. A cross cut area significantly greater than 5%, but not significantly greater than 15%, is affected.	2
The coating has flaked along the edges of the cuts partly or wholly in large ribbons, and/or it has flaked partly or wholly on different parts of the squares. A cross cut area significantly greater than 15%, but not significantly greater than 35%, is affected.	3
The coating has flaked along the edges of the cuts in large ribbons and/or some squares have detached partly or wholly. A cross cut area significantly greater than 35%, but not significantly greater than 65%, is affected.	4
Any degree of flaking that cannot be classified even by classification 4.	5

The Hauzer Flexicoat 850 tungsten filament plasma cathode source was used at maximum current (100 A) to produce plasmas using a 99.9% Argon gas feed at pressures in the range of 1×10^{-3} mbar - 10×10^{-3} mbar and for durations in the range of

180 – 660 s. The cross hatch test was used to determine if any difference in adhesion could be detected between a polymer sample exposed to plasma only during ignition of the DLC coating plasma and another polymer sample exposed to the plasma conditions and duration found to give the lowest contact angle with water.

Cross hatch tests were performed using an Elcometer 1542 adhesion tester using 2mm blade spacing. The multi-bladed knife was used to cut through the coating deposited onto a 50 x 50mm ABS plate of 1.6mm thickness. Tape was then pressed firmly onto the cut surface before peeling at an angle of 180° and rate to take approximately 2s to remove the tape from the sample. The tested samples were then observed under a microscope to determine the condition of the coating and any delamination that may have occurred. The classification of the results and the corresponding description of coating delamination is given in Table 3-7.

3.4.3 Tribology

A reciprocating pin on plate tribometer was used to determine the tribological performance of the coated polymers. A 10Hz frequency, 5mm stroke length and 10mm radius domed pin was used with 3mm thick 10 x 10mm coated polymer plates. A constant load of 8N was applied to all sample pairs. PAO base oil was used as a lubricant with the primary function of removing heat from the contact; initial tests showed frictional heat build-up in dry running conditions led to destruction of the polymer samples almost immediately upon starting the test. Contact pressure was not determined due to the uncertainty of the surface deformation due to elastic and plastic strains in both the coating and substrate.

Chapter 4. Film Deposition & Adhesion

4.1 Introduction

This chapter presents results pertaining to the deposition of the DLC films produced using the design of experiments and characterisation of film growth. Results of substrate heating, growth rate and thin film adhesion are presented.

4.2 Process characterisation

A design of experiments approach was used to characterise the MW-PECVD process and the coatings that could be produced. The design space was defined based on initial testing of parameters that were deemed feasible to sustain a stable plasma discharge; in reality the chosen set points for each parameter were not suitable and so the set points used deviated from those initially planned. The chosen parameters for a 10 leg experiment design, and the actual set points used are shown in Table 4-1.

Table 4-1 - Proposed and actual parameters used to deposit the DLC coatings.

Leg	PROPOSED			ACTUAL						
	MW Power (W)	Working Pressure (mbar)	Gas flow rate ratio (Ar & C ₂ H ₄) (%C ₂ H ₄)	MW Power (W)	Actual MW Power (W)	Working Pressure (mbar)	Gas flow rate ratio (Ar & C ₂ H ₂) (%C ₂ H ₂)	C ₂ H ₂ Flow rate (sccm)	Ar Flow rate (sccm)	Max Temp (°C)
1	900	0.013	100	1050	1032	0.012	94	722	50	70
2	1050	0.011	100	1100	1087	0.011	92	720	60	65
3	900	0.009	100	1050	1032	0.011	85	610	110	70
4	1050	0.009	10	1100	1087	0.009	40	200	300	70
5	1200	0.009	73.9	1200	1178	0.009	74	490	175	70
6	1200	0.011	10	1200	1178	0.011	42	250	350	70
7	1200	0.013	100	1200	1178	0.011	91	722	70	70
8	900	0.013	10	1050	1032	0.013	43	300	400	70
9	900	0.011	55	1050	1032	0.011	66	450	235	70
10	1050	0.013	55	1100	1087	0.013	67	520	260	70

The main points to note are that the minimum MW power of 900 W required increasing to 1050 W, and the maximum gas ratio of 100% resulted in instabilities during the process so this was reduced by introducing a small amount of argon to lower the ionisation energy

of the gas. The pressures were not always achievable due to restrictions in the maximum flow rate of C_2H_2 (722 sccm), so where applicable more argon was introduced to the mixture to increase pressure whilst maintaining the gas mixture ratios above 90% C_2H_2 . The combination of low power, pressure and high C_2H_2 % mixture meant that leg 3 was unstable; to allow deposition of a DLC film the pressure was increased using argon, leading to a reduction in C_2H_2 percentage, but the same partial pressure within the chamber.

4.2.1 Substrate Heating

During thin film deposition using the MW-PECVD process, substrates are subjected to ion bombardment from charged species that make up the plasma used for coating growth. This bombardment and subsequent film growth causes heating of the substrate due to energy transfer from the excited atoms/molecules to the substrate surface. Controlling the substrate temperature of thermally sensitive materials is important to ensure consistent quality of coatings through avoiding damage to the substrate.

The Hauzer Flexicoat 850 contains 4 thermocouples (2 static on the deposition chamber walls, and 2 on the rotating substrate table) that were used to measure the temperature of the chamber during processes. The two thermocouples located on the substrate table are positioned such that they are the same working distance from the cathodes and are subjected to the same rotational movement with respect to the cathodes, thus ensuring they experience the same heating as any substrates within the chamber. As discussed in Chapter 3, these thermocouples were used to record temperature evolution during the processes used to deposit the ten DLC coatings for the design of experiments.

Figure 4-1 shows an example of the temperature of the deposition chamber during the DLC deposition steps of the 10 processes; plots giving this data for the remaining 9 DOE coatings can be found in Appendix A. Each process was made up of multiple deposition steps to allow sufficient film thickness to develop, whilst maintaining a maximum temperature that would not damage the polymer substrates (as in [35]). The temperature

chosen was 70 °C due to the glass transition temperature of the most thermally sensitive substrate, ABS, being approximately in the range 80-125 °C depending on supplier and monomer mixture. A cooling step of 1hr was used to allow the deposition chamber and substrates to cool, allowing further deposition to take place.

Figure 4-2 shows the average heating rate of each process, calculated from the gradient of each deposition step. Each plot was given a linear fit, in the form $y=mx+c$, and error bars are the standard deviation of the three gradients used.

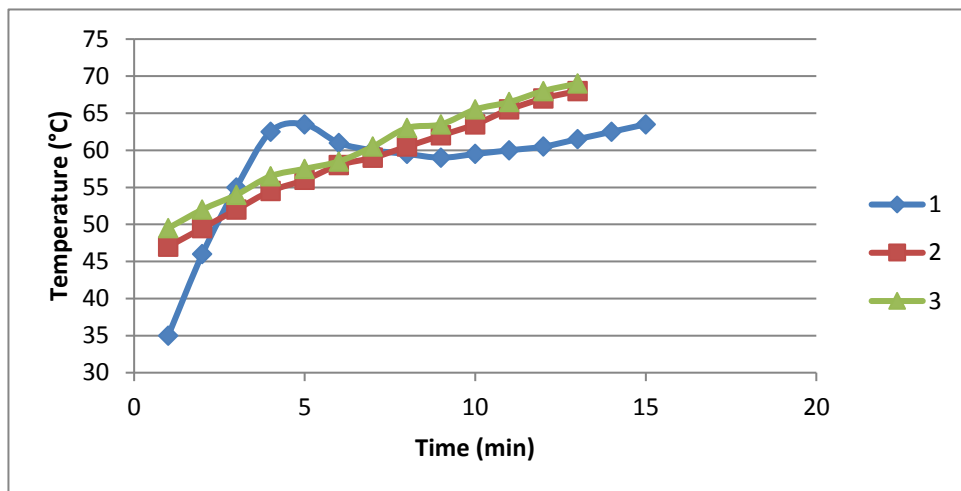


Figure 4-1 - Temperature evolution during leg 1 of DOE, with plots for each deposition step (1-3) made to deposit the coating.

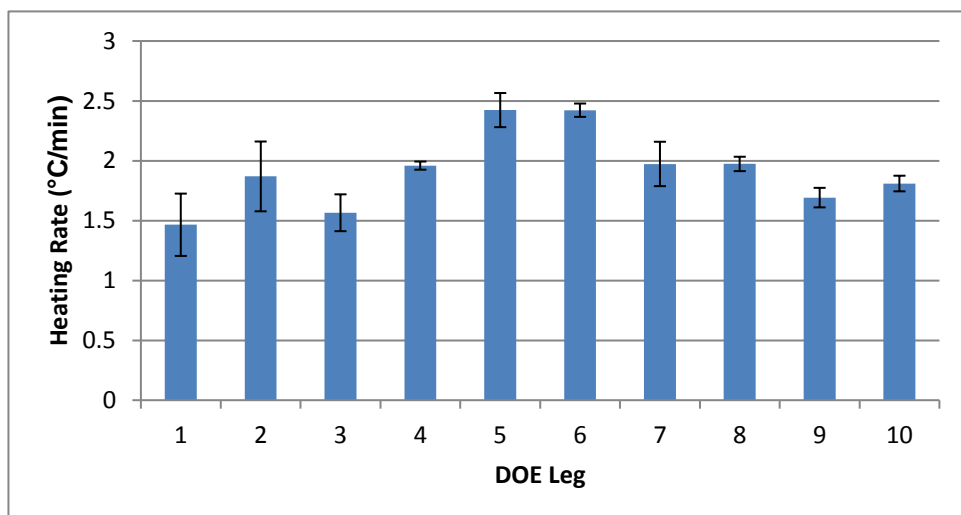


Figure 4-2 – Average heating rate of DLC deposition step from each DOE leg determined from rotating thermocouples located at the same working distance as substrates.

The heating rates of all legs are mostly linear. Where this is not the case, it can be attributed to difficulty of igniting the plasma at the beginning of the deposition step. If the machine does not detect plasma ignition, the process gases are not introduced and instead, only argon is introduced to the chamber. This results in an increase of pressure, meaning more particles are able to transfer energy to the substrate surface leading to an increase of heating rate. It can also be due to MW energy not being transferred to the gas mixture and instead to the substrates. Once the plasma is stable, the heating rate will become linear.

The highest average heating rate was found to be 2.42 °C/min for legs 5 & 6, whilst the lowest was leg 1, at 1.47 °C/min. However, due to the variability of the process, the error shows that most deposition conditions used produced similar heating rates. In practice, the small differences measured will have little impact on the optimisation of the process. Considering the difference of roughly 1 °C/min between the maximum and minimum heating rates, and that conditions inside the chamber lead to a starting temperature of roughly 40 °C with a permitted maximum temperature of 70 °C, the maximum deposition times will be between 16 – 26 minutes before overheating of the most temperature sensitive substrate.

4.2.1.1 Design of Experiments Model – Substrate Heating

A statistical model was fitted to the average heating rates shown in Figure 4-2 in order to determine the main effects of the process and to provide a prediction of heating rate within the design space. The main effects for the full model of all factors are shown in Table 4-2; a larger log worth indicates a more significant effect on the heating rate by varying that factor as explained in Chapter 3.

The factors are ordered from most significant to least significant, and the blue dashed line is equal to 2; this is calculated from the log of the p-value, in this case 0.01, giving a significance of 99%. As none of the bars pass the blue line, there are no factors with a significant effect on heating rate at a 99% trend level; this is evidenced by no p-values

being less than 0.01. However, MW power has a p-value of 0.04 and so it is significant at a 95% trend level, with gas flow rate ratio being significant to a 90% trend level. Reducing the confidence interval further would give main effects that are increasingly likely to not be real effects, therefore only these two are said to significantly affect heating rate.

Table 4-2 - Effect summary of DOE model for heating rate.








Source	Log Worth	P-Value
MW Power set point (W)	1.394 	0.04037
Gas flow rate ratio	1.091 	0.08109
Working Pressure (mbar)*Gas flow rate ratio	0.610 	0.24549
Working Pressure (mbar)	0.562 	0.27447 ^
MW Power set point (W)*Gas flow rate ratio	0.307 	0.49318
MW Power set point (W)*Working Pressure (mbar)	0.299 	0.50272
Gas flow rate ratio*Gas flow rate ratio	0.134 	0.73439

Figure 4-3 shows how the model predicts heating rate to vary as the factors are changed. The red and blue lines correspond to minimum and maximum set points for each factor respectively. The main effects summary shows that MW power has the most effect, followed by gas flow rate ratio, which is shown in the interaction profile by steeper gradients where these factors are involved. The main finding from the model is that as MW power is increased, or C₂H₂ percentage is decreased, the heating rate increases. Generally, if increased C₂H₂ percentages are used, heating rates will be equal to or lower than when the least C₂H₂ is used, and if MW power is decreased, this will always result in decreased heating rate. The interaction profile shows a potential interaction between working pressure and gas flow rate ratio, however, the corresponding p-value is too low to confirm this as a likely effect.

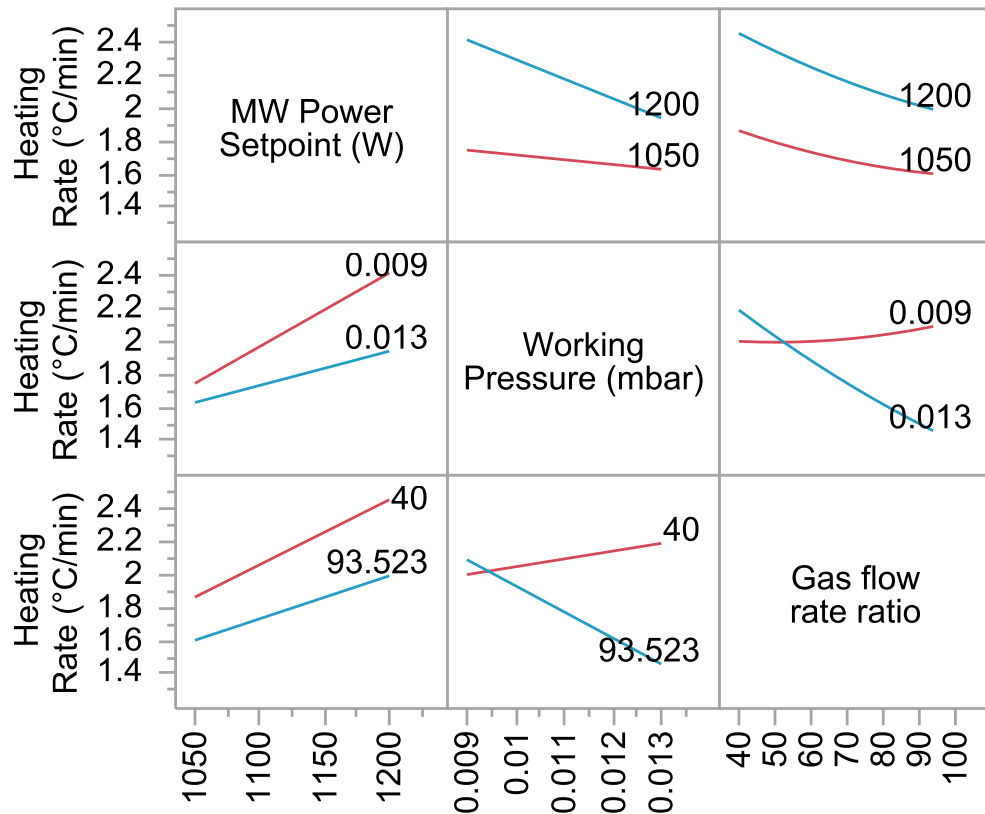


Figure 4-3 - Interaction profiles of full model for factor effect on heating rate.

4.2.2 Deposition Rate

Deposition rate of the process was determined by measuring the step height of the coating from an area of the substrate that was masked during deposition; details can be found in Chapter 3. Coating thickness of the ten coatings produced on two polymer substrates, ABS and PEI, are shown in Figure 4-4. Figure 4-5 shows the deposition rates based on the measured coating thickness and total time of deposition for the ten coatings on the two substrates.

The coating thickness varies from roughly 2 μ m in legs 4 and 6, to just over 5 μ m in leg 7, for both substrate materials. The variation of coating thickness between the substrate materials is within measurement error for most legs, and there is no trend with regards to one substrate material having thicker coatings produced versus the other.

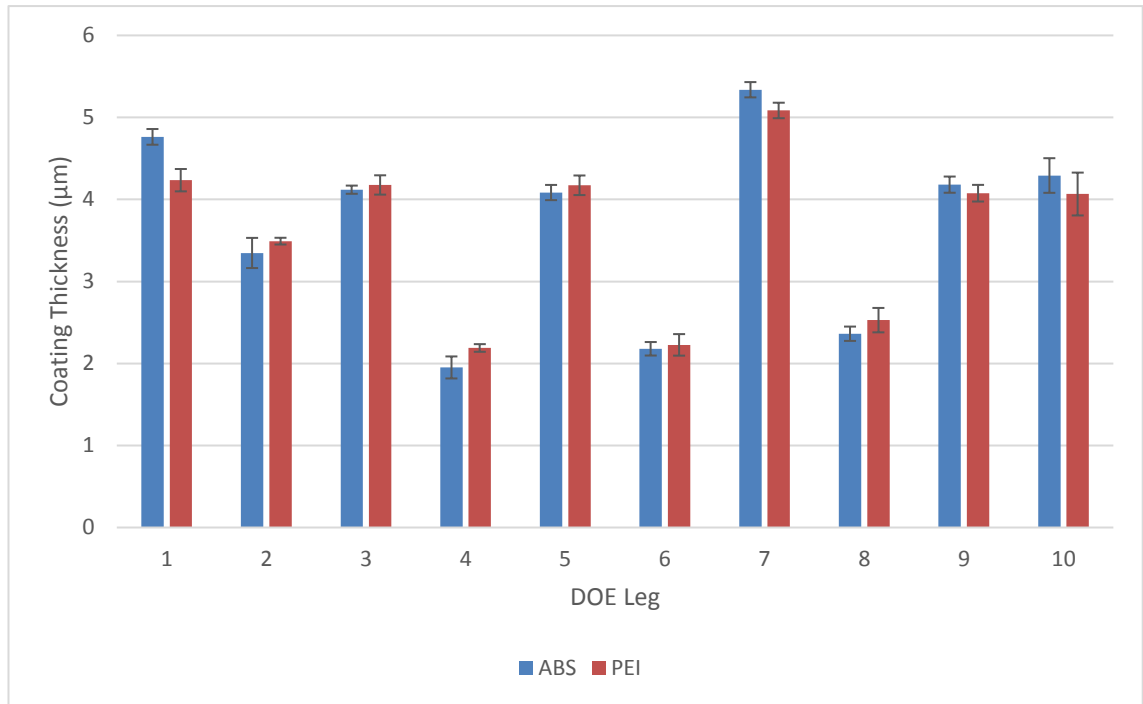


Figure 4-4 - Coating thickness of ten coatings produced for DOE.

The deposition times for each leg were different due to the need to avoid overheating the substrate and so the rates do not match the coating thickness. The lowest deposition rate was roughly 2.5 µm/hr in leg 4 whereas the highest was in leg 7, at roughly 7 µm/hr. As with coating thickness, there is no significant variation between deposition rates measured on the two substrate materials.

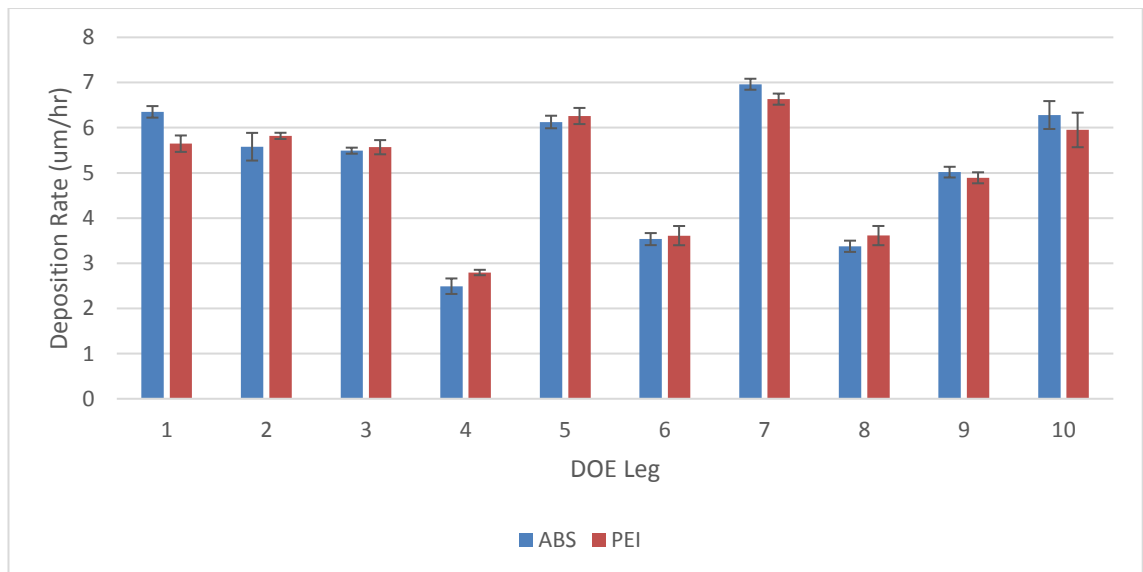









Figure 4-5 - Deposition rate of ten coatings produced for DOE.

4.2.2.1 Design of Experiments Model – Deposition Rate

4.2.2.1.1 ABS Substrate

A model was fitted to the average deposition rates shown in Figure 4-5 in order to determine the main effects of the process and to provide a prediction of deposition rate within the design space; the main effects are shown in Table 4-3.

Table 4-3 - Effect summary of DOE model for deposition rate on ABS substrate.

Source	Log Worth		P-Value
Gas flow rate ratio	2.377		0.00420
Gas flow rate ratio*Gas flow rate ratio	1.721		0.01901
MW Power set point (W)	1.672		0.02130
Working Pressure (mbar)	1.600		0.02514
Working Pressure (mbar)*Gas flow rate ratio	1.158		0.06955
MW Power set point (W)*Working Pressure (mbar)	0.931		0.11718
MW Power set point (W)*Gas flow rate ratio	0.638		0.23003

As in section 4.2.1.1, the blue line represents a confidence interval of 99%. The most influential factor for deposition rate is the gas flow rate ratio, with all three main factors of gas ratio, pressure, and MW power being significant at a 95% level.

The separation of the red and blue lines in the bottom row of plots in Figure 4-6 shows the significant effect of altering gas flow rate ratio on the deposition rate. At low gas ratios of 40%, the deposition rate remains almost constant despite changes in MW power and pressure.

Comparing the gradient of the gas ratio-pressure and gas ratio-MW power plots it can be seen that an increase of MW power does not have as significant an effect as increasing pressure. From this it can be summarised that the partial pressure of C₂H₂ is a significant factor in determining deposition rate, and that as the partial pressure increases, so does the deposition rate. High p-values indicate that any potential interactions are likely to not be real, or insignificant.

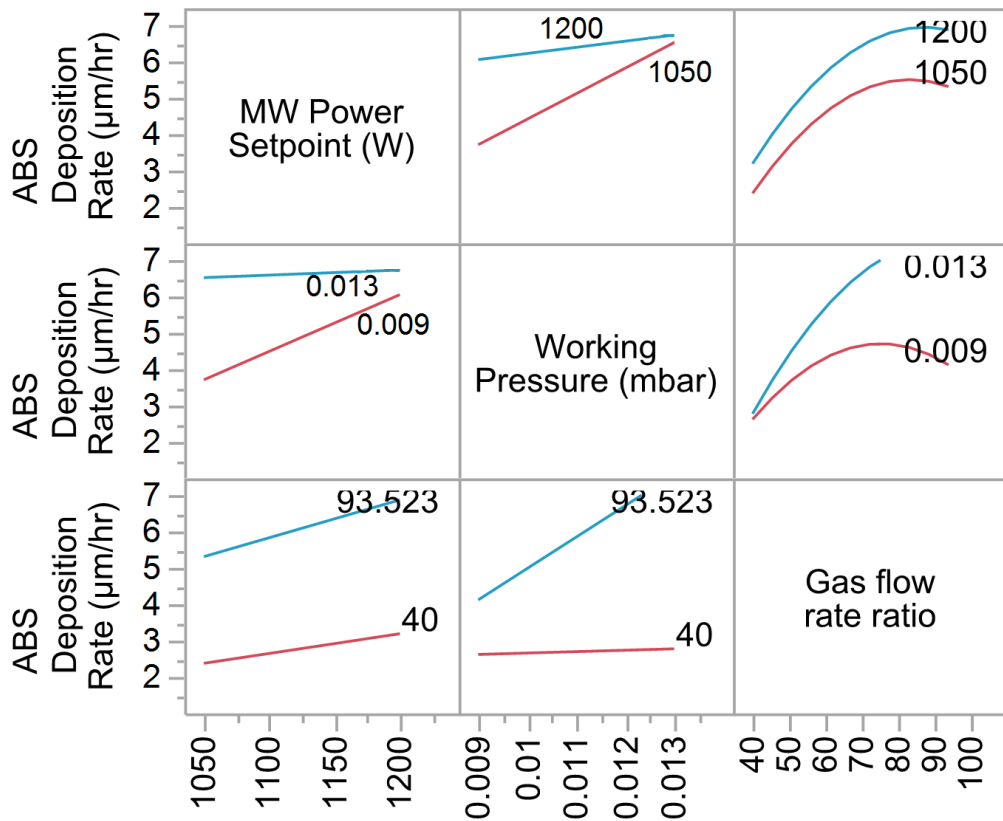


Figure 4-6 - Interaction profiles for main factors and deposition rate on ABS substrate.

By assuming the plots prediction can be extended beyond the design space used, an increase of working pressure with the same gas flow rate ratio, or an increase in gas flow rate ratio closer to pure C_2H_2 , depending on starting ratio and pressure, would result in a deposition rate above $7 \mu\text{m/hr}$. In practice, this is limited by the machine hardware as flow controllers limit the maximum throughput of process gases.

4.2.2.1.2 PEI Substrate

The main effects of the factors in the DOE on deposition rate on PEI are shown in Table 4-4. As with ABS substrates the only significant factor at a 99% confidence interval is gas flow rate ratio. The interaction profile for the model on PEI substrates can be seen in Figure 4-7; due to the similarities of the main effects for the models on ABS and PEI,

the same behaviour is shown in the interaction profiles, albeit with negligible changes in magnitude.

Table 4-4 - Effect summary of DOE model for deposition rate on PEI substrate.

Source	LogWorth	PValue
Gas flow rate ratio	2.451	0.00354
Gas flow rate ratio*Gas flow rate ratio	1.772	0.01691
MW Power Setpoint (W)	1.672	0.02130
Working Pressure (mbar)	1.129	0.07436
MW Power Setpoint (W)*Gas flow rate ratio	0.758	0.17475
MW Power Setpoint (W)*Working Pressure (mbar)	0.595	0.25436
Working Pressure (mbar)*Gas flow rate ratio	0.389	0.40877

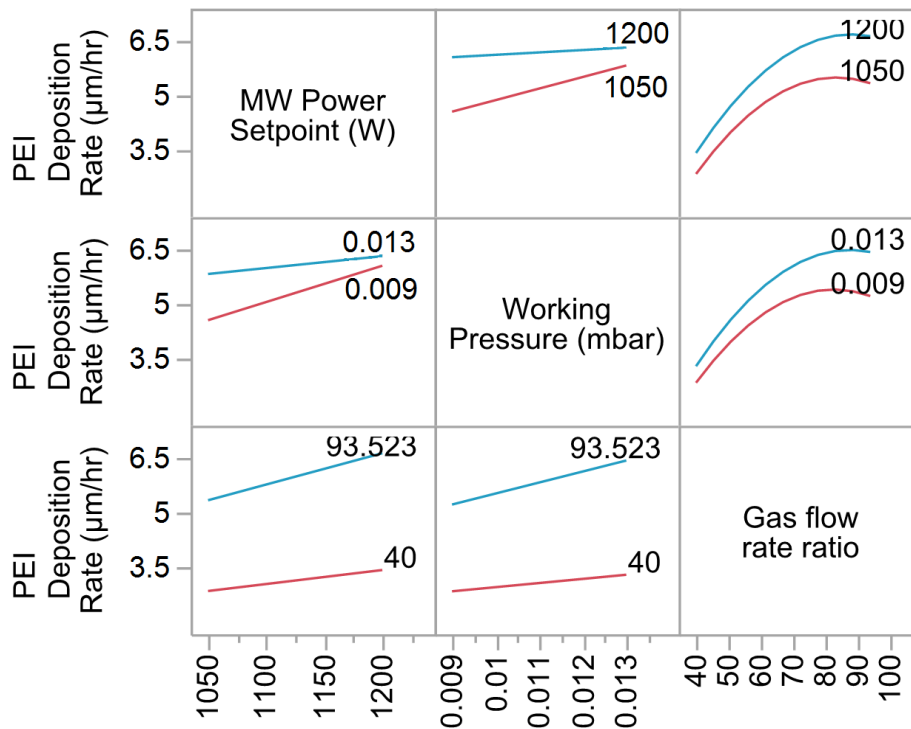


Figure 4-7 - Interaction profiles for main factors and deposition rate on PEI substrate.

4.2.3 Coating Roughness

Coating roughness was measured using white light interferometry as described in Chapter 3. Figure 4-8 and Figure 4-9 show the average surface roughness of the 10 coatings produced on the two substrate materials.

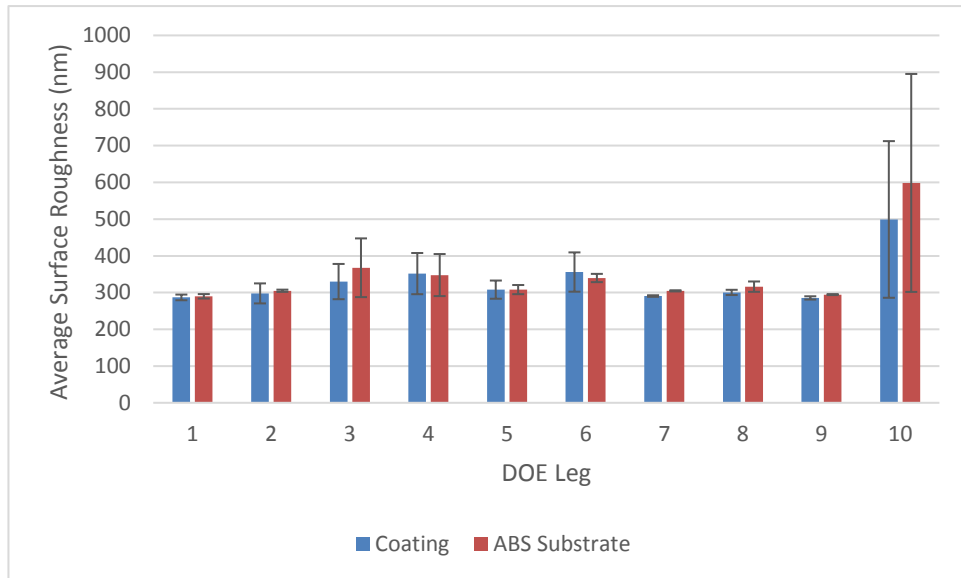


Figure 4-8 - Average surface roughness of DOE coatings on ABS substrate.

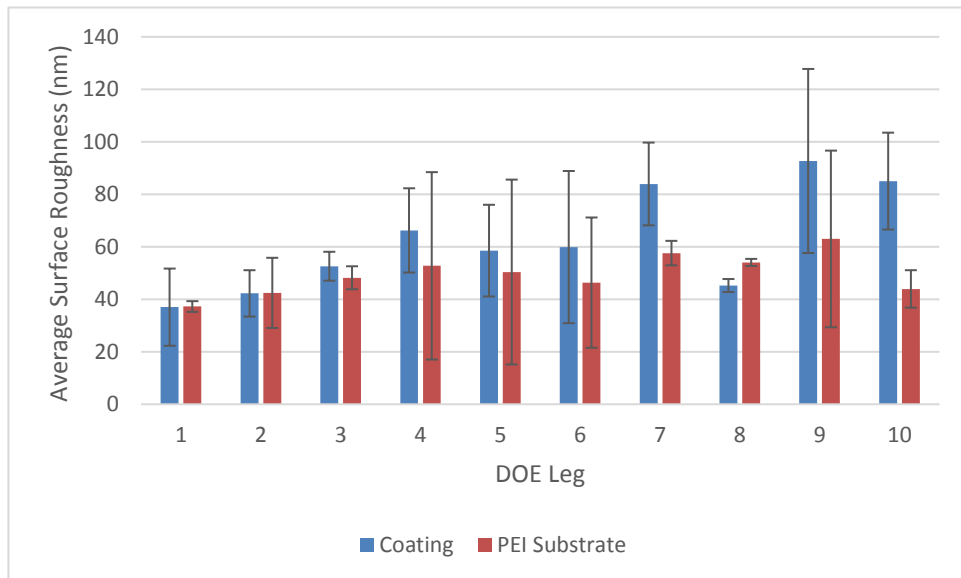


Figure 4-9 - Average surface roughness of DOE coatings on PEI substrate.

The roughness of the coatings produced on ABS (Figure 4-8) is larger than those produced on PEI substrates (Figure 4-9). This can be attributed to the differences in surface roughness of the underlying substrate. The majority of ABS samples and coatings had similar roughness values, in the range of 300-400 nm, with low measurement error. This is apparent by the physical appearance of the coatings which appear to have a much duller finish than their counterparts produced on PEI, where average surface roughness is less than 100 nm.

One of the ABS samples used for measurement of leg 10 had more scratches and damage on the surface than others, leading to the increased roughness and error. Of the two samples measured, the surface roughness for the smoother surface of the substrate and coating were 389 nm and 348 nm respectively. This value is in the same range as all other samples.

The percentage error of the PEI and coated PEI samples is greater than for ABS samples, and this can be attributed to small surface imperfections having a greater effect on surface roughness when the surface is smooth. PEI has a low surface roughness which gives the virgin substrate a reflective finish; this is also true of the coatings produced on these substrates. Despite the increased error, most measurements of substrate and coating pairs fall within the standard deviation of the measured values.

Comparing Figure 4-4 to Figure 4-8 and Figure 4-9, it can be seen that thickness variations of the coatings do not appear to have any effect on the surface roughness. The thinnest coatings (legs 4 and 6), compared to the thickest coating (leg 7), give marginally increased average surface roughness; however, all these measurements on both substrates fall within error, and the substrate measurements also follow this trend. The thickest coating measured was 5.3 μm , and the thinnest was 2.0 μm , so any smoothing properties of the coating beyond this thickness, and conversely the inability of the coating to smooth the surface by filling voids at low thickness, were not investigated.

From these results it can be assumed that the differences of coating roughness are not measureable, due to the unavoidable roughness of the polymer materials. In both cases, the coating conforms to the substrate as evidenced by the negligible changes in surface roughness following deposition, and the largest factor in determining surface roughness of the coating will be substrate selection/preparation and the resulting substrate surface roughness. Because of this, the results were not incorporated into the DOE model.

4.2.4 Coating Adhesion

The adhesion of thin films to the substrate is of paramount importance; if the coating delaminates it will be of no practical use in most cases. The measurement of adhesion of DLC coatings to polymer substrates was carried out using scratch testing and the cross hatch test as detailed in Chapter 3. Contact angle measurements were used to determine the optimum argon plasma power and exposure time to enhance adhesion.

4.2.4.1 Pre-deposition Argon Plasma Immersion

It was assumed that argon bombardment of the polymer surface would remove contaminants, and produce dangling bonds which would lead to an increase of OH functional groups upon reacting with water vapour in the air. The change in concentration of OH groups on the surface would be traceable by measuring the contact angle of deionised water on the surface. Figure 4-10 shows a contour plot of how contact angle varied after exposure to argon plasma of ABS polymer samples.

The contact angle on virgin ABS (as manufactured, prior to plasma immersion) was found to be 78°. At a constant current of 100 A, the maximum set point available using the plasma source in the Hauzer Flexicoat 850, the contact angle decreases as both pressure and time increase. Even at the lowest pressure and time, a dramatic reduction in contact angle is observed, however the minimum contact angle was achieved with pressures above 6×10^{-3} mbar and exposure times above 350 s. It should be noted that in order to produce the contour plot bi-linear interpolation is the preferred method. For experimental efficiency, not enough data points were produced to do this, and so the data was linearly interpolated first in the y-direction, and then to fill in any gaps, the x-direction. This approximation produced some artefacts, such as the discontinuity of the lowest value contour band at 550 s. However, it was assumed that due to the quasi-stable and random nature of plasma, combined with measurement errors of the contact angle goniometry procedure it is valid for the intended purpose - giving the range of

plasma source parameters that give the lowest range of measurable contact angles (<10°).

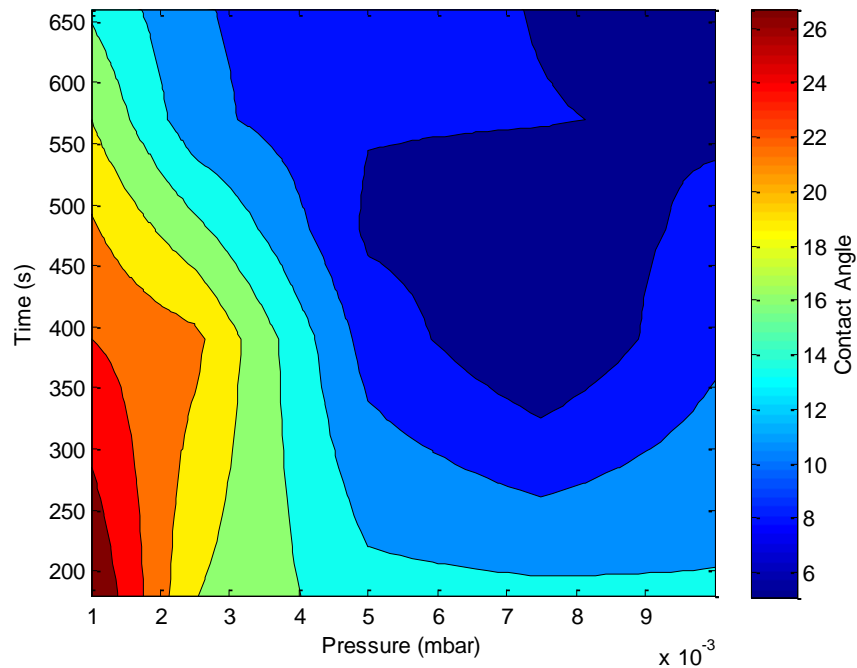


Figure 4-10 - Contact angle on ABS as pressure and duration of plasma exposure are varied.

For the adhesion tests, it was assumed that any plasma treatment at 100A, above a pressure of 7×10^{-3} mbar and duration over 500s would produce the best adhesion. Pressures and durations above those tested would be expected to eventually damage the substrate with a constant or decreased contact angle measured.

4.2.4.2 Crosshatch Test

Crosshatch tests were performed on DLC coated ABS that had not been subjected to immersion in argon plasma prior to deposition, and DLC coated ABS that had been given the optimal pre-treatment determined by contact angle measurement. The parameters used were 100A current set on the plasma source, a pressure of 7×10^{-3} mbar in 99.9% argon, and a duration of 450 s.

Figure 4-11 and Figure 4-12 show a typical result from cross hatch tests on the two coated polymer samples, both with and without plasma pre-treatment to improve

adhesion. It is clear to see that both samples pass the test with the highest classification, whereby no coating has delaminated within the cross-cut area. It should be noted that in Figure 4-11, small pieces of swarf can be seen which could be mistaken for sites of delamination. These are present following cutting into the substrate and are not the result of coating failure.

There are two possible explanations as to why both samples passed the test; either both samples have similar substrate-coating adhesion, or the test is not sensitive enough to highlight the differences. In either case, the cross hatch test is widely used to determine suitability of coating adhesion for use in industry, and by passing this test it can be shown that even with no pre-deposition plasma immersion or chemical cleaning of the surface, excellent adhesive strength can be achieved with DLC coatings on polymers using the MW-PECVD process. The same cannot be said for metallic substrates, suggesting that the mechanism of adhesion for DLC films on polymer substrates is different than on metallic substrates.

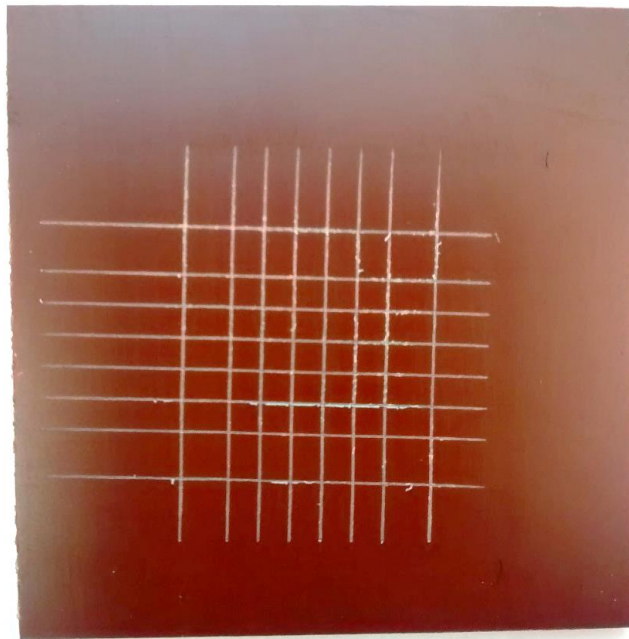


Figure 4-11 - Cross hatch test on untreated ABS polymer with DLC coating.

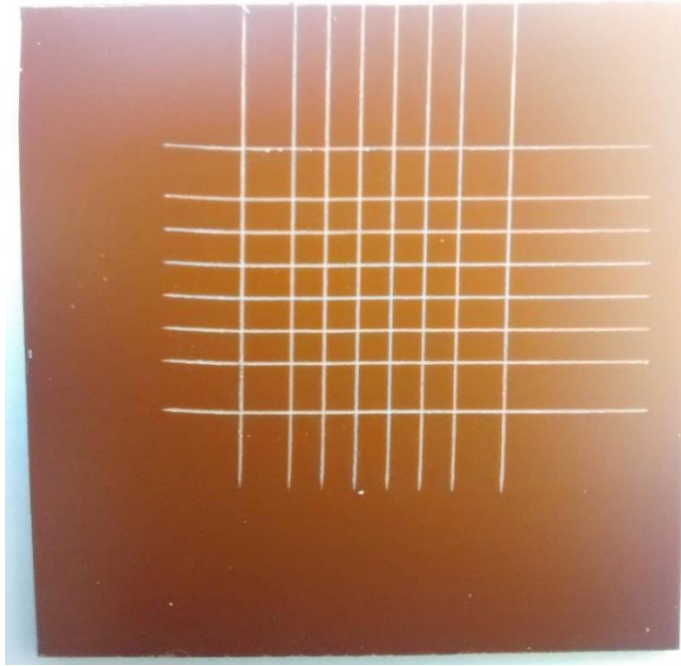


Figure 4-12 - Cross hatch test on DLC coated ABS, with optimal Ar plasma pre-treatment.

4.2.4.3 Scratch Test

Constant load scratch tests were performed on the same samples as used for cross hatch testing; the same DLC coating on two ABS substrates with no pre-treatment and the optimum pre-treatment determined from contact angle measurement. Differences in fracture and delamination of the coating indicate different levels of adhesion, with higher critical loads said to equate to better adhesion. A 500 μm radius conical diamond tip was used with a sliding speed of 5 mm/min and loads were increased until coating failure could be seen. Further details of the experiment can be found in Chapter 3.

Figure 4-13 shows the resulting coating failure from constant load scratch tests on the two DLC coated ABS samples. In all cases the scratch direction is from bottom to top of the image. At 6N there is no major fracture of either coating, but increasing the load to 7N results in fractures becoming visible on both samples.



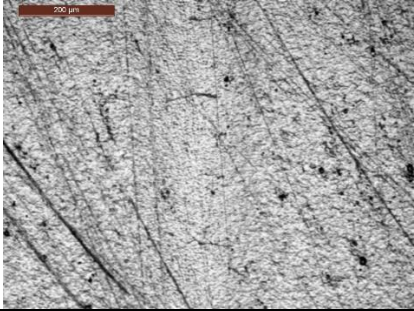

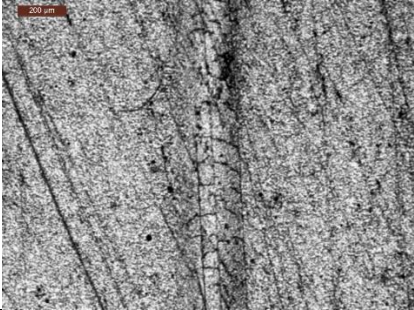
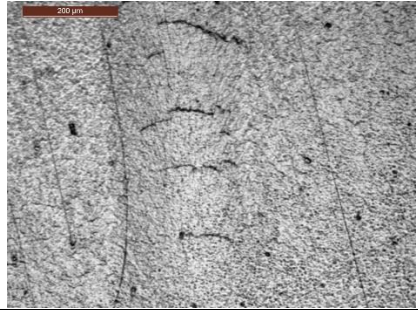
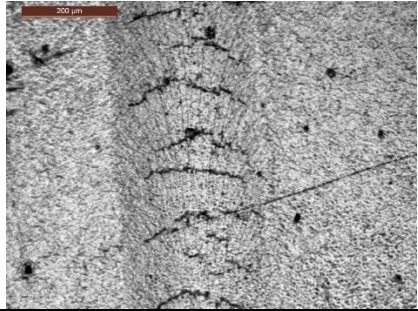

Load	Untreated	Treated
6N	 Micrograph showing the surface of an untreated material under a 6N load. The surface is highly textured and shows numerous fine scratches and some larger, dark, irregular marks. A 200 µm scale bar is visible in the top left corner.	 Micrograph showing the surface of a treated material under a 6N load. The surface appears smoother and more uniform than the untreated sample, with fewer scratches and less debris. A 200 µm scale bar is visible in the top left corner.
7N	 Micrograph showing the surface of an untreated material under a 7N load. The surface shows increased wear and more pronounced scratches compared to the 6N load. A 200 µm scale bar is visible in the top left corner.	 Micrograph showing the surface of a treated material under a 7N load. The surface remains relatively smooth with minimal wear. A 200 µm scale bar is visible in the top left corner.
8N	 Micrograph showing the surface of an untreated material under an 8N load. The surface is heavily scratched and shows significant material loss and debris. A 200 µm scale bar is visible in the top left corner.	 Micrograph showing the surface of a treated material under an 8N load. The surface shows some wear and scratches, but it is much more resistant than the untreated sample. A 200 µm scale bar is visible in the top left corner.
9N		 Micrograph showing the surface of a treated material under a 9N load. The surface shows significant wear and large, dark, irregular marks, indicating material loss. A 200 µm scale bar is visible in the top left corner.
10N		 Micrograph showing the surface of a treated material under a 10N load. The surface shows extreme wear and large, dark, irregular marks, indicating significant material loss. A 200 µm scale bar is visible in the top left corner.

Figure 4-13 - Coating response to constant load scratch test with and without adhesion pre-treatment.

The shape of the cracks suggest these occur on the leading edge of the scratch tip and so are tensile failure. As load is increased the frequency of cracks becomes increased until deformation of the sample surface is too high for the tensile strength of the coating and these concave cracks are connected by smaller cracks at loads of 9N and above on the treated sample.

As with cross hatch tests, the scratch test shows no discernible difference between the two samples, where both exhibit similar failure from 7N onwards, with similar spacing between major cracks caused by pile-up at the leading edge of the scratch tip.

90° peel tests were attempted, in order to acquire a quantitative tensile strength of adhesion, however no suitable method of removing the coating was found and so results with this method were not obtained. Combining the results of the scratch tests and cross hatch test it can be seen that that by conventional standards, the adhesive strength of the coating on the substrate is excellent, being able to score highly in the cross hatch test. However, scratch tests reveal that coating failure occurs at low loads, with a large radius tip. Despite tensile failure, no delamination of the coating occurs and so it could be that although the tensile strength of the coating causes fracture, the shear forces at the interface are not large enough to induce delamination. In this case the substrate mechanical properties allow the coating to deform during the scratch leading to failure. In such events, it could be argued that the scratch test is not able to be used to determine adhesion of such substrate-coating systems due to limitations of the substrate material. Because of the soft, ductile nature of the substrate and the contact pressures involved, flakes of the coating that would otherwise delaminate could be embedded into the substrate surface as the tip passes over despite being de-bonded.

In order to determine the effect of the substrate on the scratch test, chromium was sputtered onto ABS and the scratch hardness determined from a constant load scratch (3.5N) performed at different speeds. The results are shown in Figure 4-14 with scratch track images shown in Figure 4-15.

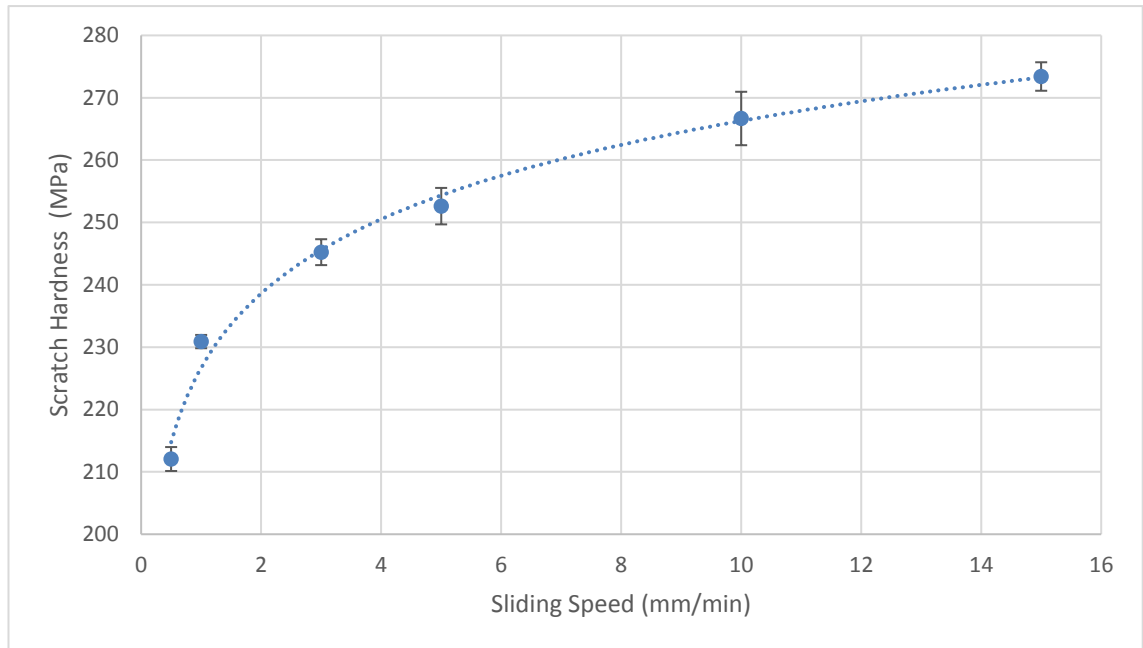


Figure 4-14 - Scratch hardness as a function of sliding speed for a Cr coated polymer.

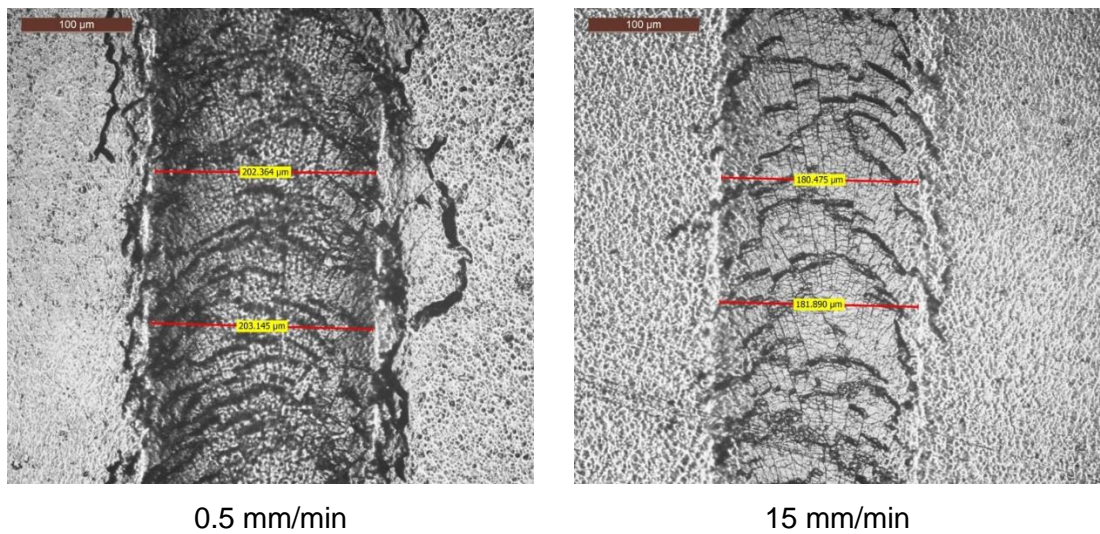


Figure 4-15 - Scratch track a width and coating fracture of 3.5N load at different sliding speeds on Cr sputtered coating on ABS. Sliding direction from bottom to top.

As sliding speed increases from 0.5 mm/min to 15 mm/min the scratch hardness increases from 212 MPa to 273 MPa; an increase of nearly 30%. It can also be seen that the relationship between sliding speed and scratch hardness is logarithmic, as shown by the trend line. Scratch hardness, in this case, is a measure of the resistance to plastic deformation of the surface because the elastic component cannot be determined by

measuring the track width after the scratch is performed. The relationship to sliding speed shows that the ABS substrate exhibits viscoplastic behaviour as the depth of the scratch track changes with strain rate. As the depth of the scratch track increases (at lower sliding speeds) the density of cracking in the coating increases, as shown in Figure 4-15. The shape of the crack in relation to the sliding direction indicates tensile cracking occurs at the leading edge of the scratch tip during the test, leaving behind a curved crack in the scratch track.

The substrate effects on the observed coating failure demonstrate that the scratch test has limited applications for testing adhesion on coated polymers due to the differences in viscoelastic and viscoplastic properties of different polymer types. It also demonstrates that crack density is a function of scratch depth rather than load, leading to the assumption that on low modulus substrates with larger modulus coatings the scratch test will be a measure of coating yield strength. This is because the substrate will have a much lower stress than the stiffer coating at a given level of deformation. In both cases the coating shows signs of severe failure, however no delamination is visible.

4.3 Conclusion

The effect of process parameters on heating rate, deposition rate and coating/substrate roughness was examined. Where applicable these responses were fitted to a statistical model that gives a prediction within the design space tested. To increase the deposition rate, the partial pressure of C_2H_2 must be increased. The contact angle of distilled water on the polymer surface was used to determine the optimum pressure and time (at maximum current) by which to enhance adhesion of thin films. Use of the cross hatch test and scratch test determined that either no difference in practical adhesion between the two substrate treatments existed or the methods to determine adhesion were unsuitable.

The scratch test, as a quantitative measure versus the qualitative measure of the cross hatch test, was examined further. It was found that the polymer substrate material had a

large effect on the measured values due to viscoplastic behaviour found by varying sliding speed with constant load. No coating delamination was seen, however the density of cracks in the coating increased as the load was increased or the sliding speed reduced.

Chapter 5. Coating Structure & Composition

5.1 Introduction

This chapter presents analysis of the structure of the 10 coatings produced through freeze fractured cross sectional SEM images, followed by compositional analysis. The chemical composition/structure is compared to the mechanical properties determined in Chapter 6.

5.2 Structure

The 10 coatings produced for the design of experiments analysis were freeze fractured using liquid nitrogen as detailed in Chapter 3. Figure 5-1 - Figure 5-10 show cross section images obtained by SEM of the coatings on ABS substrates; substrates are shown in the bottom portion of the frame, with the coating in the top portion. It should be noted that any separation of the coating from the substrate that can be seen in these images is likely due to the method used to obtain the cross section view. Freeze fracturing with liquid nitrogen will rapidly cool both substrate and coating, which have different rates and magnitudes of thermal expansion, causing compressive stresses at the interface. These stresses may be large enough to overcome the adhesive strength of the coating, however as shown in Chapter 4, the adhesion of the coatings under normal conditions is adequate to pass cross hatch tests.

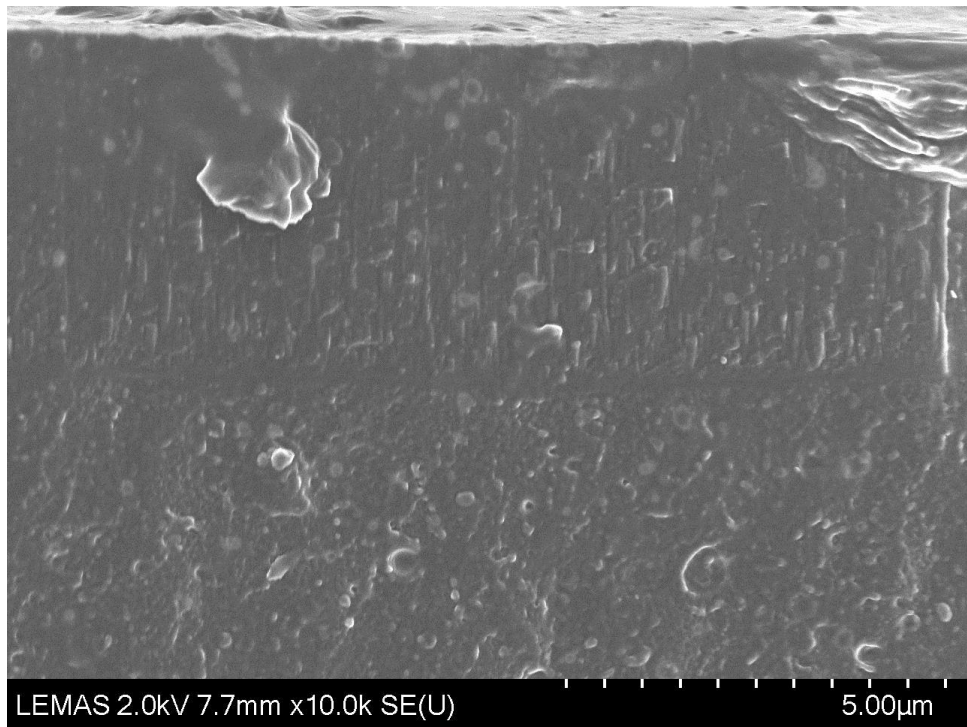


Figure 5-1 - Cross section of DOE leg 1 coating on ABS substrate.

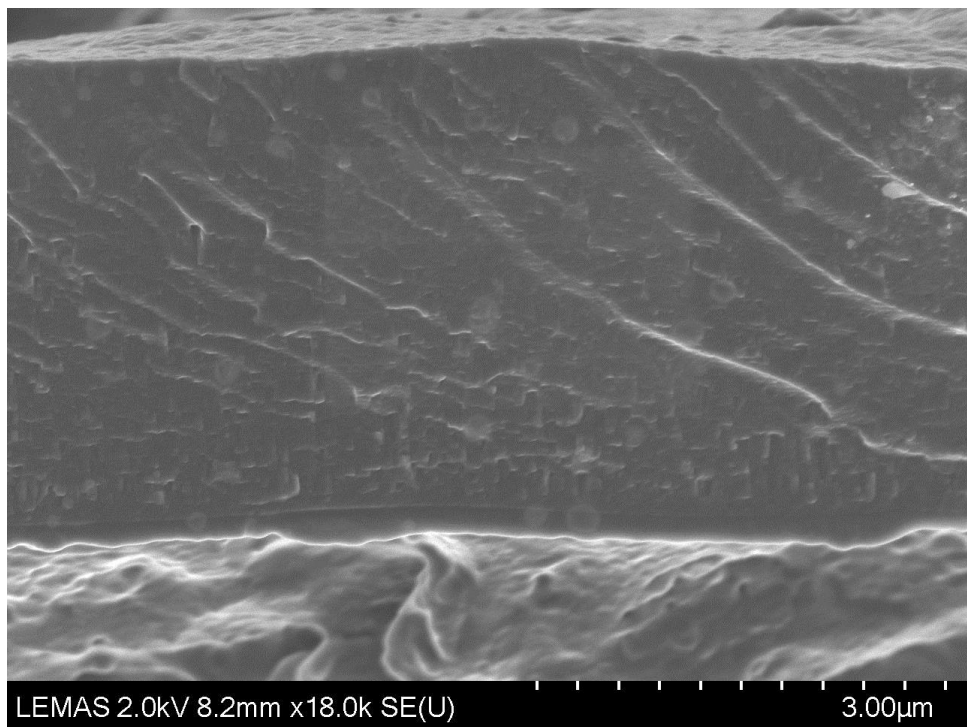


Figure 5-2 - Cross section of DOE leg 2 coating on ABS substrate.

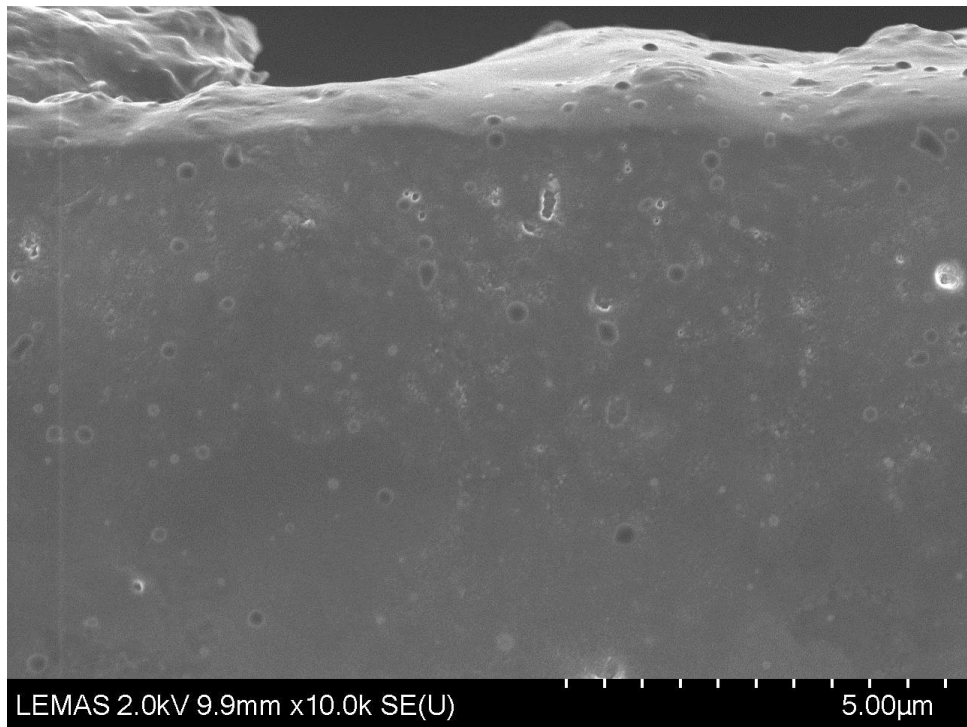


Figure 5-3 - Cross section of DOE leg 3 coating on ABS substrate.

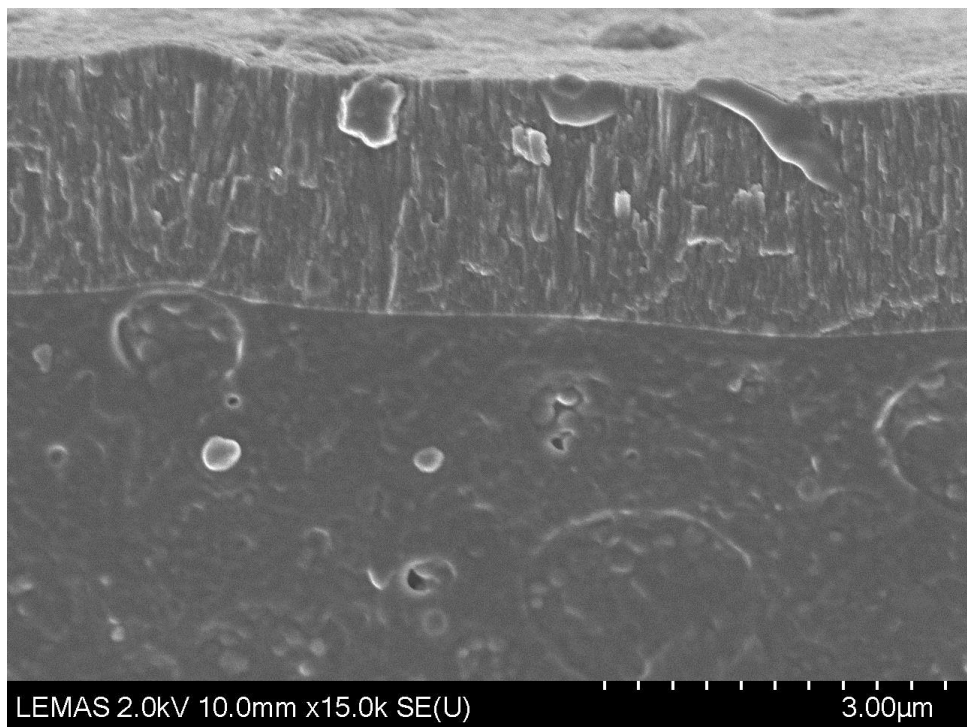


Figure 5-4 - Cross section of DOE leg 4 coating on ABS substrate.

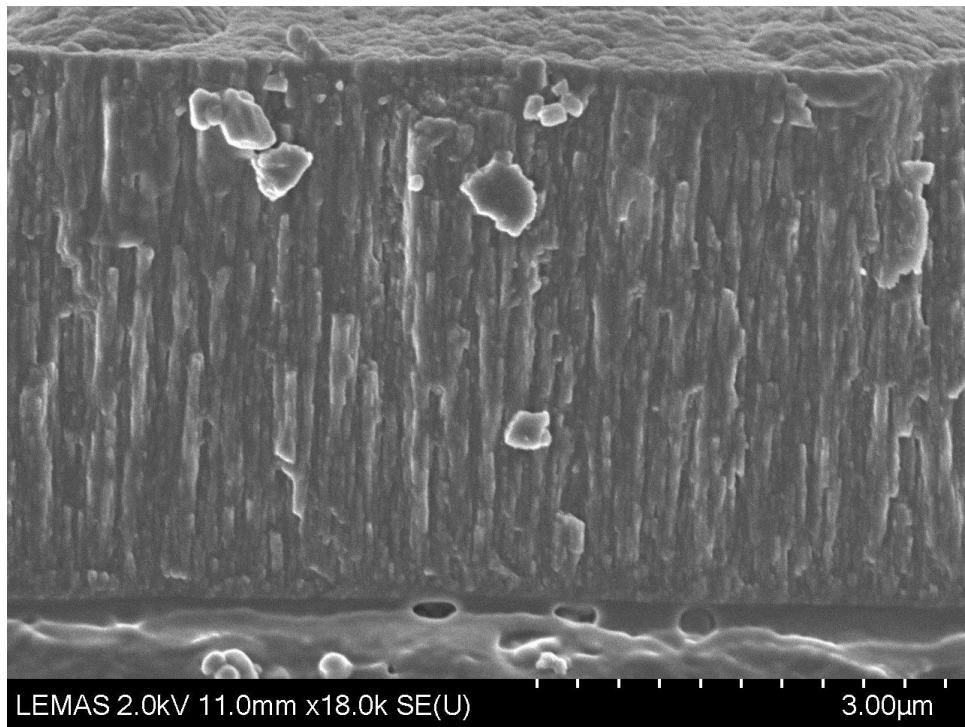


Figure 5-5 - Cross section of DOE leg 5 coating on ABS substrate.

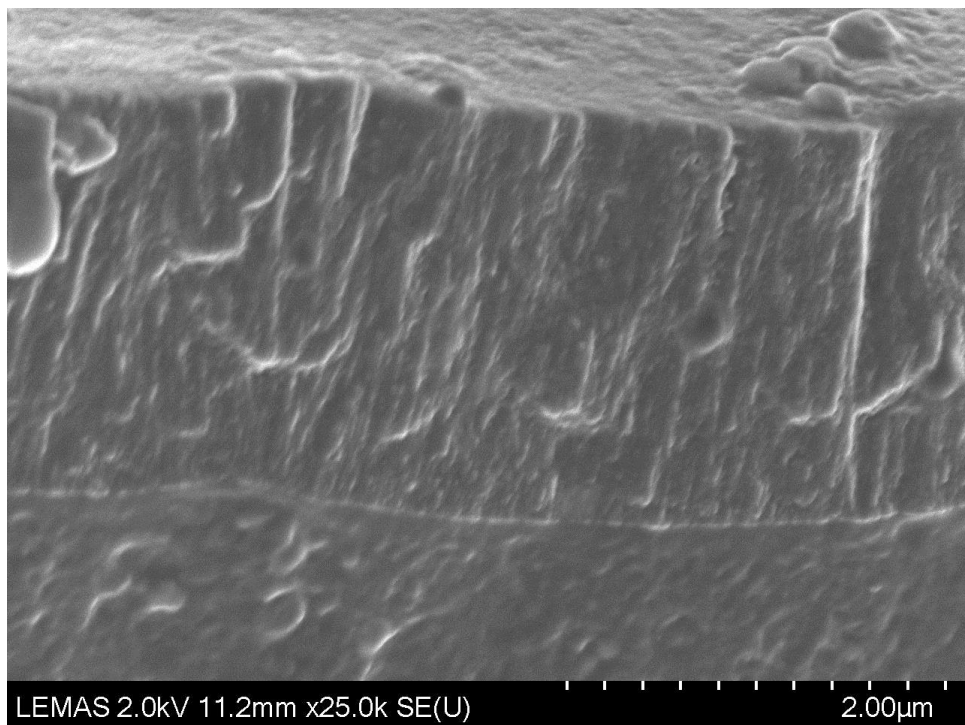


Figure 5-6 - Cross section of DOE leg 6 coating on ABS substrate.

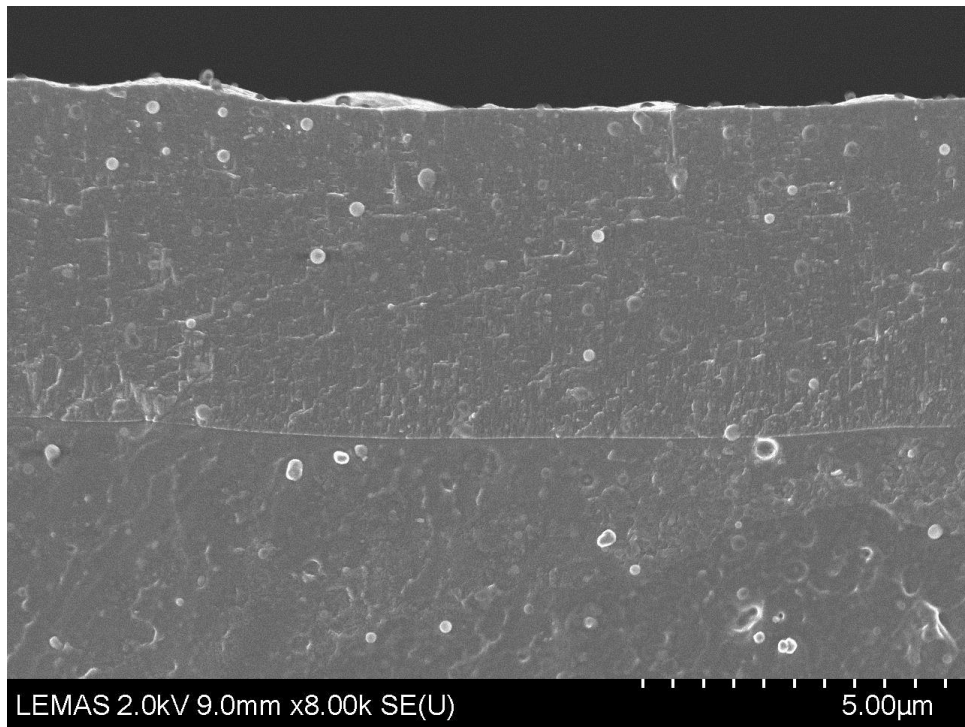


Figure 5-7 - Cross section of DOE leg 7 coating on ABS substrate.

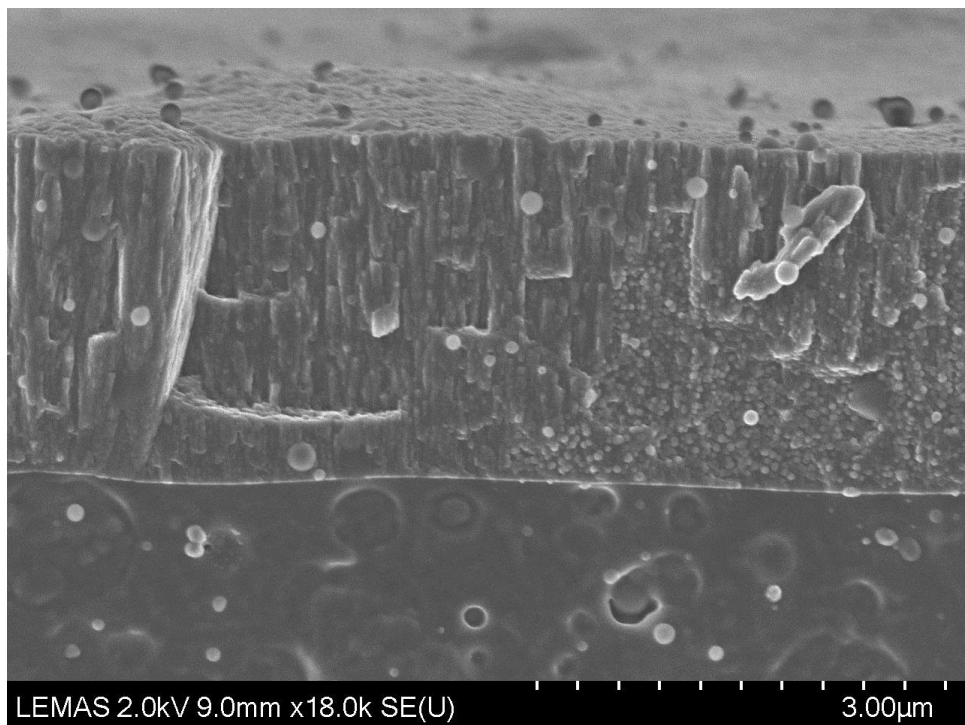


Figure 5-8 - Cross section of DOE leg 8 coating on ABS substrate.

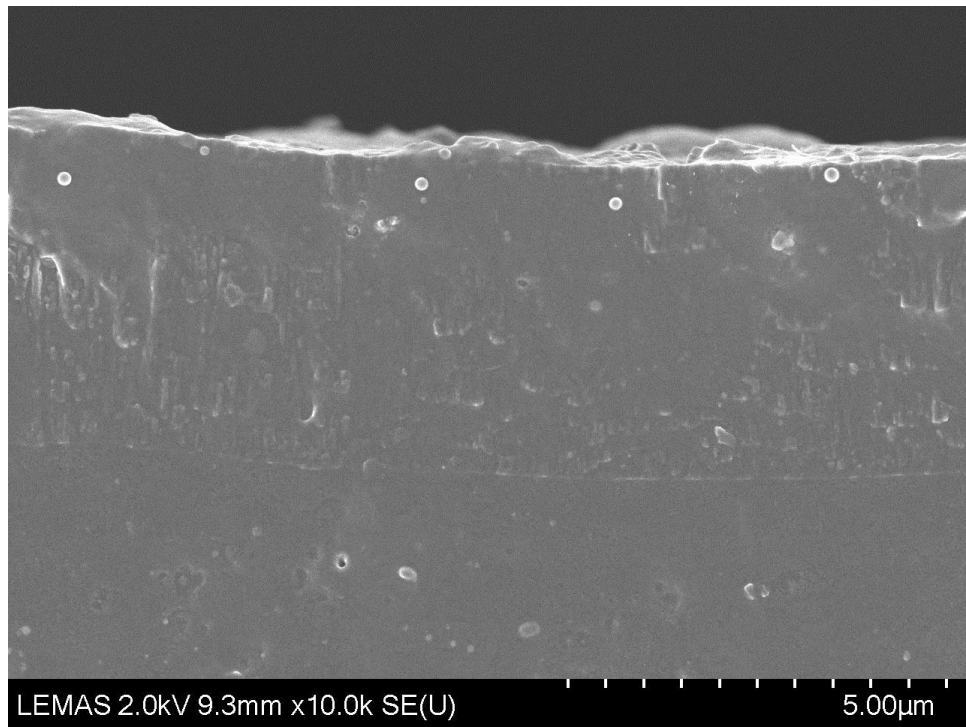


Figure 5-9 - Cross section of DOE leg 9 coating on ABS substrate.

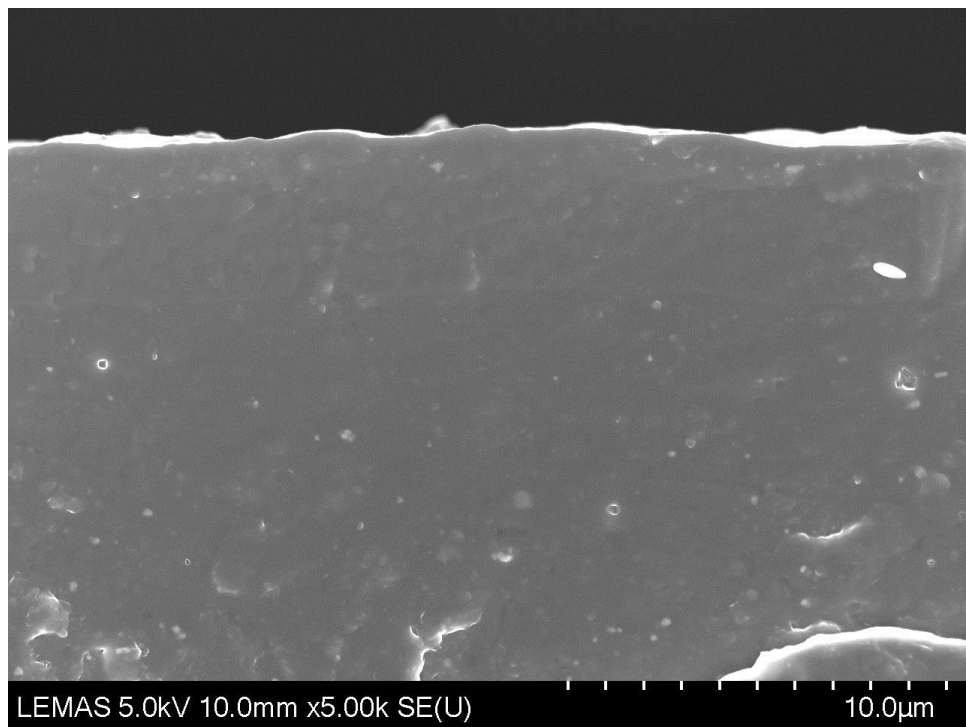


Figure 5-10 - Cross section of DOE leg 10 coating on ABS substrate.

The majority of coatings have a distinct transitional interface at the substrate that clearly distinguishes the two materials. ABS is an amorphous polymer and this can be confirmed by a lack of grain structure in the substrate in any of the above images. At high magnifications imperfections in the polymer become visible, such as voids which are most apparent in Figure 5-4. Legs 4 (Figure 5-4), 5 (Figure 5-5), 6 (Figure 5-6), and 8 (Figure 5-8) show fibrous growth. The fibrous structural features can be seen in legs 1 (Figure 5-1) and 9 (Figure 5-9), and to a lesser extent leg 2 (Figure 5-2), but only in the lower portions of the coating; those which were deposited first. The remaining coatings appear amorphous with no apparent granular structure or repetitive features. Table 5-1 summarises the deposition conditions and features seen in the cross section images of the coatings. Leg 3 shows no interface, and instead the structure appears to blend into the polymer substrate with a gradient.

Table 5-1 - Deposition conditions and observed structure from cross section images.

Leg	MW Power (W)	Working Pressure (mbar)	Gas flow rate ratio (Ar & C2H2) (%C2H2)	Structural Features
1	1050	0.012	94	Lower fibrous, upper amorphous
2	1100	0.011	92	Lower fibrous, upper amorphous
3	1050	0.011	85	Amorphous
4	1100	0.009	40	Fibrous
5	1200	0.009	74	Fibrous
6	1200	0.011	42	Fibrous
7	1200	0.011	91	Amorphous
8	1050	0.013	43	Fibrous
9	1050	0.011	66	Lower fibrous, upper amorphous
10	1100	0.013	67	Amorphous

It is worth noting that leg 8 (Figure 5-8) produced a coating with what appear to be voids filled with nodules of material. No chemical analysis was carried out on this area and no appreciable difference was found in the mechanical properties compared to the most similar coating in the study. It is therefore assumed that these areas are artefacts or

contamination from the freeze fracture method and do not represent the true structure of the coating when remaining intact.

The differences in structure can be attributed to deposition conditions, however no clear trends can be seen. It is expected that at lower energies the condensing particles will be unable to coalesce with the existing coating growth, leading to formation of new clusters of growth. These clusters give the nodular appearance of the DLC surface seen from above. It is possible that the granular structure seen is an artefact of the freeze fracture method and that all coatings have similar structure, with differences in mechanical properties brought about solely by changes in chemical composition.

5.3 Composition

The chemical composition and bond types within the coating were examined using multiple complementary techniques. The DLC coatings are a mixture of carbon and hydrogen from the working gas of acetylene, and inclusions of argon which was also introduced into the deposition chamber to decrease the ionisation energy of the gas mixture. Oxygen is to be expected to be incorporated in the surface and near surface layer due to quenching dangling bonds upon purging the vacuum after deposition. For the purposes of this section, effects arising from oxygen inclusion have been ignored as they will have no effect on bulk performance of the coating.

5.3.1 Raman Spectroscopy

Raman spectroscopy was employed as a first attempt at determining a quantitative estimate of carbon bonding types in the DLC coatings. The details of the analysis are given in Chapter 3. The results from these tests were only intended to guide the selection of samples for more intensive compositional characterisation due to the nature of the technique. Visible light Raman spectroscopy relies on excitation of the sp² bond types to measure the vibrational frequencies of these bonds and indirectly determine the sp³ content. As such, there are better techniques to determine the sp²/sp³ ratios, despite the increased complexity and cost. A visible wavelength laser (488 cm⁻¹) was used to

examine the surface to determine the D-peak and G-peak ratios of the resulting spectrum. In DLC coatings the G-peak corresponds to direct excitation of sp² bond types and the D-peak corresponds to indirect excitation of sp³ bond types. Table 5-2 shows the peak positions and intensity ratio of the D and G peaks, which has been shown to correlate with sp²/sp³ ratio. No data was collected for leg 8 as the spectrum was too broad, and with low intensity, to fit the D and G peaks. An increase in the I_D/I_G ratio indicates a higher sp³ content, which should manifest as a harder coating.

Table 5-2 - Raman D and G peak positions, with intensity ratio for each of the 10 coatings produced.

Leg	D-peak position	G-peak position	I _D /I _G
1	1328	1533	0.488
2	1326	1535	0.354
3	1320	1532	0.245
4	1368	1533	0.043
5	1335	1530	0.133
6	1365	1529	0.050
7	1343	1530	0.296
8	N/A	N/A	N/A
9	1337	1528	0.182
10	1340	1530	0.263

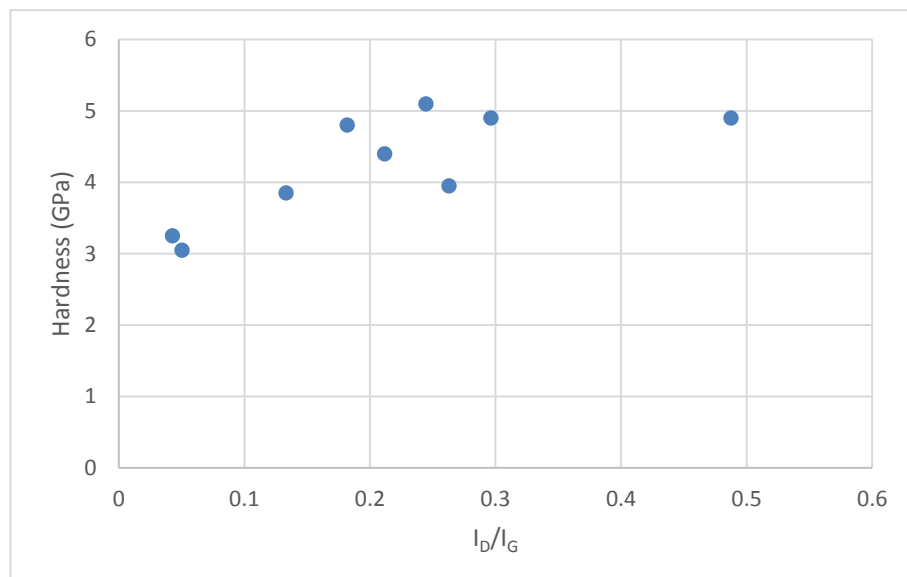


Figure 5-11 - Correlation between I_D/I_G and hardness.

In order to determine the accuracy of the I_D/I_G ratio as a measure of sp²/sp³ content of the DLC films, correlation with hardness was tested. As can be seen in Figure 5-11,

hardness and I_D/I_G are weakly correlated suggesting that increased hardness is as a result of increased sp^3 content. However, the weak correlation and determining sp^3 content from indirect excitation challenges the validity of the data. Further analysis of the coatings with respect to sp^2/sp^3 was required, utilising analytical techniques which directly measure both bond types.

5.3.2 Solid state NMR spectroscopy (SSNMR)

Solid state NMR spectroscopy was chosen to measure the sp^2/sp^3 content of three coatings (leg 1, leg 5, and leg 6). Compared to Raman spectroscopy, resources were limited and so measurement of all 10 coatings was not practical. Full details of the sample preparation and test procedure can be found in Chapter 3.

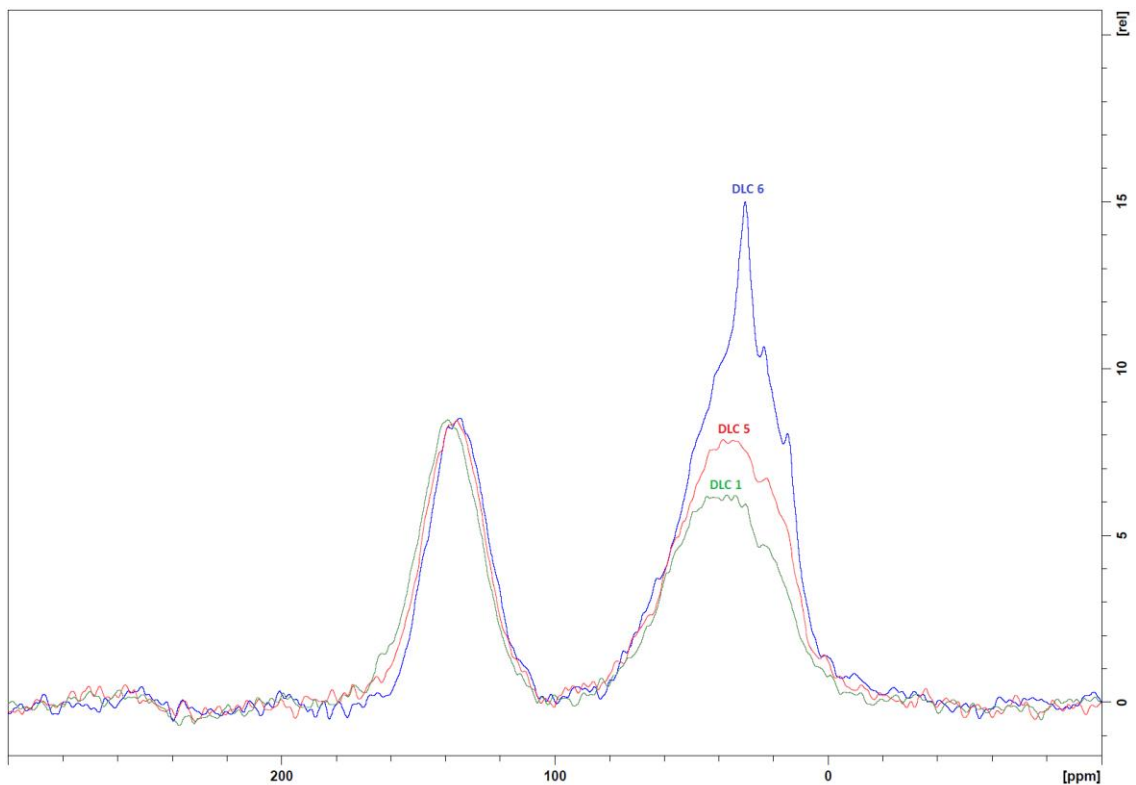


Figure 5-12 - SSNMR spectra for three DLC coatings.

Figure 5-12 shows the NMR spectra obtained for each of the three coatings. The peaks at roughly 140 ppm and 20-40 ppm correspond to sp^2 and sp^3 bonds respectively. As sp^2/sp^3 ratio increases the amount of sp^3 bonding has decreased, which should lead to a softer coating. There is a positive correlation between hardness and sp^2/sp^3 ratio; the

opposite of what would be expected with a DLC coating. The most likely reason for a decrease in hardness, with increasing sp³ content is an increase of hydrogen content in the coatings, leading to a more polymer-like molecular structure.

5.3.3 Elastic Recoil Detection (ERD)

ERD was chosen to measure the atomic ratios of carbon and hydrogen of the coatings. The coatings were as-deposited on ABS polymer substrates with a 20 nm gold film evaporated prior to analysis in order to help prevent surface charging effects. The gold coating did not stop the samples charging under the ion beam, leading to damage and removal of the gold coating in some cases.

Figure 5-13 shows the spectrum obtained for the leg 5 sample with a gold overcoat. The peak at ~ch.1080 corresponds to the gold overcoat and is fitted by two peaks. The peaks separate because of the different energy levels of DLC and Au; the gold layer is discontinuous and so the signal contains DLC covered with Au and pure Au. Once the Au film is removed the DLC charges adding extra noise to the spectrum which is seen as broadening in the region above ch.30 where the count is increased.

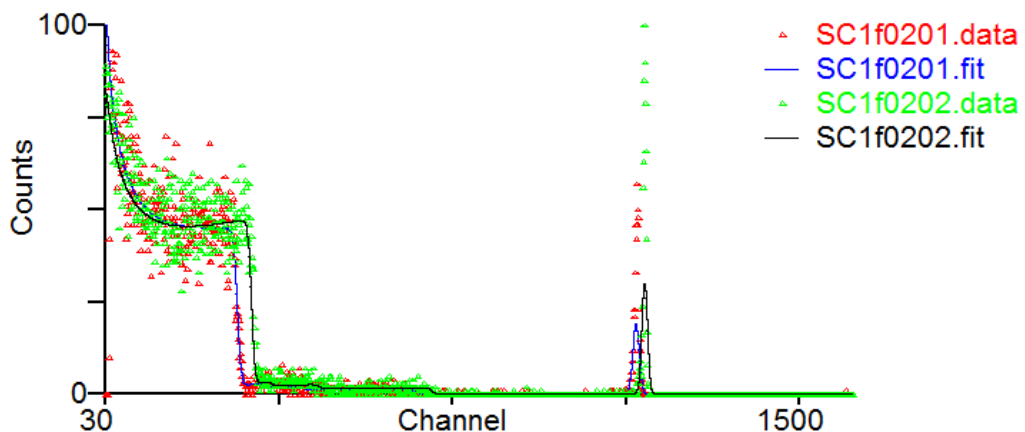


Figure 5-13 - ERD spectrum for DLC coated ABS sample with gold overcoat.

For the first run only Leg 1, 5, and 6 were analysed, with valid data obtained for only the first two samples. During the second run, two further examples of Leg 6 were included; one from the same batch as leg 6 (leg 6-2) and one from a separate batch with increased

DLC thickness (leg 6-3). A third sample was included which was produced using a conventional PECVD process with a DC discharge. Graphically presenting this data (Figure 5-14, Figure 5-15, and Figure 5-16) shows that DLC 1 contains less hydrogen than DLC5, which contains less hydrogen than DLC6. Correspondingly the same trend can be seen for carbon content, but decreasing as the leg number of the DLC increases. As such, the C/H ratio for DLC1 is greater than DLC5, which is greater than DLC6. The PECVD-DLC samples has a C/H ratio within the error of DLC5 and DLC6.

Figure 5-14 shows the separate results for all 3 DLC6 samples. All three samples are within error of each other, with error for the C and H percentages being higher for DLC6-2.

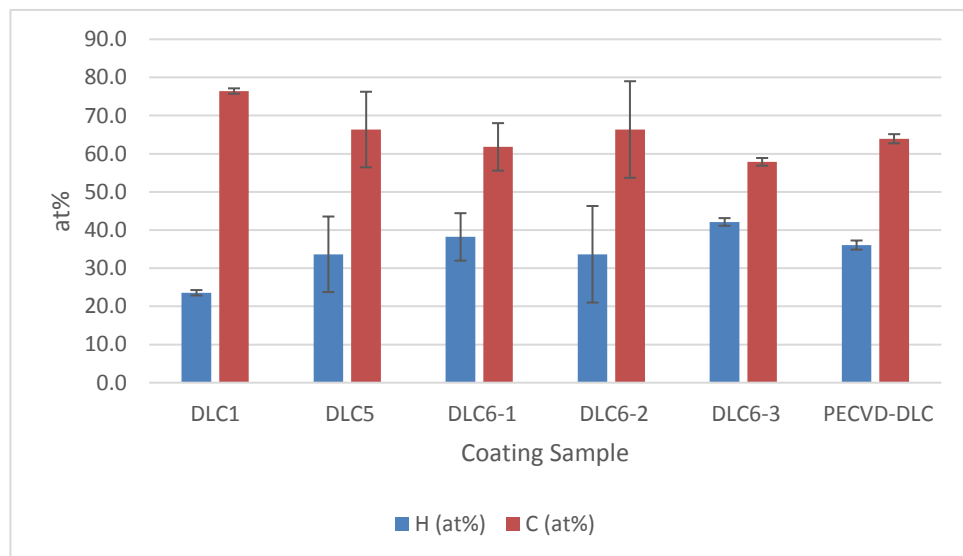


Figure 5-14 - Chart showing C and H atomic percentages for samples split by different samples analysed over multiple runs.

Figure 5-16 shows that due to the high margin of error for DLC5, the C/H ratio of this sample is within error for all the other samples analysed; this is due to only 2 measurements, with a range of 1.61. Such anomalous results are also seen for DLC6 and DLC6-2. Despite these results, the trends shown from the averages of these values, when combining all 8 measurements for variations of DLC6, show a difference between the 3 samples of primary interest despite the high margin of error. The coefficients from the fitting of the data, which allow the C and H ratios to be determined show no reason

to suspect the data is invalid. As such, and taking into account the NMR results, it can be seen that as the sp^2/sp^3 ratio decreases, the hydrogen content of the film increases.

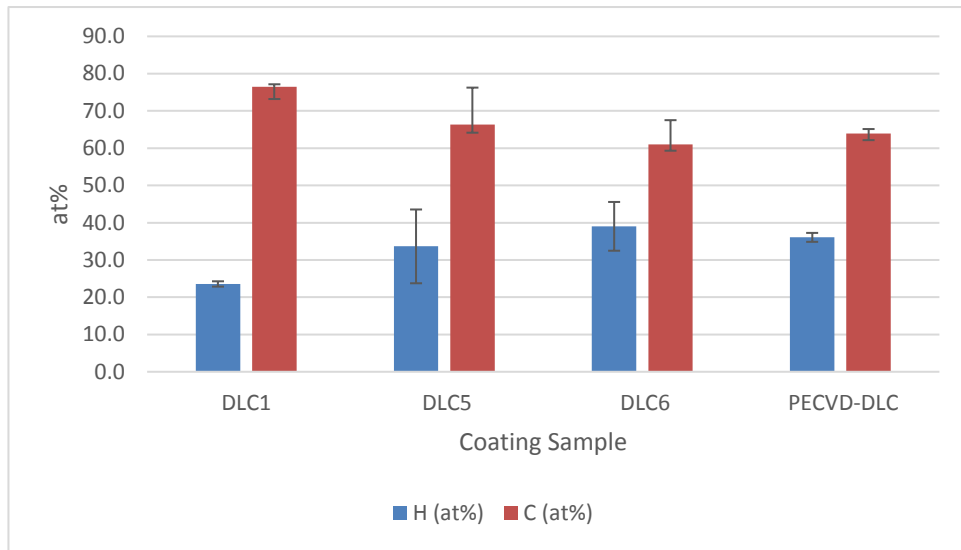


Figure 5-15 - Chart showing C and H atomic percentages for all analysed samples.

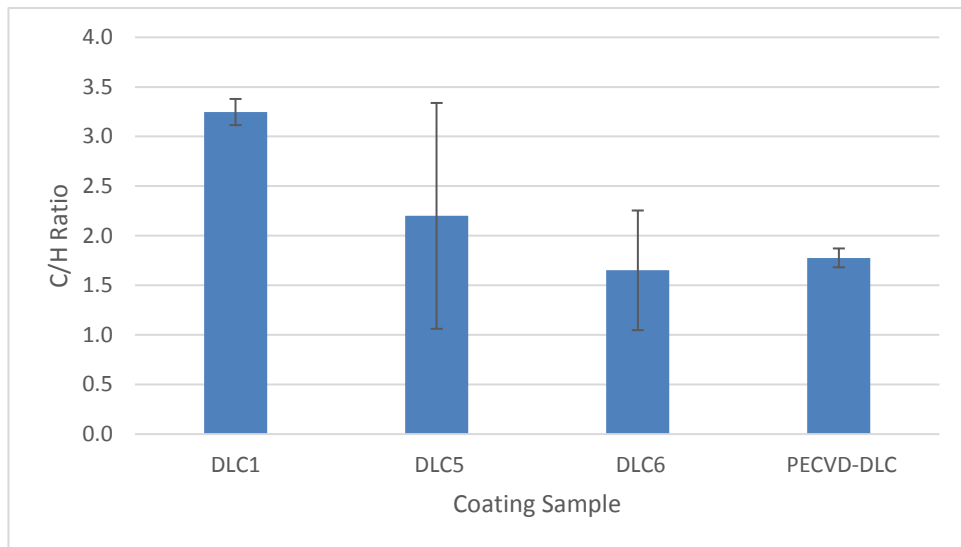


Figure 5-16 - Chart showing C/H ratios for all analysed samples.

The limited deposition conditions available for producing conventional PECVD DLC coatings on polymers using the Hauzer Flexicoat 850 deposition system means that the PECVD DLC coating analysed here is representative of what is possible to be produced, albeit with expected minor variation. As such it is worth noting that the MW-PECVD

method is capable of producing coatings that incorporate less hydrogen than the PECVD method, and so would be expected to have different mechanical properties.

5.4 Conclusion

In this chapter the structure of the ten DLC coatings produced was shown through cross sectional images produced by freeze fracturing the samples. The appearance of a fibrous structure was apparent on some samples through the thickness. On other samples the same fibrous structure was only observed near the substrate, with an amorphous film near the coating surface. In others the DLC film appeared solely amorphous. Differences can be attributed to deposition conditions and coating coalescence, but could also be due to the freeze fracture method used to obtain the images.

Raman was used in an attempt to determine the change in sp^2/sp^3 ratios of the ten samples. This was deemed to be unsuitable and so SSNMR was utilised, however with fewer samples. It was found that the softest coatings had increased sp^3 content, suggesting that they also had increased hydrogen content; this was confirmed through ERD analysis, although large measurement errors were present. These compositional differences explain the differences in mechanical properties found in Chapter 6.

Chapter 6. Mechanical Properties

6.1 Introduction

This chapter presents the results from nanoindentation tests to determine the mechanical properties of the coating and polymer substrates. Hardness and Young's modulus determined by low depth nanoindentation on the coatings as-deposited onto polymers are shown, followed by P/S^2 (resistance to plastic deformation) as a function of depth to characterise surface response to loading.

The same design of experiments approach as shown in Chapter 4 was used to characterise the mechanical properties achievable, based on deposition conditions.

6.2 Hardness

6.2.1 Polymer Properties

The hardness of the polymer substrates was determined using nanoindentation with a Berkovich diamond indenter, as detailed in Chapter 3. The hardness of the two materials at indentation depths between 100 nm and 550 nm is shown in Figure 6-1. At all measured depths the PEI is harder than the ABS material, and also there is reduced standard deviation (shown by error bars) between measurements of PEI compared to ABS. The differences in error can be attributed to surface roughness effects (Chapter 4).

At low depths, both materials exhibit slightly increased hardness compared to indentations at increased depths [123, 124]. Both ABS and PEI are amorphous and so large indentation size effects (ISE) are not expected. As the indenter geometry has an influence on the manifestation of ISE, the substrate influence on any coating properties due to ISE is not quantifiable as both the indenter geometry and coating properties would affect how the load is transferred into the substrate.

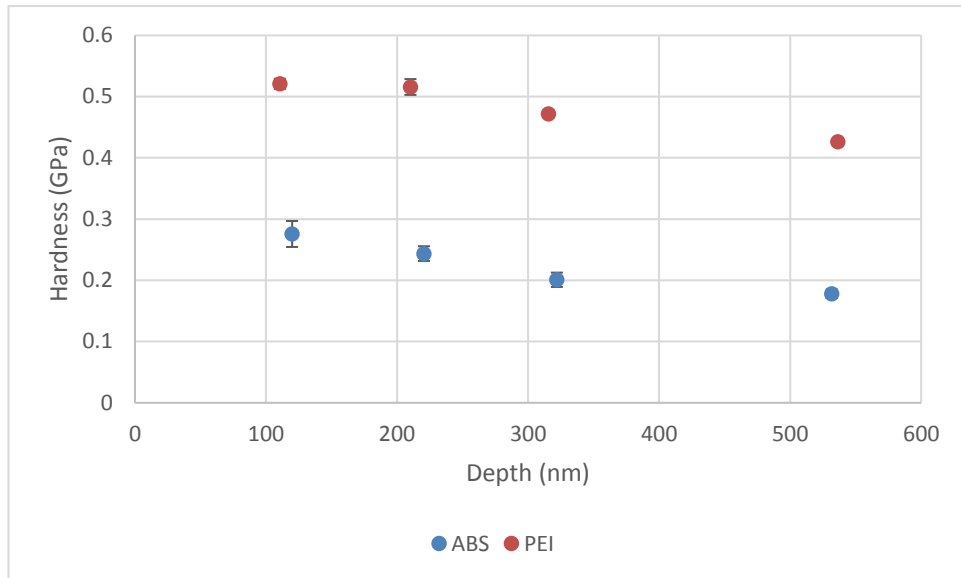


Figure 6-1 - Hardness of ABS and PEI polymer substrates at different indentation depths.

An increase in error for measurements on ABS lead to all depths being within one standard deviation of each other, the ISE on this material is negligible. The significant values for PEI are the shallowest and deepest indentations, which led to a reduction in hardness of 18% when performing the deepest indentations. Despite this, PEI remains measurably harder at all depths than ABS meaning that substrate effects on indentation measurements should be different when performed on the two coated polymers at similar depths. Including error, it is reasonable to make an approximation that PEI is roughly twice as hard as ABS.

6.2.2 Composite Properties

Figure 6-2 to Figure 6-11 show the hardness measured at depths between 1% and 10% of coating thickness for the 10 coatings produced on two polymer substrates (ABS and PEI). In all cases there is a general trend that as depth of indentation increases, hardness decreases. Due to error, it is impossible to discern between the substrates at most depths; this is more apparent at the lowest depths where surface roughness of the ABS samples result in large errors.

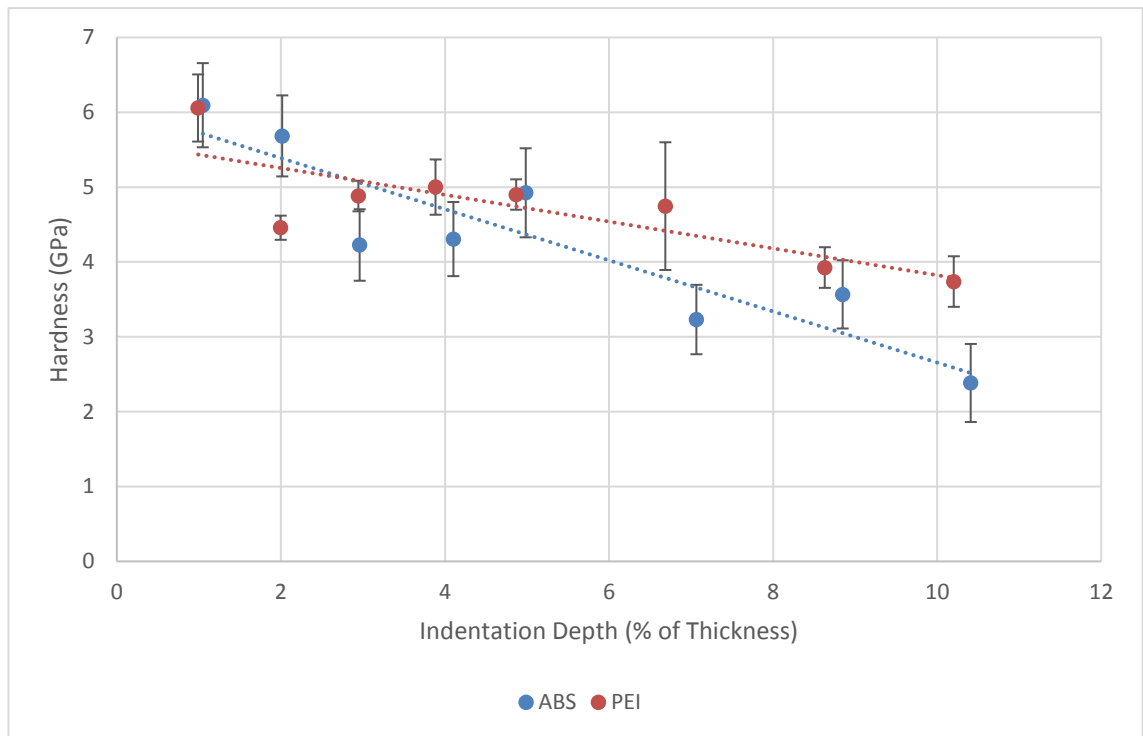


Figure 6-2 - Hardness of DOE leg 1 at increasing indentation depths.

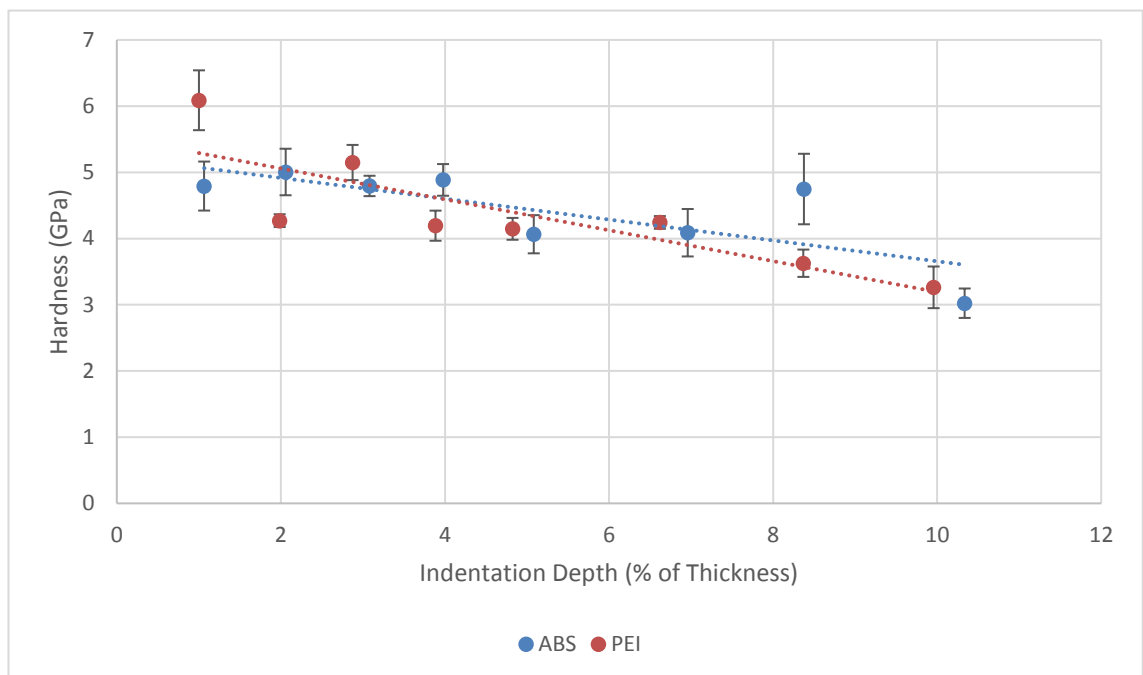


Figure 6-3 - Hardness of DOE leg 2 at increasing indentation depths.

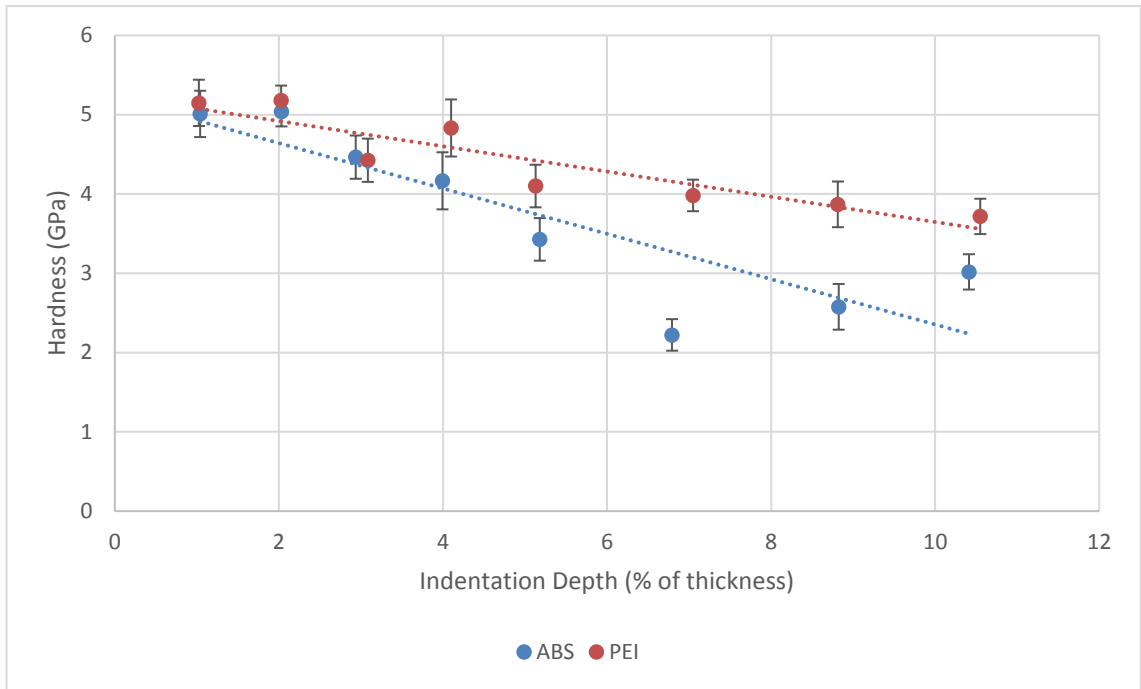


Figure 6-4 - Hardness of DOE leg 3 at increasing indentation depths.

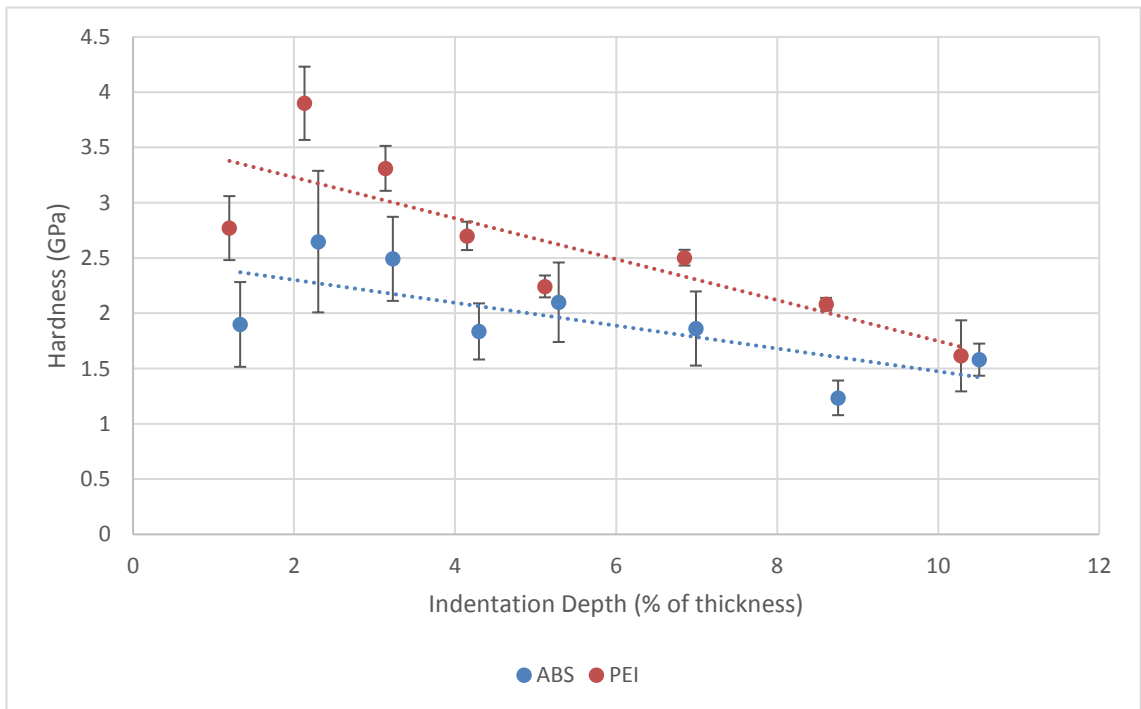


Figure 6-5 - Hardness of DOE leg 4 at increasing indentation depths.

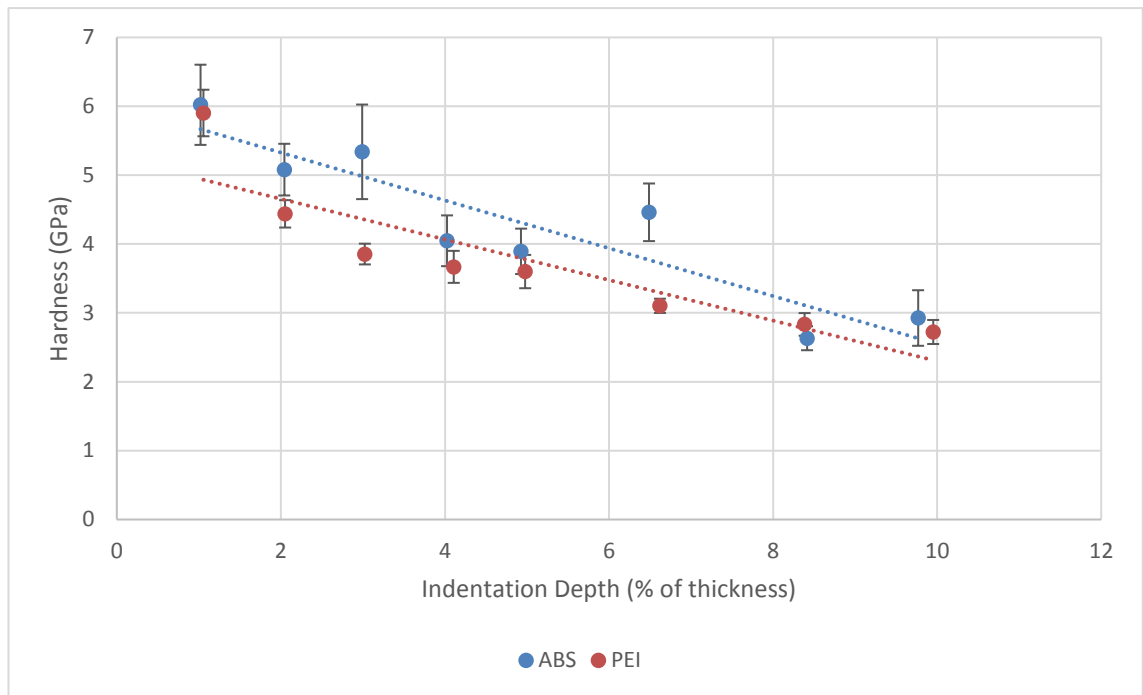


Figure 6-6 - Hardness of DOE leg 5 at increasing indentation depths.

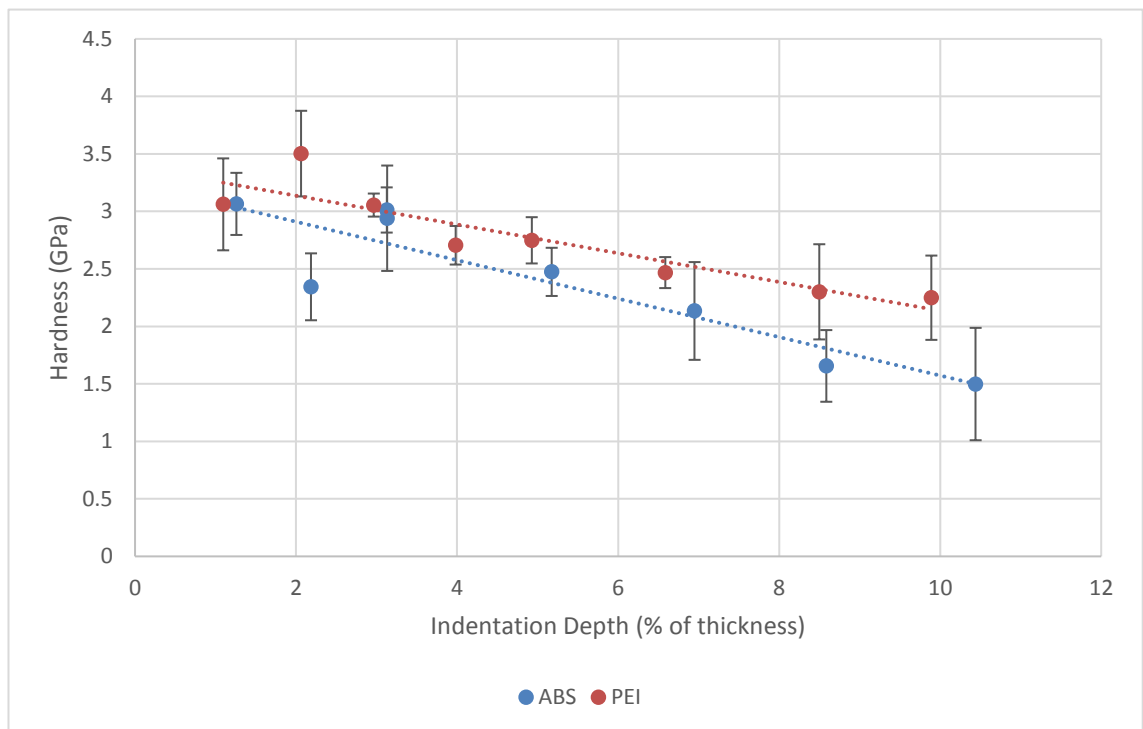


Figure 6-7 - Hardness of DOE leg 6 at increasing indentation depths.

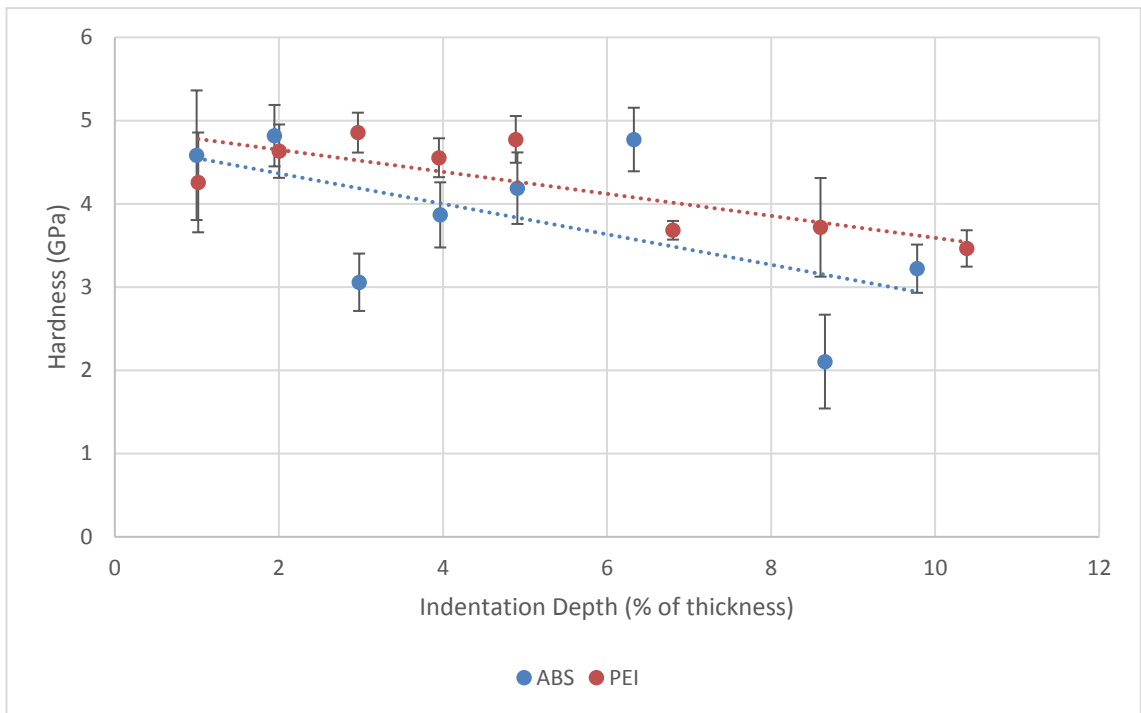


Figure 6-8 - Hardness of DOE leg 7 at increasing indentation depths.

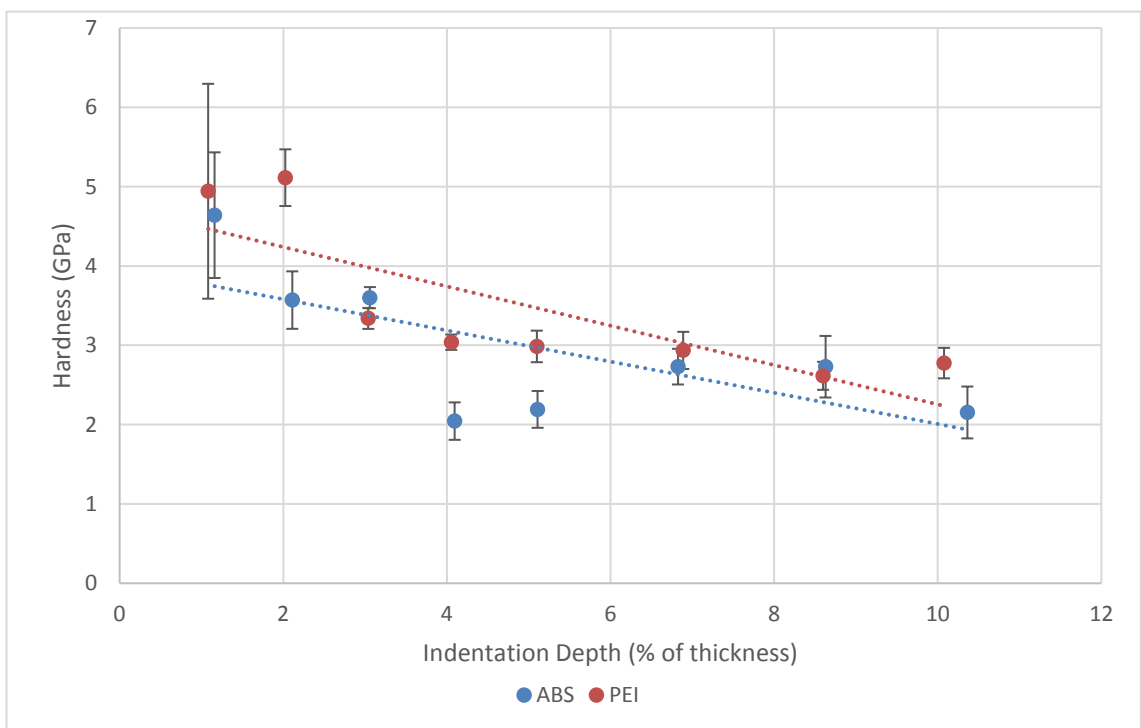


Figure 6-9 - Hardness of DOE leg 8 at increasing indentation depths.

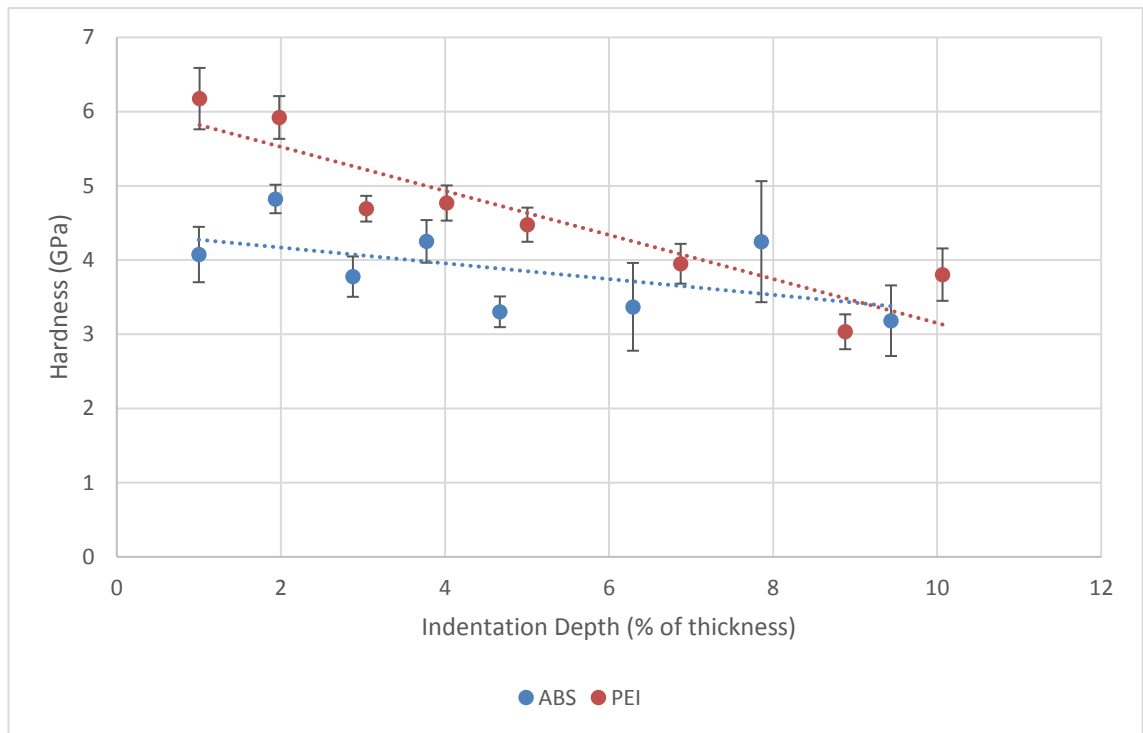


Figure 6-10 - Hardness of DOE leg 9 at increasing indentation depths.

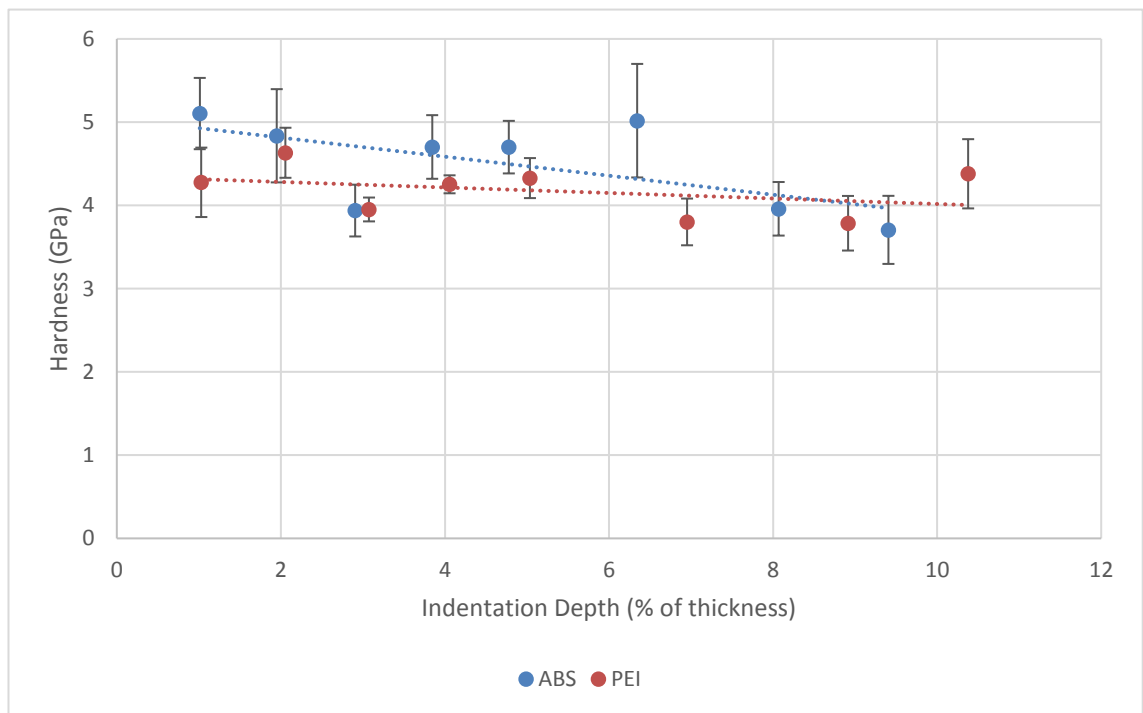


Figure 6-11 - Hardness of DOE leg 10 at increasing indentation depths.

Figure 6-12 shows the relationship between coating thickness and the hardness measured on both substrates. The hardness obtained at normalised indentation depths of 3% of coating thickness were used; this was to make sure that the values measured had reduced error, but were still shallow enough as to remove the maximum amount of substrate effects from the measurement. The cluster of results on the left hand side of the plot with low hardness and low thickness are all belonging to legs where coatings were deposited under low pressure, low acetylene ratio conditions. The cluster of data points at just over 4 μm thickness and roughly 4 – 5 GPa hardness are corresponding to those legs where increased acetylene ratios and increased pressures were used. Alternatively, low thickness and hardness coatings were deposited under low partial pressures of acetylene and harder, thicker coatings were produced under increased partial pressures of acetylene.

The majority of coatings were approximately 4 μm thick, resulting in a cluster of hardness values in the corresponding position; there were enough coatings produced at other thicknesses in order to show that there is a weak correlation between coating thickness and hardness. As coating thickness increases, so does the hardness measured at normalised depths of 3% of coating thickness. To ensure the validity of normalising the indentation depth, i.e. the hardness increases were due to changes in coating property and not increased substrate effects when indenting thinner coatings, a second sample of DOE leg 6 was produced with increased thickness. A comparison between the two thicknesses is shown in Figure 6-13.

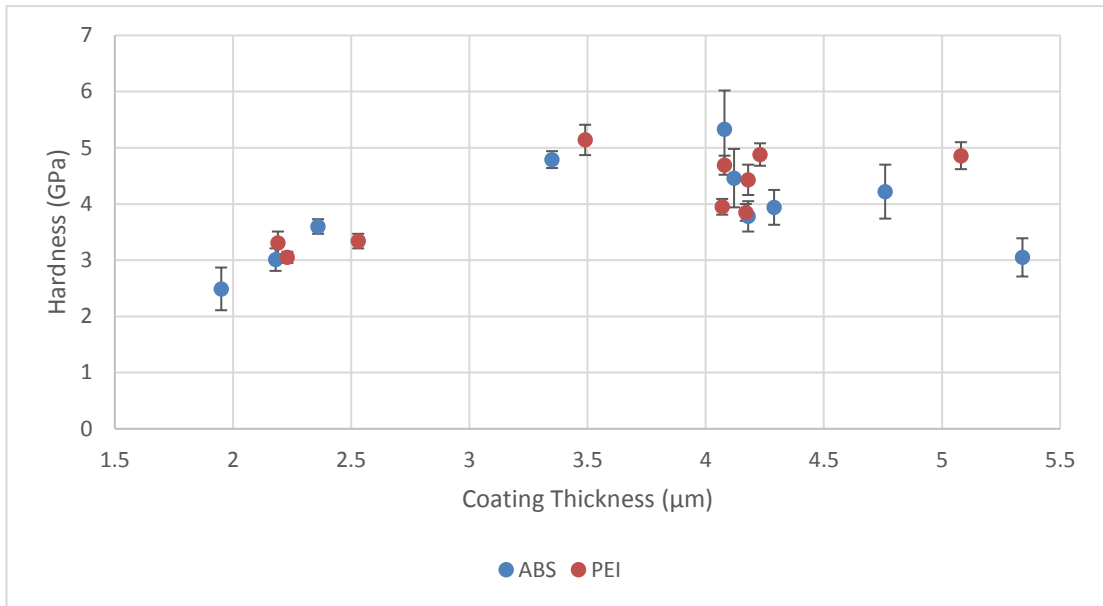


Figure 6-12 - Hardness of the coatings measured on both substrates as a function of coating thickness.

The hardness determined from indentations made on both thicknesses of the coating were within error at all depths. The small variation between calculated average values of hardness, despite large errors, shows that normalising the depth to coating thickness is valid in this case.

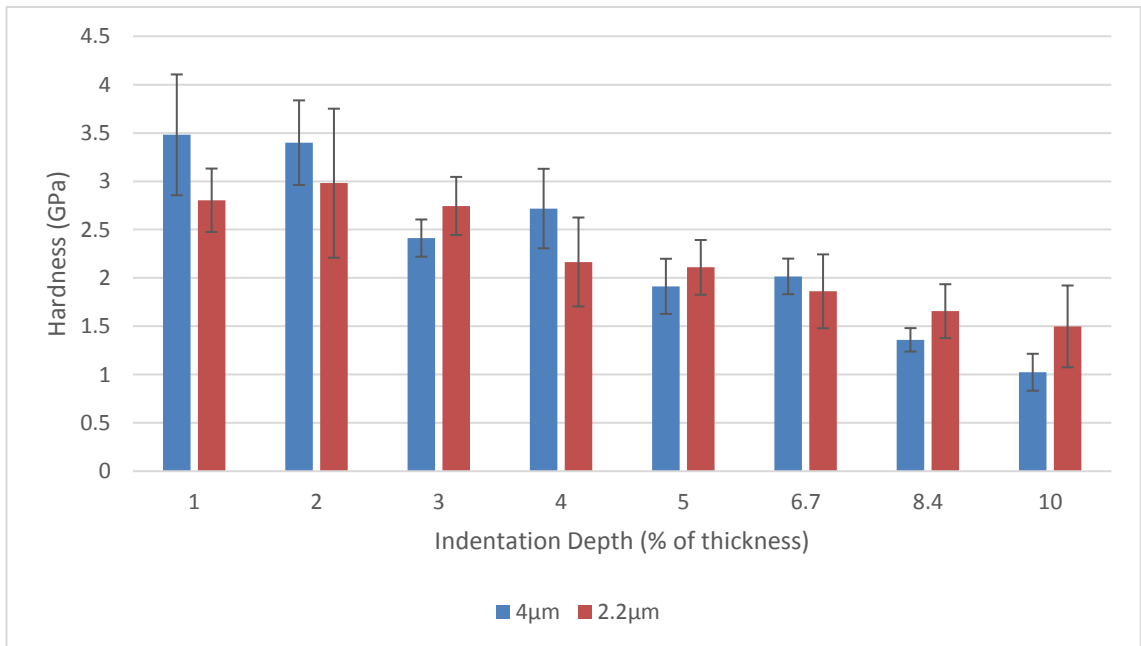


Figure 6-13 - Hardness vs normalised depth of two thickness variations (2.2 µm & 4 µm) of the coating from DOE leg 6 on ABS substrate.

Figure 6-14 and Figure 6-15 show the trend lines from hardness measurements on the two different substrates (taken from Figure 6-2 - Figure 6-11). The trend lines allow comparison of the coatings on a single figure with respect to how the hardness varies as a function of depth, but should not be taken as absolute measures of hardness. On both substrates the softest coatings were produced during legs 4 and 6, whilst many of the coatings resulted in similar hardness at low depths. Comparing the coatings on ABS to those on PEI, only 3 samples exhibited hardness above 3 GPa at 10% depth measured on ABS, whereas 6 coatings measured on PEI had hardness above 3 GPa at 10% depth. This could be attributed to the increased hardness of the substrate, in the case of PEI. On the PEI substrate, the coatings can be categorised into 3 groups; these groupings, seen in Figure 6-15, are likely due to the decreased error when indenting the smoother surfaces leading to the trend line producing a more accurate representation of the data. However, it could also be due to the differing substrate effects.

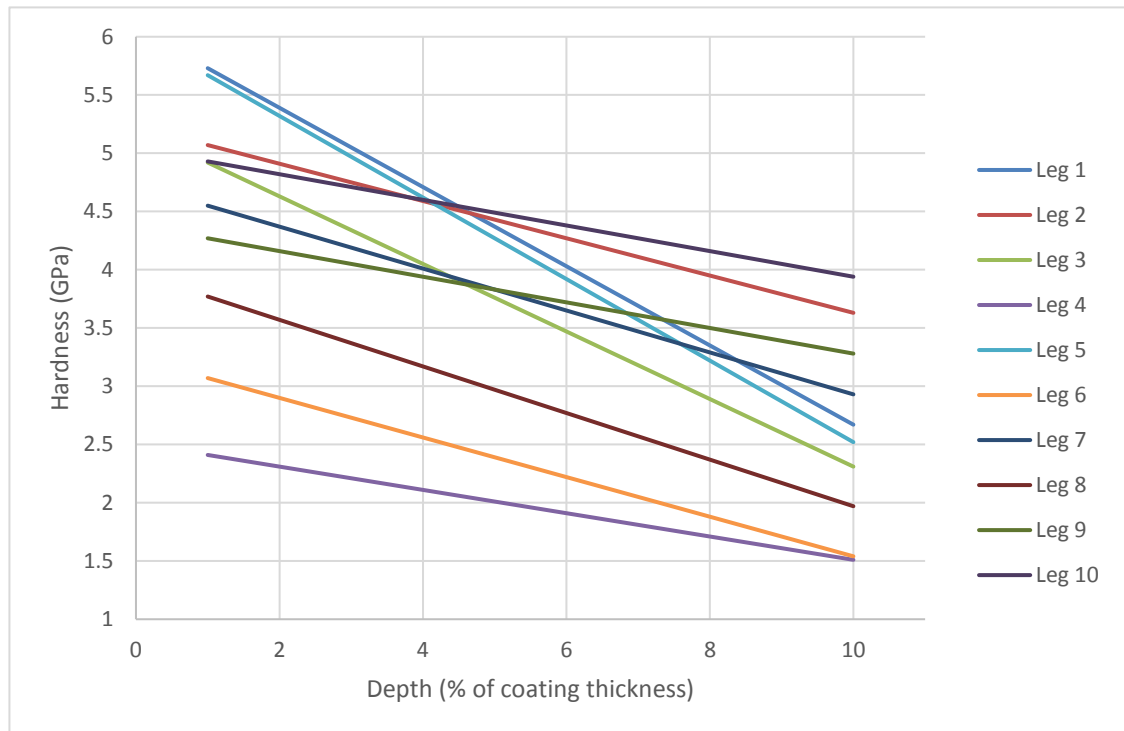


Figure 6-14 – Hardness comparison of all 10 coatings measured on ABS.

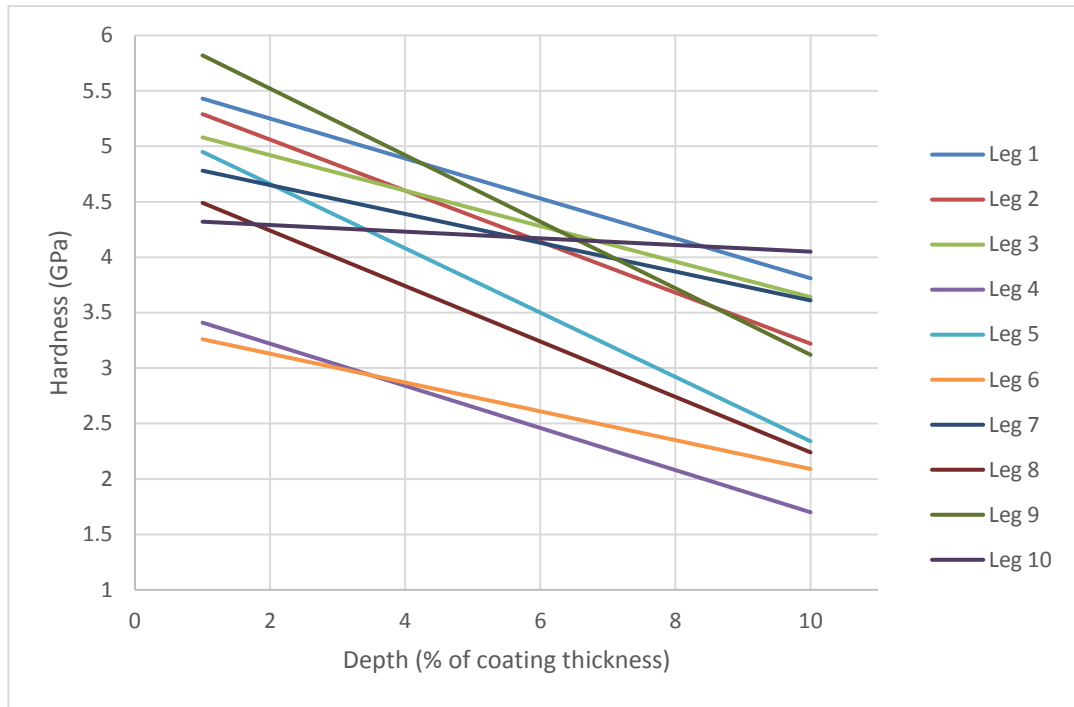


Figure 6-15 - Hardness comparison of all 10 coatings measured on PEI.

Coatings 4 & 6 remain the lowest hardness coatings throughout the depth profile. Coatings 5 & 8 have hardness at low depths comparable to the other coatings, however the hardness reduces more drastically as depth increases. The remaining 6 coatings show similar behaviour with hardness in the range of 4 - 4.5 GPa at a depth of 6 %. These differences will not be as apparent in the DOE model, due to the model incorporating a hardness value for each sample at a specific depth.

6.2.3 Design of Experiments model – Hardness








In order to input the hardness data into the DOE model, a hardness at a specific depth was chosen. At 5% depth the larger measurement errors due to surface roughness had reduced in most cases, whilst the substrate effects were minimised compared to increased normalised depths. Therefore, the hardness at 5% depth was used for both ABS and PEI substrates. The depth was kept the same for both substrates, despite the lower error of measurements on PEI samples, in order to keep consistency and allow comparison between the models produced for both substrates.

6.2.3.1 ABS Substrate

The influence of each factor on the measured hardness of the coatings produced on ABS substrates is shown in Table 6-1. The factors are ranked from most influential to least with the blue line representing a confidence interval of 99%. As none of the log worth bars pass this line, none of the factors have an influence on hardness within this confidence interval. Of the main effects, gas flow rate ratio and working pressure have a significant effect at a 95% confidence level, indicated by the p-values of 0.016 and 0.033 respectively. Because these factors are not fully independent (a higher gas flow rate at a given ratio will increase pressure) the interaction for these two factors combined is also significant.

Figure 6-16 shows how the main factors interact to produce coatings of different hardness. Greater separation between the red line (lowest set point) and blue line (highest set point) indicate a greater influence on hardness produced when varying those factors. It can be seen that to produce the hardest surface, the pressure must be increased, whilst also increasing the gas flow rate ratio. Increasing these two factors together, effectively increases the partial pressure of C_2H_2 in the chamber, meaning more carbon species are available for coating growth. A greater density of species responsible for coating growth resulting in harder surfaces could be due to a number of reasons; less inclusion of argon in the coating, a lower likelihood of hydrogen incorporation due to the energy of carbon species being high enough to displace them, and increased energy leading to the preferential formation of sp^3 bonds.

Table 6-1 – Effect summary for DOE model of hardness on ABS substrate.

Source	Log Worth	P-Value
Gas flow rate ratio	1.783 	0.01649
Working Pressure (mbar)	1.479 	0.03321
Working Pressure (mbar)*Gas flow rate ratio	1.338 	0.04596
Gas flow rate ratio*Gas flow rate ratio	1.152 	0.07051
MW Power Set point (W)	1.001 	0.09970
MW Power Set point (W)*Working Pressure (mbar)	1.001 	0.09984
MW Power Set point (W)*Gas flow rate ratio	0.017 	0.96118

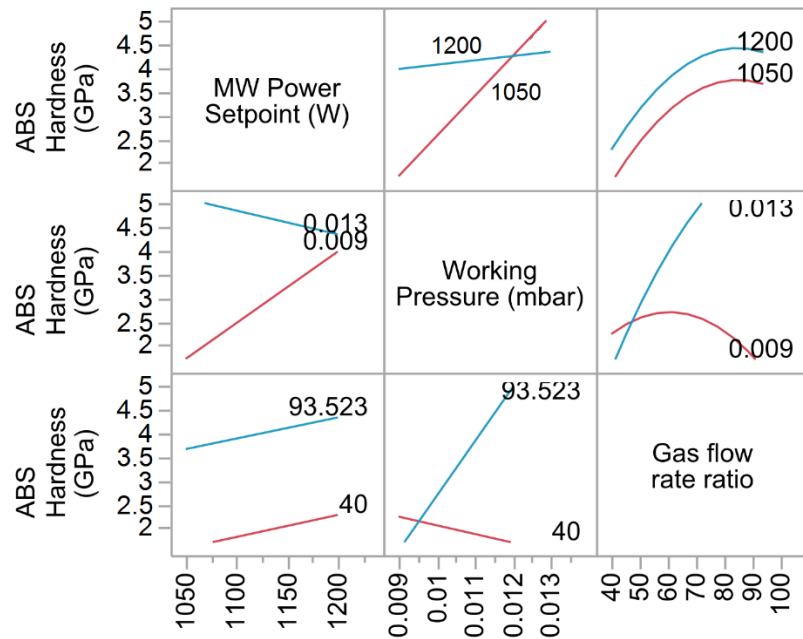


Figure 6-16 - Interaction profiles for DOE model of hardness on ABS substrate.

Due to machine limitations a stable plasma could not be sustained in 100% C_2H_2 , however if this could be achieved by increasing the power available to the microwave generators it may be possible to produce harder coatings than those produced here.

Of the possible interactions shown in the interaction profile, only the interaction between working pressure and gas mixture is significant at a 95% confidence interval. The remaining interactions are either not significant or not real.

6.2.3.2 PEI Substrate

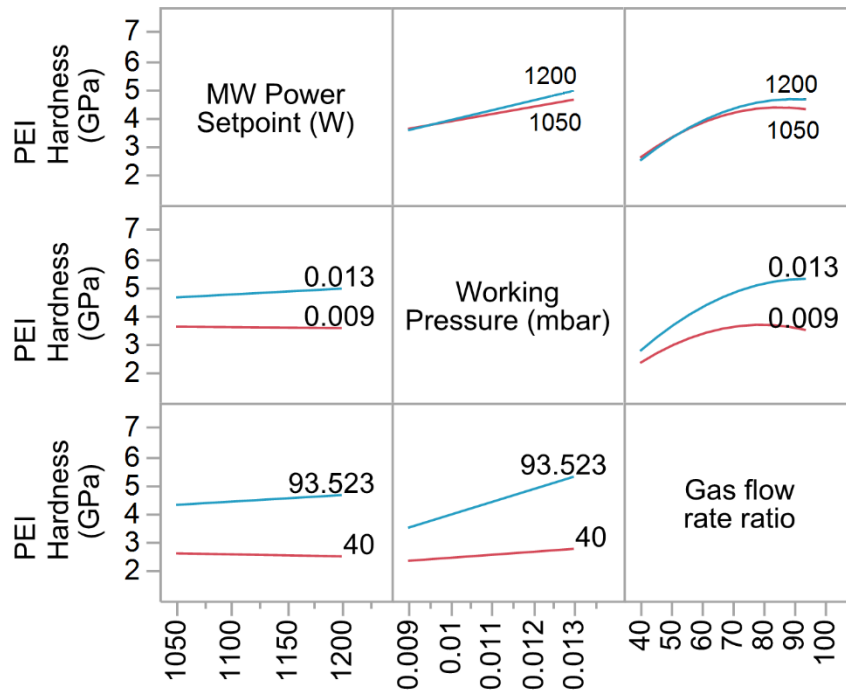


Figure 6-17 - Interaction profiles for DOE model of hardness on PEI substrate.

Table 6-2 - Effect summary for DOE model of hardness on PEI substrate.

Source	Log Worth	P-Value
Gas flow rate ratio	1.152	0.07052
Working Pressure (mbar)	0.545	0.28507
Gas flow rate ratio*Gas flow rate ratio	0.543	0.28666
Working Pressure (mbar)*Gas flow rate ratio	0.209	0.61837
MW Power Set point (W)*Gas flow rate ratio	0.138	0.72852
MW Power Set point (W)	0.102	0.79108 ^
MW Power Set point (W)*Working Pressure (mbar)	0.057	0.87790

The effect summary for hardness of the coatings measured on PEI substrates is shown in Table 6-2. As with measurements on ABS substrates, the gas flow rate ratio has the most influence on hardness, however on the PEI substrates there are no factors which have a significant effect at a 95% confidence level. The hardness at 5% depth on all PEI samples is similar for 6/10 coatings and this reduces the significance of varying the factors in the model. Despite the confidence levels being lower for PEI, they follow the same order as for ABS meaning the same conclusions can be made; increasing the

percentage of C_2H_2 in the gas mixture and the working pressure will produce the hardest coatings. Changes in microwave power alone will have negligible effects on coating hardness. These interactions are shown in

Figure 6-17.

6.3 Young's modulus

6.3.1 Polymer Properties

The Young's modulus of the polymer substrates was determined using nanoindentation with a Berkovich diamond indenter, as detailed in Chapter 3. The modulus of the two materials at indentation depths between 100 nm and 550 nm is shown in Figure 6-18. At all measured depths the PEI has larger modulus than the ABS material, and also there is reduced standard deviation (shown by error bars) between measurements of PEI compared to ABS. The differences in error can be attributed to surface roughness effects. At all depths PEI is roughly 50% stiffer than ABS.

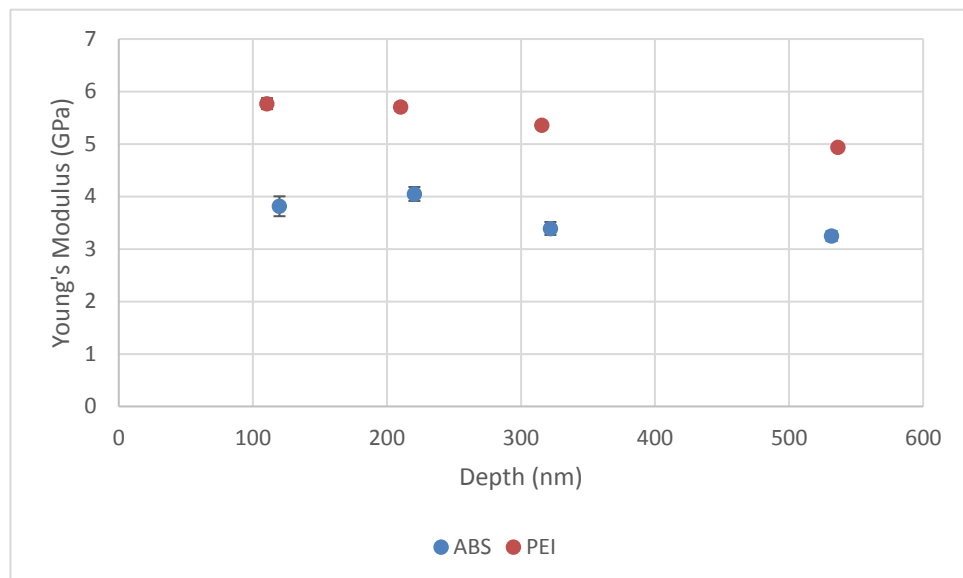


Figure 6-18 - Young's modulus of ABS and PEI polymers measured at different depths.

As with hardness measurements on the two polymers, all ABS measurements at different depths are within error, and there is a decrease in modulus as depth increases. The

difference between the lowest and highest depths measured on PEI is a 14% reduction in stiffness so indentation size effects are small, despite being present.

6.3.2 Composite Properties

Figure 6-19 shows that if indentation depths are normalised to coating thickness, the Young's modulus scales linearly with thickness. At all depths, except for 2%, the measurements are within error on the two thicknesses of coating, therefore it is valid to compare all coatings if depth is normalised. The difference at 2% can be attributed to experimental error and overlooked as the trend is apparent at all other points.

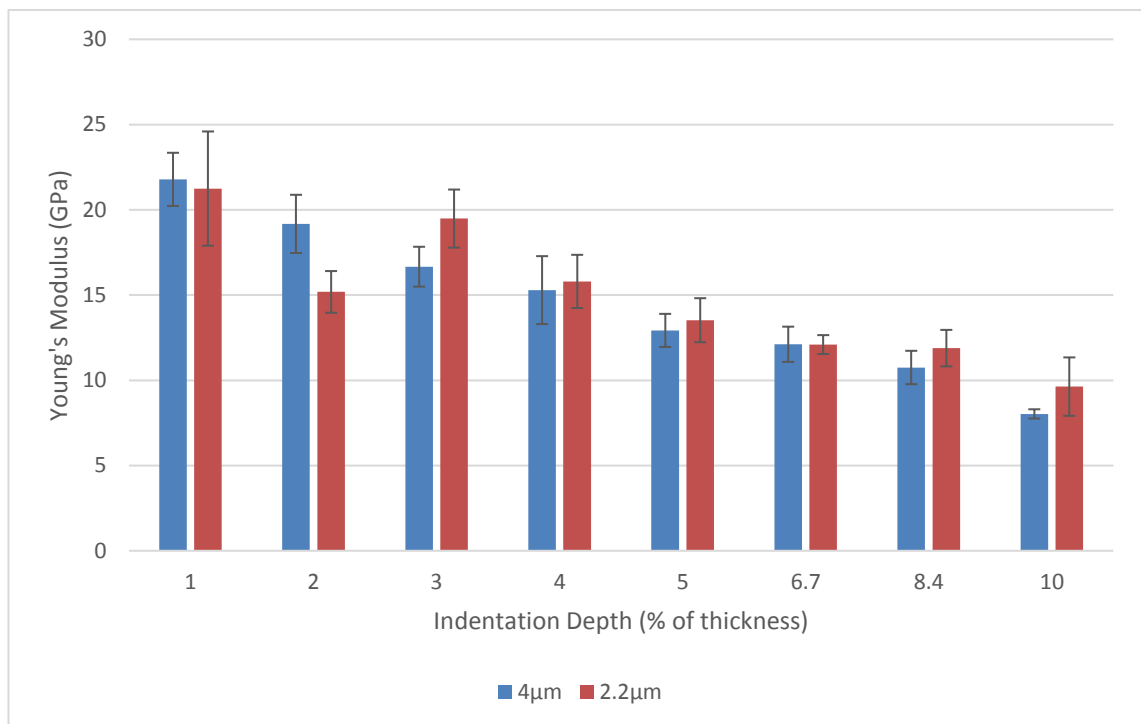


Figure 6-19 - Young's modulus as a function of depth on two coating produced at different thicknesses on ABS substrates.

Figure 6-20 - Figure 6-29 show the Young's modulus of the coatings on the two substrates as a function of depth. Generally, as depth increases Young's modulus decreases. Very similar values were measured when comparing the two substrate materials, meaning that differentiating between the two substrate-coating systems by Young's modulus measured at low depths is not possible. Despite this, the reduction in modulus as depth increases is likely due to the substrate deformation and so called

substrate effects, meaning that a single value for Young's modulus of the coatings cannot be determined solely from experimental data.

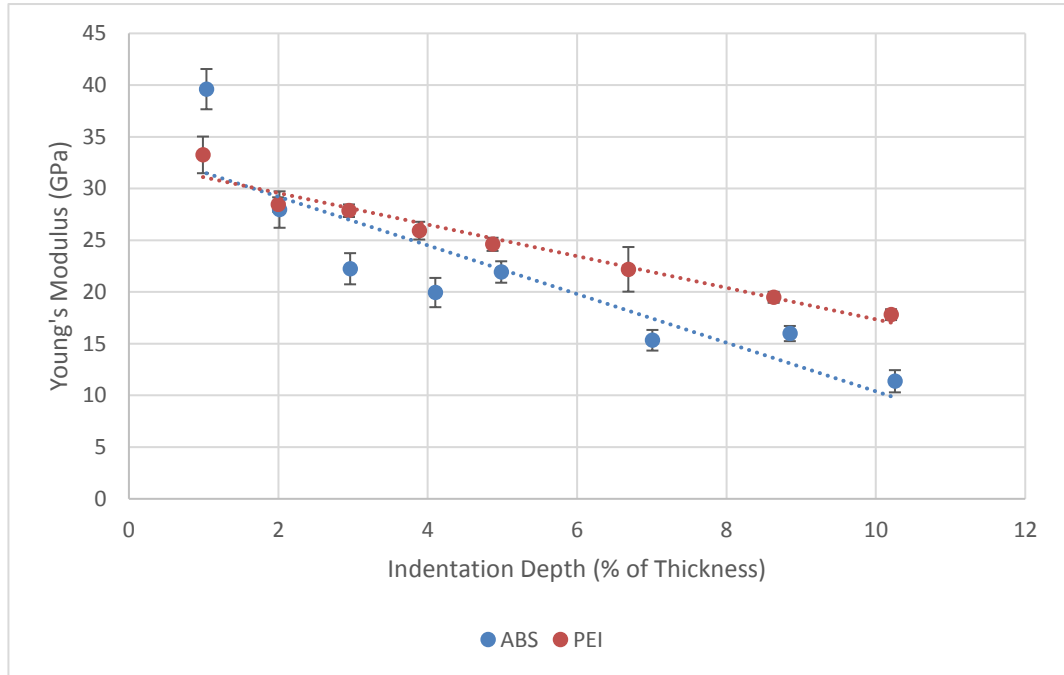


Figure 6-20 - Young's modulus as a function of depth for DOE leg 1.

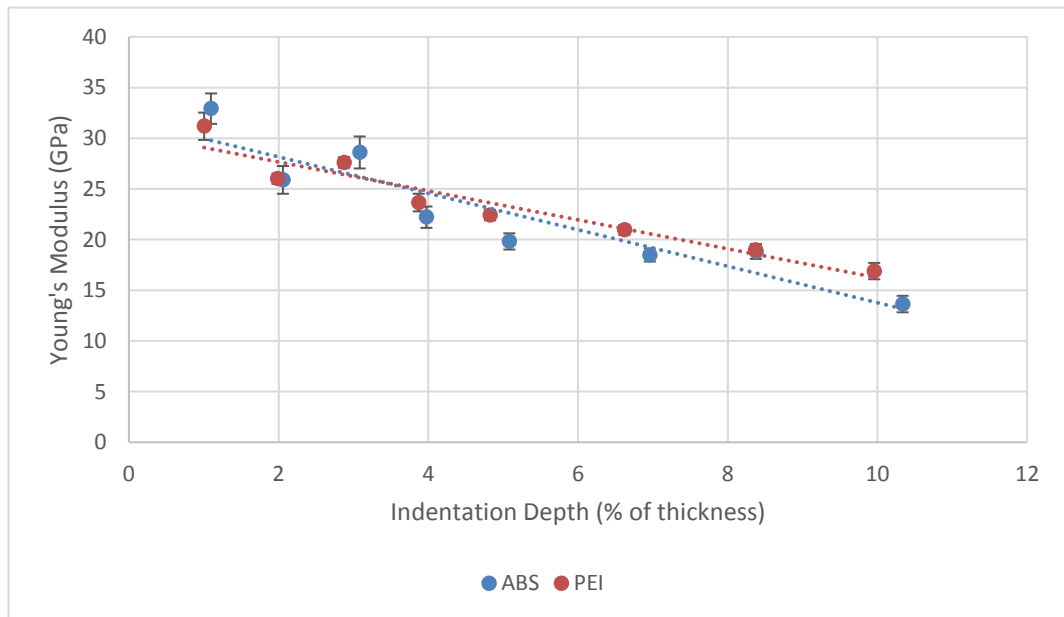


Figure 6-21 - Young's modulus as a function of depth for DOE leg 2.

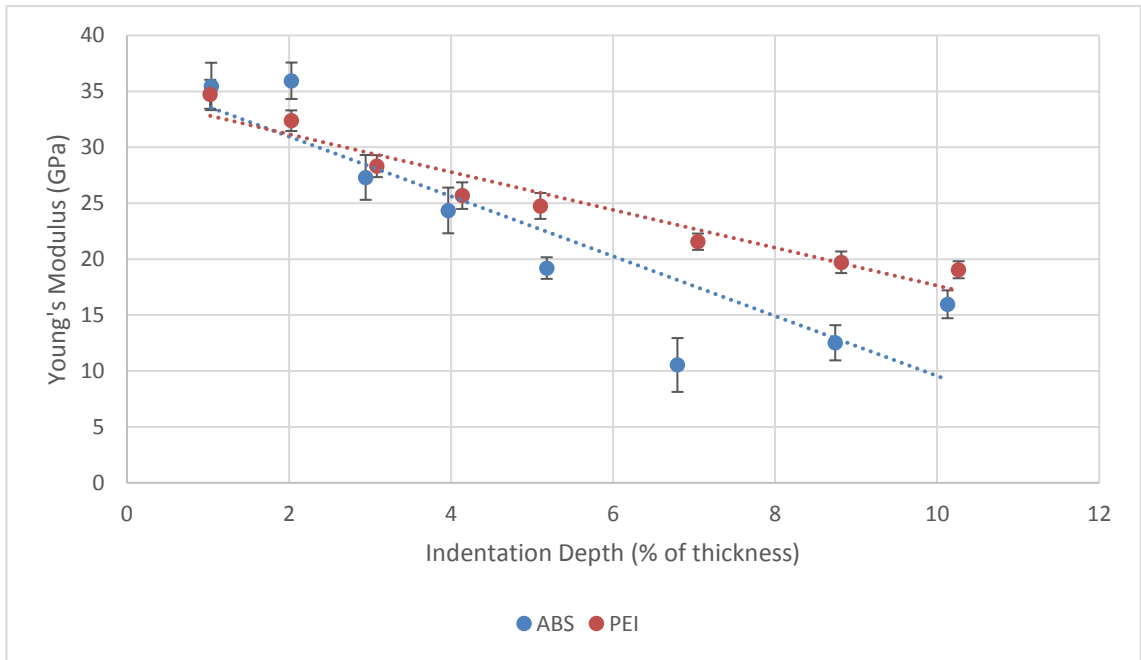


Figure 6-22 - Young's modulus as a function of depth for DOE leg 3.

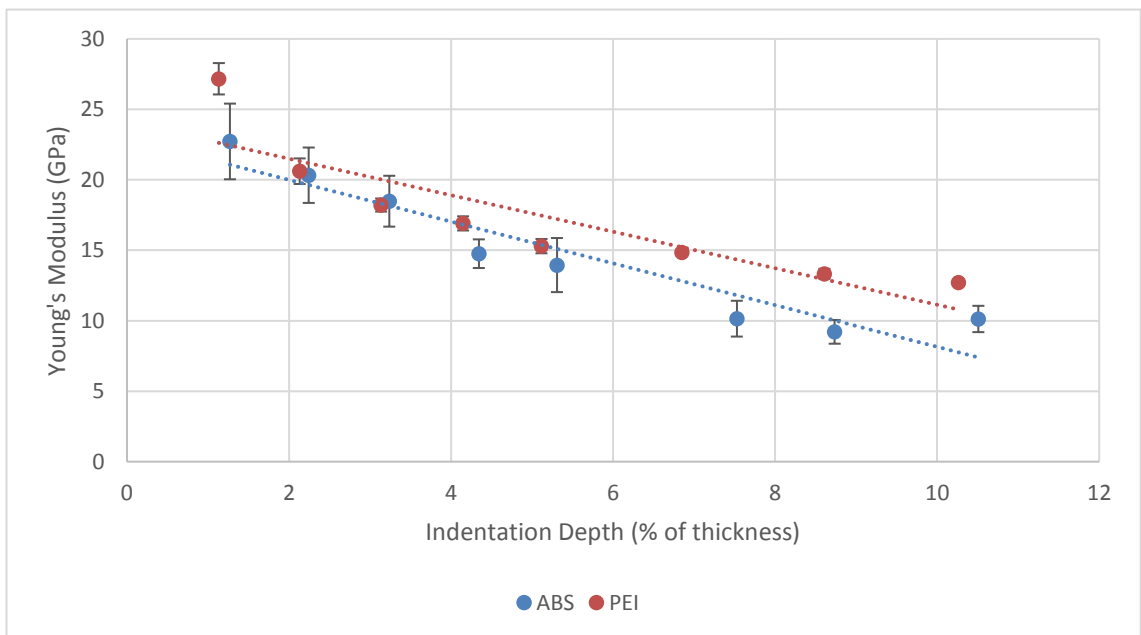


Figure 6-23 - Young's modulus as a function of depth for DOE leg 4.

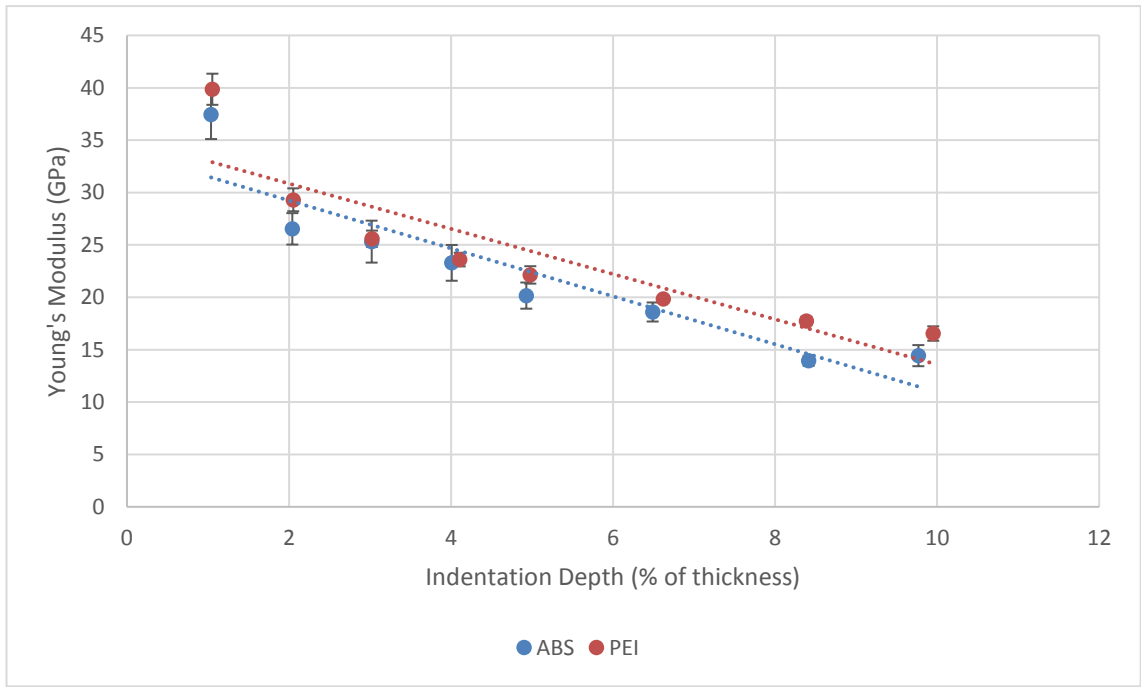


Figure 6-24 - Young's modulus as a function of depth for DOE leg 5.

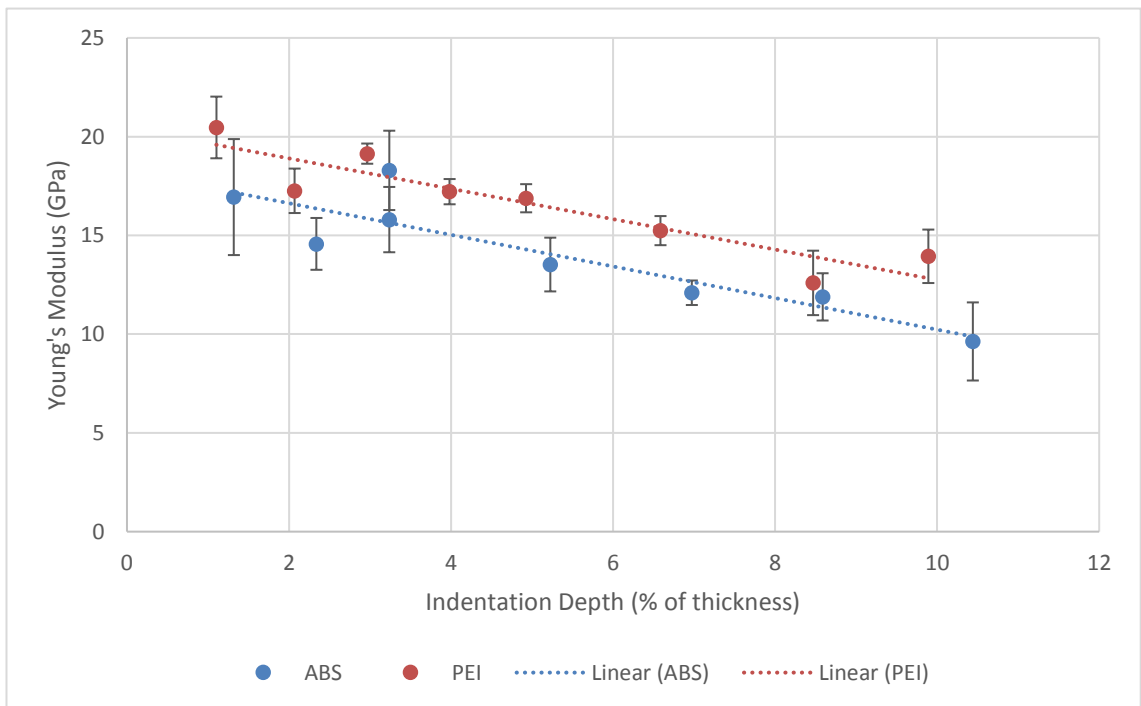


Figure 6-25 - Young's modulus as a function of depth for DOE leg 6.

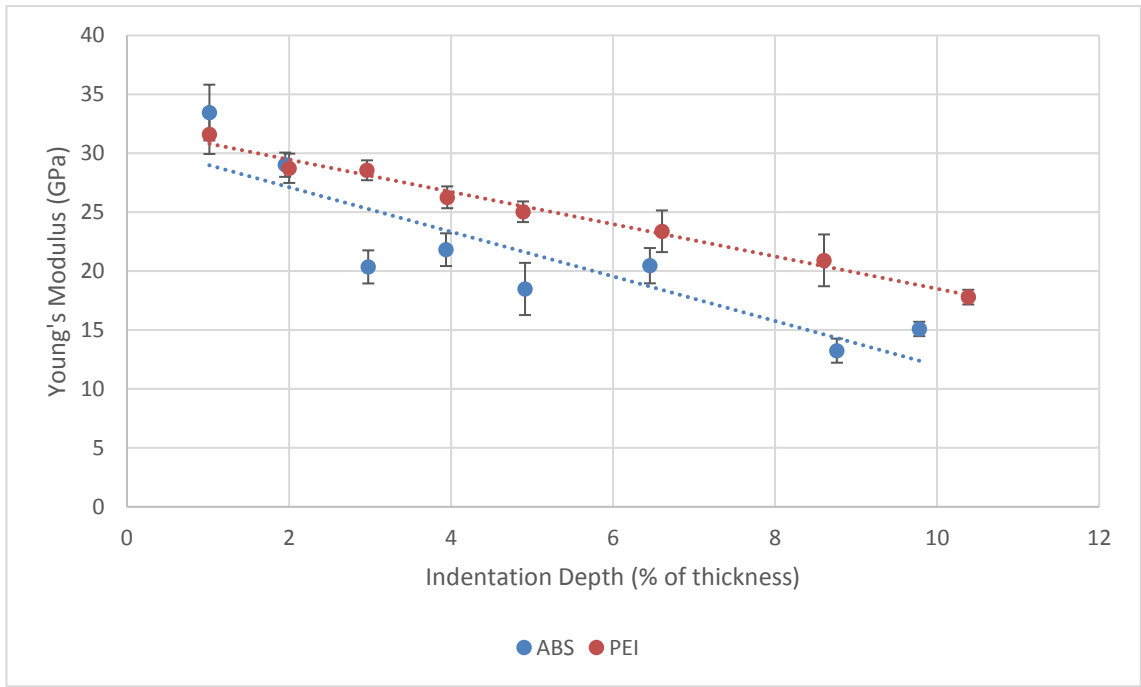


Figure 6-26 - Young's modulus as a function of depth for DOE leg 7.

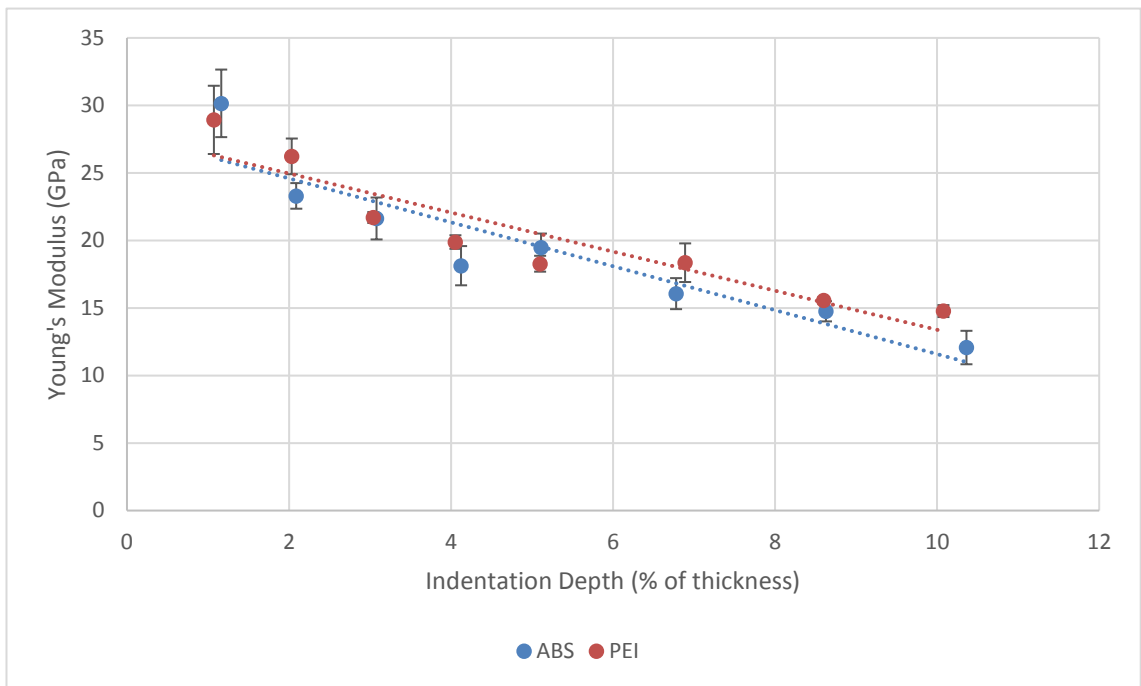


Figure 6-27 - Young's modulus as a function of depth for DOE leg 8.

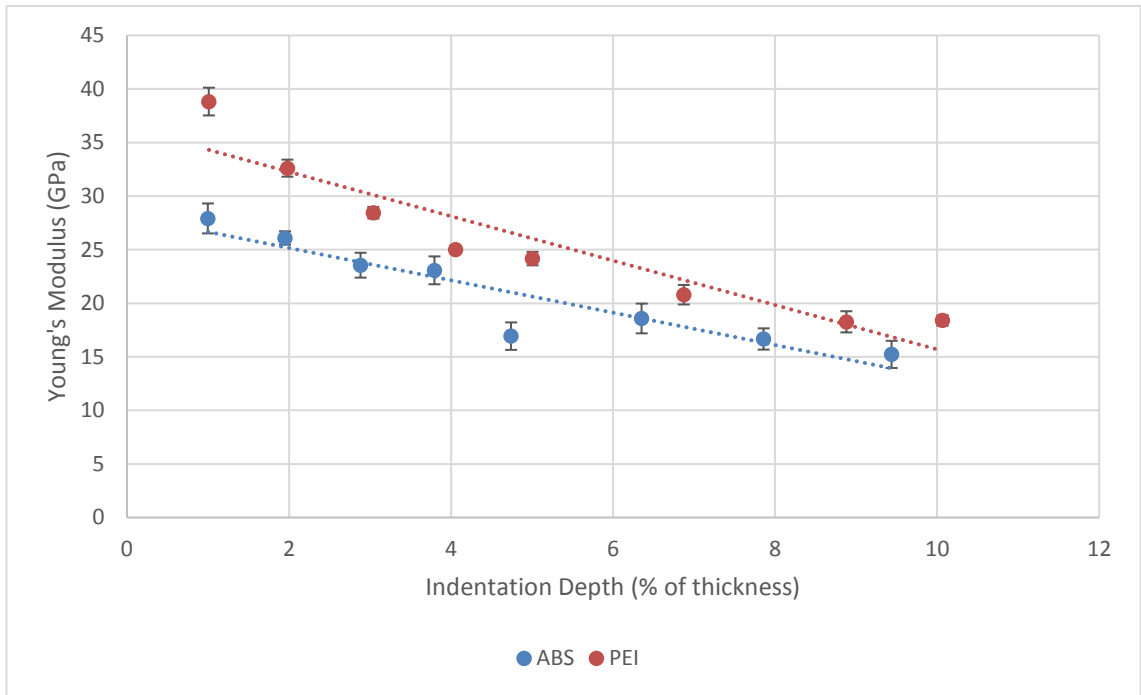


Figure 6-28 - Young's modulus as a function of depth for DOE leg 9.

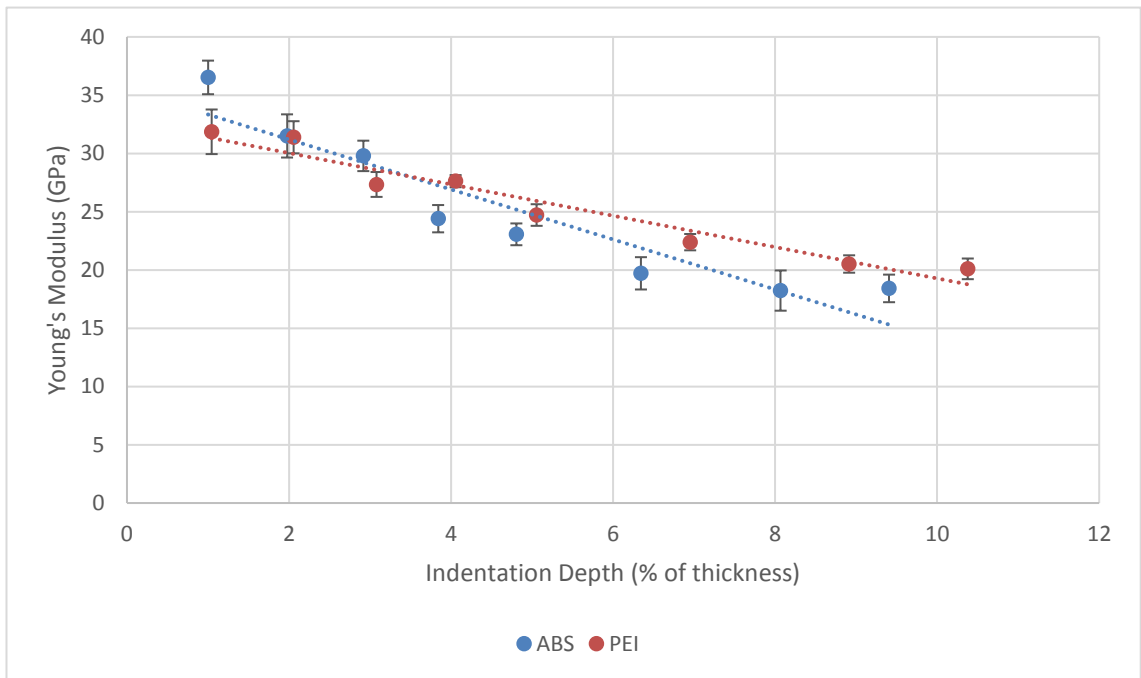


Figure 6-29 - Young's modulus as a function of depth for DOE leg 10.

Figure 6-30 and Figure 6-31 compare the Young's modulus as a function of depth of all 10 coatings that were produced on the two substrate materials. The plots are linear trend lines from Figure 6-20 - Figure 6-29 and as such should not be used to determine Young's modulus for the coatings and instead allow visualisation of how Young's modulus varies as a function of indentation depth in a single figure. As with hardness, coatings from legs 4 and 6 have the lowest modulus at all depths on both substrates, however the rest of the coatings can be said to reduce from roughly 30 GPa to 12.5 GPa in the case of the ABS substrate, and from roughly 30 GPa to 17.5 GPa in the case of the PEI substrate.

As Young's modulus is a purely elastic measure, whereas hardness is a measure of elastic and plastic deformation, the substrate effects are more clearly visible with Young's modulus measurements resulting in a decrease of modulus at 10% depth on all surfaces. This is due to the elastic strain around the indenter tip extending further into the substrate at any given depth than plastic strain, allowing greater substrate effects in the measurement when the Young's modulus is determined from the upper portion of the unloading curve.

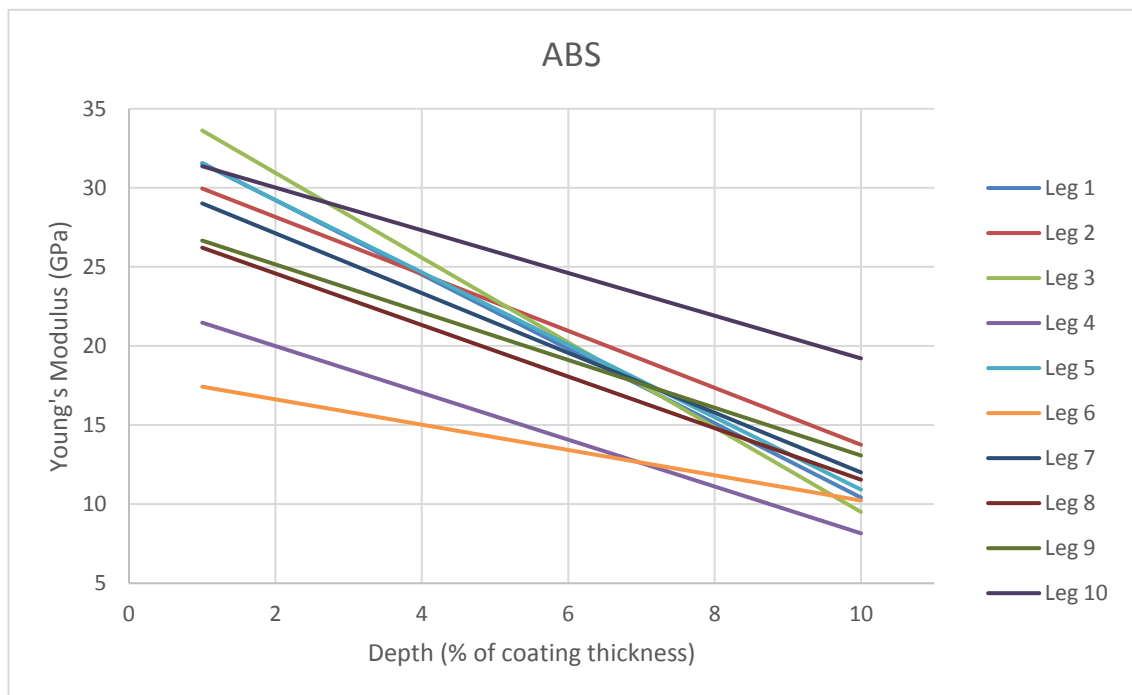


Figure 6-30 - Young's modulus comparison of all 10 coatings on ABS.

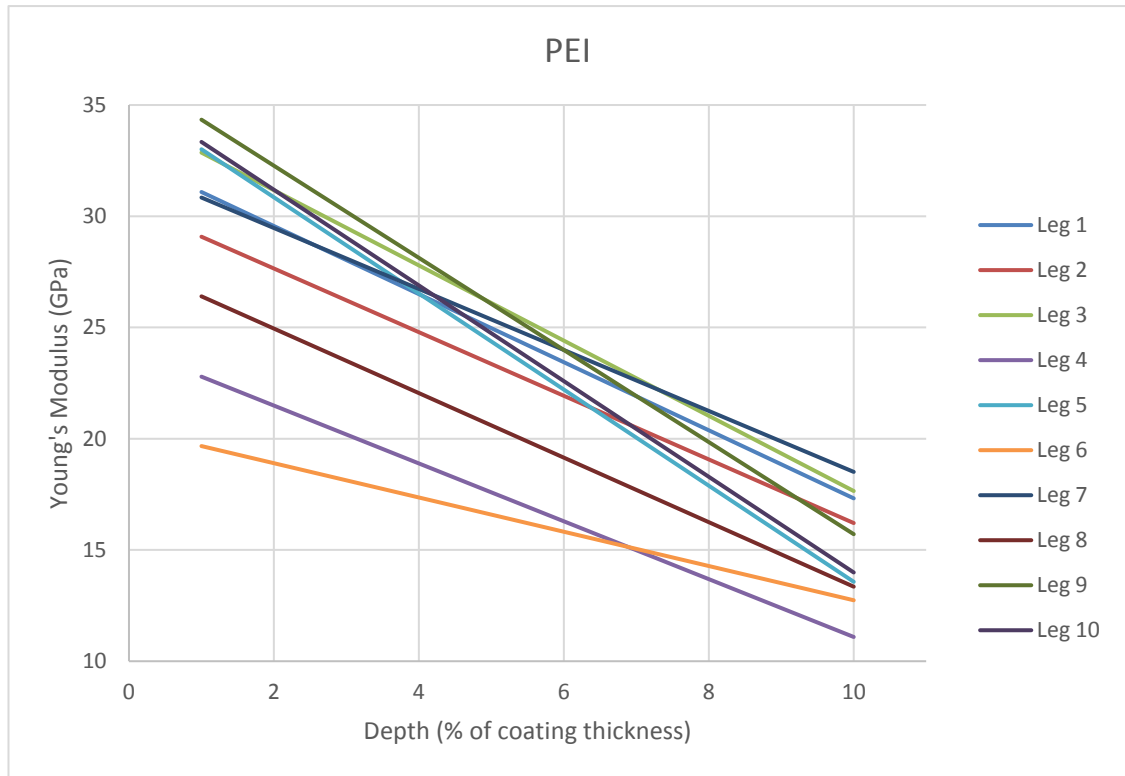


Figure 6-31 - Young's modulus comparison of all 10 coatings on PEI.

6.3.3 Design of Experiments model – Young's Modulus

As with hardness, the Young's modulus determined from indentations at a normalised depth of 5% coating thickness were used in the model.

6.3.3.1 ABS Substrate

The summary of effects is shown in Table 6-3. There is no main factor which has a significant effect on the Young's modulus measured on ABS substrates. With similar p-values/log worth, gas flow rate ratio and working pressure (as well as the interaction between both) have a similar effect on modulus. As can be seen in Figure 6-32, to increase the modulus, the working pressure and percentage of C_2H_2 should be increased. As this is also the case for hardness, Young's modulus and hardness should correlate; an increase in hardness should result in an increase in modulus.

Of note is that this model predicts no main effects at a 95% confidence interval; that is, varying any parameter is unlikely to yield a repeatable change in Young's modulus.

Table 6-3 - Effect summary for DOE model of Young's modulus on ABS substrate

Source	Log Worth	P-Value
Gas flow rate ratio	0.841	0.14426
Working Pressure (mbar)	0.837	0.14571
MW Power Set point (W)*Working Pressure (mbar)	0.817	0.15244
Working Pressure (mbar)*Gas flow rate ratio	0.480	0.33079
Gas flow rate ratio*Gas flow rate ratio	0.459	0.34770
MW Power Set point (W)*Gas flow rate ratio	0.208	0.61981
MW Power Set point (W)	0.118	0.76133 ^

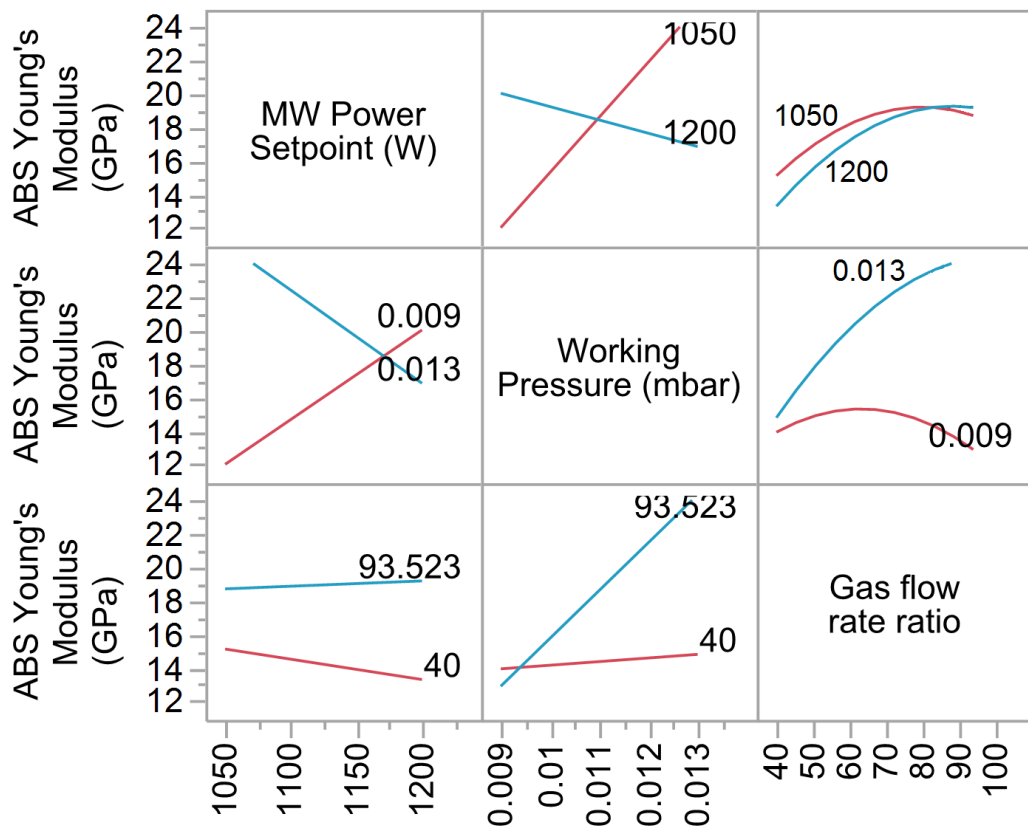


Figure 6-32 - Interaction profiles for DOE model of Young's modulus on ABS substrate.

6.3.3.2 PEI Substrate

The main effects summary and interaction profiles for Young's modulus measured on PEI substrates can be seen in Table 6-4 and Figure 6-33 respectively. Compared to ABS the most significant factor is also gas flow rate ratio, but in this case it appears to have greater influence than the other factors, or combinations of. The gas flow ratio is

significant with a 95% confidence level, which is demonstrated by the separation of the red and blue line in the interaction profiles. Once again, to produce the stiffest surface, C₂H₂ percentage should be increased, and to a lesser extent working pressure.

Table 6-4 – Effect summary for DOE model of Young's modulus on PEI substrate.

Source	Log Worth	P-Value
Gas flow rate ratio	1.446	0.03577
Gas flow rate ratio*Gas flow rate ratio	1.164	0.06853
Working Pressure (mbar)	0.615	0.24282
MW Power Setpoint (W)*Gas flow rate ratio	0.187	0.65076
Working Pressure (mbar)*Gas flow rate ratio	0.160	0.69239
MW Power Set point (W)*Working Pressure (mbar)	0.158	0.69431
MW Power Set point (W)	0.068	0.85434 ^

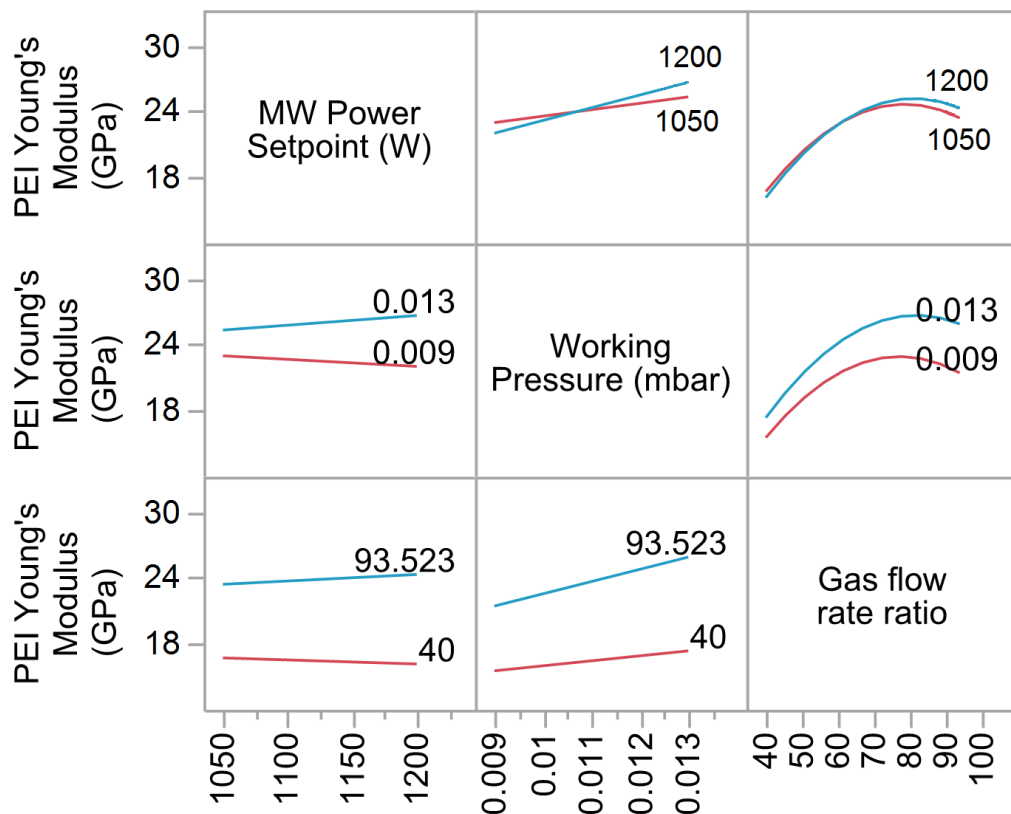


Figure 6-33 - Interaction profiles for DOE model of Young's modulus on PEI substrate.

The differences between the two models demonstrates the substrate effects on the measurements, even at very low indentation depths. The reduced confidence level with ABS can be attributed to the increased roughness. As the measurements were taken at a single depth, any measurement errors will reduce the confidence level as the shift of the mean Young's modulus at 5% depth may reduce the correlation of modulus to the main factors.

6.4 Resistance to plastic deformation (P/S^2)

6.4.1 Polymer Properties

Figure 6-34 shows the resistance to plastic deformation of uncoated ABS and PEI polymers at different indentation depths; greater P/S^2 values indicate less resistance to plastic deformation. Determination of P/S^2 does not require knowledge of the contact geometry due to the two components, maximum indentation load and unloading contact stiffness, not relying on accurate depth sensing.

On the ABS material, with a roughness on the order of 300 nm, P/S^2 becomes constant once the indentation depth is greater than the average surface roughness. P/S^2 measured on PEI substrates were all at indentation depths above average surface roughness and remains constant at roughly 10,000 nm²/mN. Once the indentation depth on ABS was greater than average surface roughness, P/S^2 converged to the same value as the PEI samples.

The resistance to plastic deformation of the two polymers using a sharp indenter tip is similar. Comparing hardness of the two materials, which combines elastic and plastic deformation when determined through nanoindentation, to P/S^2 it is possible to say that it is only the elastic properties of the two materials that differ significantly. Therefore P/S^2 measures of the coated samples should be similar due to similar substrate effects.

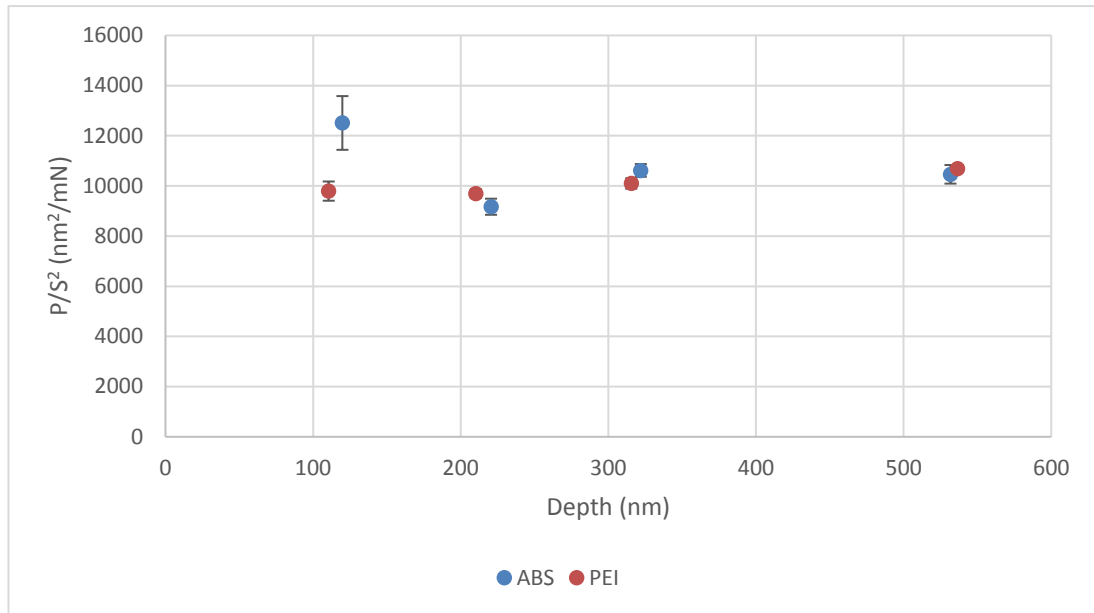


Figure 6-34 - P/S^2 at different depths of ABS and PEI polymers.

6.4.2 Composite Properties

Figure 6-35 shows P/S^2 as a function of depth normalised to coating thickness. Two thicknesses of coating on ABS were used to determine if it is valid to normalise the indentation depth when comparing P/S^2 . The average of measurements at each depth between 2% and 8.4% were within error. Measurement means at 1% and 10% were significantly different. For these reasons P/S^2 has been considered to scale linearly with coating thickness and so normalising indentation depths to coating thickness has been validated.

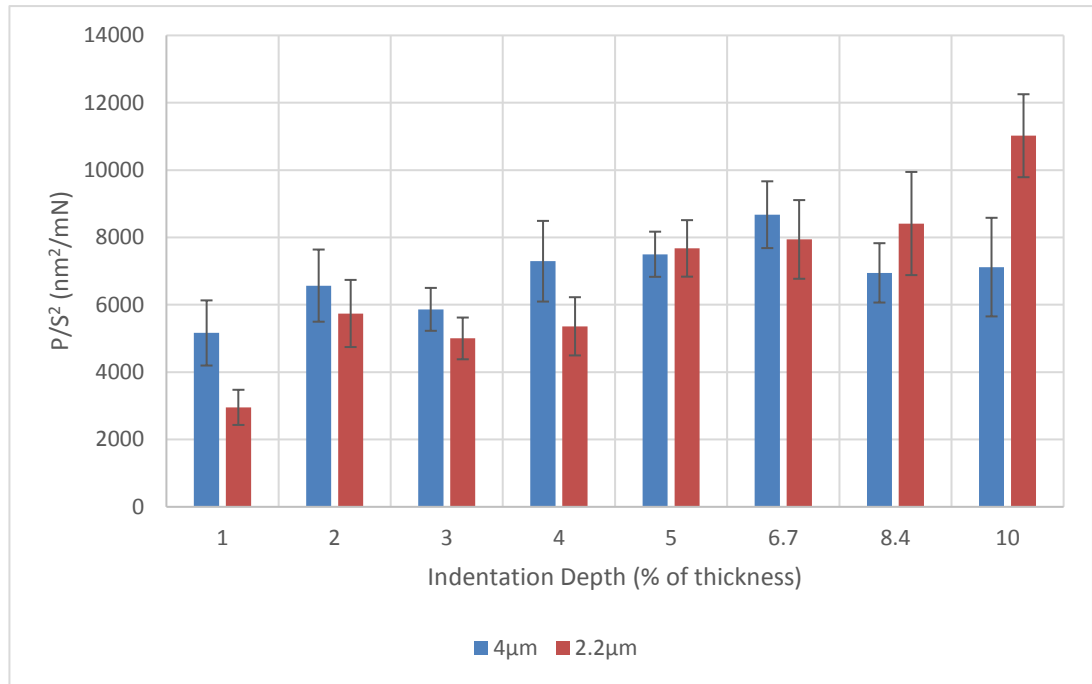


Figure 6-35 - P/S^2 as a function of depth on two thicknesses of coating on ABS substrates.

Figure 6-36 - Figure 6-45 show P/S^2 as a function of depth measured on the coatings produced for the design of experiments; indentations were carried out on the samples as-deposited on the polymer substrates. Generally, as depth increases, resistance to plastic deformation decreases. As the indentation depth increases substrate effects become more apparent due to the elastic strain field extending into the substrate and with further depth, also the plastic strain field but to a lesser extent. As the substrate materials display similar resistance to plastic deformation at low depths (Figure 6-34), the measured values of P/S^2 should be equal for the same coating. This behaviour is seen in the majority of cases where measurements are within error. In cases such as leg 5 (Figure 6-40) where trend lines diverge and measurements are significantly different, it can be attributed to sample variation and measurement error.

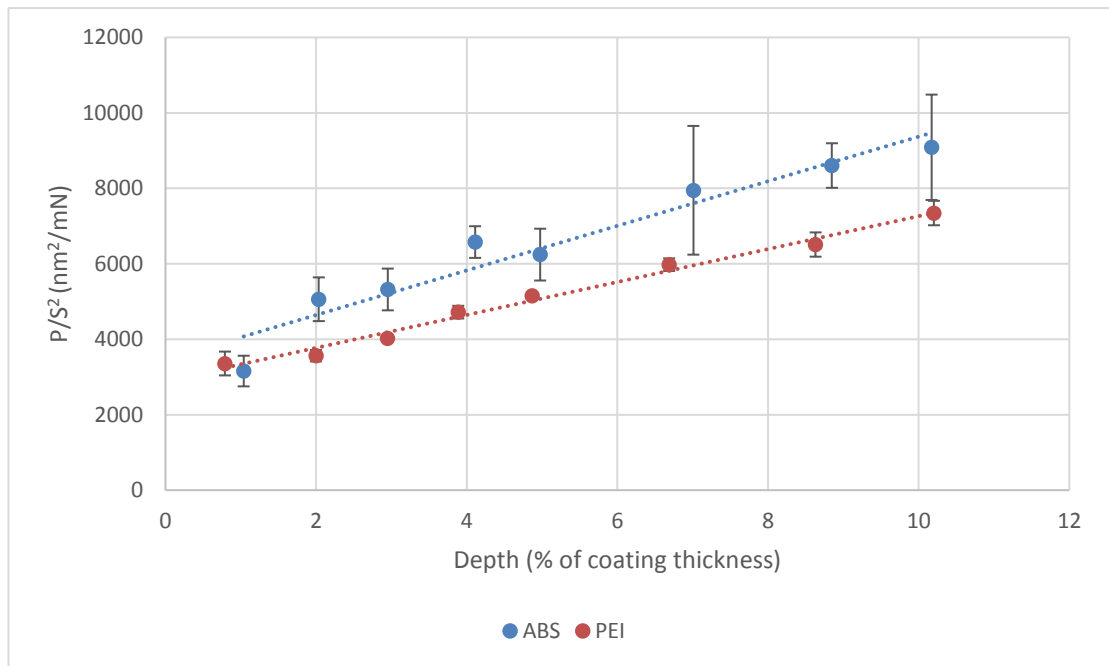


Figure 6-36 - P/S^2 as a function of depth for DOE leg 1.

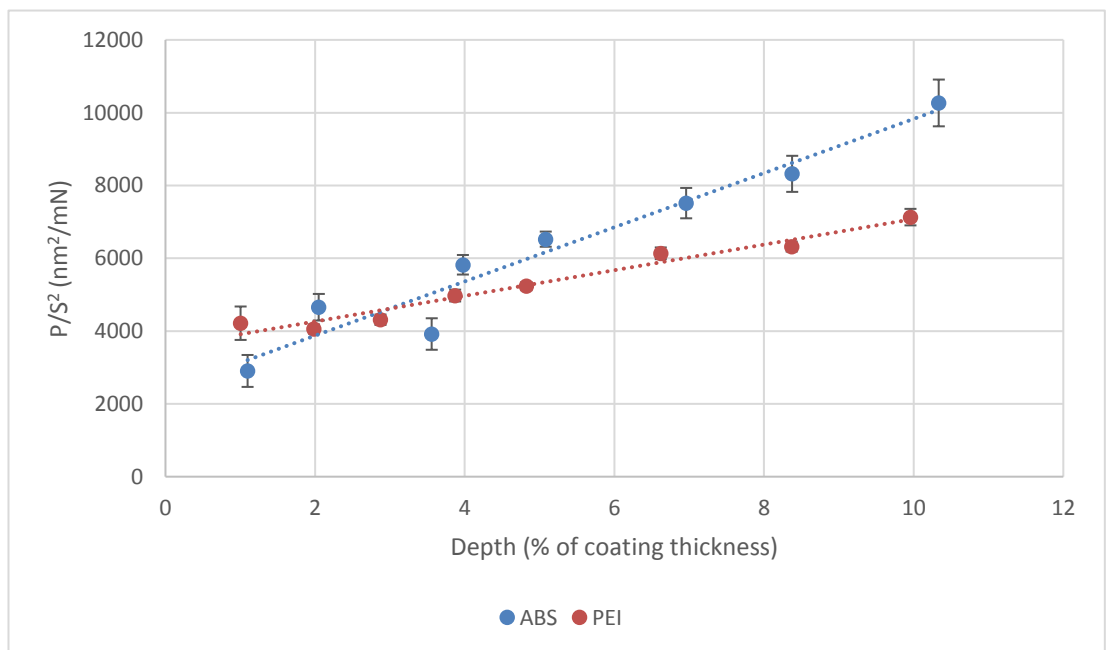


Figure 6-37 - P/S^2 as a function of depth for DOE leg 2.

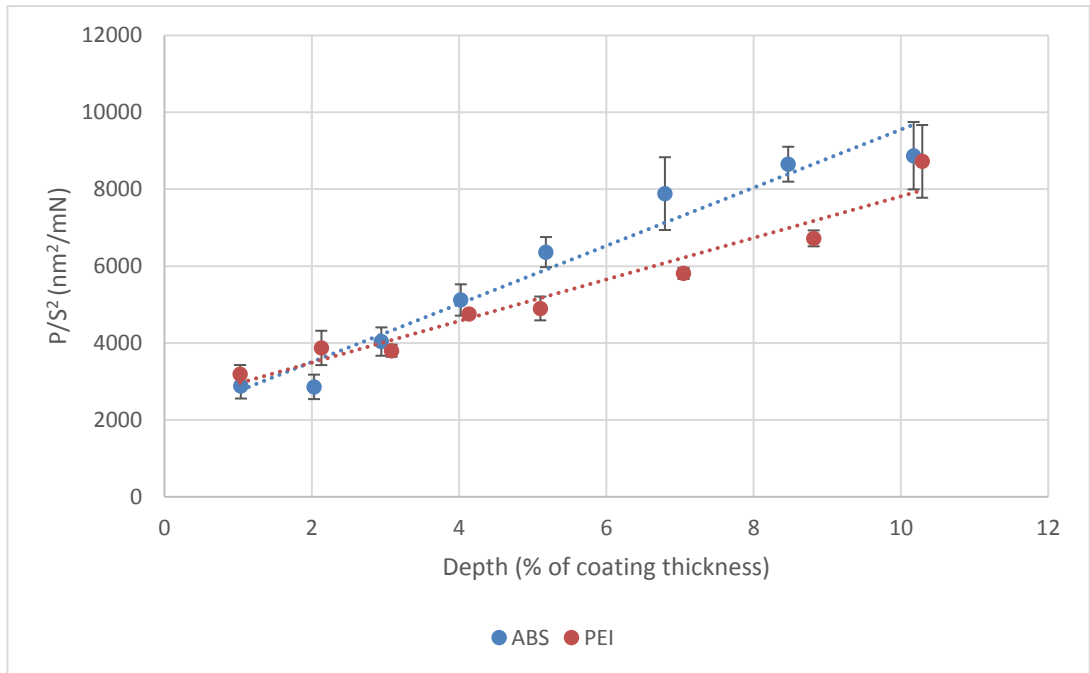


Figure 6-38 - P/S^2 as a function of depth for DOE leg 3.

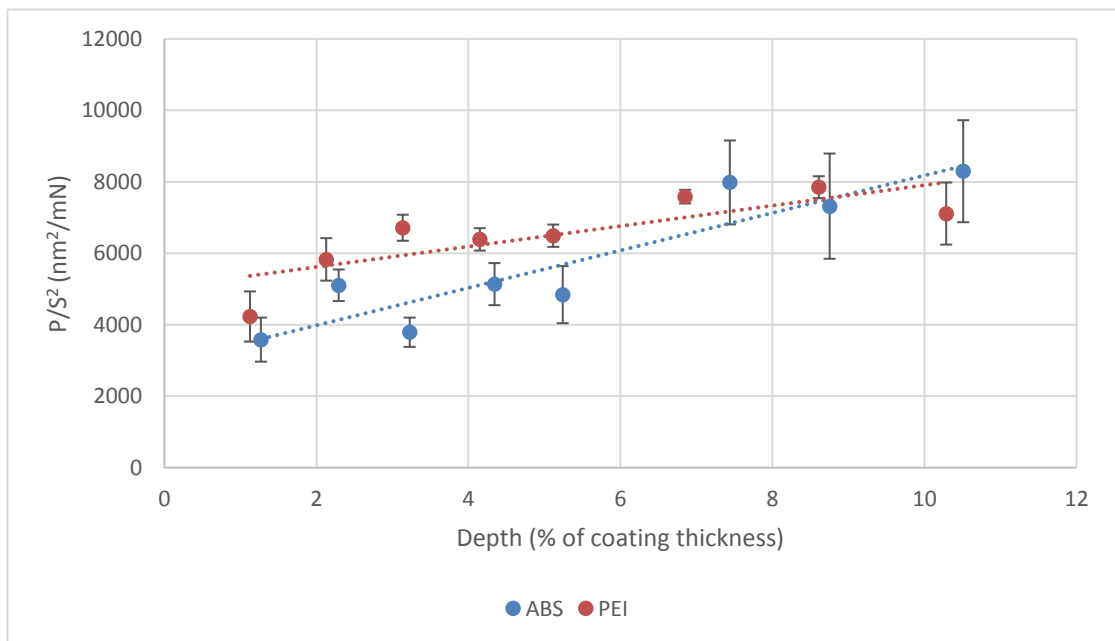


Figure 6-39 - P/S^2 as a function of depth for DOE leg 4.

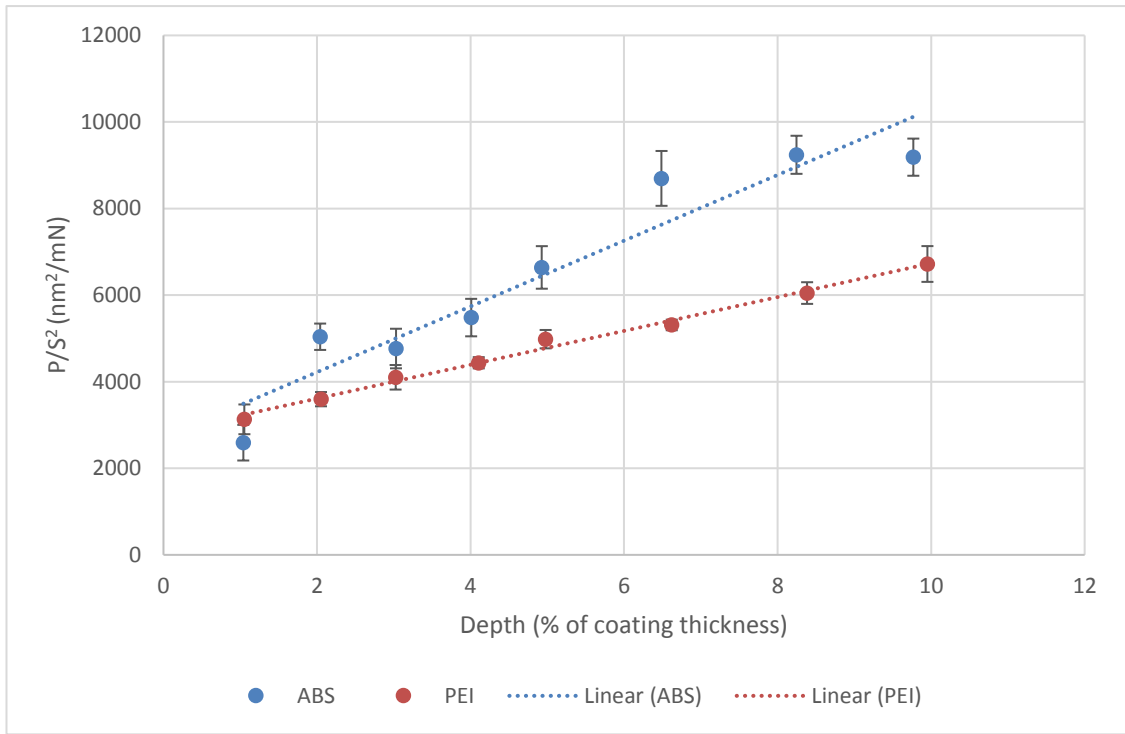


Figure 6-40 - P/S² as a function of depth for DOE leg 5.

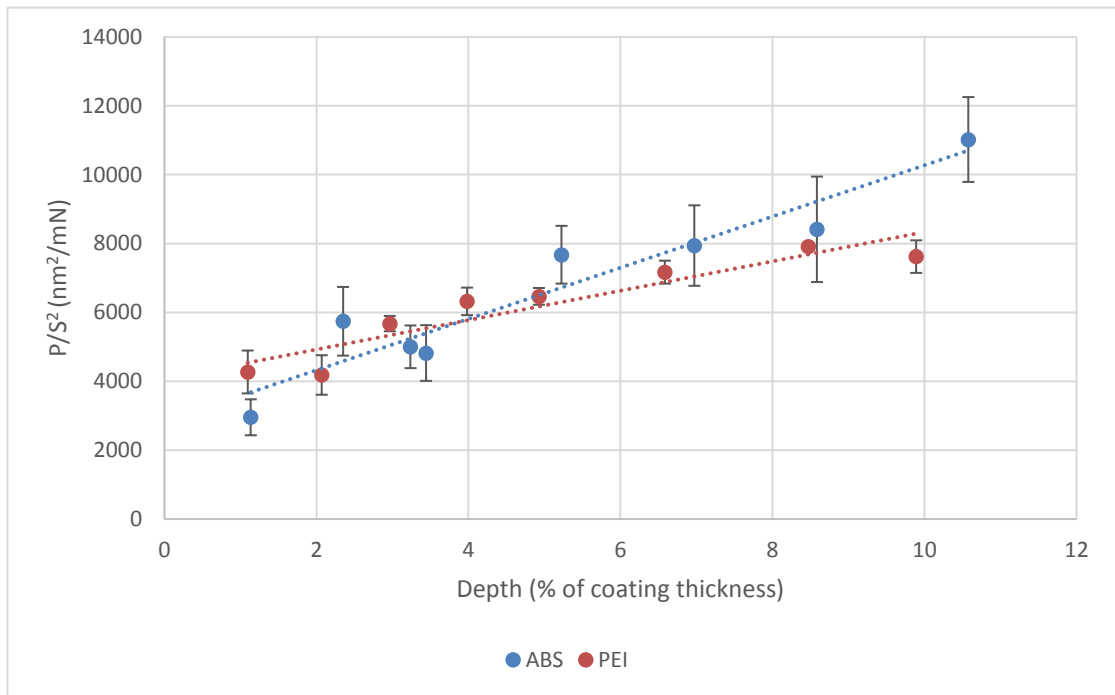


Figure 6-41 - P/S² as a function of depth for DOE leg 6.

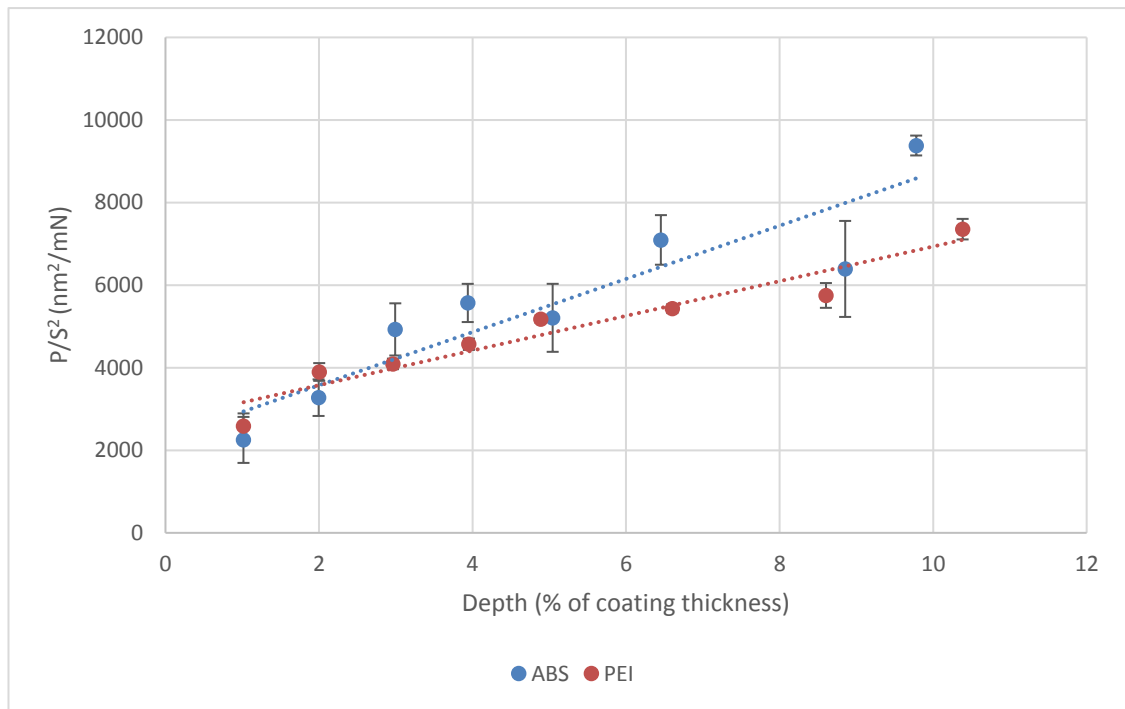


Figure 6-42 - P/S^2 as a function of depth for DOE leg 7.

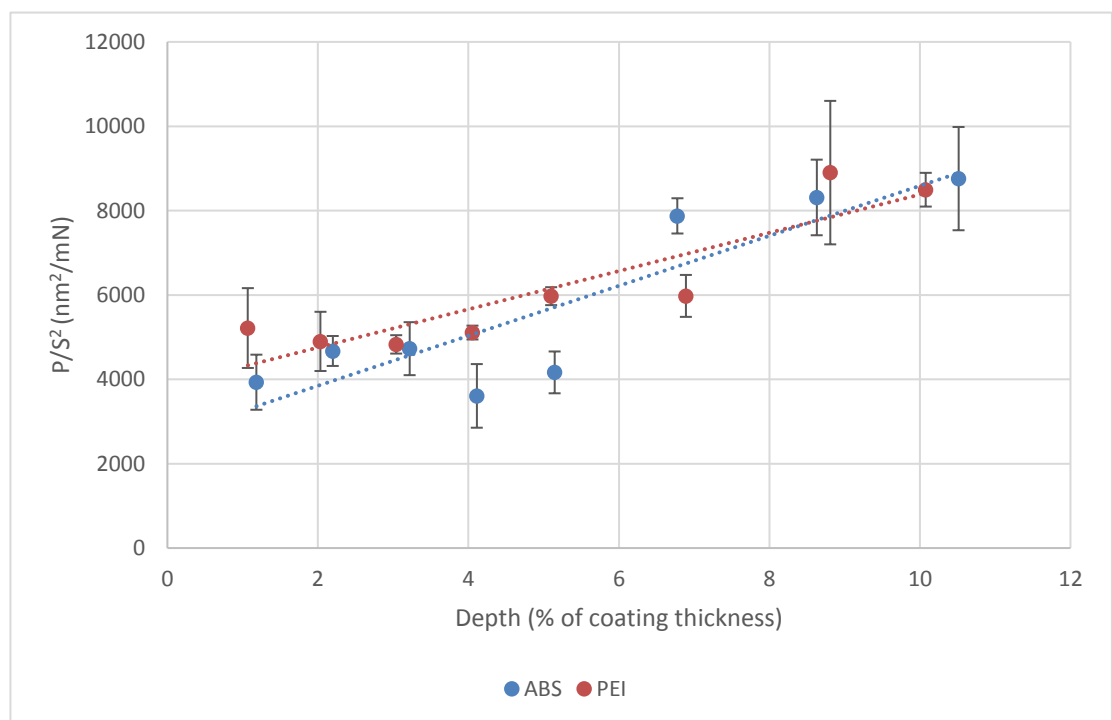


Figure 6-43 - P/S^2 as a function of depth for DOE leg 8.

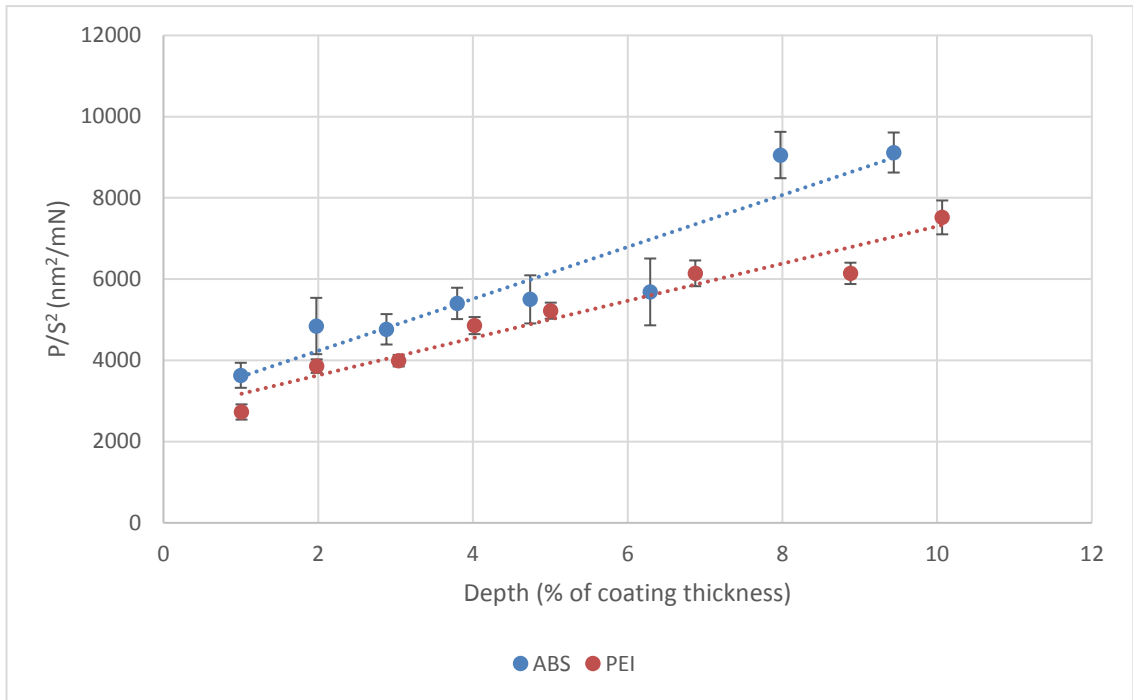


Figure 6-44 - P/S² as a function of depth of DOE leg 9.

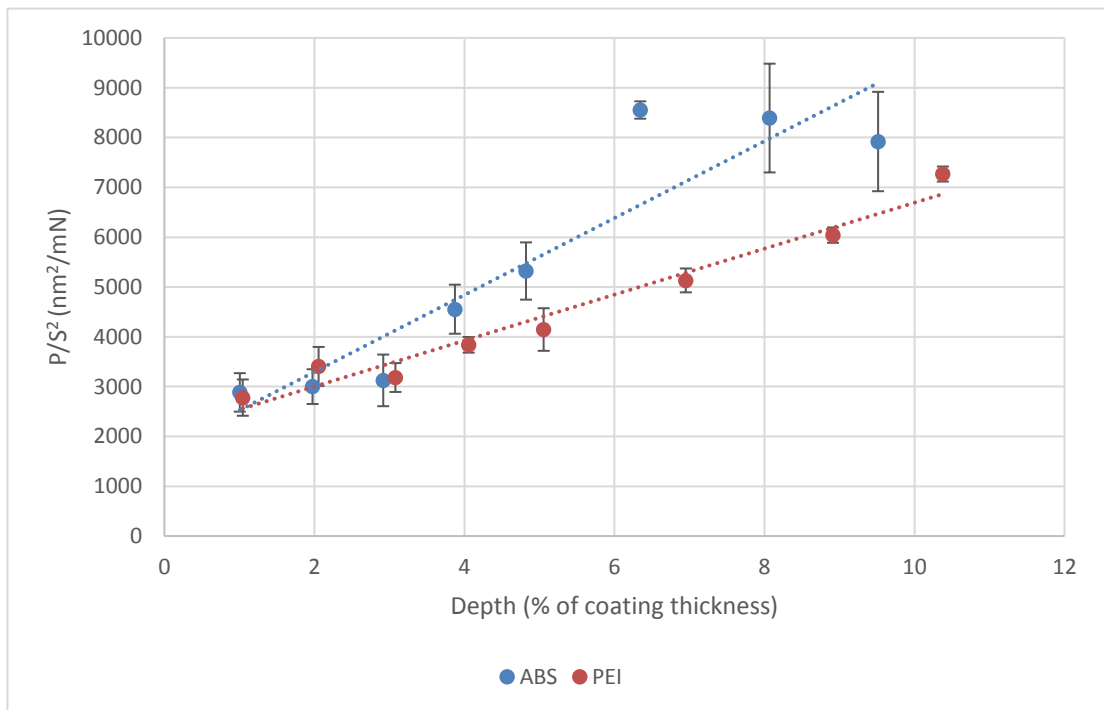


Figure 6-45 - P/S² as a function of depth for DOE leg 10.

Figure 6-46 and Figure 6-47 show the trend lines from Figure 6-36 - Figure 6-45 in order to compare the 10 coatings produced on each substrate. On each substrate the gradients of the P/S^2 vs depth are all grouped in the same area, meaning little separates them in terms of performance. As a general rule, the ABS substrate samples have a steeper gradient, meaning that the samples have reduced resistance to plastic deformation as depth increases compared to the PEI samples. This is likely caused by substrate effects as the ABS has reduced resistance to plastic deformation compared to PEI at very low indentation depths.

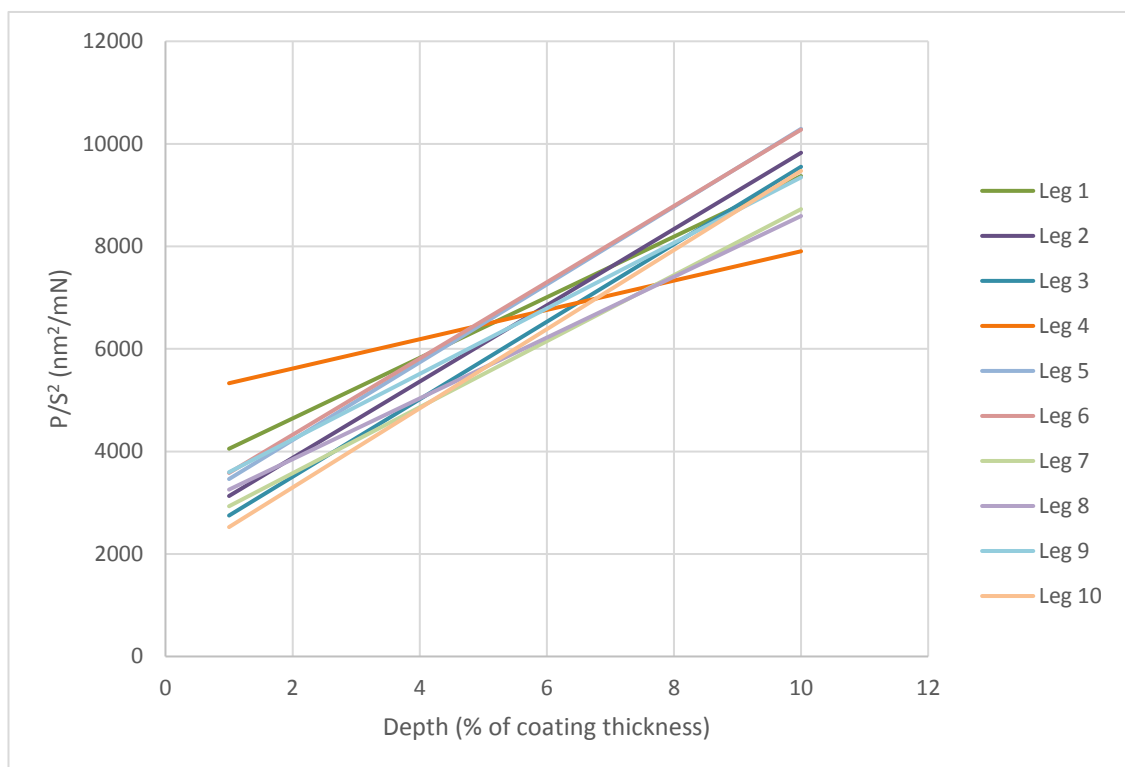


Figure 6-46 - Comparison of P/S^2 as a function of depth of all coatings on ABS.

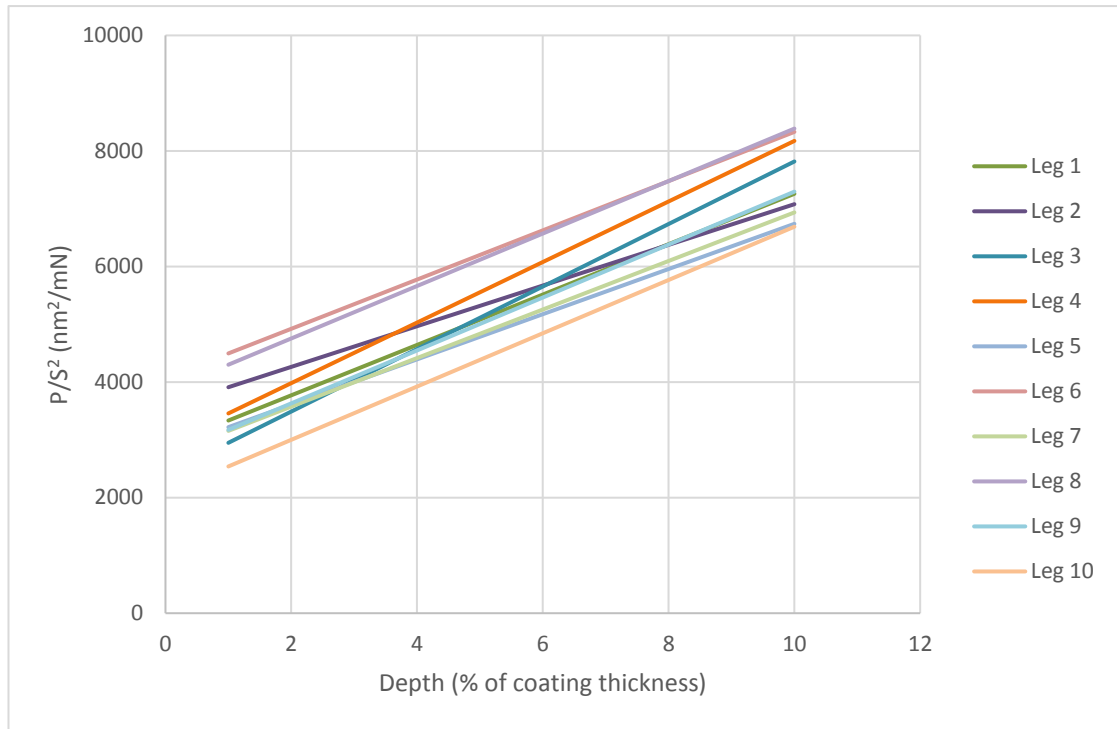


Figure 6-47 - Comparison of P/S^2 as a function of depth of all coatings on PEI.

As the P/S^2 as a function of depth remains similar for all coatings on the same substrate, differences between coatings that are apparent when comparing hardness or modulus of coatings are not visible. As it is the plastic component of deformation that will lead to visible changes of the surface it could be argued that P/S^2 as a function of depth tells us that all the coatings will perform similarly when loaded in a real application. In a tribological contact, the hardness and modulus (or estimates thereof) would potentially allow estimation of wear performance as these occur on a small scale compared to the surface deformation.

6.5 Hardness, Young's modulus, and P/S^2 at increased indentation depth.

3 variations of thickness of the same coating were produced and nanoindentation at depths up to, and exceeding coating thickness were performed to determine hardness (shown in Figure 6-48), Young's modulus (shown in Figure 6-49), and resistance to plastic deformation (Figure 6-50). Hardness and modulus both decrease in the range of 0-50% coating thickness, and from then on remain consistent. At depths above 50% of

coating thickness the coating no longer supports the majority of the load applied and so substrate properties become more important; in other words, substrate effects become more influential in measured properties than coating properties. This is confirmed by noting that both hardness and modulus values measured on the coated samples converge to the hardness and modulus of the underlying substrate.

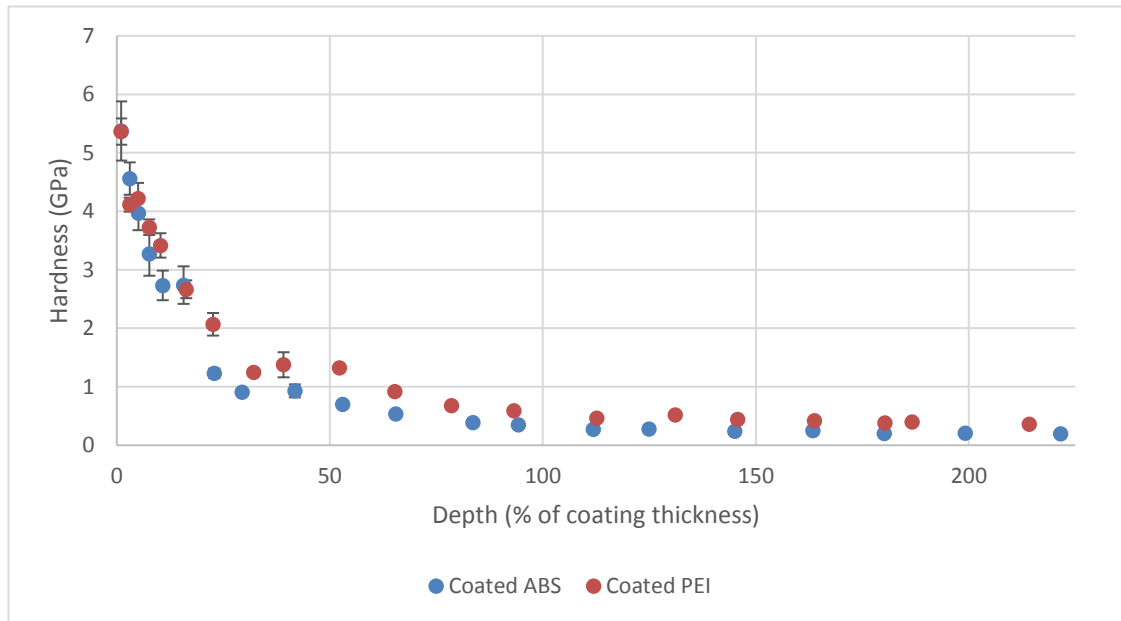


Figure 6-48 - Hardness as a function of depth for coated ABS and PEI.

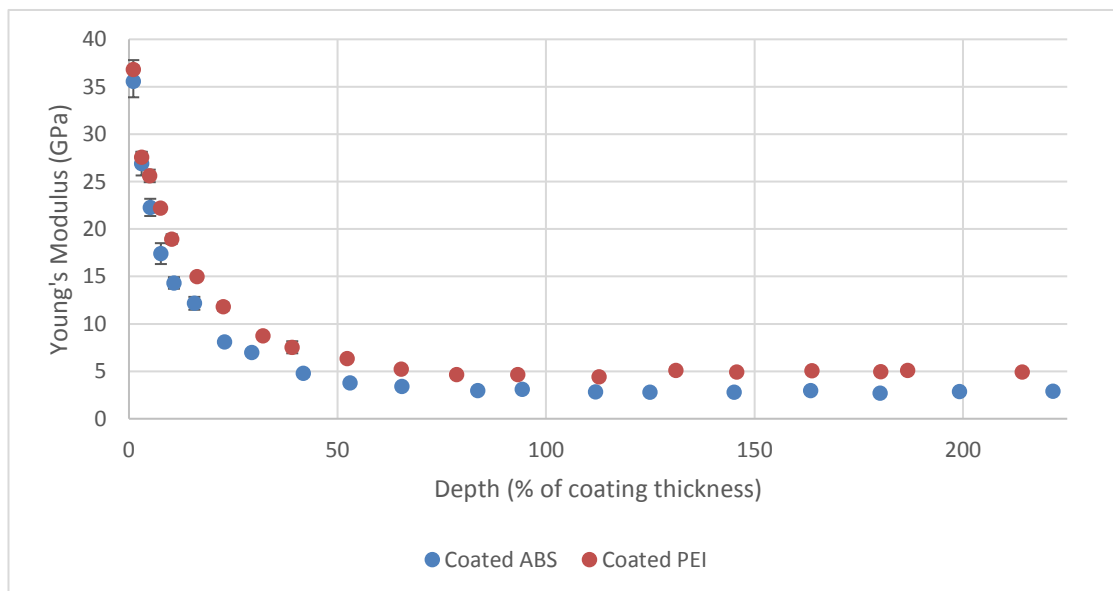


Figure 6-49 - Reduced Modulus as a function of depth for coated ABS and PEI.

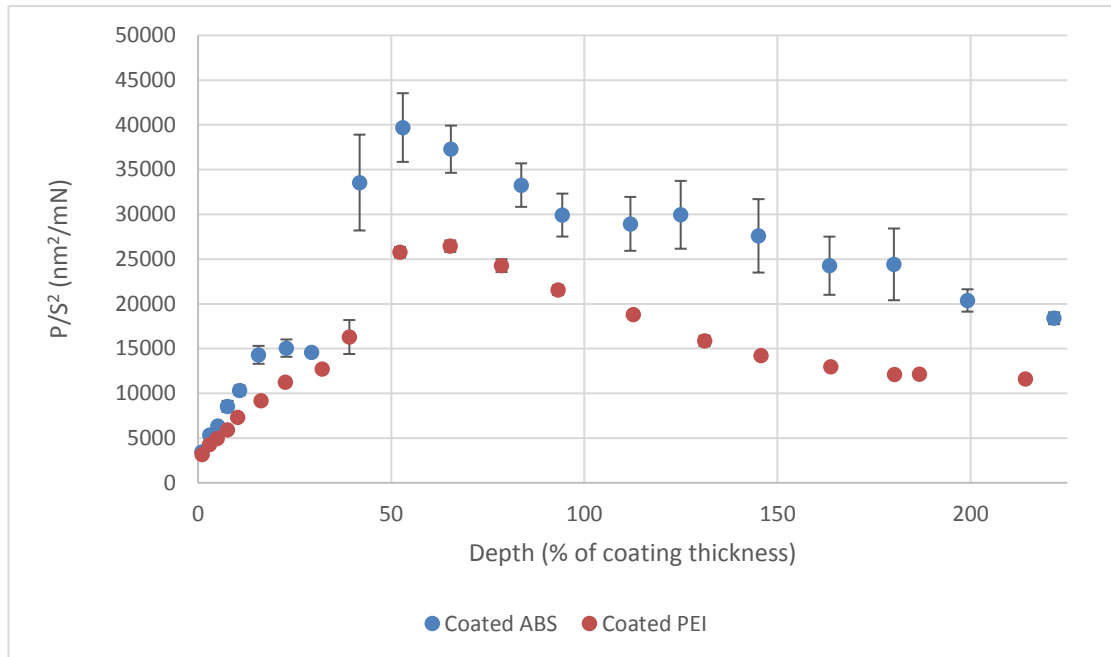


Figure 6-50 - P/S^2 as a function of depth for coated ABS and PEI.

The plot of P/S^2 shows significantly different behaviour. Resistance to plastic deformation decreases (increasing P/S^2 value) as depth increases, much like hardness and Young's modulus. The P/S^2 of the substrates were roughly 10,000 nm^2/mN at low indentation depths and only the coated PEI appears to begin to converge around this value at depths above 175% of coating thickness. At depths between 30-55% a sharp increase in P/S^2 can be seen for both samples. This depth corresponds to 'pop-ins' on the loading curve, which can be attributed to coating failure. An example of this is shown in Figure 6-51, where the pop-in behaviour is seen above depths of 40% where the gradient of the loading curve becomes shallow. As the coating fractures, it can no longer support the proportion of applied load which it did when intact, leading to a sudden increase in indentation depth as the load is transferred to the softer substrate.

Hardness and Young's modulus depth profiles do not give any indication of coating failure. The measurement error of hardness leads to no significant difference between the two samples at depths below 25% where substrate effects are reduced. Substrate effects are clearly visible, manifesting as reductions as depth increases. This means that even ultra-low depth indentations on elastically mismatched hard on soft coating systems are unsuitable for determining coating hardness independent of substrate effects without

resorting to modelling. This also applies to Young's modulus. Because of this, it could be argued that the legitimacy of stating single values of hardness and Young's modulus for such coated systems is questionable. If the substrate plays such an important role in supporting even such small loads and pressures, then stating mechanical properties as a function of depth gives more information as to how the composite could be expected to respond to any given load.

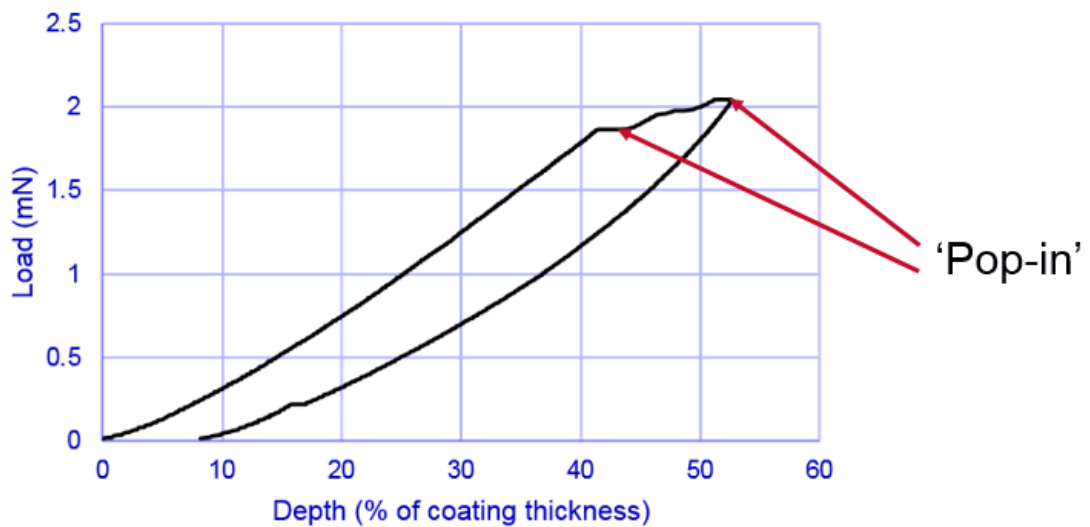


Figure 6-51 - Example loading-unloading curve from nanoindentation, showing pop-in behaviour.

Considering P/S^2 , not only does the depth profile show significant separation of the two samples, but it also indicates the depth of coating failure. In this case the depth is normalised to coating thickness, however indentation curves for two different coating thicknesses are shown in Figure 6-52. It can be seen that the strain to failure scales linearly with coating thickness. Comparing the two loading curves for each thickness, the pop-ins do not occur at exactly the same depth each time; this is expected of a real coating where defects in the coating and coating-substrate interface would lead to different fracture sites and crack propagation. However, in all four loading curves the depths of the pop-ins occur at roughly 30-60%, which corresponds to the range of depths at which P/S^2 increases in Figure 6-50.

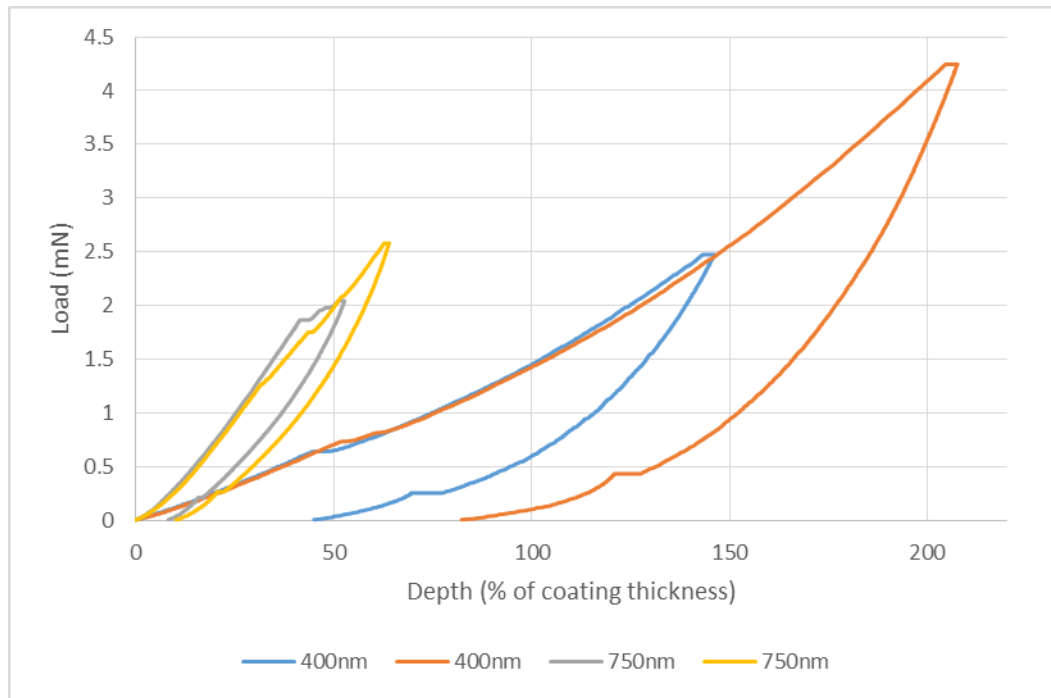


Figure 6-52 - Loading-unloading curves for two coating thicknesses.

6.6 Tribological Performance

Reciprocating pin-on-plate tribology tests were carried out as detailed in Chapter 3. Initial tests were carried out twice in order to determine repeatability of the experimental procedure. Three tribo-couples were tested; MW O₂ treated ABS with DLC coating sliding against an identical counter face, MW Ar treated ABS with DLC coating sliding against ABS, and plasma source Ar treated ABS with DLC coating sliding against ABS. Each test was run under the same conditions; mean contact pressure of 40 MPa (where both surfaces were assumed to be uncoated ABS) from an 8N load using a flat plate and 5mm radius domed pin, sliding frequency of 10 Hz, and lubricated with base oil (PAO IV). The coefficient of friction for these three tests are shown in Figure 6-53 with standard error.

The pre-treatments for the polymers are described based on the plasma generation method and the gas species in the plasma. The MW plasma was generated using the microwave antennae at 1200 W, and the PS plasma was generated using the DC plasma source consisting of a tungsten cathode and copper anode at 100 A. For example, the

MW O₂ treated ABS was exposed to an oxygen plasma generated using the MW antenna. All treatments were for a duration of 4mins at 6×10^{-3} mbar.

The repeatability of the tests is good, with standard error being less than 10%. Similar behaviour was observed for each sample with respect to running in duration before steady state friction coefficients were achieved. Because of this, for all further tests no repeats were carried out in order to allow testing of more samples using limited resources.

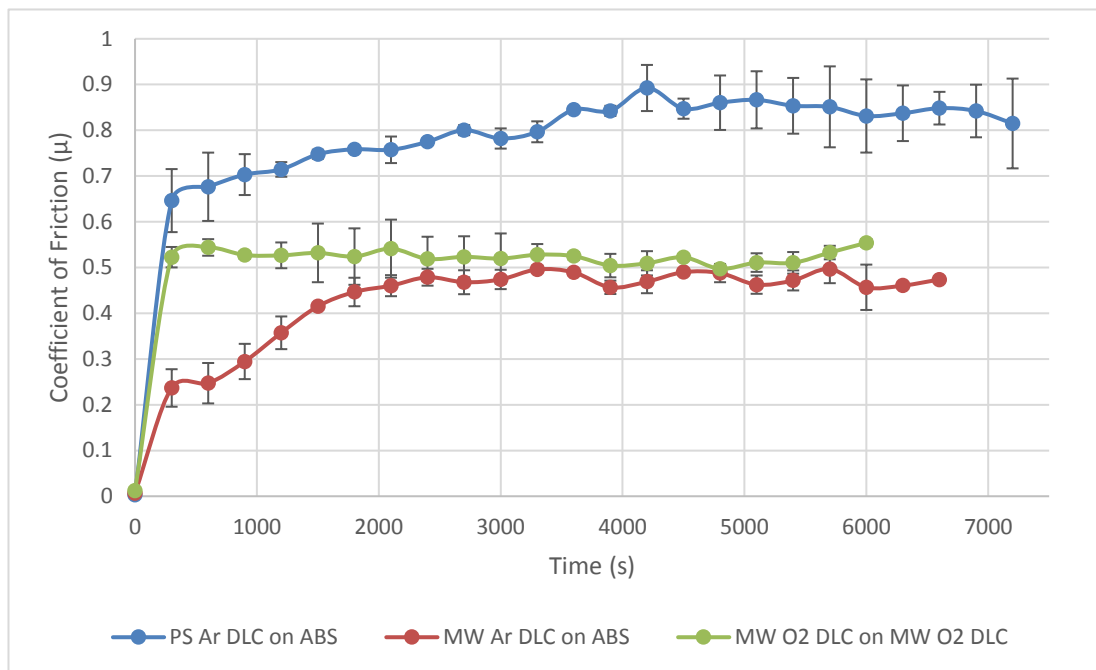


Figure 6-53 - Friction coefficient of three coated polymers in reciprocating pin-on-plate test.

Friction coefficients of various DLC coated ABS samples sliding against ABS are shown in Figure 6-54. A reference of ABS on ABS is also included. Test conditions are identical to those stated above and the DLC coating is the same for all samples. Each substrate was subjected to different plasma treatments prior to coating, using oxygen or argon as process gases and the microwave (MW) or plasma source (PS) to sustain the discharge. The two samples with the lowest coefficient of friction are ABS and MW O₂ treated ABS coated with DLC. After running-in, which is much shorter for ABS, both reach a steady state friction coefficient of approximately 0.1. The highest coefficient of friction was

observed for the plasma source argon treated ABS with DLC coating; the friction coefficient did not reach a steady state, but peaked at roughly the midpoint of the test (3900 s) at 0.85. The remaining coating, microwave argon treated ABS with DLC, reached a steady state friction coefficient of 0.45-0.5 after 3500 s. These two samples are expected to be within error, as demonstrated in Figure 6-53. Compared to the magnitude difference of these two samples compared to the others, differences in performance are negligible.

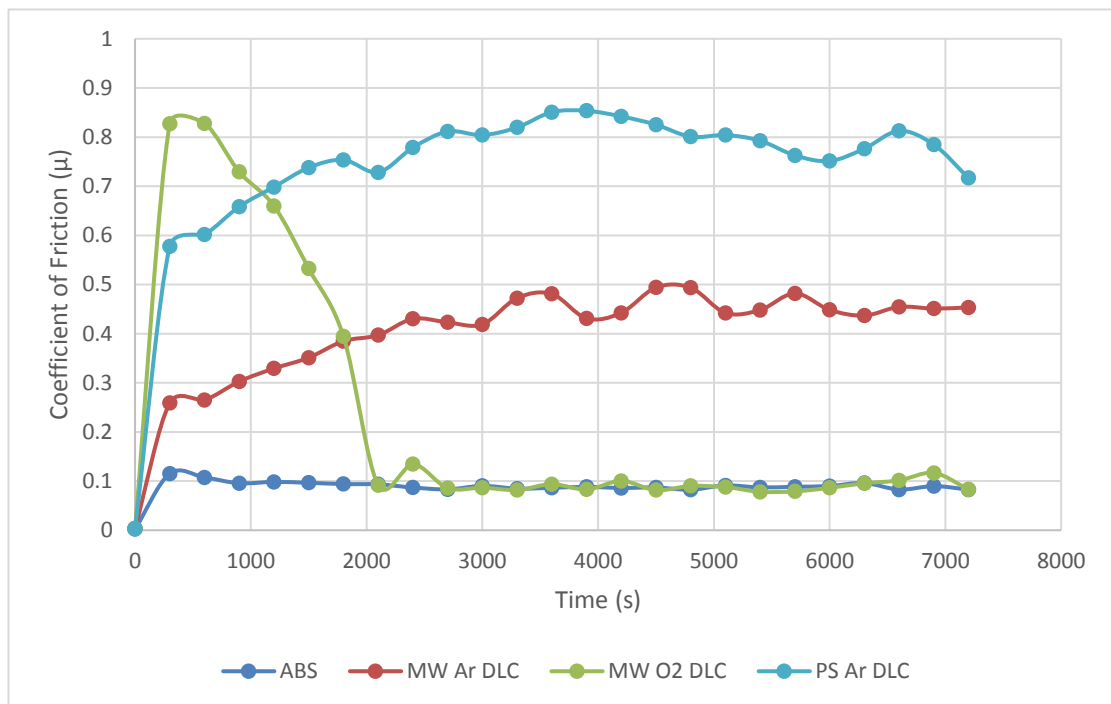


Figure 6-54 - Coefficient of friction of 4 DLC coated ABS samples sliding against ABS.

Comparing the three DLC coatings with variation of pre-deposition plasma treatment there is no similarity between the coefficient of friction, which would not be expected in such a case with three identical coatings. These differences are likely due to differences in surface roughness and imperfections (scratches etc.) in the substrate surface prior to deposition; these will create sharp, hard edges once coated which will lead to accelerated wear of the soft ABS pin and increased friction forces due to the ploughing of material from the pin during sliding. Because the ABS is far softer than the DLC, any changes in surface roughness or surface imperfections would be expected to have a

large effect on friction as little to no wear is expected on the DLC. Small surface imperfections do not fully explain the behaviour seen here, as this would be expected to have an effect on repeatability, so roughness is likely the most influential factor. However, the roughness and exact mechanical properties of the coating were not determined and so this is an area which requires further work to fully understand.

Figure 6-55 shows the difference in friction coefficient between ABS-DLC and DLC-DLC contacts. The ABS-DLC contact starts higher, but after running-in reduces to a steady state of roughly 0.1. The DLC-DLC contact has no noticeable running-in period with the frequency of data recording used here and reaches a steady state friction coefficient of roughly 0.5. The running-in period of the ABS-DLC contact is likely due to the accelerated wear of the ABS compared to DLC, leading to a transfer of ABS onto the DLC surface. This transfer film will result in the steady state friction coefficient being similar to an ABS-ABS contact. The friction coefficient of DLC-DLC is larger than ABS-ABS under the same conditions.

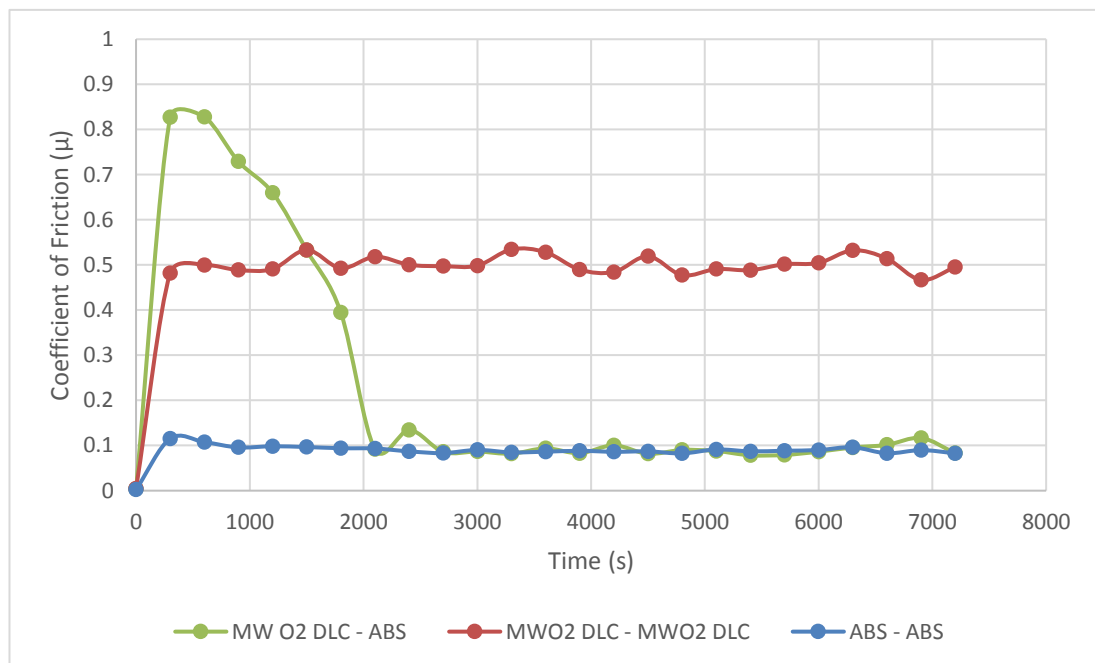


Figure 6-55 - Comparison of friction for DLC coated polymer sliding against DLC and ABS.

Figure 6-56 and Figure 6-57 show the wear tracks of ABS-ABS and DLC-DLC contacts respectively. The wear track widths following 2 hours of testing are similar meaning

contact pressures were approximately the same after this time. Differences between wear and plastic deformation of the surfaces are not separable, and surface roughness is expected to be similar (as seen in Chapter 4), therefore differences in friction coefficient can be attributed to differences of mechanical properties. Surface asperities in the DLC-DLC contact will require more work to deform leading to increased frictional forces during sliding.



Figure 6-56 - Wear track of ABS plate from ABS-ABS contact.

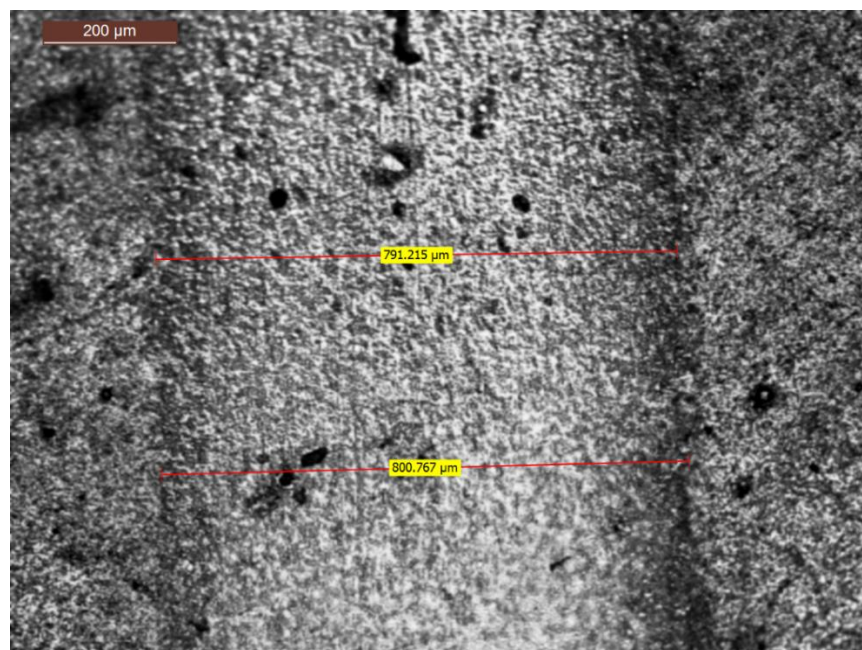


Figure 6-57 - Wear track of DLC coated ABS from DLC-DLC contact.

In order to determine the effect of surface deformation on the measured coefficient of friction, two different thicknesses of DLC6, 4 μm and 2.2 μm , were tested under the same conditions. The coefficient of friction during the test are shown in Figure 6-58, where the error bars represent the range of the two tests performed. The pin scar width following the 3000s test of the 4 μm sample was $600.1\pm 40.5\ \mu\text{m}$, and for the 2.2 μm sample, $558.0\pm 93.5\ \mu\text{m}$. The pin scar widths are similar, however both the coefficient of friction and pin scar width range is higher for the thinner coating than the thicker coating, and the mean values of both measurements larger for the thicker samples. This suggests that the thicker coating supported a larger proportion of the load during the test, which in turn had an impact on the friction measurements due to differing contact geometries.

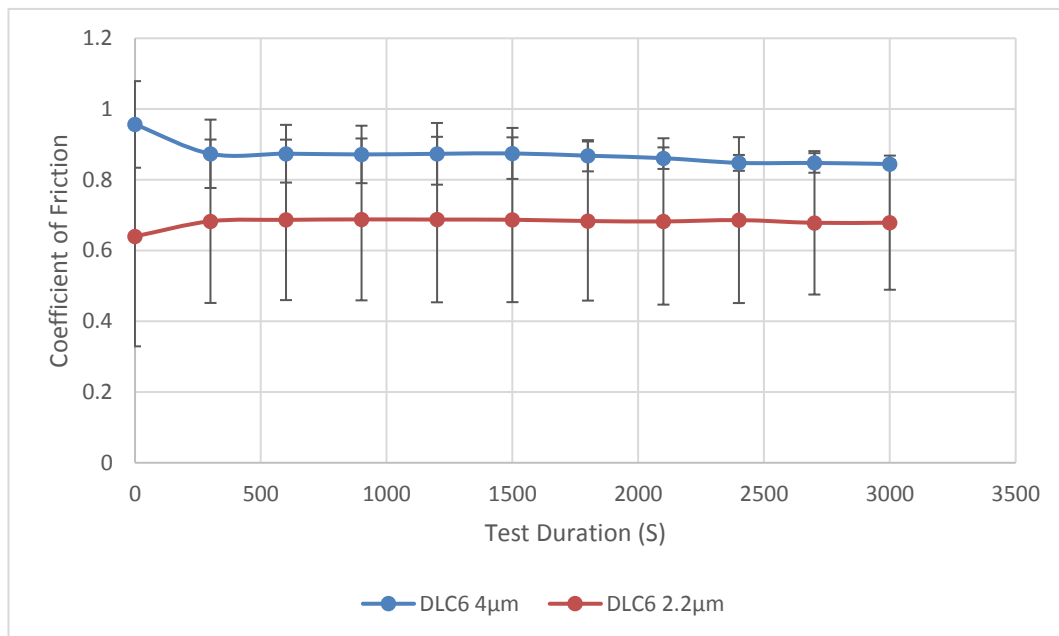


Figure 6-58 - Coefficient of friction for two samples of DLC6 with different thicknesses sliding against steel.

6.7 Conclusion

In this chapter, results of nanoindentation on multiple coatings were presented. Hardness, Young's modulus, and resistance to plastic deformation were determined for each coating produced. Where possible, this data was used to characterise the deposition process using a DOE approach, which showed how deposition conditions

influenced the mechanical performance of the coated polymers. In all cases substrate effects were included in measurements at less than 10% coating thickness and the DOE model indicated that increasing the partial pressure of C_2H_2 for film growth led to increased hardness and modulus. P/S^2 gradients were similar for all coatings, however failure could be clearly seen when measuring this parameter. Combining small indentation depth (<5% coating thickness) to determine hardness and modulus, with depth profiles of P/S^2 up to the interface of coating and substrate could provide all the information necessary to determine component mechanical performance.

Friction coefficients were also presented for DLC-ABS, ABS-ABS, and DLC-DLC tribo-couples. The DLC-DLC contact had an increased friction coefficient compared to ABS-ABS, however no trend or similarities of friction coefficient were observed in DLC-ABS contacts and this area requires further work. Differences of friction between two similar coatings of differing thickness were shown, suggesting the contact geometries are the cause.

Chapter 7. Discussion

7.1 Introduction

In this chapter the results of the experiments will be discussed with relation to the literature, and what they show in practice when considering the applications that coated polymers could be used for.

This thesis has explored the use of MW-PECVD techniques for coating polymer substrates. DLC coated polymers have the potential to be used in many industries and for a wide range of applications. DLC coatings have been successfully deposited onto two polymer substrates and characterised. The experimental results have shown that the DLC coating will increase the surface hardness and Young's modulus due to the addition of an amorphous a-C:H structure. Despite this, the limiting factor is the composite behaviour of the substrate and coating whereby the different hardness and modulus of the polymer will limit the loading scenarios in which the coating can resist failure.

Examples of DLC coated polymers can be found in the literature, however those deposited in this work were different due to the deposition technique used. The remote microwaves used to generate the plasma in the deposition chamber are able to create and sustain a plasma without the need for biasing; this translates to a uniform coating being produced at a high deposition rate on insulating substrates such as polymers.

7.2 Uniqueness of this coating system

The coating system used for this work is an industrial scale deposition chamber fitted with two remote microwave antennae, each providing up to 1200W of power. Previous work using the same equipment and metallic substrates [119] estimated the plasma density distribution throughout the chamber during deposition by measuring deposition rates of substrates mounted in different locations. Figure 7-1 shows the coating thickness, an indication of plasma density within the deposition chamber for various

positions. In the work presented in this thesis two sources were used, and it was determined that plasma density was uniform in the central portion of the chamber.

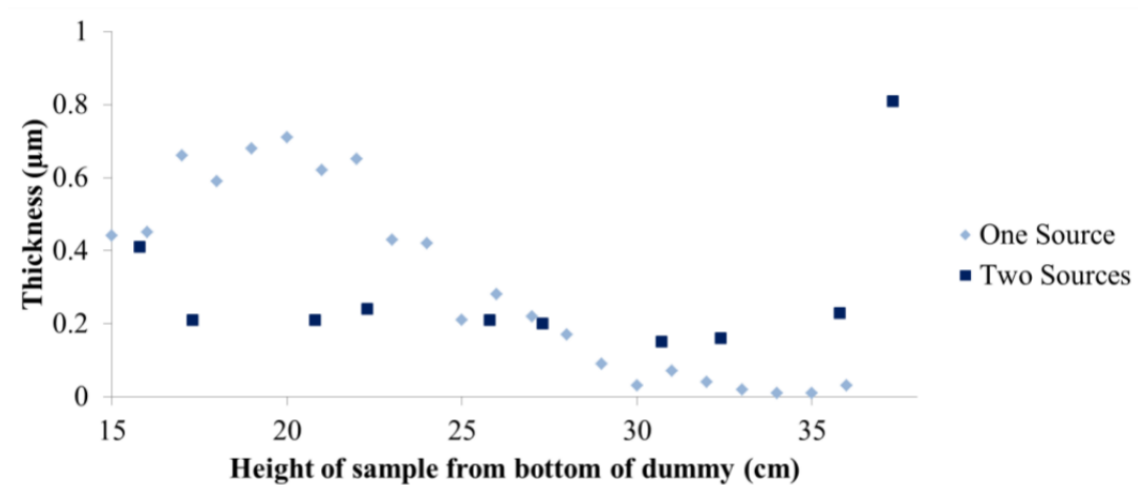


Figure 7-1 - Thickness of coating achieved during same time period based on sample position within the chamber (from [119]).

There are several advantages associated with the use of MW-PECVD techniques, chiefly the increase of deposition rate and a reduced reliance of maintaining conductivity on the anode to sustain a plasma. Deposition rates on polymer substrates with no biasing applied were measured to be in the range of 2.5 – 7.0 µm/hr (up to 27 Å/s), with higher deposition rates a result of increased precursor partial pressure.

With conventional PECVD methods, a large voltage potential difference across a working gas is required to ignite and sustain the plasma discharge. In the case of the Hauzer Flexicoat system (and many other deposition systems), this potential is created by applying a negative voltage to the substrate holder. Whilst this does provide benefits for coating metallic substrates (biasing generally increases mechanical properties by densification of the coating), this method introduces practical limitations on the coating thickness and properties achievable in some instances; some of those inherent to reactor design. Of most concern is during the deposition of non-conductive coatings, whereby the coating will deposit on the anode eventually leading to an increase in resistivity. Once the coating reaches a critical thickness based on the material and plasma conditions, a

large enough potential cannot be sustained resulting in plasma instability; the so-called 'disappearing anode'.

Using a remote MW source de-couples the biasing circuitry and plasma source, meaning that increased coating thicknesses can be realised in a single batch, and if required, biasing of the substrate for tuning of coating properties can be carried out to change plasma kinetics without adversely affecting ionisation rate of the precursor. The equipment used for the work presented in this thesis had only DC and pulsed DC biasing, which is known to rapidly increase deposition temperatures from ion bombardment. Both the increased heating rate and the use of insulating and temperature sensitive substrates meant that biasing was not investigated as it would have no effect.

RF biasing has been used to deposit densified coatings on polymers (Table 7-1), however the installation of such equipment in large scale deposition chambers presents technical problems with respect to coating uniformity. The use of RF biasing was not available for this body of work, although the author acknowledges the potential importance of this technique and a review of the current state of the art was provided in Chapter 2.

Defects within coatings normally manifest as reduced mechanical strength, reduced resistivity, or reduced light transmission. Of these properties, only mechanical performance was measured and due to the limited understanding of how these composite structures behave under loading, little can be deduced from the data presented in this thesis. Most data presented within the coating literature does not concern defect rates and instead focuses on the primary performance characteristics of a system. From the SEM cross section images, defects within these coatings are most likely to manifest as non-homogeneous structures, which in theory would reduce the energy required to fracture the coating compared to a homogeneous structure.

Table 7-1 - Mechanical properties of carbon coatings deposited on polymer from the literature.

Coating	Technique	Thickness (µm)	Substrate	Hardness (GPa)	Young's Modulus (GPa)	Ref.
DLC	PECVD	-	PA	17.46	49.9	[117]
a-C	Sputtered	-	PA	12.75	45.2	[117]
DLC	Ion-beam sputtering	>0.5	PMMA	0.4 - 0.9	-	[115]
Si-DLC	RF-PECVD	1 – 3	PC	14 - 20	-	[54]
DLC	RF-PECVD	0.3	PU	8.2 - 14.8	-	[125]
DLC	RF-Plasma based	1	PA/PPE	2.14 – 3.45	-	[126]
DLC	RF-PECVD	-	PET	3.44 – 17.96	-	[110]
DLC	RF-sputtering	1	PMMA	4.25 – 6	-	[114]
DLC	RF-sputtering	0.12	PC	13.74	-	[112]
DLC	(RF-) sputtering	-	PC	2 – 12	-	[6]
DLC	Pulsed PECVD	~1	PMMA, PET	1.2 - 15	-	[111]
a-C:H	MW-PECVD	~2 - 5	ABS, PEI	~2 – 6	~20 – 40	<i>This work</i>

As can be seen in Table 7-1, Young's modulus data is under-reported in the literature with only one author presenting this information. The coatings produced in this work were of the same order of magnitude, but were generally lower. The entry in the table relating to work presented in this thesis was taken from indentation depths of between 1 - 5% of the coating thickness. All coatings presented in this work were thicker than those presented in the literature. Lower deposition rates than those achieved using the MW-PECVD technique are likely, and confirmed where these have been reported. This is due

to most work presented in the literature employing the use of RF plasma generation/biasing, which serves to densify the coating by accelerating ions towards the substrate; this was not possible using the Hauzer Flexicoat 850 coating system used in this work, beyond the self-bias of the plasma.

In the majority of cases, and especially where RF equipment was used, the hardness of coatings reported in the literature was more than achieved in this work. There are two possible reasons for this; the RF equipment was able to bias the substrates resulting in harder coatings by increasing the energy of bombarding ions, or the authors of the work used analysis methods which aim to remove substrate effects from indentation results. The latter is unlikely as this was not stated, however the low coating thicknesses used may suggest that coating mechanical properties were measured on non-polymeric (harder and stiffer) substrates. The results presented in this thesis show that at small indentation depths (<5% coating thickness) the substrate effects, along with ISE and surface roughness effects, combine to produce a trend of hardness and Young's modulus measurements that increase as the indentation depth tends to zero.

The polymer substrates used in the literature tend to be focussed around PC, PMMA, PA, and PET. These polymers are widely used in industrial applications and the interest could be described for each polymer as: increasing scratch resistance and optical properties of PC, decreasing friction of PMMA whilst increasing bio-compatibility, increasing wear resistance of PA whilst improving friction performance, and generally improving the properties of PET as a widely used material. No examples of DLC coated ABS could be found despite their use industrially in electroplating applications, and PEI is an uncommonly used polymer due to cost. Utilising these two materials and comparing performance of similar coatings deposited on these two materials has allowed observation of substrate effects in coated polymer systems.

The increased thickness of coatings used to measure mechanical properties in this study gave indentation depths that were at the limit of what is practical to achieve reliable data using nanoindentation systems (20-50nm) when the lowest depth indentations were

made. These depths were lower than the average surface roughness of the ABS substrate (roughly 300nm across all samples), and similar to the average surface roughness of the PEI samples (mostly in the region of 40 – 60nm across samples). The reduced roughness of the PEI, in general led to reduced error of the measurements. It is therefore reasonable to assume that hardness values taken from the literature must be treated carefully, as to how the data was not only measured, but also on which substrate. A high hardness value given in the literature, which was measured on a hard metallic substrate, would not be expected to be representative of the performance that would be found when measuring the same coating on a polymeric substrate. Although the differences are small, for the ten samples tested, measurements of the same coating on harder PEI substrates were generally higher than those measured on the softer ABS material.

7.3 Discussion of results

Two polymers were used in this study, ABS and PEI, and their mechanical properties were determined through nanoindentation. At different depths of indentation a measurement range of 0.18 -0.28 GPa hardness and 3.25 – 4.05 GPa Young's modulus for ABS, and 0.43 – 0.52 GPa hardness and 4.94 – 5.77 GPa Young's modulus for PEI was determined. This variation arises both from inhomogeneity in the polymer structure (i.e. chain alignment), contact geometry (due to surface roughness on the nano-scale), and indentation size effects.

Ten DLC coatings were produced using a design of experiment approach. The hardness and Young's modulus of the coatings measured by nanoindentation at depths of 5% coating thickness are shown in Table 7-2 and Table 7-3; this data is shown graphically in Chapter 6. For shallow indentations the DLC coatings increase the surface hardness of the polymer by 7.5 – 27x in the case of ABS and 4 – 11x in the case of PEI. For Young's modulus, increases of 3 – 7x were observed for ABS and 2.5 – 5x for PEI.

Table 7-2 – Hardness of DLC coatings measured at 5% of coating thickness on ABS and PEI substrates.

Coating	1	2	3	4	5	6	7	8	9	10
ABS (GPa)	4.9	4.1	3.4	2.1	3.9	2.5	4.2	2.2	3.3	4.7
PEI (GPa)	4.9	4.1	4.1	2.2	3.6	2.7	4.8	3.0	4.5	4.3

Table 7-3 – Young’s modulus of DLC coatings measured at 5% of coating thickness on ABS and PEI substrates.

Coating	1	2	3	4	5	6	7	8	9	10
ABS (GPa)	21.9	19.8	19.2	14.0	20.2	13.5	18.5	19.5	16.9	23.1
PEI (GPa)	24.6	22.4	24.8	15.3	22.1	16.9	25.0	18.3	24.2	24.7

Figure 7-2 shows the correlation between hardness and Young’s modulus as measured by nanoindentation at depths of 5% of coating thickness, along with cross section images to show the trend of structural evolution as hardness and Young’s modulus increased. The data point representing coating 8 on the ABS substrate has been removed as an anomaly to better show the trend. As can be seen, the linear trend is that for both substrates, as the hardness increases, so does the Young’s modulus. From [117], the hardness and Young’s modulus of the two reported coatings are both larger than reported here, although a similar linear trend is seen. In this case two different deposition processes were used. Throughout the coatings produced it can be seen that when coating mechanical properties are measured on a softer substrate (ABS), even at depths as low as 5%, the general trend is that the coating properties will be affected compared to measurements made on a harder substrate (PEI). In this instance, on the harder, stiffer substrate material, similar coatings are measured to be stiffer at small indentation

depths. This can be attributed to the different effects of elastic and plastic strain, whereby the elastic strain field extends much further into the material underneath the indenter than does the plastic strain. This giving rise to the different behaviour as the determination of hardness is dominated by plastic effects during loading, and Young's modulus is dominated by elastic effects during unloading.

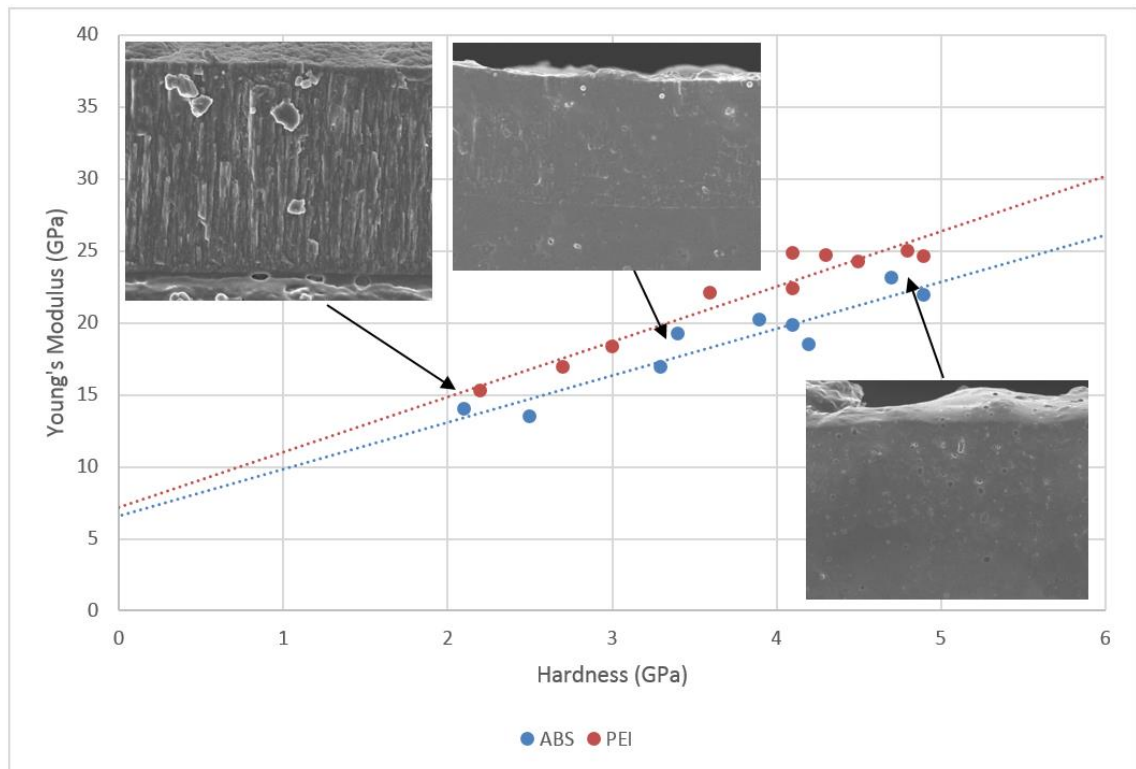


Figure 7-2 - Correlation between Hardness and Young's modulus measured by nanoindentation.

The design of experiments analysis presented in Chapter 6 showed that no single factor of deposition pressure, working gas mixture, or microwave power was significant with regards to determining hardness or Young's modulus on either substrate with a 99% confidence interval. Decreasing the confidence interval to 95% results in the working gas mixture becoming significant in determining the hardness of the coating on both substrates; the same can be said for Young's modulus, however only for PEI substrates. It could be argued that at high confidence levels (>99%) the small differences in measured H & E account for the lack of significant factors under the achievable deposition conditions (i.e. no biasing). However, when reducing the confidence interval

gas mixture becomes a significant factor for determining the H & E of coatings on PEI, but only H on ABS substrates. By removing the anomalous data point (coating 8 on ABS substrate) a clearer trend is shown for mechanical properties and this is likely to show gas mixture as a significant factor for ABS at lower confidence intervals.

Table 7-4 shows the two most significant factors of working pressure and working gas mixture for each coating produced, along with a description of the structural features observed after freeze fracturing ABS samples, and mechanical property data determined from nanoindentation at 5% coating depth (the data presented is based on measurements on PEI as these were shown to have reduced error, but follow the same trends as measurements taken on ABS). The data shows that there is a relationship between the observed structure of the coating, the deposition conditions and also the mechanical properties. The hardest coatings, produced using high ratios of acetylene and higher pressures, were shown to have amorphous or partially amorphous structures, whereby the top surface of the coating was amorphous and the interface between the coating and substrate exhibited signs of a fibrous structure.

The fibrous structure could be said to form under conditions where the frequency of carbon based species condensing on the substrate surface is reduced. Assuming all species reach the surface with similar energy, but upon reaching a stable chemical state through bonding the energy is reduced. As the coating grows from nucleation sites on the substrate, these growing sites will not have the required energy to coalesce and so will grow outwards until the surface is covered and only growth away from the surface is possible. Under conditions where species reach the surface at a higher frequency and/or energy, the nucleation sites will coalesce, forming an amorphous coating. Where there is not enough energy in the incoming species, nucleation of new structures will occur, causing defects within the coating that run parallel to the substrate surface as well as perpendicular. It is these defects which serve to reduce the density of the coating and reduce the strength of the coating, leading to a reduction in the mechanical properties measured through nanoindentation.

The intermediate structures observed whereby a fibrous structure becomes more amorphous closer to the top surface of the coating could arise in different ways. It could be that conditions become favourable for coating coalescence during different coating steps within the same batch. However, it must not be overlooked that the appearance of some of these samples could be due to the method employed to image the cross section view. Freeze fracturing using liquid nitrogen will embrittle the sample, however the fracture and crack propagation will occur based on weak points within the material as the crack dissipates energy. Any defects within the coating, such as micro-cracks due to growth stresses that do not penetrate through the whole depth of the coating, could be responsible for the structures observed.

Table 7-4 - Significant deposition conditions, coating structure and resulting mechanical properties.

Leg	Working Pressure (mbar)	Gas flow rate ratio (Ar & C ₂ H ₂) (%C ₂ H ₂)	Structural Features	Hardness (GPa) (5% coating thickness on PEI)	Young's Modulus (GPa) (5% coating thickness on PEI)
1	0.012	94	Lower fibrous, upper amorphous	4.9	24.6
2	0.011	92	Lower fibrous, upper amorphous	4.1	22.4
3	0.011	85	Amorphous	4.1	24.8
4	0.009	40	Fibrous	2.2	15.3
5	0.009	74	Fibrous	3.6	22.1
6	0.011	42	Fibrous	2.7	16.9
7	0.011	91	Amorphous	4.8	25.0
8	0.013	43	Fibrous	3.0	18.3
9	0.011	66	Lower fibrous, upper amorphous	4.5	24.2
10	0.013	67	Amorphous	4.3	24.7

Figure 7-3 shows the correlation between hardness and coating growth rate, along with examples of the structures found at the extremes of the coatings produced. As deposition rate increases, so too does hardness. This can be explained by the coating structures found through cross section SEM imagery; the fibrous, structures will have defects which under loading could slip leading to the load of the nanoindenter being spread over a smaller area. In other words the substrate, which has been shown to contribute to mechanical property measurements, would have a greater influence on such

measurements as the load will be distributed over a smaller plan area compared to when loading an amorphous structure without these 'slipping' fibrous defects and features.

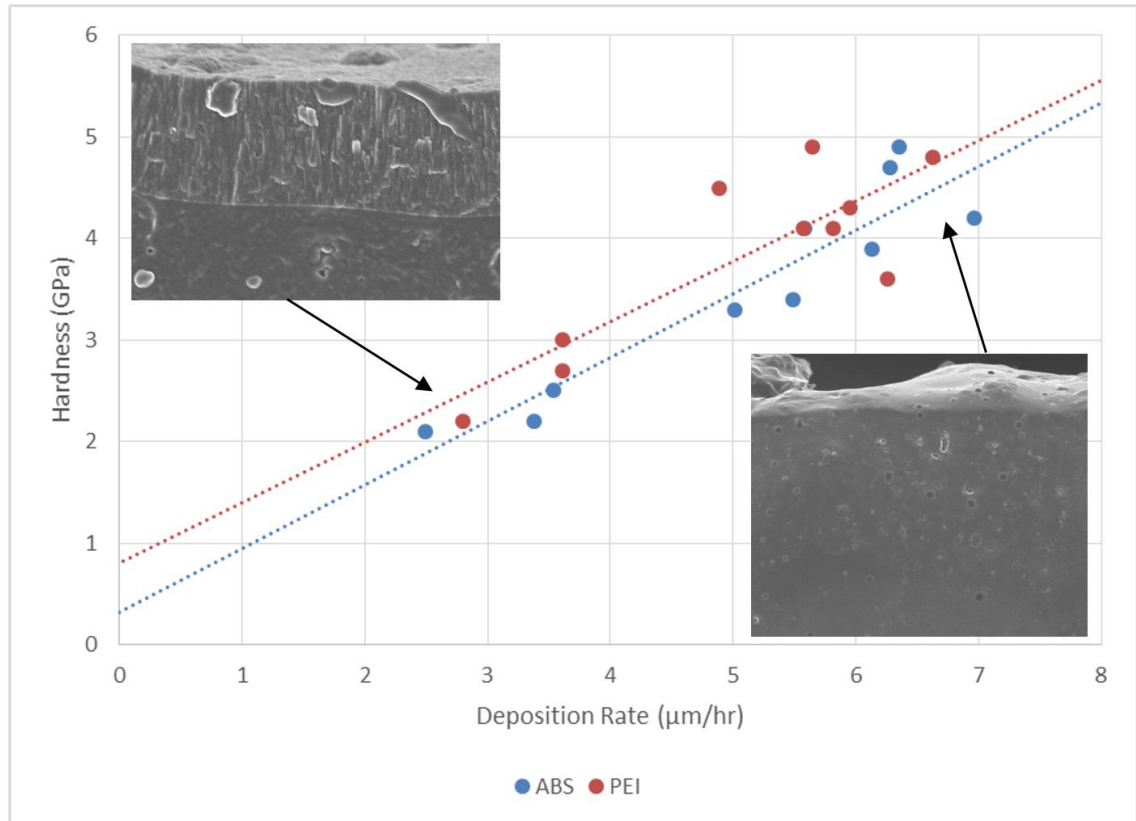


Figure 7-3 - Correlation between deposition rate and coating hardness, as measured at 5% coating depth on ABS and PEI substrates, showing observed structure for extremes in deposition rates.

This mechanism of dislocating columns/fibres is shown in Figure 7-4. The coatings that exhibit a fibrous structure still result in increased surface hardness as measured by nanoindentation and this would be due to the energy required to shear the longer, almost columnar features that are not broken up by defects that run parallel to the substrate surface. In theory, these two modes of deformation would lead to different pile-up/sink-in behaviour and this could be used to confirm this mechanism as the basis for the different mechanical performance observed. Techniques such as AFM or SEM equipped with in-situ nanoindentation would negate the need to transfer samples between equipment and locate the indentation sites, risking damage to the surface.

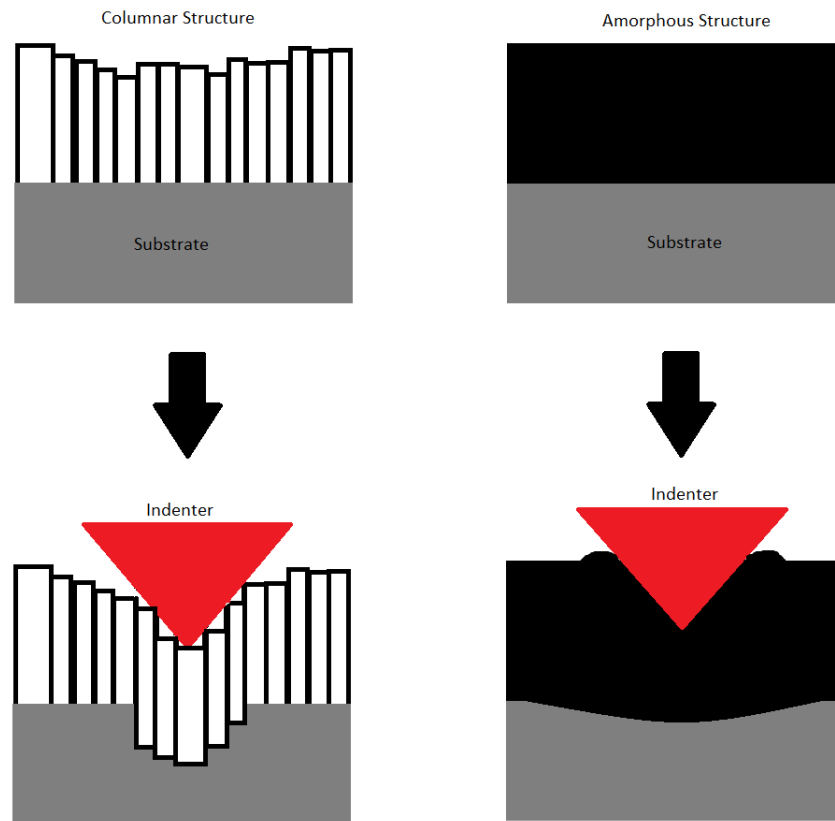


Figure 7-4 – Proposed mechanisms of coating deformation during nanoindentation for fibrous and amorphous coating structures.

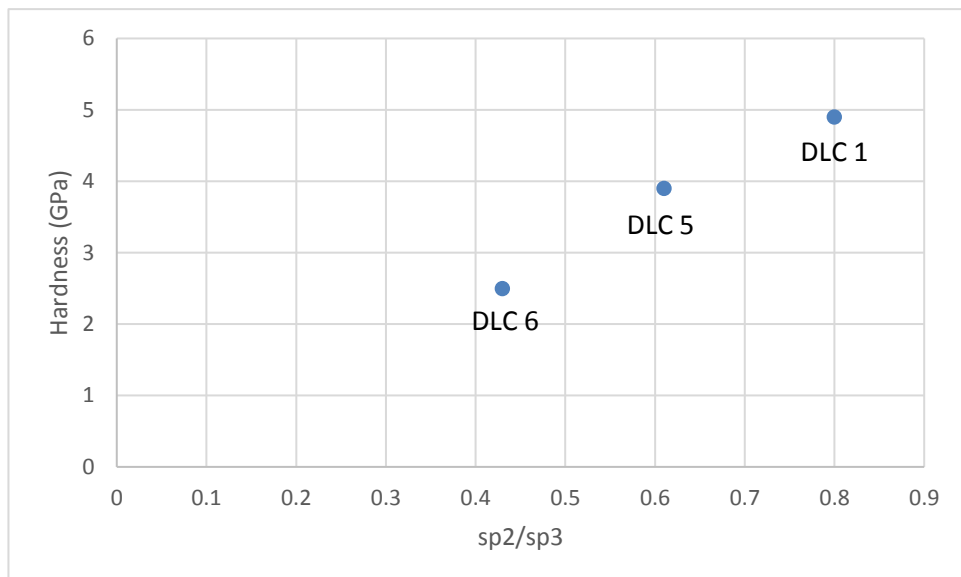


Figure 7-5 - Correlation between sp²/sp³ ratios determined by solid state NMR analysis and hardness determined by nanoindentation.

As seen in Chapter 5, the solid state NMR analysis results show that as hardness of the coatings increases, sp^2/sp^3 ratios also increase (shown in Figure 7-5). This is opposite to conventional theory whereby an increase of sp^3 content (and decrease of the ratio) would lead to increased hardness due to stronger bonding between carbon atoms. This phenomenon can be explained in two ways; the increase in sp^3 content of the coatings is due to an increase in hydrogen content, and also because of the aforementioned fibrous structures in the softer coatings.

Hydrogen content of DLC films is often not reported, this is likely due to the limited number of analysis techniques available that can quantitatively determine the composition of small atoms/species, and where this is possible, a prohibitively high cost for the information gathered. For this work, ERDA was used to determine the hydrogen content of the films in order to complement the NMR and RAMAN techniques used to determine sp^2/sp^3 content. As stated in Chapter 5 the data from the ERDA included anomalies for 2 of the three samples, however there was no reason to exclude these data points as invalid. Data for the sample DLC5 should be treated with caution due to the limited number of datapoints ($n=2$) and the range between these compared to DLC1 ($n=3$) and the combined results from 3 samples of DLC6 from different batches ($n=9$). Hydrogen content was found to decrease as the acetylene partial pressure was increased. Hydrogen content was found to be in the range of 23.6 – 42.1%.

The anomalous results in the dataset could be due to inhomogeneity of the coating. This could manifest as differences in structure within the same sample, or differences in composition, both in terms of carbon bonding and hydrogen content. The analysis techniques utilised in this work show that surface roughness is consistent in matching that of the substrate on which it was deposited and differences in structure, although apparent, could be due to the sample preparation technique used. The technique used to determine sp^2/sp^3 content requires a bulk sample and so the assumption must be made that the coating is homogenous, otherwise this data will only represent an average of the true composition over the volume of the coating analysed. ERDA analysis,

however, is a focussed beam, and any averaging based on this will be based on volumes of coating orders of magnitude lower than those used in SS-NMR. Despite this, even with a small beam diameter the analysis area would be too large to consider significant effects could arise from differences in composition between two areas of a coated sample, for example between two distinct neighbouring regions of fibrous coating and a defect free amorphous region.

The softer coatings that have been shown to contain more hydrogen could be considered as more polymer-like, with a structure that contains clusters of sp² bonded carbon, with clusters of sp³ bonded carbon that are both diamond-like and polymer-like with varying chain length. In this instance, it is not inconceivable to consider the composition varying across the sample surface depending on deposition conditions and seemingly random variation based on surface energy/chemistry and radical reactions within the plasma. The production of an inhomogeneous composition could be confirmed by mapping the mechanical properties on a sample surface and comparing those with composition mapped to the same indentation locations.

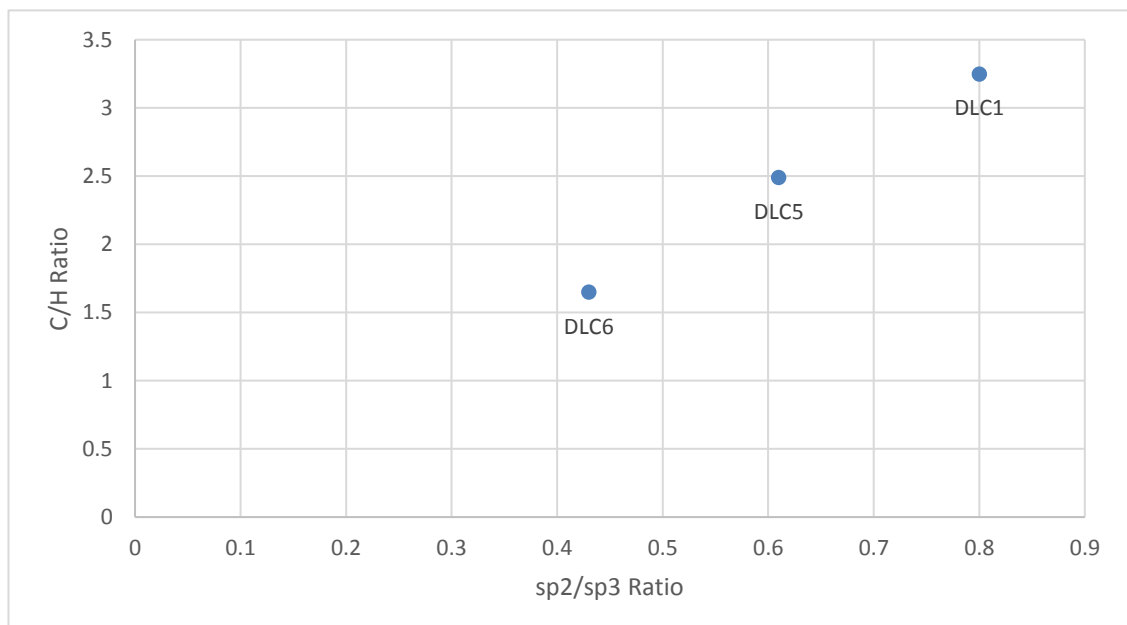


Figure 7-6 - Correlation between sp²/sp³ ratio, and C/H ratio of 3 DLC coatings.

If the average C/H ratio is taken for each sample then it can be seen that as sp² content decreases, hydrogen content increases (Figure 7-6). The increase of hydrogen content

of the films can partially, or wholly, be attributed as the cause of differing mechanical properties in the produced coatings. The increase of hydrogen content of the films and subsequent increase of sp²/sp³ ratio can be attributed to the deposition conditions. As the partial pressure of acetylene is increased during deposition, the coating becomes harder and stiffer due to a decrease in hydrogen, likely brought about by hydrogen abstraction from the surface by carbon radical during coating growth. This is shown in Figure 7-7.

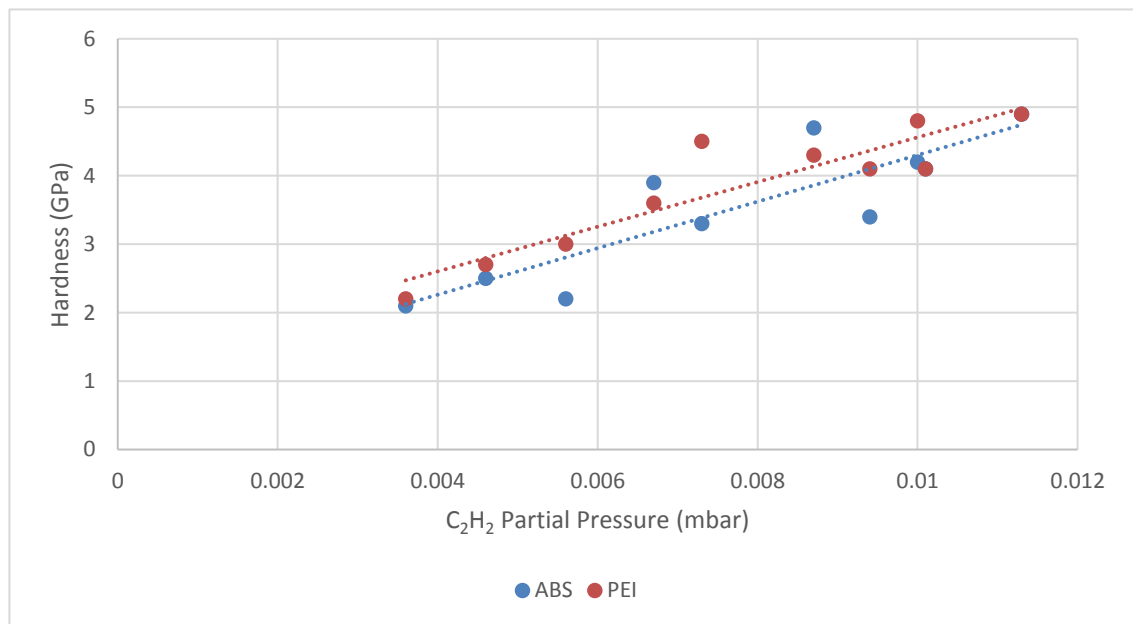


Figure 7-7 – Correlation between acetylene partial pressure and hardness (H_{5%}) of the coatings deposited on ABS and PEI substrates.

The tribology results obtained from this work are limited. Despite this some comparison with the limited literature is possible. The conditions of tests in the literature are wide ranging and so comparing the coefficient of friction (CoF) obtained for specific conditions with the CoF obtained here is not useful. Instead, certain trends can be seen; the work of Matsumoto et al. [57] showed differences in the coefficient obtained between a ceramic ball and samples with and without an oxygen plasma pre-treatment. In this work, two different plasma sources and two processing gasses were employed to produce 4 samples, which were then identically coated.

During the course of reciprocating pin on plate tests, differences between the samples became apparent as the CoF could be seen to be different. Of the identical coatings, a DC plasma source and MW plasma source utilising Ar gas for pretreatment gave differing frictional properties; the MW Ar sample settled to a steady state CoF of ~ 0.45 and the DC Ar sample a CoF of ~ 0.8 . The MW O₂ treatment reduced the CoF to ~ 0.1 from ~ 0.45 with an inert MW Ar treatment. In [57] an O₂ pre-treatment could be seen to either reduce or increase the CoF depending on the substrate material. In all cases the coating increased the CoF over that of the bare substrate.

It is worth noting that in order to have test conditions under which samples were not damaged immediately, a lubricant (PAO) was needed. The lubricant served to remove heat from the contact, without which, either the pin or plate could be seen to melt due to frictional heating. The frictional heat generated being a function of the contact pressure and sliding speed. The single test for each of the above instances gives low confidence in the presented results and so no definitive conclusion can be given on the performance exhibited. Further testing of different substrate material and coating combinations with analysis of the samples following wear of the coating would be necessary to determine the mechanisms behind the changing CoF. Limited tests of different thicknesses of the same coating suggest that the contact geometry variation arising from increased substrate effects on the deformation in the contact will affect the frictional properties of hard on soft coating systems.

Difficulties in determining the amount of deformation of the coated surfaces with respect to the loads and contact geometries used, combined with separating plastic deformation of the polymer underneath the wear track and material loss due to wear preclude detailed analysis of the wear behaviour of these samples. However, it can be theorized that in highly abrasive contacts, such as a rough DLC coating sliding against the soft ABS polymer, a transfer film of ABS will build up on the DLC surface resulting in an ABS on ABS contact. This is demonstrated by the MW O₂ treated sample reaching the same steady state CoF as bare ABS. Although not tested, increased roughening of the surface

from O₂ plasma compared to Ar plasma [118] could account for the behaviour in these tests being limited to only the O₂ etched sample.

7.4 Practical applications

The hardness and modulus measurements obtained for the ten coatings produced were shown to vary, even at low indentation depths (<10% of coating thickness). As the indentation depth decreased, both measured values increased where a maximum was obtained at depths <2% of coating thickness. The variation of which depth produced the maximum value has been mentioned previously; likely variations in contact geometry due to average surface roughness exceeding the depth of the indentation.

As such, measuring the mechanical properties of thin films on a substrate that will not be used in the final application would be expected to give false indications of the performance to be expected. If indentation depth has such a drastic effect on mechanical properties measured on soft substrates such as the polymers tested here, for a given application the composite mechanical properties should provide a more realistic estimate of system performance. In such a system, where the mechanical properties of the coating far exceed those of the substrate onto which it was deposited, the limitations of use will be a combination of the properties of the two constituent parts of the system. If high contact pressures are applied to the surface, the indentation will be expected to extend the elastic field beyond the coating and far into the substrate, leading to substrate mechanical properties dominating the observed performance. Conversely, at low contact pressures, the coating mechanical properties will have more effect.

The depth profiling of the parameter P/S^2 , shown in Chapter 6, gives an indication of the systems resistance to plastic deformation. What this can show is the indentation depth at which the coating fractures, and therefore the strain to failure of the coating dependent on the indenter geometry. The same coating was shown to fail at the same normalised indentation depth on two different substrate materials indicating the substrate had no effect on the coating's ability to support a load without failure. The expected mode of

failure would be tensile fractures at the outer edges of the indentation; this could be confirmed with SEM. From a practical standpoint, the strain to failure could vary significantly between samples of the same coating depending on coating stress variation, arising from differences in substrate geometry and the effect this would have on thermal and intrinsic growth stresses. However, utilising depth profiling nanoindentation measurements of P/S^2 to determine the indentation depth at which a sharp peak occurs would appear to be a valid method for determining strain to failure of coatings on soft substrates.

The second observation of practical importance that depth profiles of P/S^2 appear to show is the ability to more clearly separate differences of substrate materials, given the same coating has been applied. Both polymers showed similar behaviour, converging at roughly $10\text{ k nm}^2/\text{mN}$ when the indentation depth exceeded the average surface roughness; this despite clear differences in material hardness and Young's modulus measured using the same technique. At low indentation depths (<10% of coating thickness), differences between coated samples were generally within error, and as with hardness and modulus measurements, it is only as the indentation increases that more obvious differences can be seen. The measured values will converge towards that of the substrate; however, in the case of hardness and modulus the magnitude of the peak value at the lowest depths compared to the difference of properties between the two substrate materials makes this trend difficult to observe.

The P/S^2 curves begin to clearly diverge at much lower indentation depths. As the load is supported to a greater degree by the substrate, the softer and more ductile material exhibits less resistance to plastic deformation (an increase in P/S^2). As the coating begins to fail and a sudden load transfer to the substrate is made, the differences become even more apparent. The rate of the load transfer is dependent on the damping mechanisms employed by the nanoindentation equipment, however due to the sudden onset of brittle fracture and the necessity for nanoindentation equipment to capture small changes in load, it is likely that viscoelastic effects are present. These substrate effects

mean that observations by Leyland et al. [68], that parameters relating to resistance to plastic deformation better describe the wear characteristics of coatings and materials may not apply to these systems. The mechanisms of wear would be based on the elastic yield of not only the coating (small scale asperity contact), but also the substrate (larger scale yielding due to the Hertzian contact geometry). In order to investigate this further, methods for accurately determining the deflection of the composite coating system surface in a contact would need to be developed, incorporating the ductility of not only the coating, but also the ability of the substrate to yield and on what scale this is possible.

Despite both substrate materials appearing to have similar P/S^2 characteristics when uncoated, after fracture of the coating, the composite systems do not converge to the same P/S^2 value even as the indentation depth reaches beyond twice that of coating thickness. This could be due to continued load sharing between coating and substrate despite fracture, whereby the fracturing around the indenter contact does not completely separate this area of coating from the bulk; i.e. fracture extends outwards from the vertices of the indenter or an incomplete radial fracture occurs. The differences could also arise from differences of plastic behaviour not characterised at the shallow indentation depths used on the bare polymer. If indentation depths on the bare polymers were increased, the elastic/plastic strain relationships could vary. Viscoelastic and viscoplastic effects of the polymer were not investigated in this work, although in practical applications strain rate could change the behaviour observed depending on the load sharing between the elastic/plastic coating and viscoelastic/viscoplastic substrate.

The low loads used in this study and strain to failure being reached at indentation depths of 30-55%, combined with observations of rapid frictional heating under dry running conditions during tribological testing would serve to limit the use of the coating systems created and analysed in this work. DLC coatings on polymers, although in theory any coating where mechanical properties are orders of magnitude greater than the substrate material, would be limited to low strain applications. The strain to failure can be easily reached given the limited reinforcement the substrate material provides to the coating

when under load. When considering polymer substrates, the temperature limitations and insulating properties will limit the deposition techniques available for use, and this limits the range of properties that can be achieved compared to conventional methods of deposition on metallic substrates.

These temperature limitations also reduce the usefulness of these systems in high speed sliding contacts due to frictional heating reducing the polymer mechanical properties of the substrate and in extreme cases also causing melting and removal of material due to the shear forces. The use of fluids to dissipate heat would be necessary under these conditions due to the characteristic poor thermal conductivity of most polymers.

7.5 Summary

Coatings produced using a novel MW-PECVD technique were characterised using nanoindentation to determine mechanical properties at different depths. The structure and composition of the coatings were shown to effect the measured mechanical properties and the effect of the substrate on measurements was shown.

Using a design of experiments approach, it was shown that the partial pressure of C_2H_2 gas during deposition had a significant effect on the coating properties achieved. As the partial pressure increased, so too did the modulus and hardness of the coating, as well as the coating growth rate. This had no effect on coating roughness, which matched that of the underlying substrate, suggesting that within reasonable limits (i.e. shadowing) the coating would conform well to different surface geometries.

Coatings were produced with a measured peak hardness and modulus of between roughly 2 – 6GPa and 20 – 40GPa respectively. Both of these mechanical properties were seen to reduce and tend towards that of the underlying substrate as indentation depths increased. Depth profiling of P/S^2 of the coatings showed different behaviour allowing the indentation depth at which coating failure occurred to be clearly distinguished, from which strain to failure could be determined. Compared to existing examples of DLC coated polymers in the literature, the coatings presented here were in

general softer than those produced by RF-PECVD, whereby the substrates could be biased during deposition. However, where the data is given, coating growth rates using the MW-PECVD technique are greater than presented in the literature, and the coatings still result in increased hardness and stiffness as measured on the sample surface.

Tribological testing showed the coatings to have an effect on coefficient of friction compared to the substrate material (ABS), however detailed analysis of this behaviour was not carried out and so discussion is limited.

The MW-PECVD technique is a viable option for deposition of well adhered coatings to polymeric materials, that increase hardness and modulus of the sample surface, making the resulting composite more robust. However, the underlying substrate will still play a part in determining the overall performance characteristics of the system. As strain increases during indentation, substrate effects dominate, meaning these coating systems are best suited to low strain use where the increased performance of the surface can be best utilised without detrimental effects such as fracture of the coating. Although not tested, thermal conductivity of the coatings was great enough to show frictional heating during tribological reciprocating pin-on-plate testing, adding further limitations to these systems. The heating would lead to degradation of mechanical performance of the substrate, however in this case heating was extreme enough under dry running conditions that melting of the polymer occurred leading to catastrophic failure of the sample. The use of these systems would therefore need to be carefully considered for dynamic applications where removal of frictional heating would be necessary.

Chapter 8. Conclusion

This study has provided an insight into the usefulness of MW-PECVD coating techniques for depositing hard coatings onto polymeric substrates and the behaviour of these systems when subjected to mechanical loads. DLC coatings were deposited using the MW-PECVD technique on ABS and PEI substrates and the properties defined from a mechanical, structural and chemical composition perspective. The range of possible deposition parameters were explored for the deposition system used, and the conclusions are provided in this chapter.

8.1 Conclusions

8.1.1 MW-PECVD technique for coating deposition on polymers

The MW-PECVD technique used throughout this study has been shown to produce coatings at high deposition rates that conform to the substrate surface, and display good adherence to polymeric substrates. The heating rate of the deposition chamber whilst the MW plasma is ignited allows coatings to be deposited on temperature sensitive substrates ($<100^{\circ}\text{C}$), however to achieve high coating thicknesses ($>2\mu\text{m}$) it is usually necessary to deposit the coating in steps with interstitial cooling periods. The low heating rate and deposition temperatures achievable are in part due to the lack of a need to bias insulating substrates such as polymers, leading to reduced ion flux at the substrate. The Design of Experiments approach showed that increased carbon source gas (in this case C_2H_2) partial pressure, led to increased hardness and Young's modulus of the coating.

Adhesion of the DLC coatings to the ABS substrate was good enough to allow handling of the samples without precautions needed to avoid delamination, with no delamination occurring over time due to coating stresses. The cross hatch test confirmed excellent adhesion of the coating to ABS both with and without Ar^+ ion bombardment.

The range of coatings produced exhibited a range of mechanical properties, measured by nanoindentation. The hardness of the coatings, as measured at 5% depth of coating

thickness, were shown to be in the range of roughly 10 – 25x harder than the ABS substrate and the Young's modulus roughly 4 – 7x that of the ABS substrate. The surface of the ABS and PEI substrates was made more robust upon deposition of the DLC coating. The ability of the material to resist mechanical loading was increased by the coating, meaning that these coatings could have the potential to allow these polymers to be used in situations where they were not previously suitable. The caveat to this being that the substrate material still imposes mechanical limitations.

8.1.2 Substrate effects.

The lower mechanical properties of the polymer substrates used here are representative of a wide range of polymers. Indentation tests at ultra-low loads exposed that measurable differences can be seen as indentation depth is increased in the range of 1 – 10% of coating thickness; with indentations below 10% being the commonly held 'rule of thumb' used to measure coating properties with negligible substrate effects. The large property mismatch between coating and substrate led to the substrate effect being observed as a decrease in the measured coating properties as indentation depth was increased. The ultra-low load indentations resulting in depths in the range of 1 – 5% of coating thickness led to increased error, attributed to average surface roughness being a larger percentage of the total indentation depth for coatings <4 μ m thick. However, the mean measured values (both hardness and Young's modulus) could still be seen to tend towards a decreased measurement as depth increased. The validity of measuring coating properties directly on the polymer substrate, especially when the coating thickness requires indentations of depths a similar magnitude to average surface roughness, are questionable. The substrate effects in these circumstances are likely to be reducing the measured properties, even at very small indentation depths. The increased error of the measurements in the range of 1-5% of coating depth due to limitations of the technique will potentially give an untrue representation of the coating properties with a small sample size.

8.1.3 P/S^2 as a measurement of system performance

The difficulties of measuring the coating properties independently of the substrate questions the validity of providing these details for a system where in practical use, the loads and deformation of the surface will be likely to include a response from both the coating and substrate. In such cases it is arguable that a composite measurement that allows estimation of the strain to failure of the coating and the damage resistance of the system is more useful.

P/S^2 , a measure of resistance to plastic deformation, was presented as a function of depth of indentation in the range of 0.01 – 2x the thickness of the coating. The measurement is able to reliably detect the fracture of the coating, as well as show the increased component of substrate effect in the measurement.

8.2 Further Work

The work presented here has shown the limitations of current techniques widely used in the literature. As the field of coatings on polymers becomes more heavily investigated, a reliable toolkit of measurement techniques will be required in order to characterise coating and substrate systems. A thorough understanding of the coating and substrate interactions will help guide the development of these characterisation techniques based on how they behave.

As such these are the opportunities identified from this study as avenues for further work:

- Adhesion test development for coatings on soft substrates with high adhesion.
- Using carbon isotopes (^{13}C) of deposition gas to determine the adhesion mechanism of coating to substrate by tracing the origin of carbon atoms at the interface. A thorough understanding of the adhesion mechanisms of DLC coatings and different polymer materials could be given through time of flight Secondary Ion Mass Spectroscopy (tof-SIMS) analysis of the interface. The same approach would be suitable for investigating the effect of plasma based and wet chemical adhesion enhancing pre-treatment of the substrate.

- Development of nanoindentation techniques for probing coatings on soft substrates in order to determine failure strain and mechanical properties. This could be based on indenter geometry investigations, but also investigation of other nanoindentation based techniques already widely used, such as continuous stiffness measurements (CSM).
- Detailed investigation of contact mechanics of hard coatings on soft substrates to estimate contact geometry accurately and demonstrate how this changes both statically and dynamically.
- Thorough investigation of tribological properties of the type of coating systems presented here as substrate effects have been demonstrated but not investigated.

References

1. Matthews, A., Artley, R. and P, H. *2005 revisited - The UK surface engineering industry to 2010*. NASURF, 1998.
2. Mattox, D.M. and Mattox, V.H. *Vacuum Coating Technology*. Springer, 2003.
3. *PVD Decorative Coatings*. [Online]. [Accessed 01/05/2014]. Available from: <http://www.hauzertechnocoating.com/en/coating-application/decorative-applications/>
4. *Integrated Solutions for ePD Plastic Metallization*. [Online]. [Accessed 01/05/2014]. Available from: <http://www.oerlikon.com/balzers/en/products-services/integrated-solution-for-epd-plastic-metallization/>
5. Lugscheider, E., Bärwulf, S., Riester, M. and Hilgers, H. Magnetron sputtered titanium nitride thin films on thermoplastic polymers. *Surface and Coatings Technology*. 1999, **116**, pp.1172-1178.
6. Su, C., Lin, C., Chang, C., Hung, H. and Lin, T. Mechanical and optical properties of diamond-like carbon thin films deposited by low temperature process. *Thin Solid Films*. 2006, **498**(1), pp.220-223.
7. Kern, W. *Thin film processes II*. Academic press, 1991.
8. Inan, U.S. and Gołkowski, M. *Principles of plasma physics for engineers and scientists*. Cambridge University Press, 2010. ability
9. Mahan, J.E. Physical vapor deposition of thin films. *Physical Vapor Deposition of Thin Films, by John E. Mahan, pp. 336. ISBN 0-471-33001-9. Wiley-VCH, January 2000. 2000, 1*.
10. Roth, J.R. *Industrial Plasma Engineering: Volume 2-Applications to Nonthermal Plasma Processing*. CRC press, 2001.
11. Frey, H. and Khan, H.R. *Handbook of thin film technology*. Springer, 2010.
12. Mahan, J.E. and Vantomme, A. Trends in sputter yield data in the film deposition regime. *Physical Review B*. 2000, **61**(12), pp.8516-8525.
13. Oechsner, H. Sputtering—a review of some recent experimental and theoretical aspects. *Applied physics*. 1975, **8**(3), pp.185-198.
14. Window, B. and Savvides, N. Charged particle fluxes from planar magnetron sputtering sources. *Journal of Vacuum Science & Technology A: Vacuum, Surfaces, and Films*. 1986, **4**(2), pp.196-202.
15. Kelly, P. and Arnell, R. Magnetron sputtering: a review of recent developments and applications. *Vacuum*. 2000, **56**(3), pp.159-172.
16. Schiller, S., Goedicke, K., Reschke, J., Kirchhoff, V., Schneider, S. and Milde, F. Pulsed magnetron sputter technology. *Surface and Coatings Technology*. 1993, **61**(1), pp.331-337.
17. Olbrich, W., Fessmann, J., Kampschulte, G. and Ebberink, J. Improved control of TiN coating properties using cathodic arc evaporation with a pulsed bias. *Surface and Coatings Technology*. 1991, **49**(1), pp.258-262.
18. Kääriäinen, T.O., Kelly, P.J., Cameron, D.C., Beake, B., Li, H., Barker, P.M. and Struller, C.F. Nanoscratch testing of atomic layer deposition and magnetron sputtered TiO₂ and Al₂O₃ coatings on polymeric substrates. *Journal of Vacuum Science & Technology A*. 2011, **30**(1), p.01A132.

19. Sarakinos, K., Alami, J. and Konstantinidis, S. High power pulsed magnetron sputtering: A review on scientific and engineering state of the art. *Surface and Coatings Technology*. 2010, **204**(11), pp.1661-1684.
20. Alami, J. Plasma Characterization & Thin Film Growth and Analysis in Highly Ionized Magnetron Sputtering. 2005.
21. Moghal, J., Suttle, H., Cook, A.G., Grovenor, C.R. and Assender, H.E. Investigation of the mechanical properties of aluminium oxide thin films on polymer substrates by a combination of fragmentation and scratch testing. *Surface and Coatings Technology*. 2012, **206**(14), pp.3309-3315.
22. Ratova, M., West, G. and Kelly, P. HiPIMS deposition of tungsten-doped titania coatings for photocatalytic applications. *Vacuum*. 2014, **102**, pp.48-50.
23. Brown, I.G. Cathodic arc deposition of films. *Annual review of materials science*. 1998, **28**(1), pp.243-269.
24. Plyutto, A., Ryzhkov, V. and Kapin, A. High speed plasma streams in vacuum arcs. *Sov. Phys. JETP*. 1965, **20**(2), pp.328-337.
25. Boelens, S. and Veltrop, H. Hard coatings of TiN,(TiHf) N and (TiNb) N deposited by random and steered arc evaporation. *Surface and Coatings Technology*. 1987, **33**, pp.63-71.
26. Vyskočil, J. and Musil, J. Cathodic arc evaporation in thin film technology. *Journal of Vacuum Science & Technology A*. 1992, **10**(4), pp.1740-1748.
27. Martin, P. and Bendavid, A. Review of the filtered vacuum arc process and materials deposition. *Thin Solid Films*. 2001, **394**(1), pp.1-14.
28. Zhitomirsky, V., David, T., Boxman, R., Goldsmith, S., Verdyan, A., Soifer, Y.M. and Rapoport, L. Properties of SnO₂ coatings fabricated on polymer substrates using filtered vacuum arc deposition. *Thin Solid Films*. 2005, **492**(1), pp.187-194.
29. Taeschner, K., Bartzsch, H., Frach, P. and Schultheiss, E. Scratch resistant optical coatings on polymers by magnetron-plasma-enhanced chemical vapor deposition. *Thin Solid Films*. 2012, **520**(12), pp.4150-4154.
30. Zeng, L., Feng, W., Ding, G., Dechun, B. and Chunming, L. Frictional and Optical Properties of Diamond-Like-Carbon Coatings on Polycarbonate. *Plasma Science and Technology*. 2013, **15**(7), p.690.
31. Ashby, M. and Jones, D. *Engineering Materials 1: An Introduction to Properties, Applications and Design*. Great Britain: Elsevier, 2005.
32. Hall, C., Field, S., Zuber, K., Murphy, P. and Evans, D. Corrosion resistance of robust optical and electrical thin film coatings on polymeric substrates. *Corrosion Science*. 2013, **69**, pp.406-411.
33. Schulz, U. Review of modern techniques to generate antireflective properties on thermoplastic polymers. *Applied optics*. 2006, **45**(7), pp.1608-1618.
34. Weber, A., Dietz, A., Pöckelmann, R. and Klages, C.P. Metallization of Polymers Using Plasma-Enhanced Chemical Vapor Deposited Titanium Nitride as Interlayer. *Journal of The Electrochemical Society*. 1997, **144**(3), pp.1131-1135.
35. Sarto, F., Alvisi, M., Melissano, E., Rizzo, A., Scaglione, S. and Vasanelli, L. Adhesion enhancement of optical coatings on plastic substrate via ion treatment. *Thin Solid Films*. 1999, **346**(1), pp.196-201.
36. Tanberg, R. and Berkey, W. On the temperature of cathode in vacuum arc. *Physical Review*. 1931, **38**(2), p.296.

37. Dos Santos Ferreira, O., Stevens, A. and Schrauwen, C. Quantitative comparison of adhesion in metal-to-plastic systems. *Thin Solid Films*. 2009, **517**(10), pp.3070-3074.
38. Liston, E., Martinu, L. and Wertheimer, M. Plasma surface modification of polymers for improved adhesion: a critical review. *Journal of Adhesion Science and Technology*. 1993, **7**(10), pp.1091-1127.
39. Trakhtenberg, I.S., Bakunin, O., Korneyev, I., Plotnikov, S., Rubshtein, A. and Uemura, K. Substrate surface temperature as a decisive parameter for diamond-like carbon film adhesion to polyethylene substrates. *Diamond and related materials*. 2000, **9**(3), pp.711-714.
40. Teixeira, V. Mechanical integrity in PVD coatings due to the presence of residual stresses. *Thin Solid Films*. 2001, **392**(2), pp.276-281.
41. Windischmann, H. Intrinsic stress in sputter-deposited thin films. *Critical Reviews in Solid State and Material Sciences*. 1992, **17**(6), pp.547-596.
42. Stoney, G.G. The tension of metallic films deposited by electrolysis. *Proceedings of the Royal Society of London. Series A, Containing Papers of a Mathematical and Physical Character*. 1909, **82**(553), pp.172-175.
43. Lackner, J.M., Waldhauser, W., Major, L., Teichert, C. and Hartmann, P. Tribology of bio-inspired nanowrinkled films on ultrasoft substrates. *Computational and structural biotechnology journal*. 2013, **6**(7), pp.1-12.
44. Heavens, O. Some factors influencing the adhesion of films produced by vacuum evaporation. *J. Phys. Radium*. 1950, **11**(7), pp.355-360.
45. Veldkamp, J., Hattu, N. and Sniijders, V. Crack formation during scratching of brittle materials. In: *Flaws and Testing*. Springer, 1978, pp.273-301.
46. Steinmann, P., Tardy, Y. and Hintermann, H. Adhesion testing by the scratch test method: the influence of intrinsic and extrinsic parameters on the critical load. *Thin Solid Films*. 1987, **154**(1), pp.333-349.
47. Burnett, P. and Rickerby, D. The relationship between hardness and scratch adhesion. *Thin Solid Films*. 1987, **154**(1-2), pp.403-416.
48. Bull, S., Rickerby, D., Matthews, A., Leyland, A., Pace, A. and Valli, J. The use of scratch adhesion testing for the determination of interfacial adhesion: the importance of frictional drag. *Surface and Coatings Technology*. 1988, **36**(1-2), pp.503-517.
49. Thouless, M. An analysis of spalling in the microscratch test. *Engineering Fracture Mechanics*. 1998, **61**(1), pp.75-81.
50. Ollendorf, H. and Schneider, D. A comparative study of adhesion test methods for hard coatings. *Surface and Coatings Technology*. 1999, **113**(1), pp.86-102.
51. Heinke, W., Leyland, A., Matthews, A., Berg, G., Friedrich, C. and Broszeit, E. Evaluation of PVD nitride coatings, using impact, scratch and Rockwell-C adhesion tests. *Thin Solid Films*. 1995, **270**(1-2), pp.431-438.
52. Volinsky, A., Moody, N. and Gerberich, W. Interfacial toughness measurements for thin films on substrates. *Acta materialia*. 2002, **50**(3), pp.441-466.
53. Bucaille, J., Felder, E. and Hochstetter, G. Mechanical analysis of the scratch test on elastic and perfectly plastic materials with the three-dimensional finite element modeling. *Wear*. 2001, **249**(5), pp.422-432.

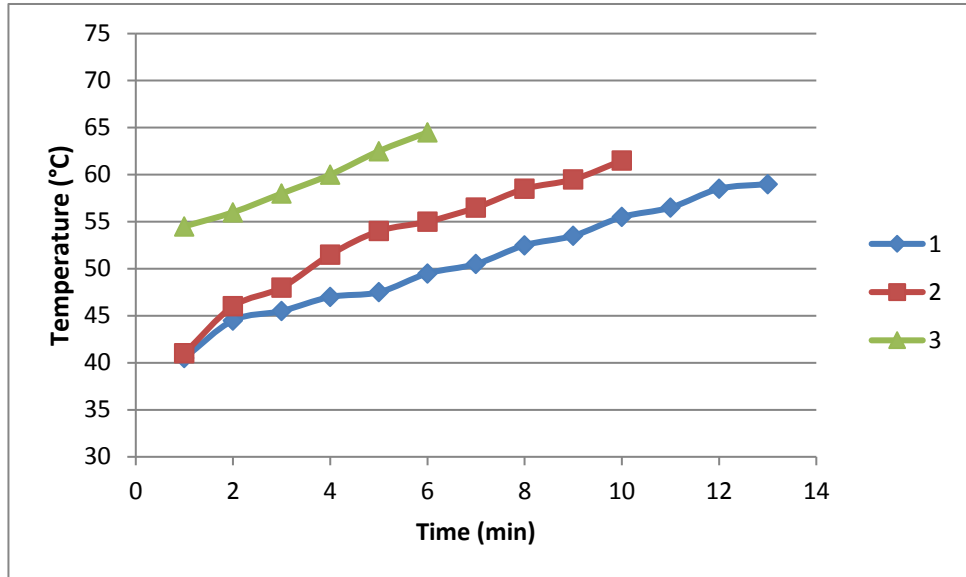
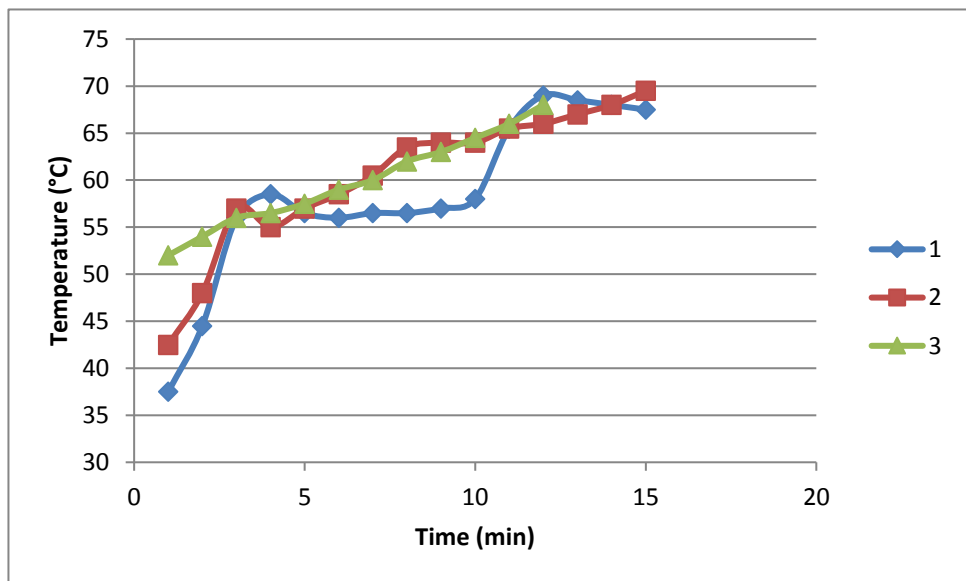
54. Damasceno, J., Camargo Jr, S. and Cremona, M. Optical and mechanical properties of DLC-Si coatings on polycarbonate. *Thin Solid Films*. 2003, **433**(1), pp.199-204.
55. Gauthier, C., Durier, A.-L., Fond, C. and Schirrer, R. Scratching of a coated polymer and mechanical analysis of a scratch resistance solution. *Tribology International*. 2006, **39**(2), pp.88-98.
56. Ollivier, B. and Matthews, A. Adhesion of diamond-like carbon films on polymers: an assessment of the validity of the scratch test technique applied to flexible substrates. *Journal of Adhesion Science and Technology*. 1994, **8**(6), pp.651-662.
57. Matsumoto, R., Sato, K., Ozeki, K., Hirakuri, K. and Fukui, Y. Cytotoxicity and tribological property of DLC films deposited on polymeric materials. *Diamond and related materials*. 2008, **17**(7), pp.1680-1684.
58. Pharr, G. and Oliver, W. Measurement of thin film mechanical properties using nanoindentation. *Mrs Bulletin*. 1992, **17**(07), pp.28-33.
59. Oliver, W.C. and Pharr, G.M. An improved technique for determining hardness and elastic modulus using load and displacement sensing indentation experiments. *Journal of materials research*. 1992, **7**(06), pp.1564-1583.
60. Pelegri, A.A. and Huang, X. Nanoindentation on soft film/hard substrate and hard film/soft substrate material systems with finite element analysis. *Composites Science and Technology*. 2008, **68**(1), pp.147-155.
61. Han, S.M., Saha, R. and Nix, W.D. Determining hardness of thin films in elastically mismatched film-on-substrate systems using nanoindentation. *Acta materialia*. 2006, **54**(6), pp.1571-1581.
62. Saha, R. and Nix, W.D. Effects of the substrate on the determination of thin film mechanical properties by nanoindentation. *Acta materialia*. 2002, **50**(1), pp.23-38.
63. Gamonpilas, C. and Busso, E.P. On the effect of substrate properties on the indentation behaviour of coated systems. *Materials Science and Engineering: A*. 2004, **380**(1), pp.52-61.
64. Sun, Y., Bell, T. and Zheng, S. Finite element analysis of the critical ratio of coating thickness to indentation depth for coating property measurements by nanoindentation. *Thin Solid Films*. 1995, **258**(1), pp.198-204.
65. Chen, S., Liu, L. and Wang, T. Investigation of the mechanical properties of thin films by nanoindentation, considering the effects of thickness and different coating-substrate combinations. *Surface and Coatings Technology*. 2005, **191**(1), pp.25-32.
66. Korsunsky, A., McGurk, M., Bull, S. and Page, T. On the hardness of coated systems. *Surface and Coatings Technology*. 1998, **99**(1), pp.171-183.
67. Joslin, D. and Oliver, W. A new method for analyzing data from continuous depth-sensing microindentation tests. *Journal of materials research*. 1990, **5**(1), pp.123-126.
68. Leyland, A. and Matthews, A. On the significance of the H/E ratio in wear control: a nanocomposite coating approach to optimised tribological behaviour. *Wear*. 2000, **246**(1), pp.1-11.
69. Shi, K., Wang, C., Gross, C. and Chung, Y.-W. Reversing the inverse hardness-toughness trend using W/VC multilayer coatings. *Surface and Coatings Technology*. 2015, **284**, pp.80-84.

70. Lin, J., Jang, J., Park, I.-w. and Wei, R. Structure and properties of CrSiCN coatings deposited by pulsed dc magnetron sputtering for wear and erosion protection. *Surface and Coatings Technology*. 2016, **287**, pp.44-54.
71. Ou, Y., Lin, J., Che, H., Sproul, W., Moore, J. and Lei, M. Mechanical and tribological properties of CrN/TiN multilayer coatings deposited by pulsed dc magnetron sputtering. *Surface and Coatings Technology*. 2015, **276**, pp.152-159.
72. Qiu, Z.-K., Zhang, P.-Z., Wei, D.-B., Wei, X.-F. and Chen, X.-H. A study on tribological behavior of double-glow plasma surface alloying W-Mo coating on gear steel. *Surface and Coatings Technology*. 2015, **278**, pp.92-98.
73. Tang, J.-l., Liu, G.-j., Wang, J., Wu, Z.-c., Zhao, Y.-j. and Fu, X.-h. Study on deposition of amorphous hydrogenate DLC films on germanium substrates by RF-PECVD. In: *4th International Symposium on Advanced Optical Manufacturing and Testing Technologies: Advanced Optical Manufacturing Technologies*: International Society for Optics and Photonics, 2009, pp.72822U-72822U-72825.
74. Hosseini, S., Shoki, B., Malekfar, R. and Sharifian, M. Dual frequency plasma enhanced chemical vapor deposition of Diamond like carbon. In: *Plasma Science-Abstracts, 2009. ICOPS 2009. IEEE International Conference on*: IEEE, 2009, pp.1-1.
75. Masami, I., Haruho, M., Tatsuya, M. and Junho, C. Low temperature Si-DLC coatings on fluoro rubber by a bipolar pulse type PBI system. *Surface and Coatings Technology*. 2011, **206**(5), pp.999-1002.
76. Noborisaka, M., Kodama, H., Nagashima, S., Shirakura, A., Horiuchi, T. and Suzuki, T. Synthesis of transparent and hard SiOC (- H) thin films on polycarbonate substrates by PECVD method. *Surface and Coatings Technology*. 2012, **206**(8), pp.2581-2584.
77. Donnet, C. and Erdemir, A. *Tribology of diamond-like carbon films: fundamentals and applications*. Springer Science & Business Media, 2007.
78. Aisenberg, S. and Chabot, R. Ion-beam deposition of thin films of diamondlike carbon. *Journal of applied physics*. 1971, **42**(7), pp.2953-2958.
79. Donnet, C. Recent progress on the tribology of doped diamond-like and carbon alloy coatings: a review. *Surface and Coatings Technology*. 1998, **100**, pp.180-186.
80. Grill, A. Tribology of diamondlike carbon and related materials: an updated review. *Surface and Coatings Technology*. 1997, **94**, pp.507-513.
81. Voevodin, A., Donley, M. and Zabinski, J. Pulsed laser deposition of diamond-like carbon wear protective coatings: a review. *Surface and Coatings Technology*. 1997, **92**(1), pp.42-49.
82. Dearnaley, G. and Arps, J.H. Biomedical applications of diamond-like carbon (DLC) coatings: A review. *Surface and Coatings Technology*. 2005, **200**(7), pp.2518-2524.
83. Hauert, R. A review of modified DLC coatings for biological applications. *Diamond and related materials*. 2003, **12**(3), pp.583-589.
84. Vetter, J. 60years of DLC coatings: Historical highlights and technical review of cathodic arc processes to synthesize various DLC types, and

- their evolution for industrial applications. *Surface and Coatings Technology*. 2014, **257**, pp.213-240.
85. Robertson, J. Diamond-like amorphous carbon. *Materials Science and Engineering: R: Reports*. 2002, **37**(4), pp.129-281.
 86. Hainsworth, S.V. and Uhure, N. Diamond like carbon coatings for tribology: production techniques, characterisation methods and applications. *International materials reviews*. 2007, **52**(3), pp.153-174.
 87. Ferrari, A. and Robertson, J. Resonant Raman spectroscopy of disordered, amorphous, and diamondlike carbon. *Physical Review B*. 2001, **64**(7), p.075414.
 88. Ferrari, A.C. Determination of bonding in diamond-like carbon by Raman spectroscopy. *Diamond and related materials*. 2002, **11**(3), pp.1053-1061.
 89. Ferrari, A., Kleinsorge, B., Adamopoulos, G., Robertson, J., Milne, W., Stolojan, V., Brown, L., LiBassi, A. and Tanner, B. Determination of bonding in amorphous carbons by electron energy loss spectroscopy, Raman scattering and X-ray reflectivity. *Journal of non-crystalline solids*. 2000, **266**, pp.765-768.
 90. Tai, F.-C., Lee, S.-C., Wei, C. and Tyan, S. Correlation between ID/IG Ratio from Visible Raman Spectra and sp²/sp³ Ratio from XPS Spectra of Annealed Hydrogenated DLC Film. *Materials transactions*. 2006, **47**(7), pp.1847-1852.
 91. Ferrari, A.C. and Robertson, J. Raman spectroscopy of amorphous, nanostructured, diamond-like carbon, and nanodiamond. *Philosophical Transactions of the Royal Society of London A: Mathematical, Physical and Engineering Sciences*. 2004, **362**(1824), pp.2477-2512.
 92. Irmer, G. and Dorner-Reisel, A. Micro-Raman Studies on DLC coatings. *Advanced Engineering Materials*. 2005, **7**(8), pp.694-705.
 93. Vasquez-Borucki, S., Achete, C.A. and Jacob, W. Hydrogen plasma treatment of poly (ethylene terephthalate) surfaces. *Surface and Coatings Technology*. 2001, **138**(2), pp.256-263.
 94. Vandencastele, N. and Reniers, F. Plasma-modified polymer surfaces: Characterization using XPS. *Journal of Electron Spectroscopy and Related Phenomena*. 2010, **178**, pp.394-408.
 95. Iseki, T., Mori, H., Hasegawa, H., Tachikawa, H. and Nakanishi, K. Structural analysis of Si-containing diamond-like carbon. *Diamond and related materials*. 2006, **15**(4), pp.1004-1010.
 96. Doyle, B. and Percy, P. Technique for profiling 1H with 2.5-MeV Van de Graaff accelerators. *Applied Physics Letters*. 1979, **34**(11), pp.811-813.
 97. Suzuki, M., Ohana, T. and Tanaka, A. Tribological properties of DLC films with different hydrogen contents in water environment. *Diamond and related materials*. 2004, **13**(11), pp.2216-2220.
 98. Konishi, Y., Konishi, I., Sakauchi, N., Hayashi, S., Hirakimoto, A. and Suzuki, J. Measurement of hydrogen content in diamond like carbon thin films by ERDA. *Nuclear Instruments and Methods in Physics Research Section B: Beam Interactions with Materials and Atoms*. 1996, **118**(1-4), pp.312-317.
 99. Ohkawara, Y., Ohshio, S., Suzuki, T., Ito, H., Yatsui, K. and Saitoh, H. Quantitative analysis of hydrogen in amorphous films of hydrogenated carbon nitride. *Japanese journal of applied physics*. 2001, **40**(12R), p.7007.

100. Ma, W.J., Ruys, A.J., Mason, R.S., Martin, P.J., Bendavid, A., Liu, Z., Ionescu, M. and Zreiqat, H. DLC coatings: effects of physical and chemical properties on biological response. *Biomaterials*. 2007, **28**(9), pp.1620-1628.
101. Rossnagel, S., Cuomo, J. and Westwood, W. *Handbook of Plasma Processing Technology: Fundamentals, Etching, Deposition and Surface Interactions*. New York: Noyes Publications, 1990.
102. Xiao, W. and Jiang, X. Optical and mechanical properties of nanocrystalline aluminum oxynitride films prepared by electron cyclotron resonance plasma enhanced chemical vapor deposition. *Journal of crystal growth*. 2004, **264**(1), pp.165-171.
103. Hofrichter, A., Bulkin, P. and Drévilion, B. Plasma enhanced chemical vapour deposition of SiO_xN_y in an integrated distributed electron cyclotron resonance reactor. *Applied surface science*. 1999, **142**(1), pp.447-450.
104. Aanesland, A., Bredin, J., Chabert, P. and Godyak, V. Electron energy distribution function and plasma parameters across magnetic filters. *Applied Physics Letters*. 2012, **100**(4), p.044102.
105. Martinu, L. and Poitras, D. Plasma deposition of optical films and coatings: A review. *Journal of Vacuum Science & Technology A: Vacuum, Surfaces, and Films*. 2000, **18**(6), pp.2619-2645.
106. Chapman, B. *Glow Discharge Processes Sputtering and Plasma Etching*. Canada: John Wiley and Sons inc., 1980.
107. Fischer, C.B., Rohrbeck, M., Wehner, S., Richter, M. and Schmeißer, D. Interlayer formation of diamond-like carbon coatings on industrial polyethylene: Thickness dependent surface characterization by SEM, AFM and NEXAFS. *Applied surface science*. 2013, **271**, pp.381-389.
108. Hoshida, T., Tsubone, D., Takada, K., Kodama, H., Hasebe, T., Kamijo, A., Suzuki, T. and Hotta, A. Controlling the adhesion between diamond-like carbon (DLC) film and high-density polyethylene (HDPE) substrate. *Surface and Coatings Technology*. 2007, **202**(4), pp.1089-1093.
109. Mattox, D.M. *Handbook of physical vapor deposition (PVD) processing*. William Andrew, 2010.
110. Pandiyaraj, K.N., Selvarajan, V., Heeg, J., Junge, F., Lampka, A., Barfels, T., Wienecke, M., Rhee, Y.H. and Kim, H.W. Influence of bias voltage on diamond like carbon (DLC) film deposited on polyethylene terephthalate (PET) film surfaces using PECVD and its blood compatibility. *Diamond and related materials*. 2010, **19**(7), pp.1085-1092.
111. Ohtake, N., Uchi, T., Yasuhara, T. and Takashima, M. Characteristics of Diamond-Like Carbon Films Deposited on Polymer Dental Materials. *Japanese journal of applied physics*. 2012, **51**(9R), p.090128.
112. Lin, C.-R., Wei, D.-H., Chang, C.-K., Liao, W.-H. and Peng, K.R. Diamond-like carbon films deposited at room temperature on flexible plastics substrates for antireflection coating. *Japanese journal of applied physics*. 2011, **50**(3R), p.035802.
113. Guo, C. Diamond-like carbon films deposited on polycarbonates by plasma-enhanced chemical vapor deposition. *Thin Solid Films*. 2008, **516**(12), pp.4053-4058.
114. Lin, Z., Lv, S.-B., Yu, Z.-J., Li, M., Lin, T.-Y., Ba, D.-C., Choi, C.-K. and Lee, I.-S. Effect of bias voltage on Diamond-like carbon film deposited on PMMA substrate. *Surface and Coatings Technology*. 2008, **202**(22), pp.5386-5389.

115. Li, D., Cui, F., Gu, H. and Li, W. Ion beam-assisted deposition of DLC films on PMMA and TiN/PMMA. *Vacuum*. 2000, **56**(3), pp.205-211.
116. Cuong, N., Tahara, M., Yamauchi, N. and Sone, T. Diamond-like carbon films deposited on polymers by plasma-enhanced chemical vapor deposition. *Surface and Coatings Technology*. 2003, **174**, pp.1024-1028.
117. Fruth, W., Meerkamm, H., Krumpiegl, T., Schaufler, C., Erkens, G. and Ruttor, M. Tribological behaviour of PVD-coated PA plastic material sliding against metal counterparts. *Surface and Coatings Technology*. 1999, **120**, pp.470-475.
118. Baba, K. and Hatada, R. Deposition of diamond-like carbon films on polymers by plasma source ion implantation. *Thin Solid Films*. 2006, **506**, pp.55-58.
119. Austin, L.B. *Evaluation and optimisation of diamond-like carbon for tribological applications*. University of Leeds, 2014.
120. Sansonetti, J.E. and Martin, W.C. Handbook of basic atomic spectroscopic data. *Journal of Physical and Chemical Reference Data*. 2005, **34**(4), pp.1559-2259.
121. Shen, V., Siderius, D., Krekelberg, W. and Hatch, H. *NIST chemistry webbook, NIST standard reference database number 173, National Institute of Standards and Technology, Gaithersburg MD, 20899*. 2017. [Accessed 14/09/2017].
122. Strinić, A., Malović, G., Petrović, Z.L. and Sadeghi, N. Electron excitation coefficients and cross sections for excited levels of argon and xenon ions. *Plasma Sources Science and Technology*. 2004, **13**(2), p.333.
123. Briscoe, B., Fiori, L. and Pelillo, E. Nano-indentation of polymeric surfaces. *Journal of Physics D: Applied Physics*. 1998, **31**(19), p.2395.
124. Chong, A.C. and Lam, D.C. Strain gradient plasticity effect in indentation hardness of polymers. *Journal of materials research*. 1999, **14**(10), pp.4103-4110.
125. Ohgoe, Y., Hirakuri, K.K., Tsuchimoto, K., Friedbacher, G. and Miyashita, O. Uniform deposition of diamond-like carbon films on polymeric materials for biomedical applications. *Surface and Coatings Technology*. 2004, **184**(2), pp.263-269.
126. Igarashi, A., Hayashi, H., Yamanobe, T. and Komoto, T. Structure and morphology of diamond-like carbon coated on nylon 66/poly (phenylene ether) alloy. *Journal of molecular structure*. 2006, **788**(1), pp.238-245.

Appendix A: Temperature evolution during deposition.**Figure A.1- Temperature evolution during leg 2 of DOE.****Figure A.2 - Temperature evolution during leg 3 of DOE.**

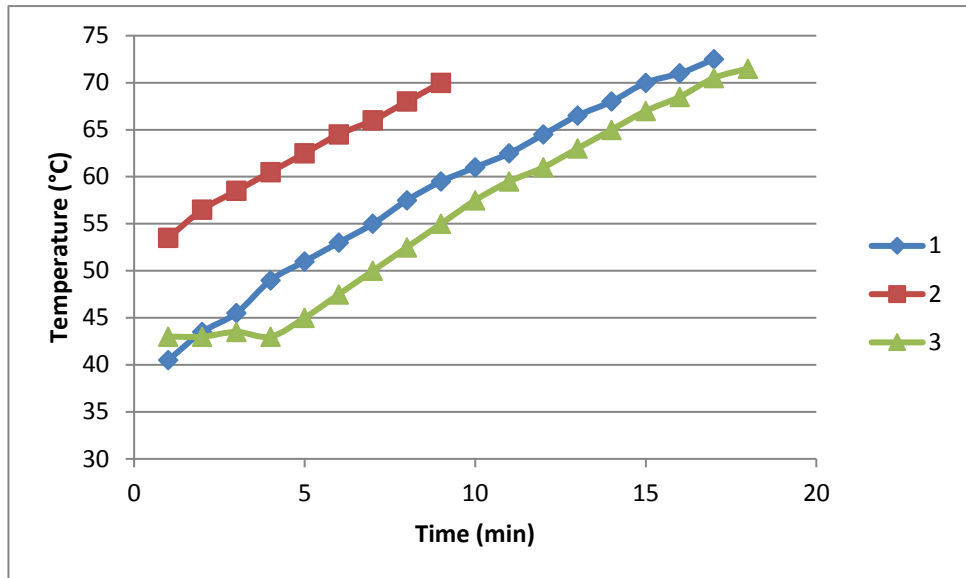


Figure A.3 - Temperature evolution during leg 4 of DOE.

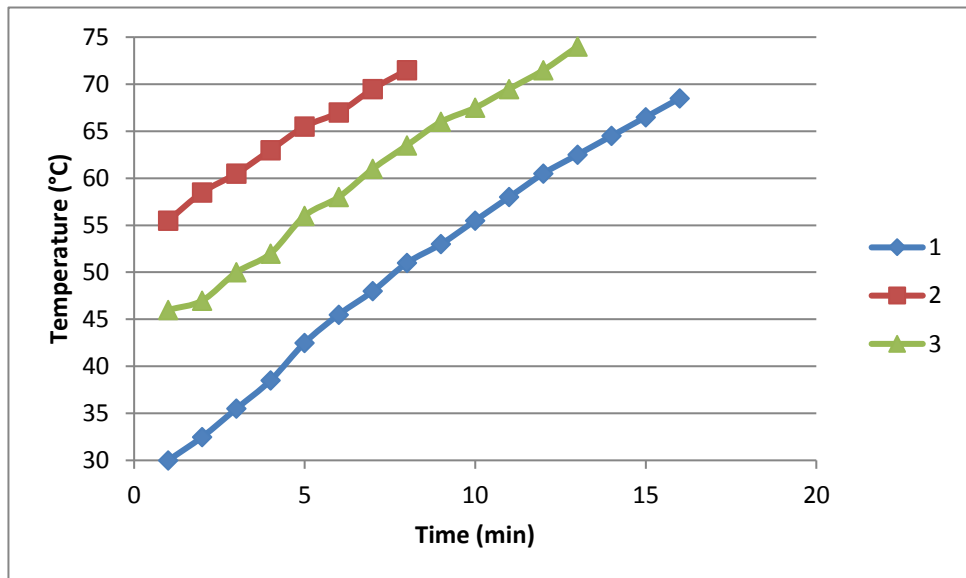


Figure A.4 - Temperature evolution during leg 5 of DOE.

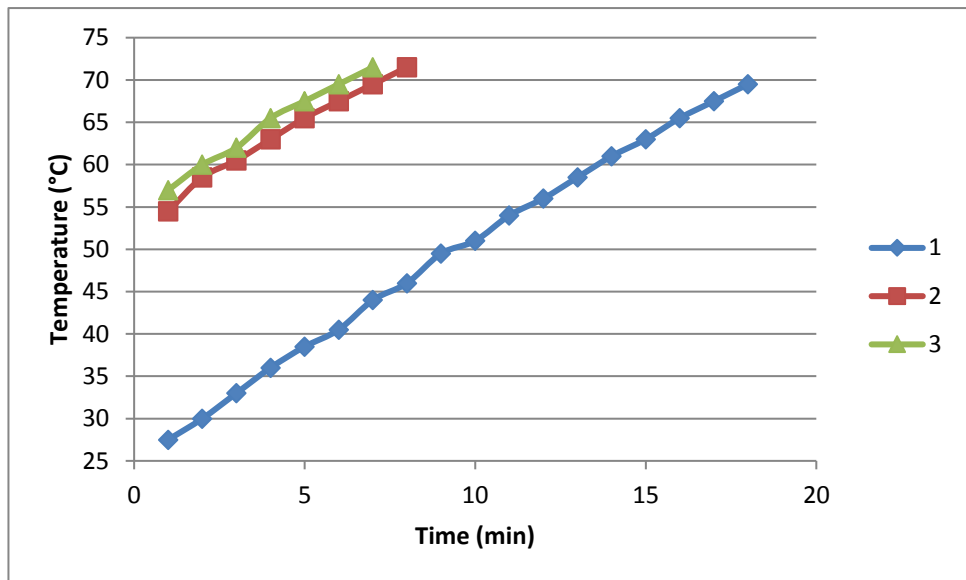


Figure A.5 - Temperature evolution during leg 6 of DOE.

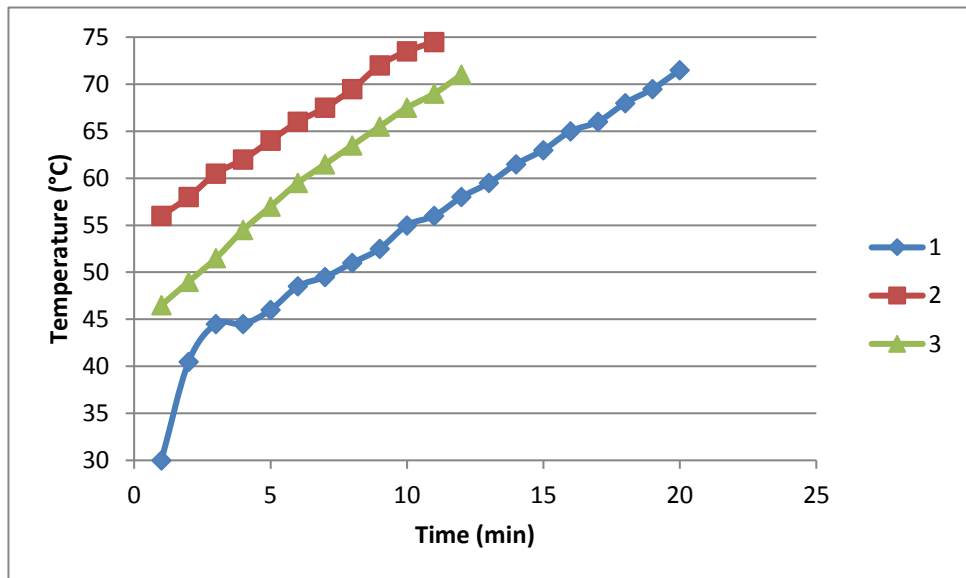


Figure A.6 - Temperature evolution during leg 7 of DOE.

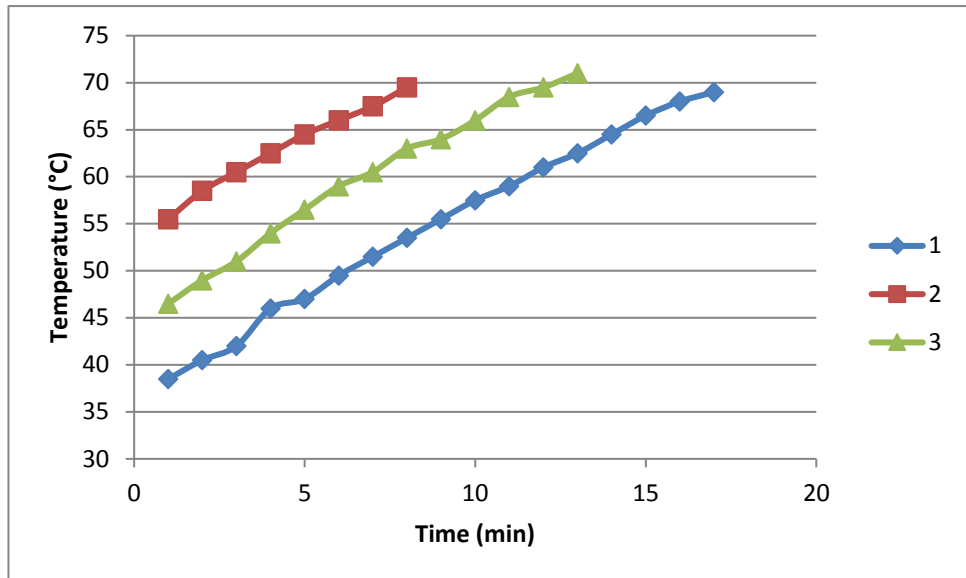


Figure A.7 - Temperature evolution during leg 8 of DOE.

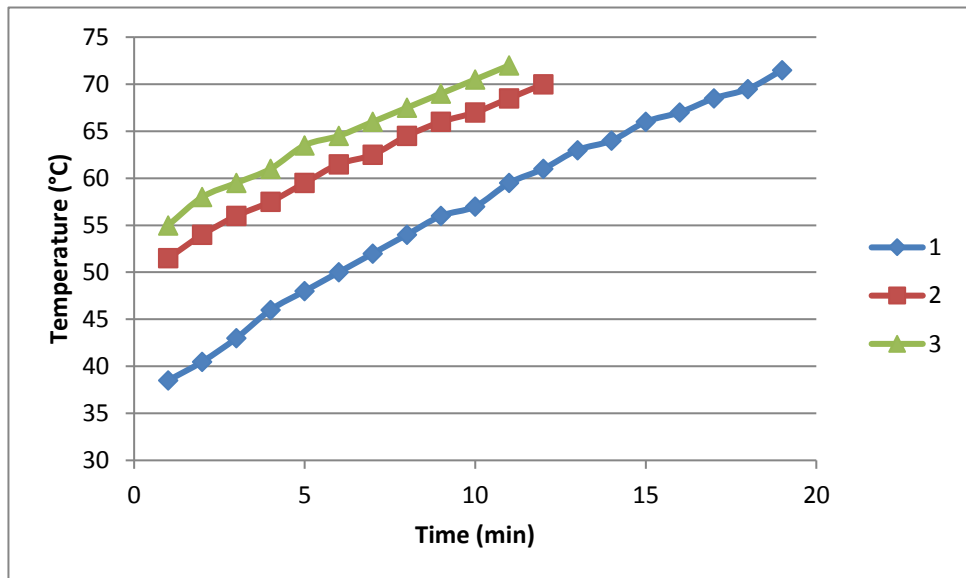


Figure A.8 - Temperature evolution during leg 9 of DOE.

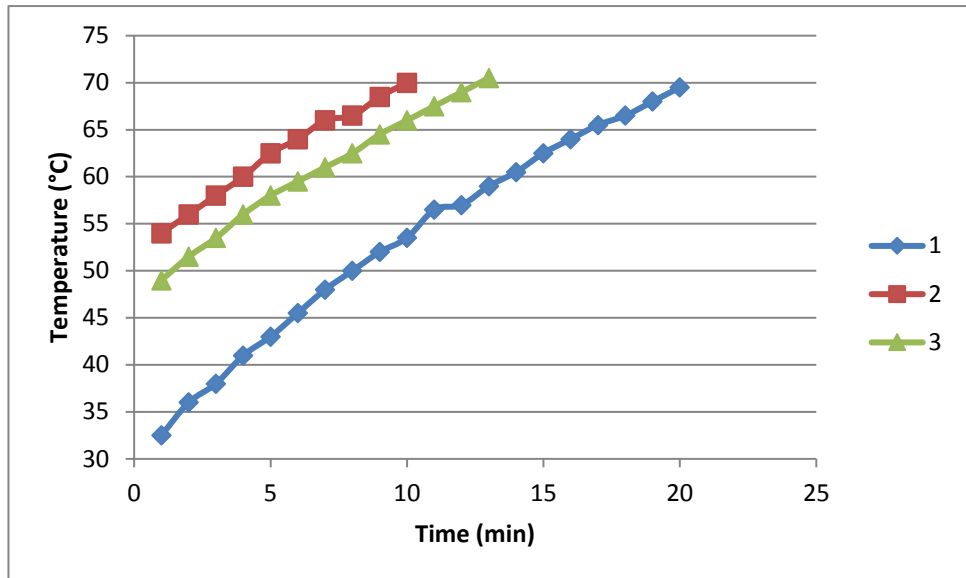


Figure A.9 - Temperature evolution during leg 10 of DOE.

Appendix B: Supplementary DOE Analysis data.

Response Heating Rate (°C/min)

Actual by Predicted Plot

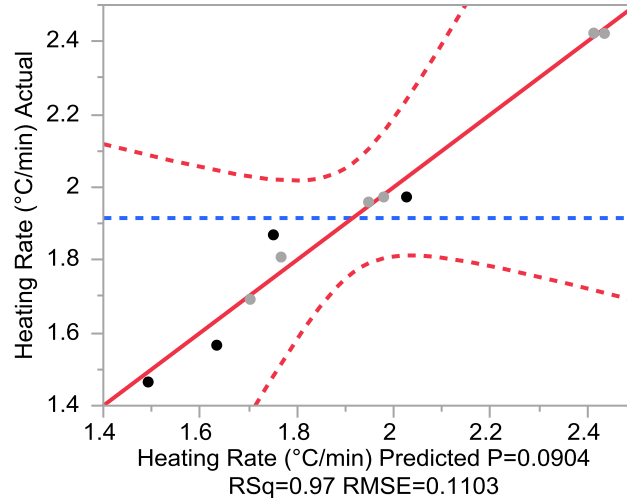


Figure B.1 – Actual by predicted plot for heating rate.

Table B.1 – Summary of fit for heating rate.

RSquare	0.973279
RSquare Adj	0.879753
Root Mean Square Error	0.110348
Mean of Response	1.915
Observations (or Sum Wgts)	10

Table B.2 – ANOVA table for heating rate.

Source	DF	Sum of Squares	Mean Square	F Ratio
Model	7	0.88701877	0.126717	10.4066
Error	2	0.02435323	0.012177	Prob > F
C. Total	9	0.91137200		0.0904

Response ABS Deposition Rate ($\mu\text{m/hr}$)

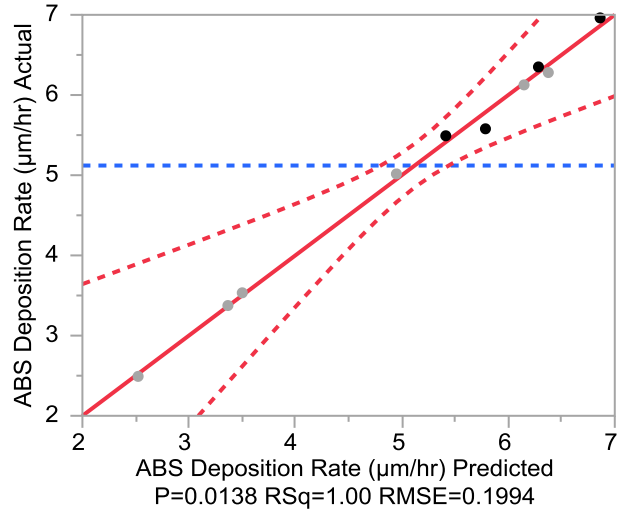


Figure B.2 – Actual by predicted plot for ABS deposition rate.

Table B.3 – Summary of fit for ABS deposition rate.

RSquare	0.996042
RSquare Adj	0.982189
Root Mean Square Error	0.199426
Mean of Response	5.120673
Observations (or Sum Wgts)	10

Table B.4 – AONVA table for ABS deposition rate.

Source	DF	Sum of Squares	Mean Square	F Ratio
Model	7	20.016731	2.85953	71.9005
Error	2	0.079541	0.03977	Prob > F
C. Total	9	20.096273		0.0138*

Response PEI Deposition Rate ($\mu\text{m/hr}$)

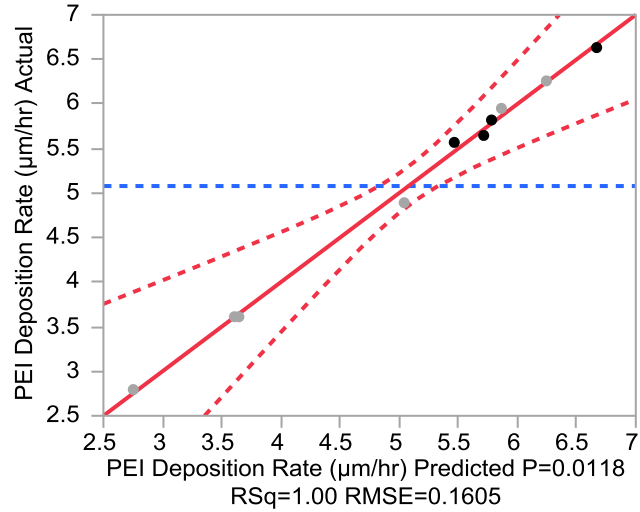


Figure B.3 – Actual by predicted plot for PEI deposition rate.

Table B.5 - Summary of fit for PEI deposition rate.

RSquare	0.99662
RSquare Adj	0.984788
Root Mean Square Error	0.160474
Mean of Response	5.078484
Observations (or Sum Wgts)	10

Table B.6 – ANOVA table for PEI deposition rate.

Source	DF	Sum of Squares	Mean Square	F Ratio
Model	7	15.184518	2.16922	84.2351
Error	2	0.051504	0.02575	Prob > F
C. Total	9	15.236022		0.0118*

Response ABS Hardness (GPa)

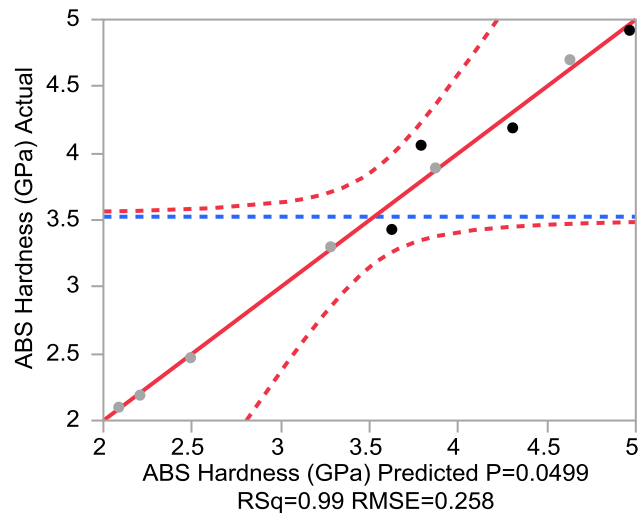


Figure B.4 – Actual by predicted plot for ABS hardness.

Table B.7 – Summary of fit for ABS hardness.

RSquare	0.985493
RSquare Adj	0.934718
Root Mean Square Error	0.257959
Mean of Response	3.525
Observations (or Sum Wgts)	10

Table B.8 – ANOVA table for ABS hardness.

Source	DF	Sum of Squares	Mean Square	F Ratio
Model	7	9.0407647	1.29154	19.4092
Error	2	0.1330853	0.06654	Prob > F
C. Total	9	9.1738500		0.0499*

Response PEI Hardness (GPa)

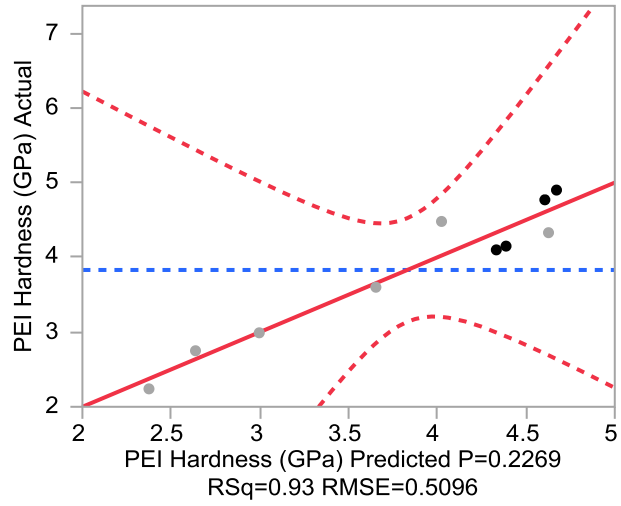


Figure B.5 – Actual by predicted plot for PEI hardness.

Table B.9 – Summary of fit for PEI hardness.

RSquare	0.929127
RSquare Adj	0.681071
Root Mean Square Error	0.509632
Mean of Response	3.831
Observations (or Sum Wgts)	10

Table B.10 – ANOVA table for PEI hardness.

Source	DF	Sum of Squares	Mean Square	F Ratio
Model	7	6.8098401	0.972834	3.7456
Error	2	0.5194499	0.259725	Prob > F
C. Total	9	7.3292900		0.2269

Response ABS Young's Modulus (GPa)

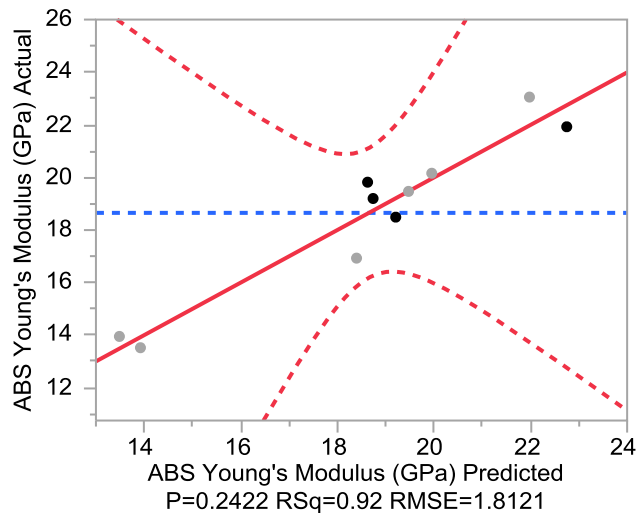


Figure B.6 – Actual by predicted plot for ABS Young’s modulus.

Table B.11 – Summary of fit for ABS Young’s modulus.

RSquare	0.923828
RSquare Adj	0.657224
Root Mean Square Error	1.812136
Mean of Response	18.653
Observations (or Sum Wgts)	10

Table B.12 – ANOVA table for ABS Young’s modulus.

Source	DF	Sum of Squares	Mean Square	F Ratio
Model	7	79.653539	11.3791	3.4652
Error	2	6.567671	3.2838	Prob > F
C. Total	9	86.221210		0.2422

Response PEI Young's Modulus (GPa)

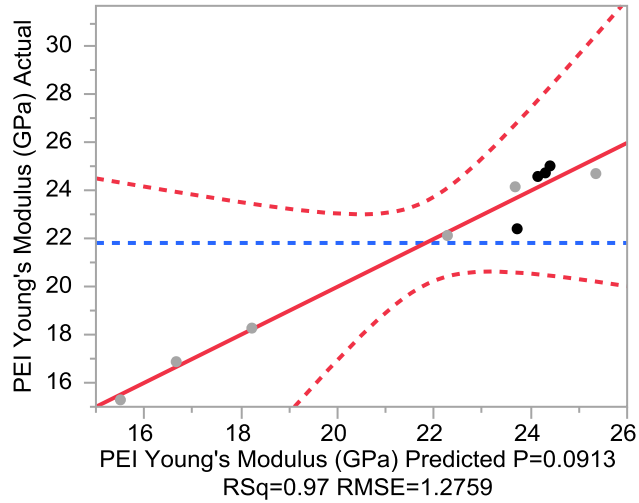


Figure B.7 – Actual by predicted plot for PEI Young’s modulus.

Table B.13 – Summary of fit for PEI Young’s modulus.

RSquare	0.973016
RSquare Adj	0.878573
Root Mean Square Error	1.27586
Mean of Response	21.829
Observations (or Sum Wgts)	10

Table B.14 – ANOVA table for PEI Young’s modulus.

Source	DF	Sum of Squares	Mean Square	F Ratio
Model	7	117.39625	16.7709	10.3027
Error	2	3.25564	1.6278	Prob > F
C. Total	9	120.65189		0.0913